# AN ABSTRACT OF THE DISSERTATION OF

Hossein Dormohammadi for the degree of Doctor of Philosophy in Civil Engineering presented on September 19, 2018.

Title: Investigation of Iron Passivity and Chloride-induced Depassivation in Alkaline Electrolytes using Reactive Force Field Molecular Dynamics (ReaxFF-MD)

Abstract approved:

_____

O. Burkan Isgor

The corrosion and passivity of iron (and carbon steel) in media with different alkalinity as well as iron depassivation have been studied extensively using electrochemical methods and nano-scale surface characterization studies. The electrochemical techniques provide valuable information about the average electrochemical behavior of relatively large metal surfaces, typically in centimeter-square scale or larger. However, electrochemical processes on these surfaces typically occur in nanometer scale. Although nano-scale surface characterizations provide valuable information about passive films that form on carbon steel and iron in alkaline electrolytes, and their chloride-induced depassivation, they cannot explain the dynamic processes that lead to their formation as they can only provide data at particular instants. Atomistic modeling techniques such as Reactive Force Field Molecular Dynamics (ReaxFF-MD) have the potential to fill this gap. This research used ReaxFF-MD simulations to answer fundamental questions on iron corrosion, passivation and chloride-induced depassivation in four interrelated thrusts:

Thrust 1: ReaxFF-MD was used to study the initial stages of iron corrosion in pure water. The simulations were performed on iron under various applied external electric fields and temperatures. Oxide film formation was accompanied by iron dissolution in water, indicating active corrosion and supporting the expected thermodynamic

behavior of iron in pure water. Oxide film thickness and iron dissolution increased with increasing applied external electric field. Corrosion rates increased slightly with increasing temperature within the temperature range of this investigation (300–350 K). Critical stages of the iron corrosion process during the simulations were identified as dissociation of water to $OH^-$ and $H^+$, adsorption of $OH^-$ on the iron surface, penetration of oxygen into iron to form iron oxides, and dissolution of iron into solution. Comparisons of the simulated charge distributions and pair distribution functions to those of reference oxides showed the formed oxide compositions were not pure phases, but rather a mixture of oxides.

Thrust 2: The applicability of the classical EDL models was investigated to study corrosion and passivity of iron in neutral and alkaline media using ReaxFF-MD. The performance of the classical EDL models were studied in the ReaxFF-MD simulations of iron exposed to neutral (pH = 7) and highly alkaline (pH = 13.5) electrolytes under applied electric fields. Although the Helmholtz model was able to produce iron corrosion in the neutral electrolyte, it did not result in passive film formation in the highly alkaline solution system. The Gouy-Chapman model was not capable of simulating passivity for iron in the highly alkaline solution system or active corrosion in the neutral electrolyte. The Stern model was the only model that could simulate passivity and corrosion of iron for highly alkaline and neutral electrolytes, respectively. This study showed that ReaxFF-MD simulations of iron in neutral and alkaline electrolytes should use the Stern model for representing the EDL.

Thrust 3: The passivity of Fe(110) in a 0.316 M NaOH solution (pH = 13.5) was investigated using ReaxFF-MD. The simulations were carried out under an applied electric field of 30 MeV/cm. The electrical double layer was modeled using the Stern model. Under these conditions, following the expected thermodynamic behavior, a protective passive film formed during 500 ps simulation time. The initial stages of passivation differed from simulations that had been carried out in neutral electrolytes such that the highly alkaline environment allowed the stabilization of the metal through the formation of an $Fe(OH)_2$ layer on the metal surface. This created conditions for oxygen diffusion into metal without dissolution of iron atoms into the electrolyte. The passive film had a multiple oxide structure such that outer layers were in the form of

$Fe_2O_3$, middle layers were in the form of $Fe_3O_4$, and the inner layer was in the form of FeO. This multi-layer structure is in agreement with theoretical passivity models that are based on an inner barrier layer that forms directly on the metal substrate (FeO), and outer layers ($Fe_3O_4$ and $Fe_2O_3$) that precipitates through the further oxidation of the iron ejected from the inner layer. A parallel XPS investigation confirmed the findings of ReaxFF-MD simulations.

Thrust 4: Chloride-induced depasivation of iron in pH 13.5 NaOH solution was studied using ReaxFF-MD, electrochemical tests and x-ray photoelectron spectroscopy (XPS). The breakdown of the passive film by chlorides initiates with iron dissolution from the first layer of the passive film into the electrolyte. Iron dissolution and corresponding iron vacancy formation in the first layer of the passive film take place in four stages that involves local acidification of the electrolyte adjacent to the metal surface, followed by iron dissolution into the electrolyte in the form of $Fe(OH)Cl_2$ and $FeCl_3$. Chloride in the electrolyte mainly acts as a catalyst and do not penetrate into the passive film. The four-step process for the initiation of the passive film breakdown was used to explain the concept of a critical chloride threshold and the well-documented electrochemical observation that critical chloride thresholds are higher in solution with solution with higher pH. The ReaxFF-MD simulations support the depassivation hypothesis that is described by the point defect model. Both ReaxFF-MD simulations and XPS analysis showed that chlorides increase the $Fe^{+3}/Fe^{+2}$ of the passive film, and this increase is more evident in the inner and middle layers of the film.

It is expected that these fundamental findings of this research will facilitate the development of new corrosion mitigation strategies such as customized corrosion inhibitors and inexpensive corrosion-resistant steels.

# Investigation of Iron Passivity and Chloride-induced Depassivation in Alkaline Electrolytes using Reactive Force Field Molecular Dynamics (ReaxFF-MD)

by
Hossein Dormohammadi

A DISSERTATION

submitted to

Oregon State University

in partial fulfillment of
the requirements for the
degree of

Doctor of Philosophy

Presented September 19, 2018
Commencement June 2019

Doctor of Philosophy dissertation of Hossein Dormohammadi presented on September 19, 2018

APPROVED:

Major Professor, representing Civil Engineering

Head of the School of Civil and Construction Engineering

Dean of the Graduate School

I understand that my dissertation will become part of the permanent collection of Oregon State University libraries. My signature below authorizes release of my dissertation to any reader upon request.

Hossein Dormohammadi, Author

# ACKNOWLEDGEMENTS

Firstly, I would like to thank my mother, my father, my sisters, my brothers, and other members of my family, for all they have done for me during my time as a graduate student at Oregon State University. I have always had my family to count on when times were rough, and they have always been there for me.

I would like to express my sincere appreciation to my advisor Professor O. Burkan Isgor for his patience, enthusiasm, immense knowledge, and most importantly, for his continued support of my Ph.D. research. His expertise and his strong support helped me in all aspects of my study, research, and writing of this dissertation. I am honored for being a part of his research team. I will always be thankful of having the chance to work with him during my academic life.

I would like to highlight my special thanks to Professor Líney Árnadóttir for her guidance toward advancing my understanding of the molecular dynamics simulations and her continued support during my research. Her expertise on quantum mechanics and atomistic/molecular simulation techniques was instrumental in helping me analyze and interpret my results.

I would like to thank Qin Pang, my research partner in this project, who used density functional theory to produce supportive and comparative data for my molecular dynamic simulations.

I would like to express my appreciation to Pratik Vinod Murkute for his leadership and expertise in providing validating experimental data using x-ray photoelectron spectroscopy.

I would like to express my sincere gratitude to my committee members Professors Jason Weiss, Jason H. Ideker, Líney Árnadóttir and John Sessions, whose guidance was critical for the success of this research.

Thank you to the engineering support group, especially Paul Montagne, at the School of Civil and Construction Engineering and Mike Sander at HPC cluster of College of Engineering for the troubleshooting all the cluster computer issues raised during my research.

Thank you to the staff in the School of Civil and Construction Engineering, in particular, Kathy Westberg, Cindy Olson, Dana Ainsworth, Michelle McAllaster and Tara Cooper, for always being there for me to answer all my questions.

I also would like to express my appreciation to my wonderful colleagues and friends, especially Dr. Vahid Jafari Azad, who were always available to discuss my research and provide emotional support and their friendship whenever I needed.

This study was fully funded by the National Science Foundation, DMMI, Grant No. 1435417. In addition, part of this work used the Extreme Science and Engineering Discovery Environment (XSEDE) Comet at the San Diego Supercomputer Center (SDSC) allocation TGENG170002. XSEDE is supported by National Science Foundation grant number ACI-1053575. I would like to express my deepest gratitude for both organizations.

# CONTRIBUTION OF AUTHORS

Professor O. Burkan Isgor advised me in all simulations, analysis and interpretation of the results, and writing the manuscripts and the dissertation.

Professor Líney Árnadóttir assisted me in the simulations, analysis and interpretation of the results, and writing the manuscripts.

Qin pang used density functional theory to produce supportive and comparative data for my molecular dynamic simulations. She also assisted me in editing and reviewing the manuscripts.

Pratik Vinod Murkute provided experimental support and validation data for the simulations using X-ray photoelectron spectroscopy (XPS) and was involved in the writing of manuscripts 3 and 4.

# TABLE OF CONTENTS

TABLE OF CONTENTS (Continued)

Page

TABLE OF CONTENTS (Continued)

Page

TABLE OF CONTENTS (Continued)

Page

# LIST OF FIGURES

# LIST OF FIGURES (Continued)

# LIST OF FIGURES (Continued)

Figure Page

# LIST OF FIGURES (Continued)

Figure Page

# LIST OF FIGURES (Continued)

# LIST OF FIGURES (Continued)

Figure Page

# LIST OF FIGURES (Continued)

Figure Page

# LIST OF APPENDICES

# LIST OF APPENDIX FIGURES

# LIST OF APPENDIX FIGURES (Continued)

# LIST OF APPENDIX FIGURES (Continued)

Figure Page

# LIST OF APPENDIX TABLES

# 1. General introduction and literature review

## 1.1. Scope and layout of this dissertation

This doctorate thesis follows the manuscript option for the Doctor of Philosophy degree as described in the 2018 Oregon State University Graduate School Thesis Guide. The research presented in this dissertation is an investigation of iron passivity and chloride-induced depassivation in alkaline electrolytes using Reactive Force Field Molecular Dynamics (ReaxFF-MD). The dissertation is presented through a literature review, four manuscripts, and general conclusions. The details of each chapter are described as follows:

Chapter 1: *General Introduction and Literature Review* – This chapter provides the critical need for research, proposed approach, and a literature review. The literature review focuses on iron passivity and chloride-induced depassivation studies, the use of ReaxFF-MD in studying similar processes, and Electrical Double Layer (EDL) models that are relevant to the work presented here.

Chapter 2: *Manuscript 1* – The first manuscript in this dissertation is titled "Atomistic simulation of initial stages of iron corrosion in pure water using reactive molecular dynamics." The main goal of this chapter is to investigate the capability of the ReaxFF-MD to study corrosion in iron-electrolyte systems. The simulations were performed on iron and pure water to explore the oxide film formation and the critical stages of iron corrosion process. Active corrosion was observed supporting the expected thermodynamic behavior of iron in pure water. By studying the oxide film, it was shown that the formed oxide compositions were not pure phases, but rather a mixture of oxides. This manuscript has been published in Computational Materials Science in January 2018 [1].

Chapter 3: *Manuscript 2* – The second manuscript in this dissertation is titled "Investigation of the applicability of classical electrical double layer models to study corrosion and passivity of iron in neutral and alkaline electrolytes." The EDL plays a major role in the electrochemical processes at the interface between the metal surface and the electrolyte. The main goal of this chapter is to investigate the applicability of classical EDL models to study passivity of iron in highly alkaline media. ReaxFF-MD simulations were conducted to simulate the EDL between pure iron and a highly alkaline electrolyte using three well-known EDL models: Helmholtz, Gouy-Chapman and

Stern. As a control study a system with iron and a neutral solution was also simulated. It was shown that the Stern model was able to yield iron corrosion in neutral solutions and passive film formation in alkaline electrolytes. This manuscript will be submitted to the Journal of the Electrochemical Society in September 2018.

Chapter 4: *Manuscript 3* – The third manuscript in this dissertation is titled "Molecular dynamics modeling of iron passivity in alkaline electrolyte." The main goal of this chapter is to perform a detailed study on the initial stages of iron passivity and investigate the oxide states of the passive film. The simulations were performed in a highly alkaline electrolyte surrogating for concrete pore solutions. As per the outcome of Chapter 3, Stern model for EDL was used in all simulations. The processes that lead to iron passivation were identified and iron oxides in the passive film were characterized. This manuscript will be submitted to Corrosion Science in September 2018.

Chapter 5: *Manuscript 4* – The forth manuscript in this dissertation is titled "Investigation of chloride-induced depassivation in alkaline electrolyte: A molecular dynamics study." There are knowledge gaps and a number of research questions raised in chloride-induced depassivation of iron in alkaline environments. Even though several researchers presented a few hypotheses to fill these gaps, ReaxFF-MD modeling of the depassivation is needed to develop fundamental understanding of the chloride-induced depassivation process. The passive film produced in Chapter 4 was exposed to chloride containing alkaline electrolytes. In order to study the concept of chloride threshold, ReaxFF-MD simulations were conducted with different concentrations of sodium chloride. The compositions of the depassivated film was studied and was compared to the experimental data. This manuscript will be submitted to Nature Materials in September 2018.

Chapter 6: *General Conclusions* – A summary of major findings and conclusions of the research completed in this dissertation are provided in this chapter.

Chapter 7: *References* – This chapter includes a comprehensive list of references used in this dissertation including the present chapter.

Appendix A: *Supplementary Material of Manuscript 1*- ReaxFF-MD simulations of the manuscript 1 were performed on pure iron surfaces for different surface orientations (i.e., (1 1 1), (1 1 0) and (1 0 0)). Since the results of the simulations of different iron surfaces were similar,

only the results of the Fe(1 1 0)-water simulations are presented in the main body of the manuscript. The simulations of (1 1 1) and (1 0 0) orientations are provided in this chapter.

### 1.2. Critical need and proposed approach

Corrosion of the steel reinforcement in concrete is one of the leading causes for infrastructure failure and service interruptions. It also creates considerable financial burden; for example, the annual cost of corrosion in highway bridges alone is estimated to be above $13.6 billion as of 2013 [2]. The Federal Highway Administration estimates that it will cost $20.5 billion annually for the next 16 years to properly update existing bridges, more than 60% of what is currently being spent [3].

Typical corrosion mitigation strategies involve various methods to delay or mitigate the onset of steel corrosion such as the use of high-quality and thick concrete cover above reinforcement, corrosion-resistant reinforcement (e.g. stainless or galvanized steels), barrier coatings applied on steel reinforcement (e.g. epoxy) or on the exposed surfaces of concrete (e.g. sealers), and corrosion inhibitors that are either added into the concrete mixture or applied externally (e.g. migrating inhibitors). Some of these techniques can be highly effective, as in the case of stainless steels, however, their high cost has limited their widespread utilization. Other methods are not always feasible or effective, especially in highly aggressive environments or when the structures experience multiple sources of distress [4-8]. There is a need to develop new technologies (e.g. new corrosion resistant steels or custom-designed corrosion inhibitors) that are inexpensive and highly effective.

The development of such technologies has been slow and mostly unsuccessful because of the knowledge gaps in the fundamental understanding of the passivity of steels in concrete and lack of tools to intelligently design and test them. However, closing these knowledge gaps has also been proven to be rather challenging. As it will be shown later, passivity and corrosion of steel in concrete are phenomena that take place within a very thin layer on the metal surface in atomic/molecular scale. Therefore, studies to develop fundamental understanding need to combine electrochemical observations, nano-scale material characterization techniques, and

atomic/molecular scale simulation methods such as Molecular Dynamics (MD) or Density Functional Theory (DFT).

Passivity and chloride-induced corrosion initiation/propagation of iron and carbon steel in highly alkaline environments, such as the ones provided by concrete, have been studied extensively using electrochemical [9-22] and nano-scale surface characterization techniques [23-29]. The electrochemical studies have mostly provided macro-scale bulk observations that do not necessarily help explain nano-scale processes. Analytical surface characterization studies have shown snapshots of different stages of passivity in nano-scale; however, they do not provide any insight into the dynamic processes that lead to passivation, corrosion initiation or propagation. Research utilizing atomic/molecular scale simulation methods (e.g. MD or DFT) has been limited because this is a relatively new area that has recently become useful as a result of the recent advances in computational power and resources that can handle the highly extensive computational needs of such methods.

The ultimate goal of proposed research is to use MD to make transformational contributions to the understanding of passivity and chloride-induced corrosion of iron in alkaline media. Since the ultimate goal is to develop fundamental understanding, and considering the computational cost of the proposed approach, this research will mainly focus on pure iron in simulated and simplified solutions.

## 1.3. Background and literature review

### 1.3.1. Iron passivity and chloride-induced depassivation

Within the highly alkaline environment provided by concrete (pH > 13), steel is covered with a protective layer, so called passive film, such that the rate of metal loss is not significant. However, in the presence of deteriorative processes such as chloride ingress or carbonation of the concrete cover, steel can lose its passive film. The breakdown of passivity, also called depassivation, can lead to higher rates of metal loss (active corrosion) and concerns for the structural integrity of reinforced concrete elements [30-33].

Electrochemical studies have shown that the composition of the concrete pore solution can affect the nature of the passive film and its breakdown [21, 22, 34, 35]. In case of chloride-induced depassivation, it has been shown that critical chloride concentration for the rebar depassivation in concrete varies within a wide range and has a large degree of uncertainty (Figure 1-1) [36-38]. It is well established that several factors are responsible for this variability and uncertainty. Some of these factors include the alkalinity of the pore solution [13, 15, 17, 39-41]; the presence of auxiliary ions such as sulfates, sodium and potassium [9, 18, 42-46]; rebar surface condition [15, 17, 19]; the properties of the rebar-concrete interface [47-49]; chloride binding in concrete [50-52]; and oxygen availability around the reinforcement [40, 47, 52-54].

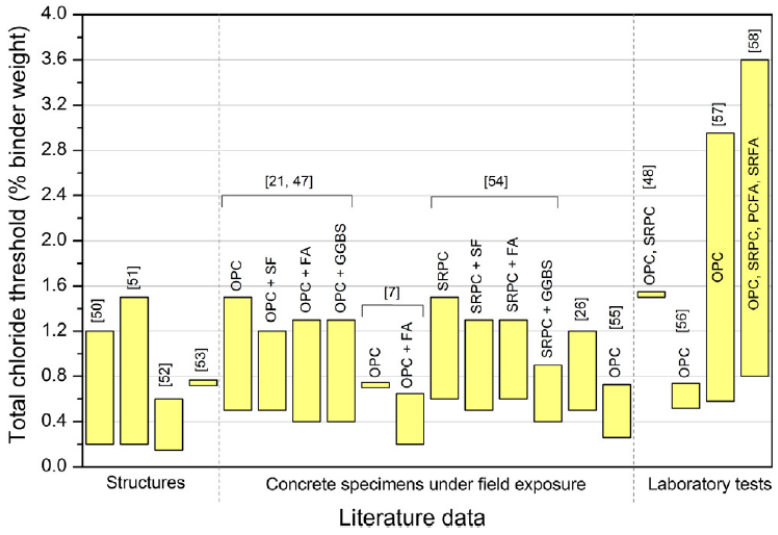


Figure 1-1: Reported chloride threshold for structures, field exposures and laboratory experiments with external sources of chlorides [38].

Several researchers used nanoscale surface characterization techniques to develop fundamental understanding of the mechanisms of passivity and chloride-induced depassivation for iron and different types of steel in various environments [55-71]. However, majority of these works were focused on passivity and depassivation of metals in near neutral or mildly alkaline solutions, which are not representative of the highly alkaline media provided by concrete pore solutions (pH > 12.5). The number of studies that focused on highly alkaline exposures of iron and carbon steel is rather limited, but increased in recent years.

Among these recent studies, Sanchez et al. [72] proposed a model which was based on a two-layered passive film. The inner layer was composed of mixed iron oxides with a stoichiometry similar to that of magnetite (i.e., $Fe_3O_4$ or $FeO+Fe_2O_3$), where oxidation and reduction processes take place between the iron substrate and $Fe^{II}$ oxides. The outer external layer mainly composed of $Fe^{III}$ oxides. The proposed mechanistic model involved a solid state reaction between $Fe^{II}$ and $Fe^{III}$ oxides in the bulk film. Joiret et al. [28] made similar observations using in-situ Raman spectroscopy studies on passive film structure of carbon steel exposed to NaOH solutions. Sanchez et al. [29] also showed using electrochemical studies that the formation of the passive film occurred in two stages: within hours of exposure of the iron substrate to a simulated pores solution, it was hypothesized that passivity was related to the formation of an $Fe^{II}$ oxide layer. During the following days of exposure, it was proposed that the passive film thickened further. This two-stage model is in agreement with theoretical passivity models that are based on an inner barrier layer that forms directly on metal substrate, and an outer layer that precipitates through the hydrolysis of cations ejected from the inner layer [73, 74].

Ghods et al. investigated the nano-scale properties of passive films that form on carbon steel in simulated concrete pore solutions and their chloride-induced depassivation using multiple techniques [23-26]. Using TEM, Ghods et al. [23] showed that the oxide films that form on carbon steel in concrete pore solutions were composed of multiple oxide/hydroxide layers with a total thickness of 5 to 13 nm (Figure 1-2). The inner layer (~2-3 nm thick) on the steel surface was in an epitaxial relationship with the underlying substrate, while the thicker (~5-10 nm) outer regions contained signatures of elements that only existed in the passivating solutions ─ suggesting either that these elements (e.g. calcium or potassium) were incorporated into the oxide during the film formation process or that they diffused into the outer region of the film from the pore solution. However, the authors could not conclude definitely whether these species were in fact inside the passive film or they were mainly the artifacts of the microscopic technique identifying the signals of these species from the precipitates on the metal surface. Furthermore, we still do not understand the dynamic processes that lead to the formation of passive films on iron in alkaline solutions.

Ghods et al. [23] also showed that the addition of chlorides, at concentrations lower than typical depassivation thresholds, did not change the physical appearance of the film, but chloride signal

was observed in the outer oxide/hydroxide region. The authors could not conclude if these chlorides were inside the film, adsorbed on the surface, or artifacts of salt precipitation on the metal surface. After exposure to chlorides in amounts larger than typical depassivation thresholds, the oxide films were not continuous but had areas of bare steel surface (Figure 1-2). The average thickness of the remaining film was also smaller than the thickness of the oxide film before exposure to chlorides, and evidence of initial pit forming sites were found on the steel surface. However, there is still significant debate regarding how chlorides breakdown passive film to initiate active corrosion [15, 17, 19, 20].

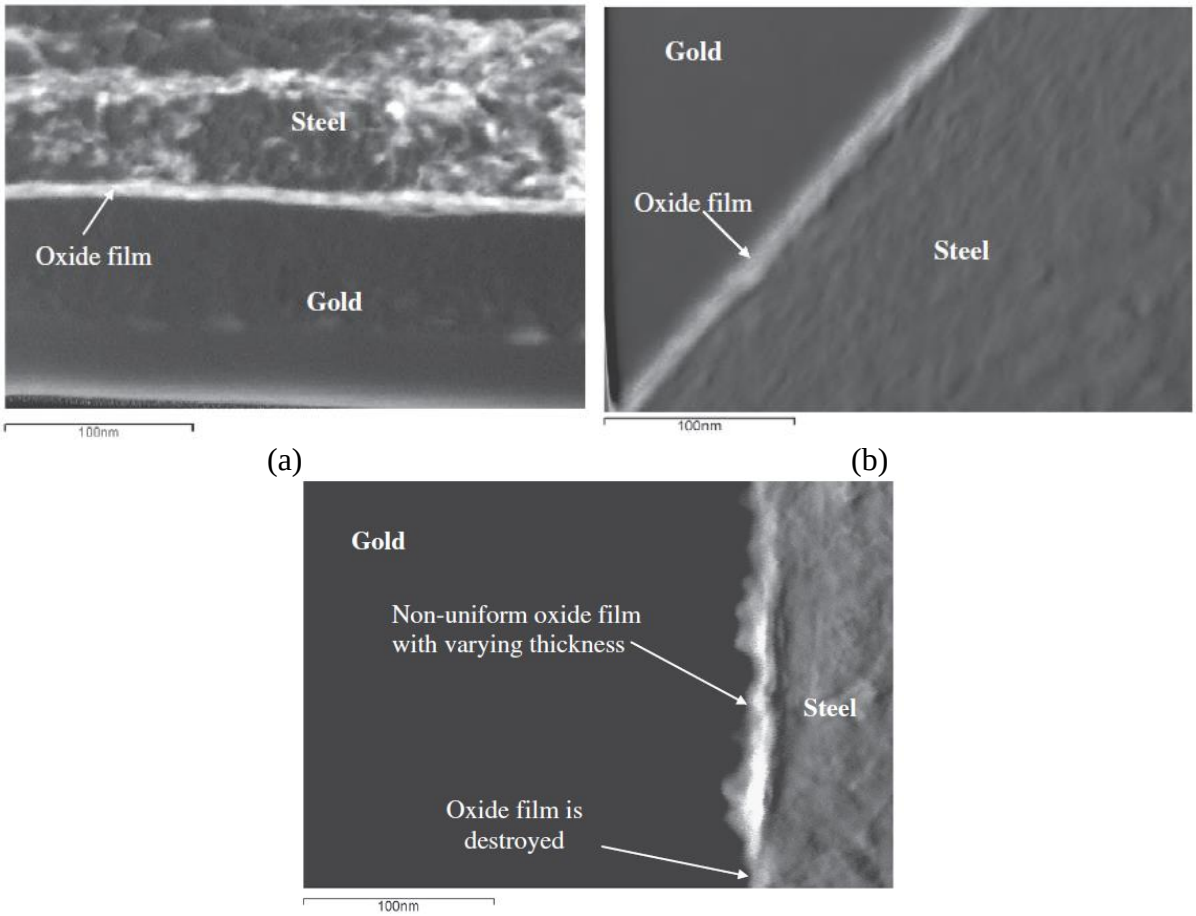


Figure 1-2: STEM images of the passive film on the carbon steel in simulated concrete pore solution before (a, b) and after (c) exposure to chloride. Before chloride exposure, the sample was exposed to the (a) saturated $Ca(OH)_2$ solution with a pH of 12.5 (film thickness: 5 to 8 nm) and (b) solution with a pH of 13.5 contained common ionic compounds (e.g. NaOH, KOH) that exist in typical concrete pore solution in addition to $Ca(OH)_2$ (film thickness: 8 to 13 nm), (c) oxide film after exposure to chloride [23].

Using x-ray photoelectron spectroscopy (XPS), Ghods et al. [24, 25] reported that the inner film was mainly composed of $Fe^{II}$ oxides while the outer region consisted mostly of $Fe^{III}$ oxides. The addition of chloride to the passivating solution changed its stoichiometry such that near the film/substrate interface the $Fe^{II}/Fe^{III}$ ratio decreased (Figure 1-3). The decrease in protective nature of the passive oxide film with increasing chloride concentration suggests that $Fe^{II}$ oxides near the steel substrate were protective, and as their concentration decreased with respect to the $Fe^{III}$ oxides, carbon steel lost its passivity. Therefore, the breakdown of the passive film in the presence of chlorides was attributed to the further oxidation of the inner protective region of the oxide film, which is mainly composed of $Fe^{II}$ oxides, to the non-protective $Fe^{III}$ oxides. The authors could not explain how this transformation took place.

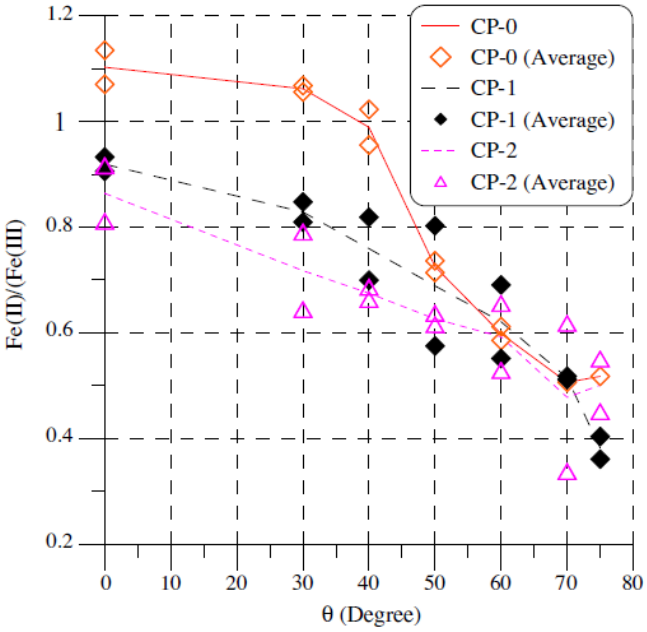


Figure 1-3: XPS results for the comparison of the $Fe^{II}$ / $Fe^{III}$ for a passive film before exposure to chloride (CP-0), a passive film exposed to 0.45 M chloride (CP-1), and a passive film exposed to 3 M chloride (CP-2) [24].

A more recent investigation further characterized the atomic structure of the oxide films using electron energy-loss spectroscopy (EELS) [26]. The experiments were conducted on specimens that were exposed to two different types of simulated concrete pore solutions with pH of 12.5 (CH solution) and 13.5 (CP solution). The films that had formed on carbon steel in the simulated

concrete pore solutions contained indistinctly layered regions. Regardless of the simulated pore solution used for passivation, the inner regions that had formed on the Fe substrate were composed of FeO, which is known to be protective in alkaline media [75]. Above this layer, some traces of $Fe_3O_4$ emerge in the intermediate region, while FeO become less evident. The outer regions of the oxide film that formed in the CH solution showed resemblance to $Fe_3O_4$. In the specimens passivated in the CP solution, along with $Fe_3O_4$, some signs of $\alpha$-$Fe_2O_3$ were also present in the outer regions of the film. The $Fe_3O_4$, as a transition state between the $Fe^{II}$ and $Fe^{III}$, is known to be non-stoichiometric [76]; therefore, the outer $Fe_3O_4$ region in the oxide film is likely to have defects that may help facilitate the ingress of chloride into the oxide film [77]. However, there was no direct evidence for such an ingress. After chloride addition, fingerprints of FeO were not observed in the inner oxide film; instead, $\gamma$-$Fe_2O_3$ and $\beta$-FeOOH were found. In the specimens exposed to the CP solution, after chloride addition, the fingerprints of $Fe_3O_4$ were also revealed in addition to FeO in the inner oxide film (Figure 1-4). These observations suggest that the role of chloride may be related to the change in the oxidation state of the inner most part of the film. However, we still do not understand the reaction dynamics process that leads to this effect.

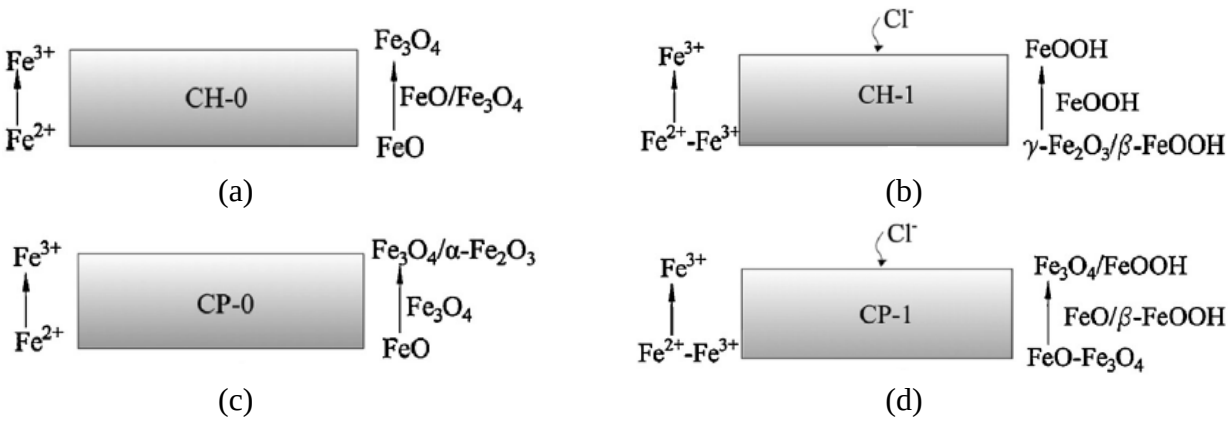


Figure 1-4: The schematic representation of the EELS results for chemical composition and the changes in the oxidation state of the oxide films: (a) specimen exposed to saturated $Ca(OH)_2$ solution, CH, with a pH of 12.5, (b) specimen passivated in the CH solution after exposure to chlorides, (c) specimen exposed to simulated concrete pore solution, CP, (d) specimen passivated in the CP solution after exposure to chlorides [26].

Gunay et al. [34] studied the dynamic process of passivity and chloride-induced depassivation of pure iron exposed to simulated concrete pore solution using electrochemical quartz crystal nano-

balance (EQCN), EIS and open circuit potential (OCP) monitoring. It was shown that passivity formed rapidly in the first 10-20 minutes of exposure to the passivating solution followed by a gradual formation of an unprotective oxide film (Figure 1-5). Chloride addition initially caused mass gain and then mass loss. During the mass gain, which was interpreted as the adsorption (and/or possible ingress) of chloride on the outer layers of the passive film, the specimen remained passive. The period of mas gain until depasivation was also interpreted as the induction time. The depassivation was accompanied with mass loss. These observations support the predictions of a number of depassivation models that hypothesize the adsorption and ingress of chlorides though the outer layers of oxides. Even though this study provided some information on the dynamic processes of passivation and chloride-induced depassivation, since the only measured data was the change in mass on the iron surface, the observations were mostly hypothetical.

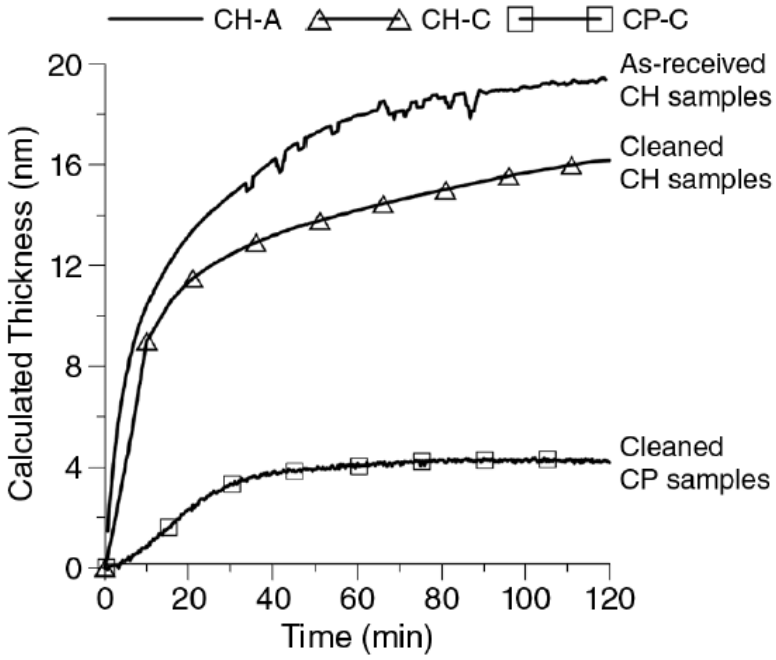


Figure 1-5: Thickness calculation during the passivity formation on different samples. CH or CP indicates the type of passivating solution: CH is the saturated $Ca(OH)_2$ solution with a pH of 12.5 and CP is simulated concrete pore solution. As-received and cleaned present the surface pre-treatment condition. The calculations assume that $Fe^{II}$ oxides form within the first 30 minutes of exposure to passivating solutions followed by the formation of $Fe^{III}$ oxides [34].

Several passive film formation models exist in the literature [70, 78-86]. Some models, so called electric field-assisted models, explain the film formation under an electrical potential. The Hopping model presented by Cabrera and Mott [85] and Kruger [86] explains the formation of the passive film by the hopping of cations to find empty sites in oxygen lattice. Point defect model developed by Chao et al. [82] describes the oxide film growth with ionic movement which is controlled by an electric field. This model provides an analytical approach for the iron oxide formation on the atomic scale on the reactive metal surface. Sakashita and Sato [84] proposed the bipolar fixed charge induced model, which suggests that there is a bipolar film on the passive surface in the form of a cation layer on the solution side and an anion layer on the metal side. The ionic migration can be reduced by the bipolar film with retarding the anodic current in the anodic direction. Unlike the electric field-assisted models, the ion exchange model presented by Sato and Cohen [83] does not require an electric field to move ions through the passive film. In this model, the adsorbed oxygen atom on the metal surface exchange its place with underlying metal atom. This exchange is simultaneously and the oxide film growth continues with the adsorption of the second layer of oxygen on the surface and exchange their places with the metal atoms.

Nano-scale surface characterization studies are in agreement with theoretical passivity models that propose an inner barrier layer that forms directly on the metal substrate, and outer layer that precipitate through the hydrolysis of cations ejected from the inner layer [9, 18]. However, we do not know that which passive film formation model is capable to explain the dynamics of the iron passivity process. Moreover, there is still significant debate regarding how chlorides breakdown these films to initiate active corrosion [15, 17, 19, 20]. In particular, we still do not understand how chlorides change the structure of the inner protective film.

Based on the experimental studies several models have been introduced to describe the mechanisms of passive film breakdown such as ion adsorption model [87, 88], ion exchange model [89], and point defect model [90] (Figure 1-6). In the ion adsorption model, the passive film is considered as a film that forms due to oxygen adsorption, and breakdown occurs when a damaging anion (e.g. chloride) displaces the oxygen forming the passive film. After anion adsorption, the breakdown process is initiated because the bonding of the metal ions to the metal lattice is weakened. Ion exchange model proposes that the breakdown starts with the adsorption of chloride

on the surface. The second step is the ingress of chloride into the passive film by exchanging with the bulk oxygen atoms or occupying vacancies in the passive film. The breakdown of the passive film occurs with the accumulation of chloride. The first step of the point defect model is similar to the ion exchange model. In this model, adsorbed chlorides leads to iron vacancy formation, and when the rate of vacancy formation exceeds the rate of vacancy disappearance, the voids form and the passive film breaks down. Even though researchers proposed aforementioned models to describe the events leading to depassivation but we still do not know which one happens during the depassivation process.

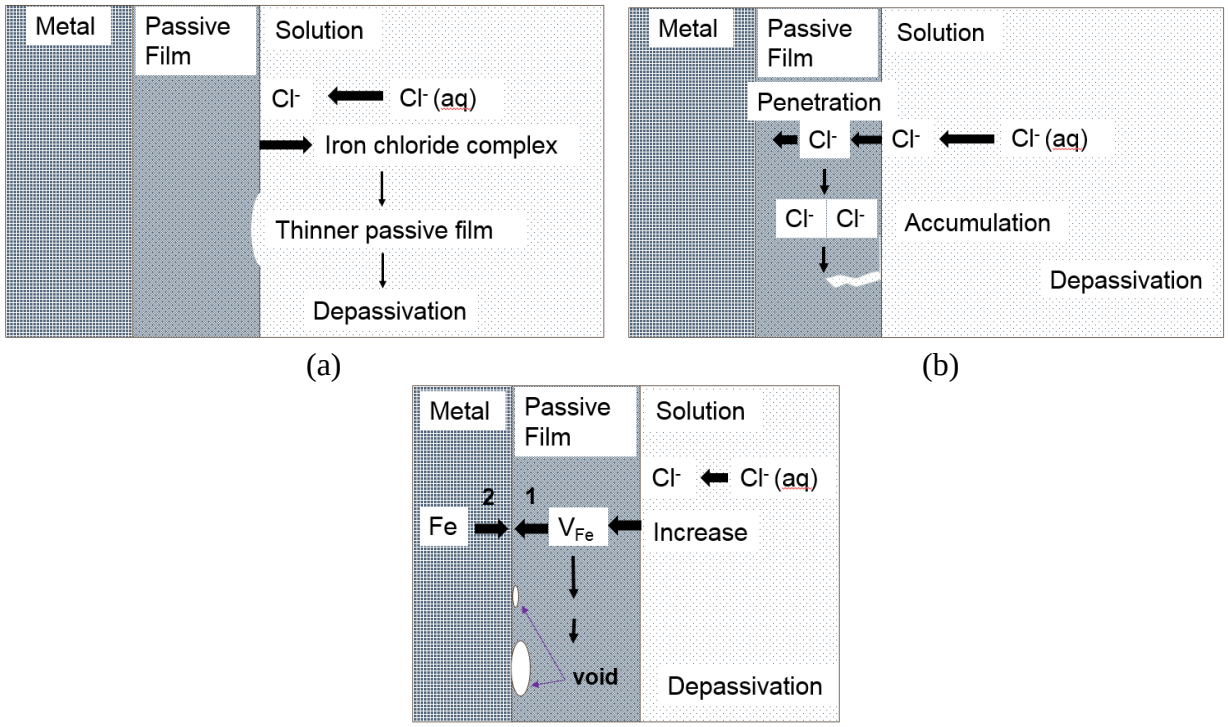


Figure 1-6: The schematic representation of the chloride-induced depassivation models, (a) adsorption model, (b) ion exchange model, (c) point defect model [91].

The testing of the hypotheses on the passivity and chloride-induced depassivation processes of iron or carbon steel in highly alkaline environments is inherently challenging due to the limitations of the nanoscale analytical or spectroscopic techniques in observing dynamic processes. These techniques do not allow in-situ monitoring of the surfaces while processes such as film formation and dissolution take place. On the other hand, atomistic modeling has the potential to serve as a

tool in developing fundamental understanding of corrosion, passivity and depassivation behaviors of steels in concrete.

### 1.3.2. Molecular Dynamics (MD)

The classical MD is based on the numerical solution of the Newton's second law of motion to obtain the time evolution of atomic/molecular systems [92-95]. This law can be defined by a second order differential equation in a multi-particle system as [96, 97]:

$$\boldsymbol{F}_i = m_i \boldsymbol{a}_i \tag{1-1}$$

where $\boldsymbol{F}_i$ is the force on the atom $i$, $m_i$ and $\boldsymbol{a}_i$ are the mass and acceleration of atom $i$, respectively. This equation can be integrated in time for each degree-of-freedom using the finite difference method. The force exerted on atom $i$, $\boldsymbol{F}_i$, can be obtained as the gradient of the interatomic potential energy function, $V$:

$$\boldsymbol{F}_i = -\nabla_i V \tag{1-2}$$

The core of any MD scheme is the interatomic potential energy function (IPEF) that is used to analytically describe the atomistic interactions. The calculation of the IPEFs is also the most computationally intensive step of MD simulations, typically taking up to 95% of the total simulation time. In classical MD, a single atom is affected by the potential energy functions of every other atom in the system, either in the form of bonded neighbors and non-bonded atoms. In general, an IPEF in classical MD is defined as:

$$V(\boldsymbol{R}) = E_{bonded} + E_{non-bonded} \tag{1-3}$$

where $\boldsymbol{R}$ is the vector of the positions of the atoms in the system and $V(\boldsymbol{R})$ is the interatomic potential energy. $E_{bonded}$ and $E_{non-bonded}$ are the energy associated with bonded and non-bonded atoms, respectively. The IPEFs of non-bonded atoms can be classified under two categories: non-reactive and reactive. Non-reactive IPEFs such as Sutton-Chen (SC) [98] and Lennard-Jones (LJ) [99] only consider van der Waals and electrostatic potentials such that

$$E_{non-bonded} = E_{vdWaals} + E_{Coulomb} \tag{1-4}$$

where $E_{vdWaals}$ and $E_{Coulomb}$ are van der Walls and electrostatic (Coulomb) energy between non-bonded atoms, respectively. If the MD scheme uses this type of IPEF, it is called "non-reactive

MD" [100-103]. Non-reactive MD simulation methods cannot model the reactive processes such as electrochemical processes or corrosion. They are mainly used to determine the mechanical properties of the atomic systems and their response to strains and stresses. Figure 1-7 represents regions of attraction and repulsion in LJ interatomic potential, schematically.

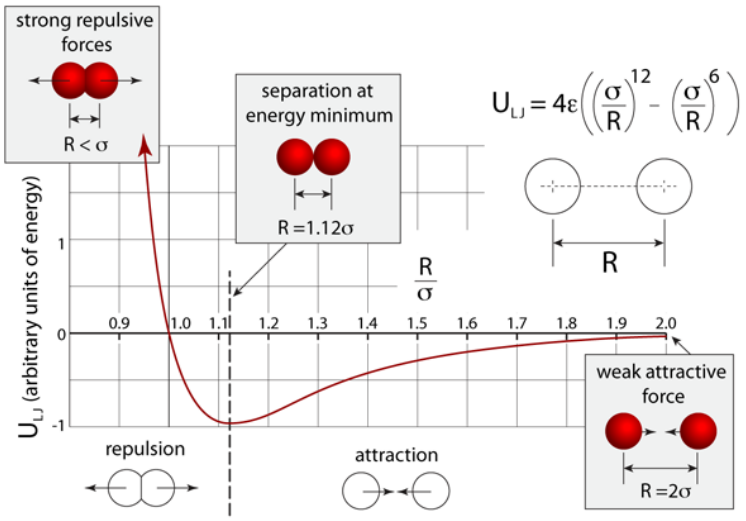


Figure 1-7: The schematic representation regions of attraction and repulsion in Lennard Jones (LJ) interatomic potential. Atoms try to minimize their potential energy. When the atomic separations are to the left of the minimum energy they repel, otherwise they attract one another [104].

Unlike non-reactive IPEFs, reactive IPEFs (e.g. ReaxFF) consider both non-bonded and bonded energy functions:

$$E_{system} = E_{non-bonded} + E_{bonded} = E_{bond} + E_{over} + E_{under} + E_{val} + E_{tor} + E_{lp} + E_{H-bond} + E_{vdWaals} + E_{Coulomb} \quad (1\text{-}5)$$

where $E_{bond}$ is the energy associated with forming atomic bonds; $E_{over}$ and $E_{under}$ are respectively the over-coordination and under-coordination penalty energies; $E_{tor}$ is the energy associated with torsion angle terms; and $E_{lp}$ and $E_{H-bond}$ are long-pair energies and hydrogen-bond energies, respectively. The last two energy terms, $E_{vdWaals}$ and $E_{Coulomb}$, are computed for all atom pairs, while all other energy terms are calculated for the bond order between particles $i$ and $j$. Reactive MD applies the reactive IPEFs to define the interaction between atoms and molecules, and is capable of simulating breaking and forming the bonds. As a result, reactive MD simulation methods, such as ReaxFF-MD [105, 106], can be used to model reactive phenomena

such as electrochemical processes and corrosion on metal/electrolyte interfaces. In this research, we use ReaxFF-MD to study the iron passivity and chloride-induced depassivation of iron in alkaline electrolyte.

Unlike computationally expensive quantum mechanical (QM) calculations, ReaxFF treats chemical bonding implicitly, which yields significant computational efficiency. In other words, ReaxFF bridges the gap between the non-reactive MD and the computational quantum-chemistry [107]; therefore, ReaxFF-MD approach is well suited to study complex systems such as metal-electrolyte interfaces.

The fundamental assumption of the reactive force field is that the bond order, BO, between a pair of atoms, i and j, can be calculated as [105]:

$$BO_{ij} = exp\left[p_{bo,1}\left(\frac{r_{ij}}{r_o^{\sigma}}\right)^{p_{bo,2}}\right] + exp\left[p_{bo,3}\left(\frac{r_{ij}^{\pi}}{r_o^{\pi}}\right)^{p_{bo,4}}\right] + exp\left[p_{bo,5}\left(\frac{r_{ij}^{\pi\pi}}{r_o^{\pi\pi}}\right)^{p_{bo,6}}\right] \quad (1\text{-}6)$$

where $r_{ij}$ is the interatomic distance; $r_o^{\sigma}$ , $r_o^{\pi}$ and $r_o^{\pi\pi}$ are equilibrium bond lengths for sigma, pi and double-pi bonds; and $p_{bo}$ terms are empirical parameters [108-110]. The system energy, $E_{system}$, is calculated using various partial energy contributions as Equation 1-5.

In the ReaxFF theory, atomic charges are calculated using a geometry-dependent charge distribution that is determined using the QEq methods [111-113]. Individual atomic charges and electrostatic energy change over time dynamically. The corresponding electrostatic energy $E(\boldsymbol{q})$ is calculated as:

$$E(q) = \sum_{i=1}^{N}\left[\omega_i q_i + \mu_i q_i^2 + Tap(r_{ij})k_c\frac{q_i q_j}{\left(r_{ij}^3+\gamma_{ij}^{-3}\right)^{1/3}}\right] \quad (1\text{-}7)$$

where $q_i$ is the charge on ion $i$; $N$ is the total number of ions; $q$ is the vector of length $N$ containing the charges; $\omega_i$ and $\mu_i$ are the electronegativity and hardness of ion $i$, respectively; $Tap(r_{ij})$ is a seventh-order taper function to avoid energy discontinuities when charged species move in and out of the non-bonded cutoff radius; $k_c$ is the dielectric constant; and $\gamma_{ij}$ is a parameter for shielding between atoms $i$ and $j$. The atomic charges, which are dependent on the geometry of the system, are calculated at each time step.

### 1.3.3. ReaxFF-MD studies for investigating corrosion processes

In recent years, ReaxFF-MD as a reactive potential based method, has emerged as a simulation framework to investigate reactive processes [106, 107, 114-121]. For example, Jeon et al. [122] used ReaxFF-MD to study iron oxidation as it relates to surface reactivity in catalysis and energy applications (Figure 1-8).

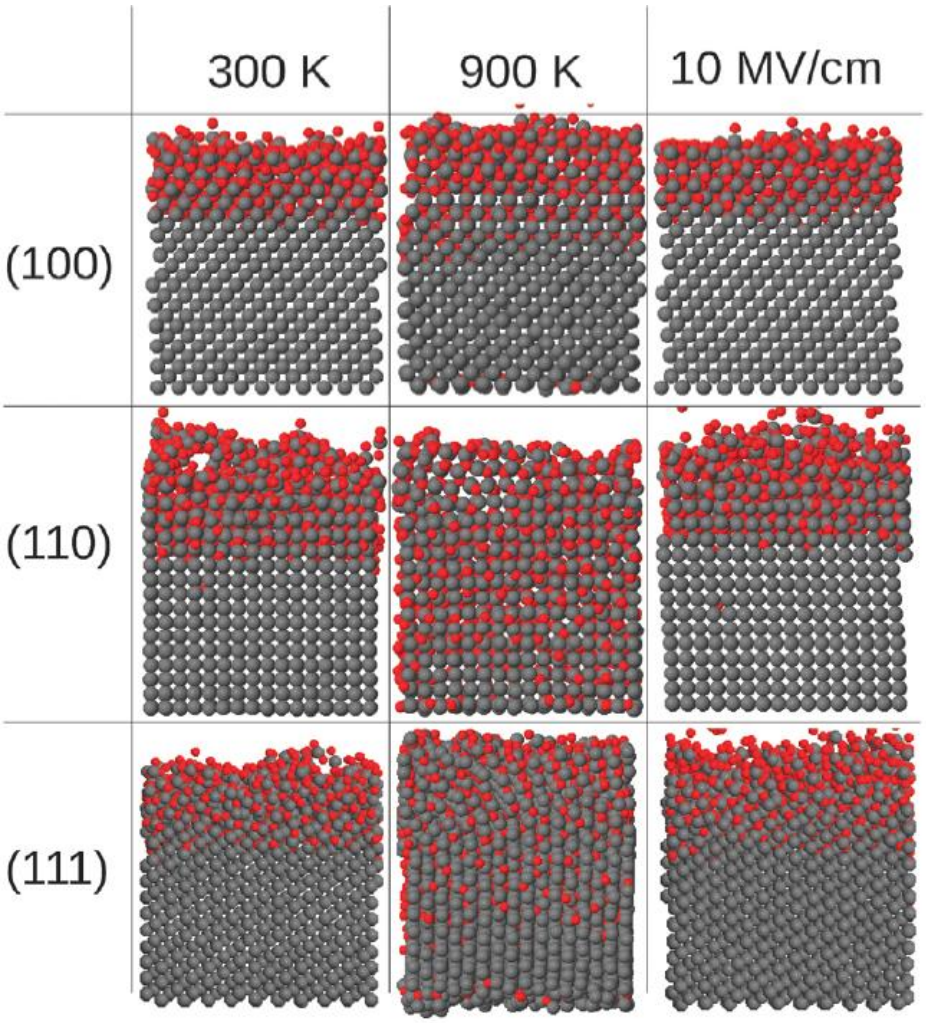


Figure 1-8: Side views of ReaxFF-MD simulation results for iron-oxygen systems at 1 ns oxidation. Top, middle and bottom figures are for Fe(100), Fe(110) and Fe(111). Left figures are with the temperature of 300K and middles are for 900K with no external electric field. Figures on the right are the results with the applied external electric field in 300K. It was observed that Fe(100) shows the least amount of oxide growth in all cases. The gray and red spheres represent iron and oxygen atoms, respectively [122].

These simulations were performed on different surface orientations of pure iron surfaces under applied external electric fields in a non-aqueous (dry) environment containing oxygen. It was shown that ReaxFF-MD was successful in simulating oxidation of such systems and providing complementary information to existing experimental data. They simulated several known pure iron oxide phases, i.e. FeO, $Fe_2O_3$ and $Fe_3O_4$, as reference oxide structures and provided the distribution of iron and oxygen atoms (Figure 1-9) and charge states of the reference oxides (Figure 1-10). By comparing these with those of reference oxide phases, they showed that the compositions of the film from ReaxFF-MD simulation are in agreement with experimental results. They also explained the early stages of oxide film growth on iron surface. Such studies do not exist for passivity and chloride-induced depasivation of iron in alkaline solutions.

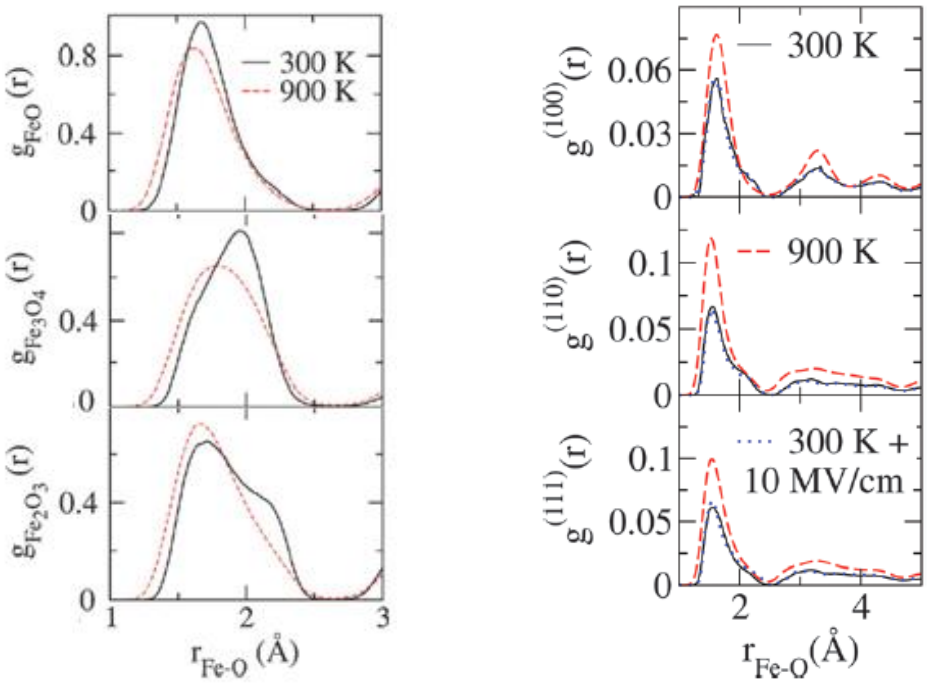


(a) (b)

Figure 1-9: Iron-oxygen Pair Distribution Function (PDF) at 300K and 900K, (a) reference oxides: FeO (wustite) has a dominant peak at 1.65 Å at 300K. $Fe_3O_4$ (magnetite) shows a main peak at about 2.0 Å with a slight transition at 1.6 Å while $Fe_2O_3$ (hematite) has a main peak at 1.7 Å with a transition at 2.15 Å, (b) simulation results of Fe(100), Fe(110) and Fe(111) oxidation. Comparisons of the simulated PDF to those of reference oxides implies that the formed oxide compositions are not pure phases, but rather a mixture of oxides [122].

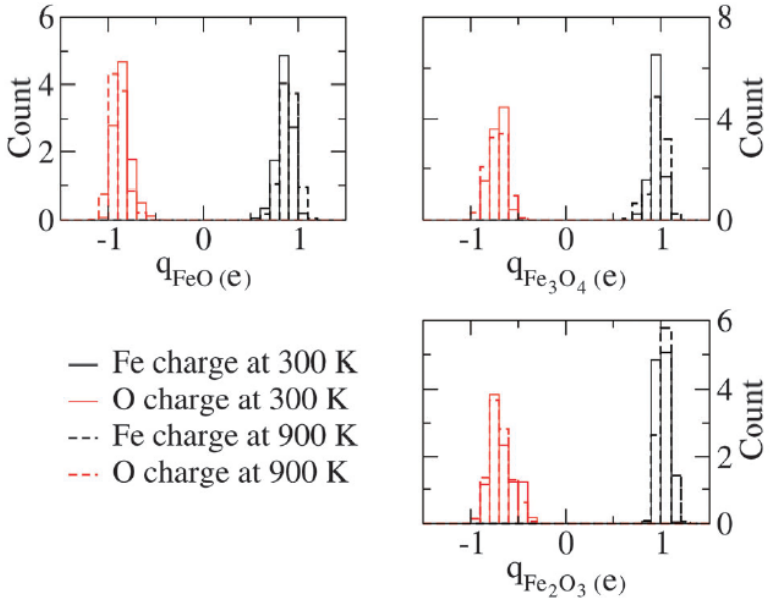


(a)

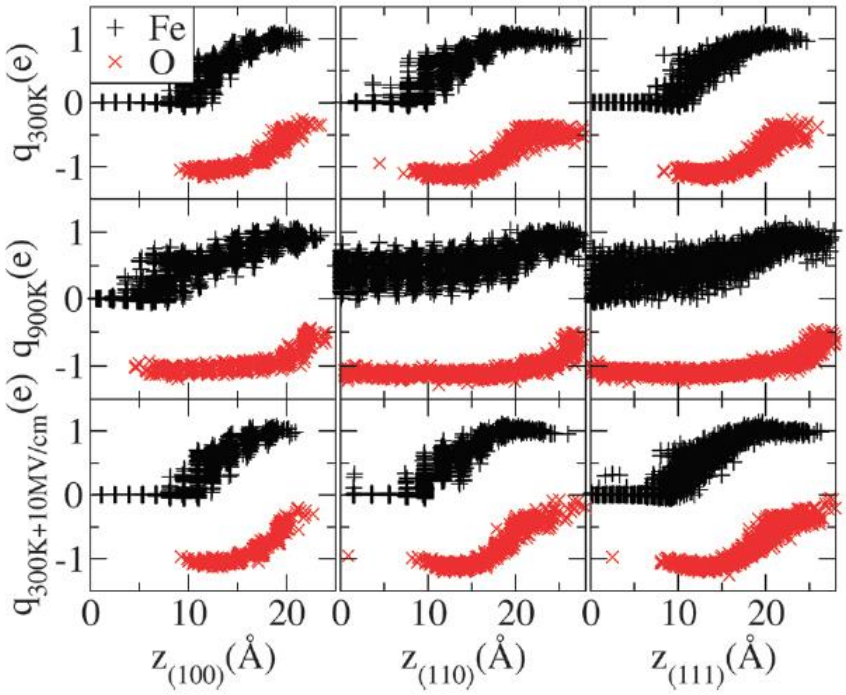


(b)

Figure 1-10: Charge distributions of iron and oxygen, (a) reference oxides. $Fe_2O_3$ (hematite) shows the highest cation charges and the lowest anion charges, while FeO (wustite) has the lowest cation charges and the highest anion charges. $Fe_3O_4$ (magnetite) has an intermediate states of cation and anion charges, (b) simulation results of iron oxides on Fe(100), Fe(110) and Fe(111). Anion charges of the oxide layers close to metal-oxide interface are less than -1 eV, implying that the formed iron oxides are non-stoichiometric [122].

Although several ReaxFF-MD investigations exist for the study of passivity of other metals, oxidation and corrosion processes in non-ferrous metals [107, 117-120], the investigation of iron oxidation in such environments is limited [123, 124].

Assowe et al. [107] investigated the interaction of a nickel substrate with water molecules using ReaxFF-MD method. It was shown that the oxide film formation is not accompanied with the nickel atoms dissolution in the solution, which means nickel passivation (Figure 1-11). Their results support the expected thermodynamic behavior of nickel in pure water. They showed that the oxide growth was enhanced by nickel dissolution and oxygen ingress. Different steps of nickel oxidation including adsorption, dissociation of water, deprotonation, dissolution, and growth of hydroxide/oxide were observed.

Using the ReaxFF-MD, Russo et al. [117] examined the reaction dynamics associated with the dissociation of water on an aluminum cluster. The adsorption of water molecules in the gas phase onto the aluminum cluster was observed at the first step and then dissociation of water molecules. It was shown that with the assistance of a solvated water molecule, the dissociation of an adsorbed water is possible via a reduction in activation barrier. This is a two-step reaction: firstly the solvated water removes a hydrogen from the adsorbed water to become $OH^-_{ads}$ and $H_3O^+_g$. In the second step the formed hydronium ion donates one hydrogen atom to the aluminum surface if a free site is available. The authors also investigated the aluminum oxide layer covering the cluster surface (Figure 1-12). This oxide layer decreased the availability of available surface reaction sites. Therefore, water molecules adsorption on the aluminum cluster and the subsequent dissociation process was reduced.

The interaction of copper substrates and chlorine under aqueous conditions was investigated using ReaxFF-MD by Jeon et al. [118]. It was observed that increased concentration of chlorine and higher ambient temperature expedite the corrosion of copper. In order to study the effect of solution states on the corrosion resistance of copper, it was shown that higher corrosion rate occurs at partial fraction hydroxide environment. When the chloride concentration was low, oxygen or hydroxide ion adsorption onto copper surface was confirmed in partial fraction hydroxide environment.

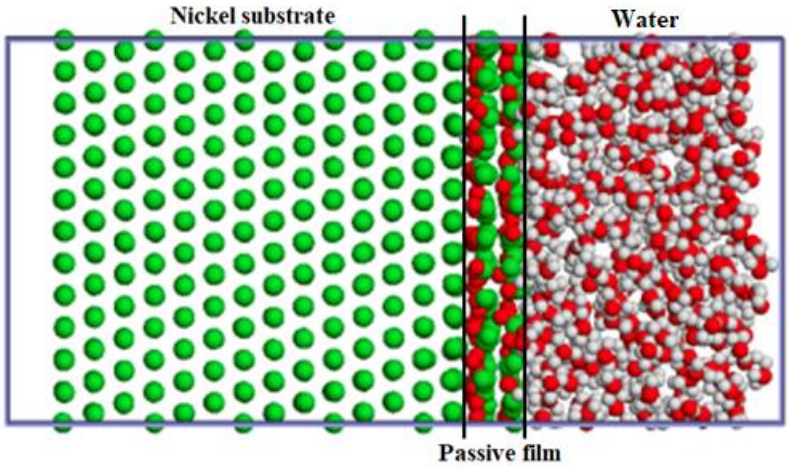


(a)

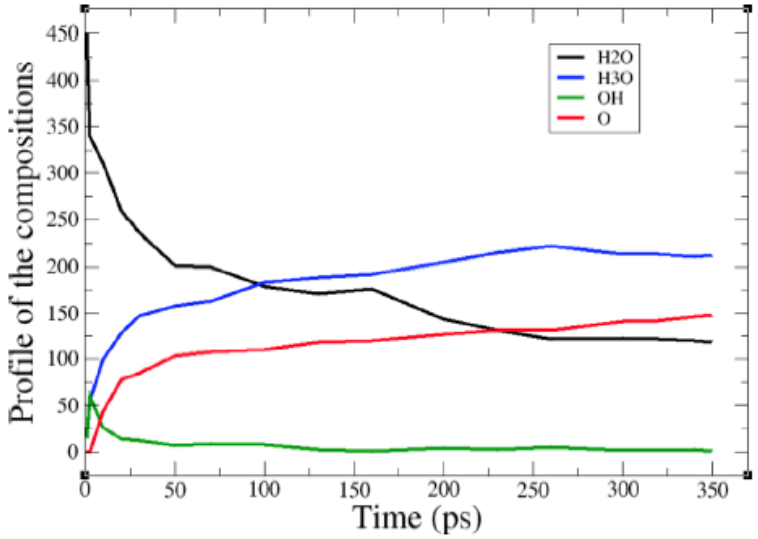


(b)

Figure 1-11: Simulation results of nickel-water system: (a) Snapshot of ReaxFF-MD simulation 350 ps. The result shows the passivation for the nickel supporting the expected thermodynamic behavior of nickel exposure to pure water. The green, white and red spheres represent nickel, hydrogen and oxygen atoms, respectively. (b) Evolution of the chemical compositions in the nickel-water system over time. The number of water molecules decreased because they reacted with the and dissociated into $OH^-$ and $H^+$. The hydroxide dissociated and the resulting oxygen atoms reacted with the nickel forming the oxide film, while the hydrogen reacted with water molecule to form $H_3O^+$ [125].

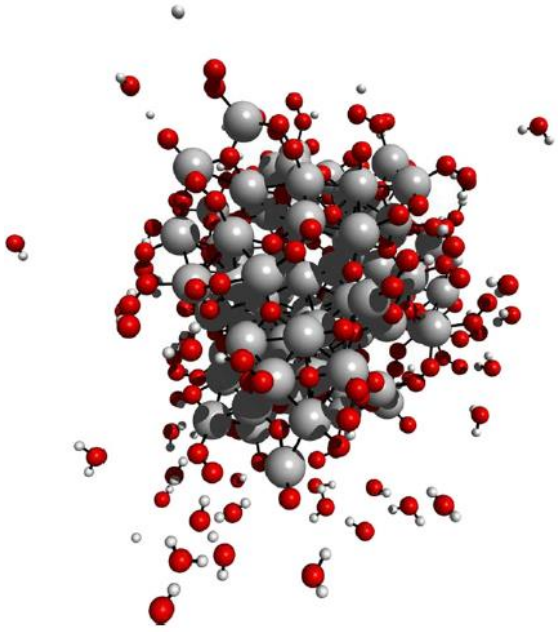

Figure 1-12: Image of ReaxFF-MD simulation result for the aluminium cluster with an oxide layer formed on the surface. This oxide layer on the aluminum cluster reduced the dissociation process by decreasing the availability of available surface reaction sites. The gray, red and white spheres represent iron, oxygen and hydrogen atoms, respectively [117].

Using ReaxFF-MD, Jeon et al. [119] studied chloride ion adsorption and transport through copper oxide thin films under aqueous conditions to understand the chemical interaction at the interface between metal-oxide and aqueous media containing chlorides (Figure 1-13). The structural evolution of the copper oxide film from thinning to breakdown was observed. In addition, extended defects in the metal substrate occurred at high concentration of adsorbed chlorides. The results of their study showed that the initial stages of the breakdown is associated with rapid depletion of adjacent chlorides. The dissolved copper cations gained higher charges by interaction with chlorides and chlorides diffused into the local corrosion sites promoting further corrosion.

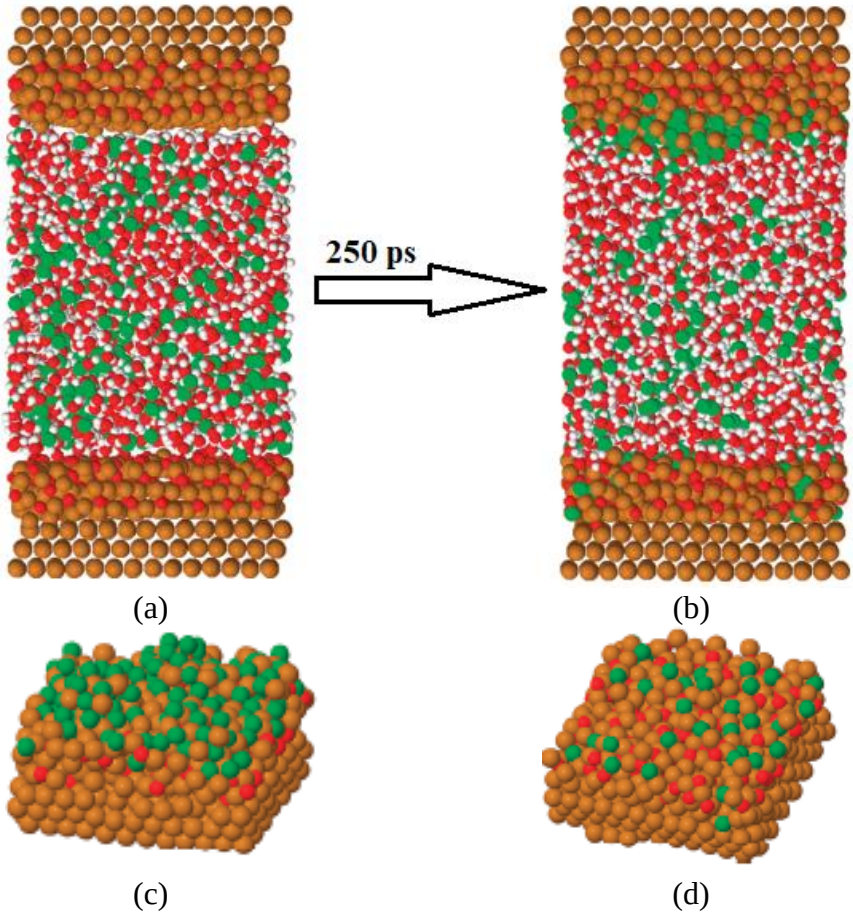


Figure 1-13: Reactive molecular dynamics study of chloride ion interaction with copper oxide surfaces in aqueous media: (a) initial configuration, (b) simulation result at 250 ps. The solution part in the middle is a 20 M chloride aqueous media and relaxed at 300K. The effect of surface condition of oxide on the initial adsorption of chloride was studied. (c) Higher chlorides adsorbed onto upper oxide film which copper atoms exist at the top of oxide layer (copper-terminated surface) and therefore has higher surface copper density. (d) Lower oxide film has higher oxygen density (oxygen-terminated surface) and chlorides adsorption is resisted. The white, red, green and brown spheres represent hydrogen, oxygen, chloride and copper atoms, respectively [119].

Pan and van Duin [123] and Pan [124] demonstrated the possibility of using ReaxFF-MD in simulating iron oxidation at the iron-water interface and its potential to study passivation and depassivation processes (Figure 1-14). These simulations identified three distinct stages of iron oxidation based on the chemical species generated and oxidation rate. In early stages, oxides were mixed and unstable; however, in later stages stable oxides were formed, followed by a significant reduction in oxidation rates. Pan [124] described the last stage of oxide formation as passivation of the iron surface, which is not expected in pure water (pH = 7) [126]. Thus there was a need to

investigate the applicability of ReaxFF-MD in modeling the iron passivity and chloride-induced depassivation.

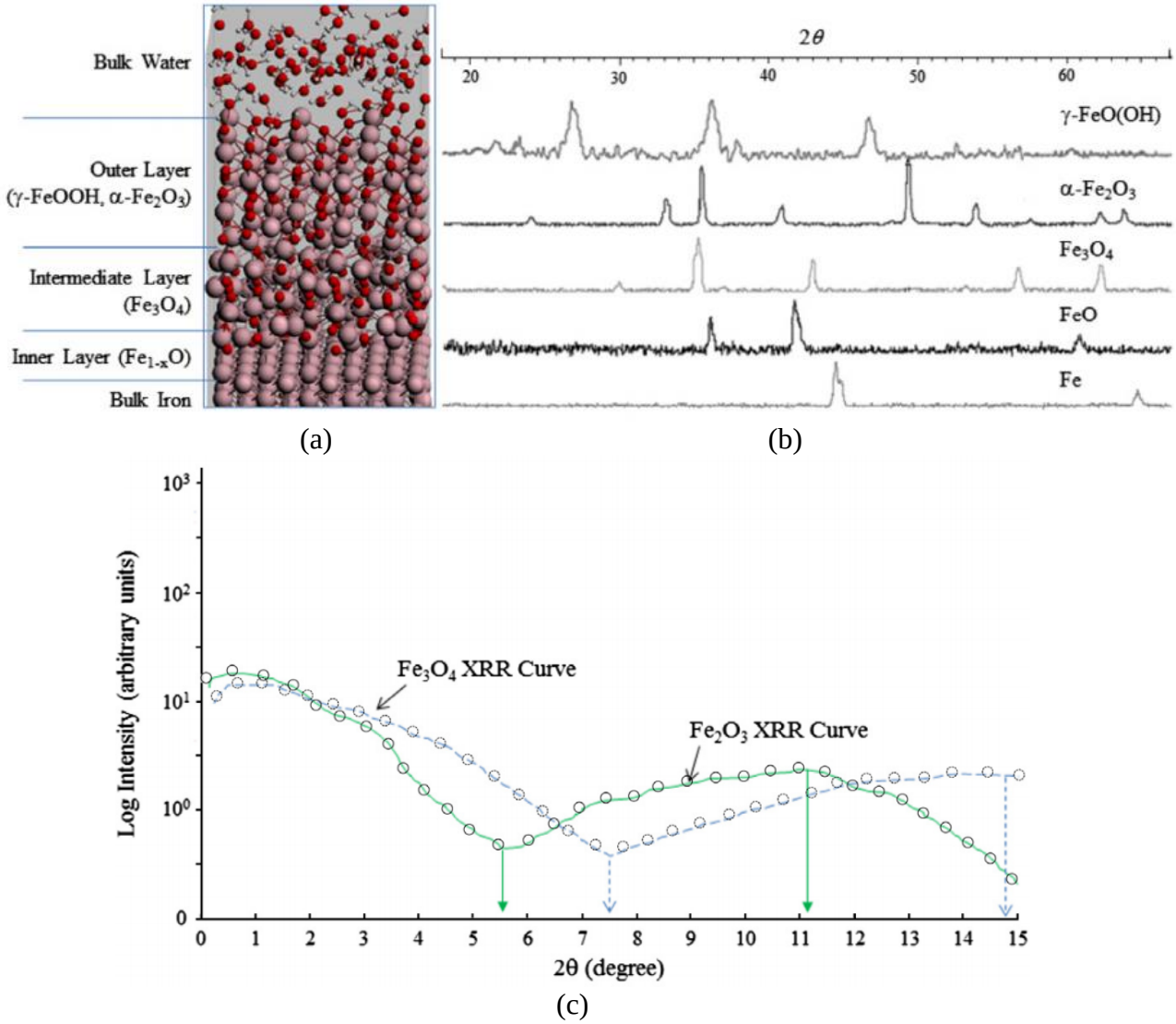


Figure 1-14: Oxidation results of iron-water system [123, 124], (a) a snapshot of ReaxFF-MD simulation result with the predicted chemical compositions of the oxide film. Three different layers of iron oxides were observed between bulk iron and bulk water. The brown, red and white spheres represent iron, oxygen and hydrogen atoms. (b) XRD spectra: the outer layer of the oxide film is mainly α-$Fe_2O_3$ with little amount of γ-FeOOH. The intermediate layer contains $Fe_3O_4$, and the inner layer is a wustite-like ($Fe_{1-x}O$) material, (c) XRR curves: two different layers were observed in the last stage of oxidation; one of α-$Fe_2O_3$ and the other of magnetite $Fe_3O_4$.

### 1.3.4. Electrical Double Layer (EDL) models

The contact between any electrode surface and an electrolyte results in an arrangement of ion distribution near the electrolyte surface and formation of a specific interfacial region. This region is called Electrical Double Layer (EDL) [127-132]. This EDL consists of a layer of electrons on the surface of the electrode and an adsorbed layer with an ionic zone which forms simultaneously when electrolyte becomes in contact with the electrode and results in a fall of the electric potential. The electrical properties of this layer are important since they affect significantly the electrochemical measurements. The study of the physical properties as well as mathematical formulation of the EDL began in 1897 by Hemann von Helmholtz [127].

EDL at the electrode-electrolyte interface plays an important role in all electrochemical processes including passivity and chloride-induced depassivation of iron in alkaline electrolytes. There have been numerous studies conducted to model EDL [133-137]. Among many others, three models have been widely used in the past to describe the EDL in electrochemical systems, which are referred here as classical models: Helmholtz [127], Gouy-Chapman [128, 129] and Stern [130] models (Figure 1-15).

Several researchers studied the formed double layer at the electrode-electrolyte interface and used EDL models in order to develop the fundamental understanding of the EDL and the applications of the EDL models for various systems [100, 131, 133-143]. However, there are a few studies on the EDL models for metal oxidation application using MD [122, 125].

Based on our best knowledge, the classical EDL models have not been used to study iron passivity and chloride-induced depassivation using the ReaxFF-MD method, and we do not know if any of these models are appropriate to simulate iron corrosion and passivity in neutral and highly-alkaline environments.

As mentioned earlier, it was shown using nano-scale surface characterization studies that the oxide film on carbon steel in concrete pore solutions were composed of multiple oxide/hydroxide layers. Thus it was of great importance to study the nature of passive layer using ReaxFF-MD with appropriate EDL models and compare them with the experimental results. In order to simulate the

chloride-induced depassivation process, we need to simulate the formation of a proper passive film so that it could be exposed to chlorides.

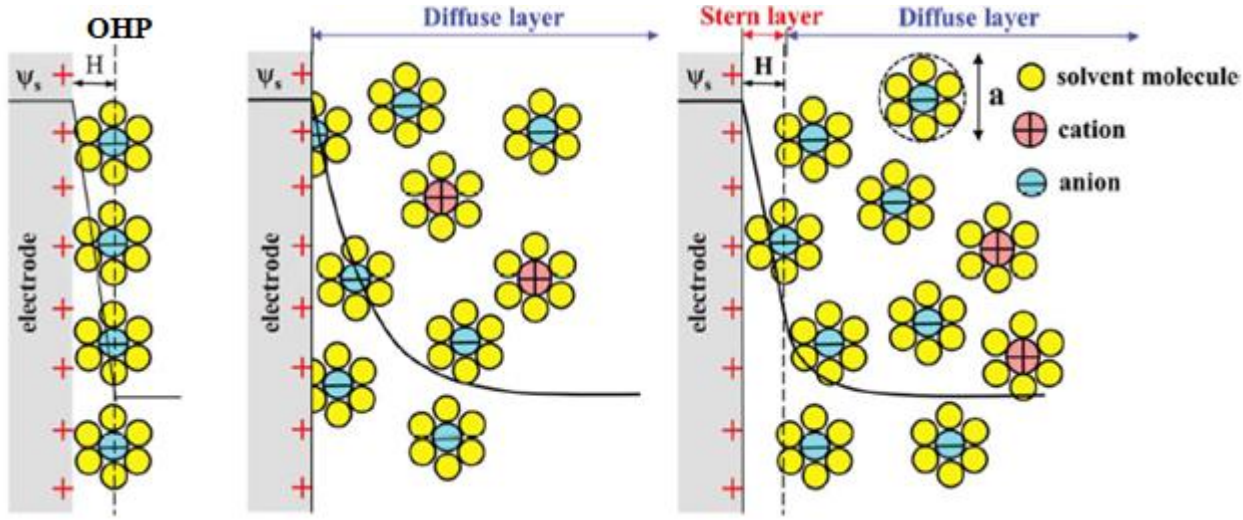


(a) (b) (c)

Figure 1-15: The schematic representation of Electrical Double Layer (EDL) structures according to (a) Helmholtz model: ions are arranged as a packed layer on the Outer Helmholtz Plane (OHP), therefore the charge density within the layer (distance H) is zero. In this model electric potential drops linearly from $\Psi_s$ at the electrode surface to zero at OHP, (b) Gouy-Chapman model: ions are arranged in the whole bulk of the solution and the potential drops exponentially within the diffuse layer, (C) Stern model. Stern model is a combination of Helmholtz and Gouy-Chapman models [140].

### 1.3.4.1 Helmholtz model

Helmholtz [127] was the first who proposed the simplest model of the concept of the EDL (Figure 1-15a). This model considers the charge separation at the interface between an electrolyte solution and a metallic electrode. Helmholtz assumed that immersed charged electrode in electrolyte solution attracts ions with opposite charges to its surface while repel the ions with the same charges. The distributed charge at the surface of the electrode is balanced by redistribution of the oppositely charged amount of ions in the solution. The two layers of charges of opposite signs that form at the interface of electrode and electrolyte is called the electric double layer (EDL). This structure is comparable to the conventional dielectric capacitors with planar electrodes. The

potential in the Helmholtz model drops within the interface is linear and described by the Poisson-Boltzmann (PB) differential equation in one dimension (1D) as follows [132]:

$$\frac{\partial^2 \varphi}{\partial x^2} = -\frac{\rho(x)}{\varepsilon_r \varepsilon_0} \quad (1\text{-}8)$$

where $\varphi$ is the electric potential across the Helmholtz layer, $x$ is the distance from the metallic electrode, $\rho$ is the charge density, $\varepsilon_r$ is the relative permittivity of the medium, and $\varepsilon_0$ is the permittivity of the vacuum. As we could consider the ions as point charges and they are arranged on the Outer Helmholtz Plane (OHP) (Figure 1-12a), the potential density within the layer is equal to zero ($\rho(x) = 0$), and Equation 1-8 can be simplified between two layers as [131]:

$$\frac{\partial^2 \varphi}{\partial x^2} = 0 \quad (1\text{-}9)$$

The main drawback of this model is the neglect of the interactions that occur outside of the Helmholtz double layer [132].

Zarzycki et al. [142] presented an MD simulation of the EDL at the silver chloride (AgCl) - aqueous electrolyte (KCl) interface. The simulation showed the formation a bi-layer layer which consisted of two sublayers of water molecules interconnected with hydrogen bonds. The adsorbed ion-water layers formed a rigid structure confirms the applicability of the Helmholtz model in a high concentration electrolyte (Figure 1-16). Profiles of the charge density, electric field, electrostatic potential, free and adsorption energies across the simulation cell were presented. They found a good agreement between the calculated properties in both quantum and classical approaches and the experiment with relatively small deviations.

Assowe et al. [125] introduced an external electric field using Helmholtz EDL model to study the oxidation of nickel. The simulations were performed on nickel-water system using ReaxFF-MD. The applied electric field intensity varied between 10 MeV/cm to 20 MeV/cm. The presence of the external electric field led to oxidation of the nickel surface and a passive film formed. It was shown that increasing the electric field intensity sped up the oxidation of nickel (Figure 1-17a). Moreover, the results showed that the thickness of the oxide film increased linearly with increasing electric field intensity (Figure 1-17b).

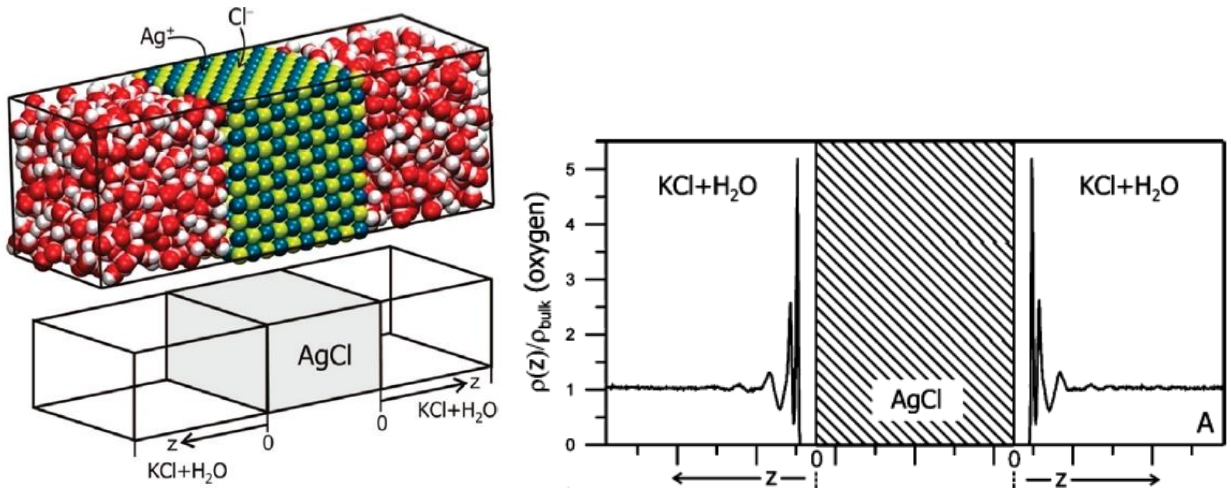


(a) (b)

Figure 1-16: MD simulation study of the EDL at AgCl-electrolyte Interface: (a) initial configuration of MD model, (b) water density profiles: a schematic picture of the system with the oxygen density profiles near the surfaces are shown [142].

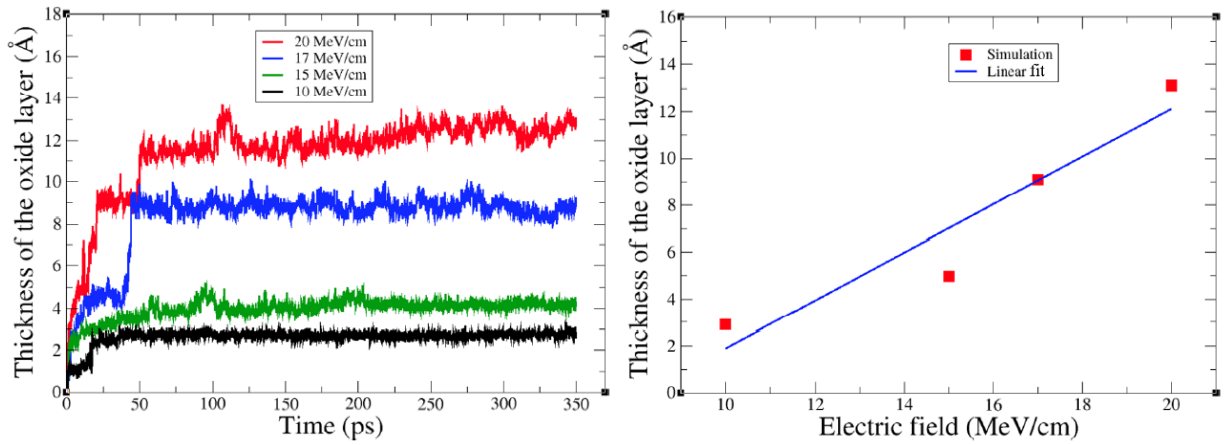


(a) (b)

Figure 1-17: Effect of an applied electric field to study oxidation of Ni(111) in pure water: (a) evolution of the nickel oxide film thickness at room temperature for various applied electric field intensities, (b) thickness of the oxide film as a function of the electric filed intensity. See also Figure 1-11 [125].

In order to increase the initial oxidation kinetics of the single crystal iron surface in iron-oxygen system (Figure 1-18a), Jeon et al. [122] applied an external electric field with the intensity of 10 MeV/cm. Comparing to the simulations with no electric field, the applied electric field facilitated the initial oxidation by promoting oxygen transport through the iron lattice interstitial sites. It was found that the effect of electric field on the oxide structure, oxide activation energy, and the

compositions was minimal and similar oxide formation stages were maintained. The evolution of the number of oxygen ions in the iron oxide film (Figure 1-18b) demonstrated that the applied electric field affected oxide growth significantly for all surface orientations.

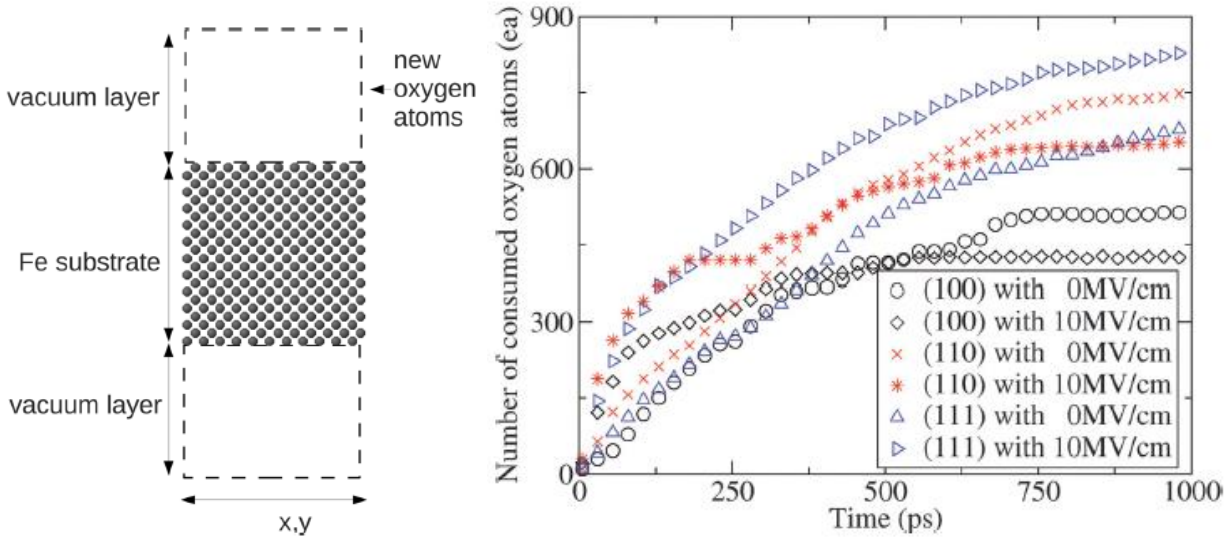


(a) (b)

Figure 1-18: Iron oxidation study using ReaxFF-MD: (a) initial configuration of the iron-oxygen system, (b) effect of an external electric field on the number of consumed oxygen ions. Multiple steps of iron oxidation are observed. Iron surface orientations Fe(110) and Fe(100) show a strong transition during the first 100 ps, and then the growth rate decreases. This changing in the oxidation rate corresponds to the transition from fast to slow oxidation. Then the saturation of oxide growth for the Fe(110) and Fe(100) is found at 500 ps and 700 ps. For Fe(111), the transition from fast to slow is similar to the other orientations but oxide growth is not saturated at 1 ns, implying continuous formation of oxides.

### 1.3.4.2 Gouy-Chapman model

Gouy and Chapman [128, 129] developed a model considering for the fact that ions in the electrolyte solution are mobile under the combined effects of electromigartion driven by the potential gradient, i.e. electric field, and ion diffusion driven by concentration gradient [140] (Figure 1-15b). This results in the so-called diffuse layer (DL) which the ions of opposite charge attract to the metal surface and co-ions repel by it. In the Gouy-Chapman model the ions are treated as point charges, and this allows us to apply the PB differential equation (Equation 1-8) to the

charge distribution of ions as a function of distance from the surface. The total charge density per unit volume for all ionic species is [132]:

$$\rho(x) = \sum_i n_i z_i e \tag{1-10}$$

where $z_i$ and $e$ are the charge of ion $i$ and the unit charge, respectively, and $n_i$ is the distribution of the ions described by the Boltzmann distribution as [132]:

$$n_i = n_i^0 \exp\left(\frac{-z_i e\varphi}{kT}\right) \tag{1-11}$$

where $n_i^0$ is the concentration of the ion $i$ in the solution, $\varphi$ is the potential, $k$ is the Boltzman constant and $T$ is the temperature. By combining Equation 1-8, 1-10 and 1-11 the PB equation, Equation 1-8, can be written as [132]:

$$\frac{\partial^2\varphi}{\partial x^2} = -\frac{e}{\varepsilon_r\varepsilon_0}\sum_i n_i^0 z_i \exp\left(\frac{-z_i e\varphi}{kT}\right) \tag{1-12}$$

The Gouy-Chapman model is a proper EDL model for electrode-electrolyte studies with low concentration, but not for high concentration, electrolytes [141].

Wang and Pilon [141] developed an accurate numerical tools for simulating EDL formed near an ultramicroelectrode and to assess the validity of existing models (Figure 1-19). The model considers the finite size of the ions, a packed and a diffuse layer of ions representing the Helmholtz and Gouy-Chapman layer, and the dependency of the electrode permittivity on the local electric field. Their study reveals that models reported in the literature have limitations to simulate the EDL capacitance of ultramicroelectrodes. It was shown that the main drawback of the Helmholtz model is the neglect of interactions that occur away from the outer Helmholtz plane even though it is a proper model for high concentration electrolytes [132, 144, 145]. It was also shown that Gouy-Chapman model has been successful for electrolytes with low ionic strength while it is known to overestimate ionic concentrations close to charged surface [146-148].

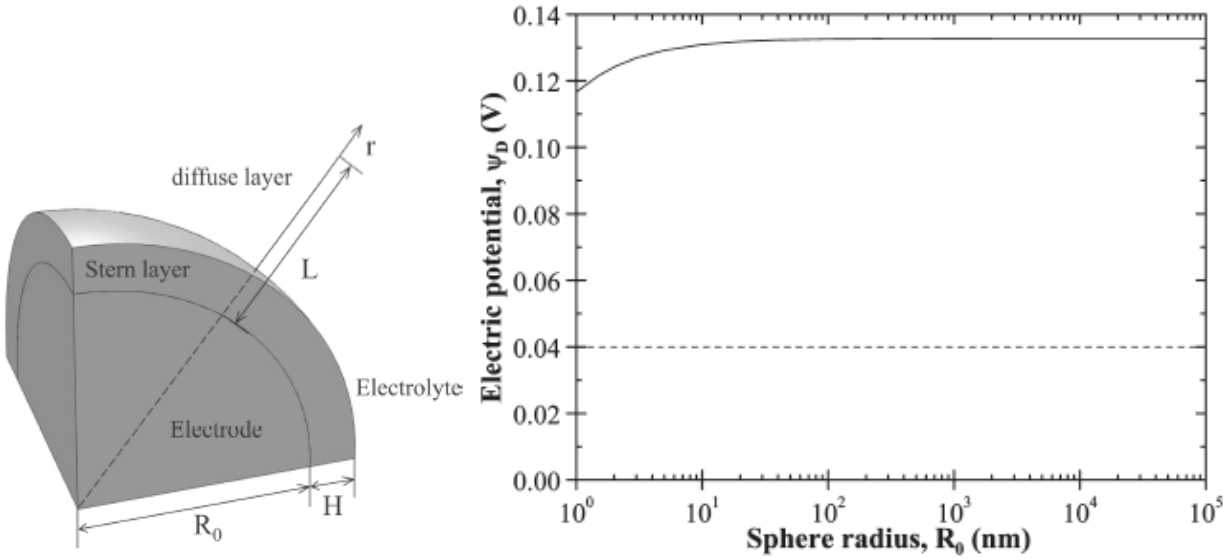


(a) (b)

Figure 1-19: Simulations of electric double layer capacitance: (a) schematic initial configuration of the model. A spherical electrode with the radius $R_0$ was immersed in an electrolyte. Electrolyte consists of two layers: (1) a Helmholtz layer of the thickness H and (2) a diffuse Gouy-Chapman layer beyond, (b) predicted electric potential at the diffuse layer boundary (R=H=0.33 nm) as a function of sphere radius obtained by numerical solving. The predicted potential for all values of sphere radius is larger than the maximum calculated potential ($\psi_{max}$ = 0.04V), indicating that the Stern model is not accurate for computing the properties of the diffuse layer for such a high concentration electrolyte [141].

### 1.3.4.3. Stern model

Stern [130] combined the Helmholtz and the Gouy-Chapman models and simply developed the EDL model as two layers, which is a more realistic model to describe the physical situation at the interface (Figure 1-15c). This model describes the EDL as two layers. First, the Helmholtz layer, referring to the compact layer of immobile ions which adsorb to the electrode surface and are located at a finite distance from the electrode. Second, the diffuse layer of the Gouy-Chapman model where the ions are mobile and diffusely spread out in the solution. In mathematical terms, Equation 1-9 can be applied to the compact layer of ions (Helmholtz layer) and Equation 1-12 can be applied to the Gouy-Chapman layer extending into the bulk solution.

Philpott and Glosli [138] used MD to show that systems containing water and sodium chloride exhibit the main components of the EDLs at charged metal surfaces. Particularly, in the chosen

system, there are clearly identifiable regions as a layer of localized oriented water close to the electrode, a diffuse layer and a bulk electrolyte zone. Therefore the immersed-electrode approximation [139] presenting Stern EDL model was chosen for the simulations (Figure 1-20a). It was observed that the width of the diffuse layer increases with decrease in salt concentration. Unlike the Gouy-Chapman theory where there is no correlation, the simulations placed no restrictions on either water-ion or ion-ion correlations.

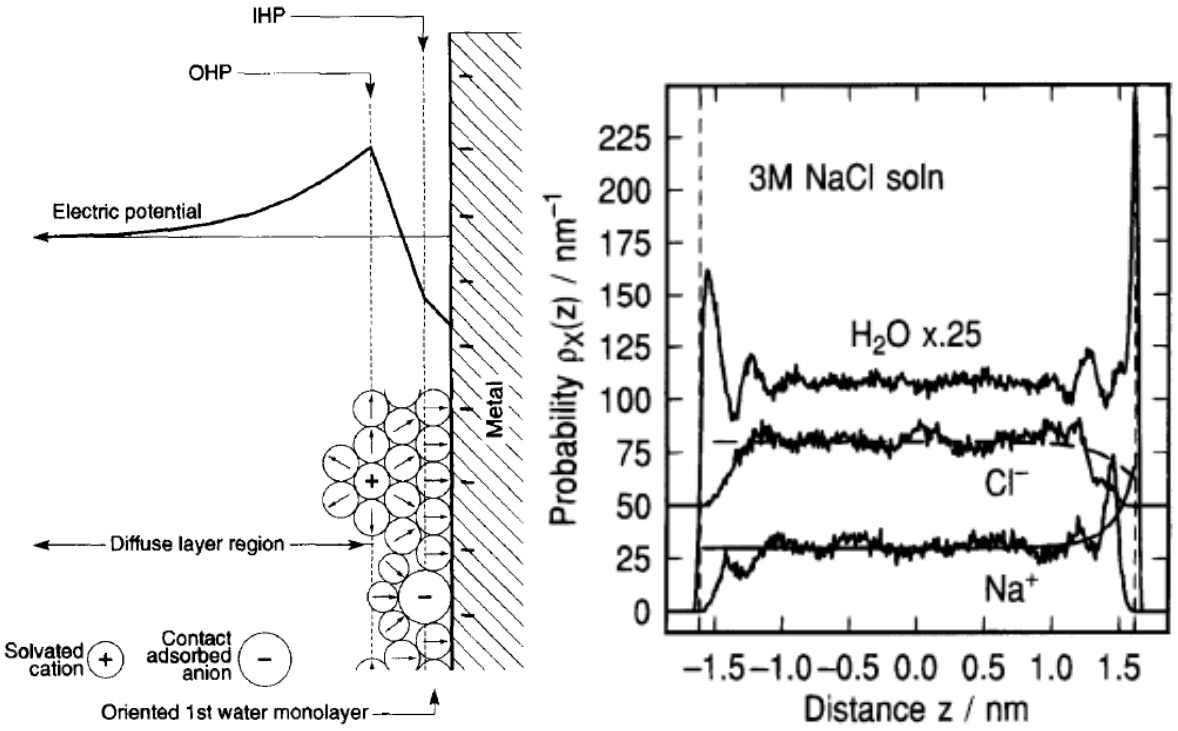


(a) (b)

Figure 1-20: Screening of charged electrodes in aqueous electrolyte: (a) schematic diagram of the electrode-electrolyte interface and the potential drop [139], (b) water and ion probability density distributions for salt solution and electrode. The water density shows a localized layer of water at 1.62 nm. A sharp peak can be seen on the cation distribution at 1.45 nm. It corresponds to the excess positive ions screening the negatively charged electrode. The Gouy-Chapman distribution for anions and cations is shown superimposed on the sodium (solid line) and chloride (dashed line) ion distribution.

Philpott et al. [139] used MD to model the structure and dynamics of EDLs that form when a metal electrode is in contact with an aqueous electrolyte solution. Stern double layer consisted of the Helmholtz layer accompanied with the diffusion region (Gouy-Chapman layer) was used in the calculations (Figure 1-20a). The electric field and potential across the system were calculated

(Figure 1-21). It was pointed out that MD is a powerful tool reproduces qualitatively many phenomena familiar from experiments on the electrochemical interface.

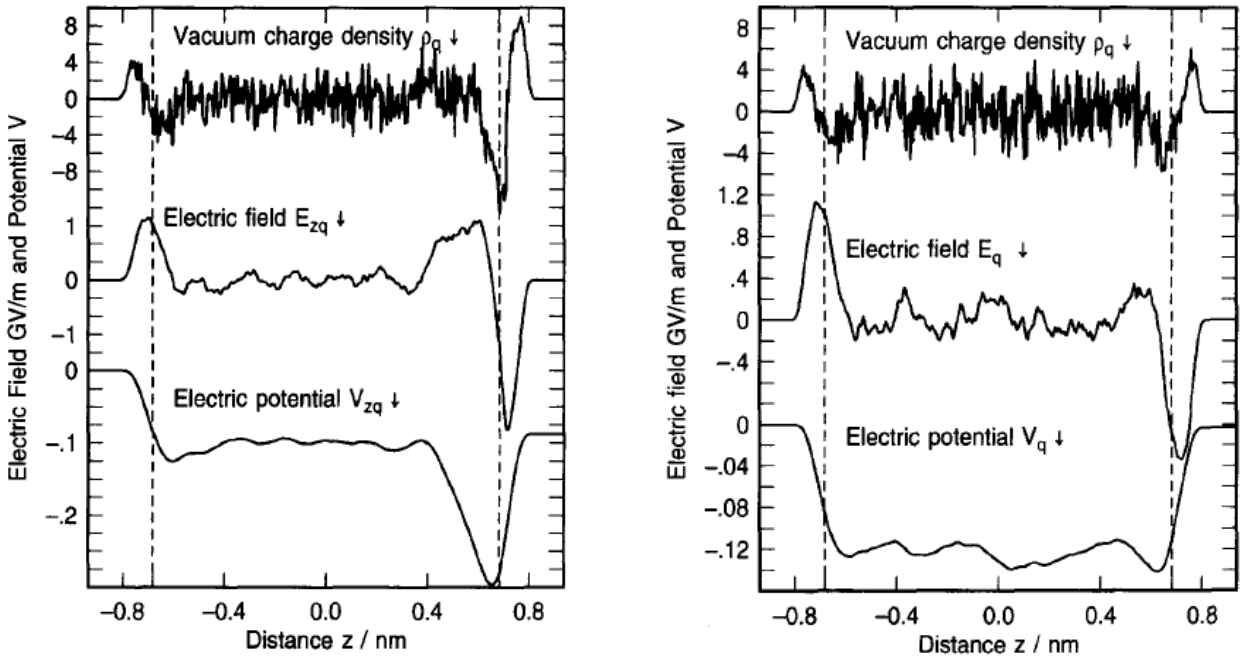


Figure 1-21: Charge, electric field and potential for (a) LiI, and (b) LiF solutions. In both systems the electric field obtained by integrating the charge density and the potential obtained by integrating the electric field. Electric fields for both solutions are about constant close to the electrode and then drops.

### 1.4. Summary

The goal of this chapter was to give the reader in-depth information on the background of the work that is performed in this research. The critical need and proposed approach of the research were presented. A literature review of the experimental works on iron passivity and chloride-induced depassivation was provided to identify the knowledge gaps. The formulation of the ReaxFF-MD technique was presented with relevant works from the literature. Finally, different EDL models and how different researchers have used them for different electrode-electrolyte systems were presented.

The ultimate goal of proposed research is to use ReaxFF-MD to make transformational contributions to the fundamental understanding of passivity and chloride-induced depassivation of iron in highly alkaline media. From the literature review, several knowledge gaps were identified leading to the main objectives of the proposed research, which involve the investigation of

- the feasibility of using ReaxFF-MD to investigate electrochemical processes iron in neutral and alkaline electrolytes
- the applicability of classical electrical double layer models to study corrosion and passivity of iron in neutral and alkaline media using ReaxFF-MD;
- iron passivity in alkaline media using ReaxFF-MD;
- chloride-induced depassivation of iron in alkaline media using ReaxFF-MD.

Chapters 2-5 presents four individual manuscripts as the completed works to fulfill the research objectives. Chapter 6 presents a summary of major findings and conclusions of the research.

### 1.5. References

[1] H. DorMohammadi, Q. Pang, O.B. Isgor, L. Árnadóttir, Atomistic simulation of initial stages of iron corrosion in pure water using reactive molecular dynamics, Computational Materials Science, 145 (2018) 8.
[2] Highwas and bridges: Corrosion resources for highways and bridges, NACE International, (2013).
[3] Corrosion Cost and Preventive Strategies in the United States, FHWA-RD-01-156
[4] A.A. Sagues, K. Lau, R.G. Powers, R.J. Kessler, Corrosion of epoxy-coated rebar in marine bridges-Part 1: A 30-year perspective, Corrosion, 66 (2010) 13.
[5] R.E. Weyers, W. Pyc, M.M. Sprinkel, Estimating the service life of epoxy-coated reinforcing steel., Aci Mater J, 95 (1998) 12.
[6] S.M. Trepanier, B.B. Hope, C.M. Hansson, Corrosion inhibitors in concrete - Part III. Effect on time to chloride-induced corrosion initiation and subsequent corrosion rates of steel in mortar, Cement Concrete Res, 31 (2001) 6.
[7] L. Mammoliti, C.M. Hansson, B.B. Hope, Corrosion inhibitors in concrete - Part II: Effect on chloride threshold values for corrosion of steel in synthetic pore solutions, Cement Concrete Res, 29 (1999) 7.
[8] K. Lau, A.A. Sagues, R.G. Powers, Corrosion of epoxy-coated rebar in marine bridges-Part 2: Corrosion in cracked concrete, Corrosion, 66 (2010) 16.
[9] C. Andrade, C.L. Page, Pore solution chemistry and corrosion in hydrated cement systems containing chloride salts - a study of cation specific effects, Brit Corros J, 21 (1986) 5.

[10] U. Angst, B. Elsener, C.K. Larsen, O. Vennesland, Critical chloride content in reinforced concrete - A review, Cement Concrete Res, 39 (2009) 17.
[11] U.M. Angst, B. Elsener, C.K. Larsen, O. Vennesland, Chloride induced reinforcement corrosion: Electrochemical monitoring of initiation stage and chloride threshold values, Corros Sci, 53 (2011) 14.
[12] P. Ghods, O.B. Isgor, G.A. McRae, G.P. Gu, Electrochemical investigation of chloride-induced depassivation of black steel rebar under simulated service conditions, Corros Sci, 52 (2010) 11.
[13] S. Goni, C. Andrade, Synthetic concrete pore solution chemistry and rebar corrosion rate in the presence of chlorides, Cement Concrete Res, 20 (1990) 15.
[14] C.M. Hansson, A. Poursaee, A. Laurent, Macrocell and microcell corrosion of steel in ordinary Portland cement and high performance concretes, Cement Concrete Res, 36 (2006) 5.
[15] L. Li, A.A. Sagues, Chloride corrosion threshold of reinforcing steel in alkaline solutions - Open-circuit immersion tests, Corrosion, 57 (2001) 10.
[16] L. Li, A.A. Sagues, Chloride corrosion threshold of reinforcing steel in alkaline solutions - Cyclic polarization behavior, Corrosion, 58 (2002) 12.
[17] L.T. Mammoliti, L.C. Brown, C.M. Hansson, B.B. Hope, The influence of surface finish of reinforcing steel and pH of the test solution on the chloride threshold concentration for corrosion initiation in synthetic pore solutions, Cement Concrete Res, 26 (1996) 6.
[18] P. Ghods, O.B. Isgor, G. Mcrae, T. Miller, The effect of concrete pore solution composition on the quality of passive oxide films on black steel reinforcement, Cement Concrete Comp, 31 (2009) 10.
[19] R.G. Pillai, D. Trejo, Surface condition effects on critical chloride threshold of steel reinforcement, Aci Mater J, 102 (2005) 7.
[20] P. Ghods, O.B. Isgor, G.A. McRae, J. Li, G.P. Gu, Microscopic investigation of mill scale and its proposed effect on the variability of chloride-induced depassivation of carbon steel rebar, Corros Sci, 53 (2011) 9.
[21] M.F. Montemor, A.M.P. Simoes, M.G.S. Ferreira, Analytical characterization of the passive film formed on steel in solutions simulating the concrete interstitial electrolyte, Corros Rev, 54 (1998) 7.
[22] J. Gui, T.M. Devine, Analytical characterization of the passive film formed on steel in solutions simulating the concrete interstitial electrolyte, Corros Sci, 36 (1994) 21.
[23] P. Ghods, O.B. Isgor, G.J.C. Carpenter, J. Li, G.A. McRae, G.P. Gu, Nano-scale study of passive films and chloride-induced depassivation of carbon steel rebar in simulated concrete pore solutions using FIB/TEM, Cement Concrete Res, 47 (2013) 14.
[24] P. Ghods, O.B. Isgor, J. Brown, F. Bensebaa, D. Kingston, XPS depth profiling study on the passive oxide film of carbon steel in saturated calcium hydroxide solution and the effect of chloride on the film properties, Applied Surface Science, 257 (2011) 9.
[25] P. Ghods, O. Burkan Isgor, F. Bensebaa, D. Kingston, Angle-resolved XPS study of carbon steel passivity and chloride-induced depassivation in simulated concrete pore solution, Corros Sci, 58 (2012) 9.
[26] H.B. Gunay, P. Ghods, O.B. Isgor, G.J. Carpenter, X. Wu, Characterization of atomic structure of oxide films on carbon steel in simulated concrete pore solutions using EELS, Applied Surface Science, 274 (2013) 8.

[27] M. Sánchez-Moreno, H. Takenouti, J.J. García-Jareño, F. Vicente, C. Alonso, A theoretical approach of impedance spectroscopy during the passivation of steel in alkaline media, Electrochimica Acta, 54 (2009) 5.
[28] S. Joiret, M. Keddam, X.R. Novoa, M.C. Perez, C. Rangel, H. Takenouti, Use of EIS, ring-disk electrode, EQCM and Raman spectroscopy to study the film of oxides formed on iron in 1 M NaOH, Cement Concrete Comp, 24 (2002) 9.
[29] M. Sánchez, J. Gregori, C. Alonso, J.J. García-Jareño, H. Takenouti, F. Vicente, Electrochemical impedance spectroscopy for studying passive layers on steel rebars immersed in alkaline solutions simulating concrete pores, Electrochimica Acta, 52 (2007) 8.
[30] L. Bertolini, B. Elsener, P. Pedeferri, R. and Polder, Corrosion of Steel in Concrete: Prevention, Diagnosis, Repair, Weinheim: Wiley-VCH, (2000).
[31] H. Bohni, Corrosion in concrete structures, New York: CRC Press, (2005).
[32] J.P. Broomfield, Corrosion of steel in concrete New York: Taylor & Francis, (2007).
[33] P.K. Mehta, P.J.M. Monteiro, Concrete: microstructure, properties, and materials, New York: McGraw-Hill Professional., (2005).
[34] H. Burak Gunay, O.B. Isgor, P. Ghods, Kinetics of passivation and chloride-induced depassivation of iron in simulated concrete pore solutions using electrochemical quartz crystal nanobalance, Corrosion, 71 (2015) 13.
[35] J. Williamson, O.B. Isgor, The effect of simulated concrete pore solution composition and chlorides on the electronic properties of passive films on carbon steel rebar, Corros Sci, 106 (2016) 14.
[36] G.K. Glass, N.R. Buenfeld, The presentation of the chloride threshold level for corrosion of steel in concrete, Corros Sci, 39 (1997) 13.
[37] C. Alonso, C. Andrade, M. Castellote, P. Castro, Chloride threshold values to depassivate reinforcing bars embedded in a standardized OPC mortar, Cement & Concrete Research, 30 (2000) 9.
[38] G.R. Meira, C. Andrade, E.O. Vilar, K.D. Nery, Analysis of chloride threshold from laboratory and field experiments in marine atmosphere zone, Construction and Building Materials, 55 (2014) 10.
[39] V.K. Gouda, Corrosion and corrosion inhibition of reinforcing steel: 1-Immersion in alkaline solution, Brit Corros J, 5 (1970) 6.
[40] K. Pettersson, Chloride threshold value and the corrosion rate in reinforced concrete, Cement Concrete Res, 24 (1994) 10.
[41] B.H. Oh, S.Y. KJang, Y.S. Shin, Experimental investigation of the threshold chloride concentration for corrosion initiation in reinforced concrete structures, Magazine of Concrete Research, 55 (2003) 8.
[42] H.E.H. Bird, B.R. OPearson, P.A. Brook, The breakdown of passive films on iron, Corros Sci, 28 (1988) 6.
[43] C.M. Hansson, B. Sorensen, The threshold concentration of chloride in concrete for the initiation of reinforcement corrosion, in: N.S. Berke, V. Chaker, D. Whitting (Eds.), Corrosion Rates of Steel in Concrete, ASTM (STP1065), (1988) 14.
[44] S.E. Hussain, Rasheeduzzafar, A. Al-Musallam, A.S. Al-Gahtani, Factors affecting threshold chloride for reinforcement corrosion in concrete, Cement Concrete Res, 25 (1995) 13.
[45] M. Thomas, hloride thresholds in marine concrete, Cement Concrete Res, (1996) 7.

[46] O.A. Kayyali, M.N. Haque, The Cl-/OH-ratio in chloride-contaminated concrete-A most important criterion, Magazine of Concrete Research, 47 (1995) 8.
[47] J.A. Gonzalez, E. Otero, S. Feliu, W. Lopez, Initial steps of corrosion in the steel/Ca(OH)ZCl system: The role of heterogeneities on the steel surface and oxygen supply, Cement Concrete Res, 23 (1993) 8.
[48] G.K. Glass, N.R. Buenfeld, The inhibitive effects of electrochemical treatment applied to steel in concrete, Corros Sci, 42 (2000) 5.
[49] C.L. Page, Initiation of chloride-induced corrosion of steel in concrete: role of the interfacial zone, Materials and Corrosion, 60 (2009) 7.
[50] S. Rasheeduzzafar, E. Hussain, S.S. Al-Saadoun, Effect of tricalcium aluminate content of cement on chloride binding and corrosion of reinforcing steel in concrete, Aci Mater J, 89 (1993) 10.
[51] S.E. Hussain, A.S. Al-Gahtani, Chloride threshold for corrosion of reinforcement in concrete, Aci Mater J, 93 (1996) 5.
[52] N.R.B. G.K. Glass, The influence of chloride binding on the chloride induced corrosion risk in reinforced concrete, Corros Sci, 42 (2000) 16.
[53] K.H. Pettersson, Factors influencing chloride induced corrosion of reinforcement in concrete, Durability Build, Material Components, 1 (1996) 8.
[54] P.S. Mangat, B.T. Molloy, Factors influencing chloride-induced corrosion of reinforcement in concrete, Materials and Structures, 25 (1992) 8.
[55] N.S. McIntyre, D.G. Zetaruk, X-ray photoelectron spectroscopic studies of iron oxides, Analytical Chemistry, 49 (1977) 9.
[56] G.C. Allen, P.M. Tucker, R.K. Wild, Characterization of iron/oxygen surface reactions by X-ray photoelectron spectroscopy, Philosophy Magazine B, 46 (1982) 11.
[57] S. Haupt, C. Calinski, U. Collisi, H.W. Hoppe, H.D. Speckmann, H.H. Strehblow, XPS and ISS examinations of electrode surfaces and passive layers with a specimen transfer in a closed system, Surface and Interface Analysis, 9 (1986) 9.
[58] T. Fujii, F.M.F. De Groot, G.A. Sawatzky, F.C. Voogt, T. Hibma, K. Okada, In situ XPS analysis of various iron oxide films grown by NO2-assisted molecular-beam epitaxy, Physical Review B, 59 (1999) 8.
[59] A.P. Grosvenor, B.A. Kobe, M.C. Biesinger, N.S. McIntyre, Investigation of multiplet splitting of Fe 2p XPS spectra and bonding in iron compounds, Surface and Interface Analysis, 36 (2004b) 11.
[60] B. Poter, I. Parezanovic, M. Spiegel, In-situ scanning electron microscopy and electron backscatter diffraction investigation on the oxidation of pure iron, Materials at High Temperatures, 22 (2005) 9.
[61] M. Nagayama, M. Cohen, The anodic oxidation of iron in a neutral solution, J Electrochem Soc, 109 (1962) 10.
[62] J. Gui, T.M. Devine, In situ vibrational spectra of the passive film on iron in buffered borate solution, Corros Sci, 32 (1991) 20.
[63] A.J. Davenport, M. Sansone, High resolution in situ XANES investigation of the nature of the passive film on iron in a pH 8.4 borate buffer, J Electrochem Soc, 142 (1999) 6.

[64] L.J. Oblonsky, T.M. Devine, A surface enhanced Raman spectroscopic study of the passive films formed in borate buffer on iron, nickel, chromium and stainless steel, Corros Sci, 37 (1995) 25.
[65] V. Schroeder, T.M. Devine, Surface enhanced Raman spectroscopy study of the galvanostatic reduction of the passive film on iron, J Electrochem Soc, 146 (1999) 10.
[66] M.P. Ryan, R.C. Newman, G.E. Thompson, An STM study of the passive film formed on iron in borate buffer solution, J Electrochem Soc, 142 (1995) 3.
[67] S. Ahn, H. Kwon, D.D. Macdonald, Role of chloride ion in passivity breakdown on iron and nickel, J Electrochem Soc, 152 (2005) 9.
[68] S.P. Harrington, F. Wang, T.M. Devine, The structure and electronic properties of passive and prepassive films of iron in borate buffer, Electrochimica Acta, 55 (2010) 11.
[69] K. Yazdanfar, X. Zhang, P.G. Keech, D.W. Shoesmith, J.C. Wren, Film conversion and breakdown processes on carbon steel in the presence of halides, Corros Sci, 52 (2010) 8.
[70] A. Veluchamy, D. Sherwood, B. Emmanuel, I.S. Cole, Critical review on the passive film formation and breakdown on iron electrode and the models for the mechanisms underlying passivity, Journal of Electroanalytical Chemistry, 785 (2017) 20.
[71] I. Diez-Perez, C. Vericat, P. Gorostiza, F. Sanz, The iron passive film breakdown in chloride media may be mediated by transient chloride-induced surface states located within the band gap, Electrochemistry Communications, 8 (2006) 6.
[72] M. Sánchez-Moreno, H. Takenouti, J.J. García-Jareno, F. Vicente, C. Alonso, A theoretical approach of impedance spectroscopy during the passivation ofsteel in alkaline media, Electrochimica Acta, 54 (2009) 5.
[73] M. Sánchez, J. Gregori, M.C. Alonso, J.J. García-Jareño, F. Vicente, Anodic growth of passive layers on steel rebars in an alkaline medium simulating the concrete pores, Electrochimica Acta, 52 (2006) 7.
[74] D.D. Macdonald, S.R. Biaggio, H.K. Song, Steady-state passive films - interfacial kinetic effects and diagnostic-criteria, J Electrochem Soc, 139 (1992) 8.
[75] C. Colliex, T. Manoubi, C. Ortiz, Electron-Energy-Loss-Spectroscopy near-edge fine-structures in the iron-oxygen system. , Physical Review B, 44 (1991) 10.
[76] N.N. Greenwood, A. Earnshaw, Chemistry of elements, Elsevier, (1997).
[77] S. Behrens, Preparation of functional magnetic nanocomposites and hybrid materials: recent progress and future directions. , Nanoscale, 3 (2011) 6.
[78] T.E. Pou, O.J. Murphy, V. Young, J.O.M. Bockris, L.L. Tongson, Passive films on iron: The mechanism of breakdown in chloride containing solutions, J Electrochem Soc, 131 (1984) 9.
[79] M. Kamrunnahar, J.E. Bao, D.D. Macdonald, Challenges in the theory of electron transfer at passive interfaces, Corros Sci, 47 (2005) 29.
[80] J. Kruger, Passivity and its breakdown on iron and iron base alloys, USA-Japan Seminar, NACE, Houston TX, (1976).
[81] A.T. Fromhold Jr, J. Kruger, Space-Charge and Concentration-Gradient effects on anodic oxide film formation. , J Electrochem Soc, 120 (1973) 8.
[82] C.Y. Chao, A point defect model for anodic passive films. I. film growth kinetics, J Electrochem Soc, 128 (1981) 8.
[83] N. Sato, M. Cohen, The kinetics of anodic oxidation of iron in neutral solution, J Electrochem Soc, 111 (1964) 8.

[84] M. Sakashita, N. Sato, Bipolar fixed charge-induced passivity, Passivity of metals, J Electrochem Soc, (1978) 5.
[85] N. Cabrera, N.F. Mott, Theory of the oxidation of metals, Reports on Progress in Physics, 163 (1949) 22.
[86] J. Kruger, Passivity of metals-A materials perspective, International Materials Reviews, 33 (1988) 18.
[87] J.M. Kolotyrkin, Effects of anions on the dissolution kinetics of metals, J Electrochem Soc, 108 8.
[88] H.P. Leckie, H.H. Uhlig, Environmental factors affecting the critical potential for pitting in 18–8 stainless steel, J Electrochem Soc, 113 (1966) 6.
[89] T.P. Hoar, D.C. Mears, G.P. Rothwell, The relationships between anodic passivity, brightening and pitting, Corros Sci, 5 (1965) 11.
[90] D.D. Macdonald, The point defect model for the passive state, Journal of Electroanalytical Society, 139 (1992) 16.
[91] Q. Pang, H. DorMohammadi, O.B. OIsgor, L. Árnadóttir, Effects of surface defects on the interactions of Cl and α-$Fe_2O_{-3}$ (0001) surface: A density functional theory study, AVS Symposium, Oregon State University, (2017).
[92] M. Griebel, S. Knapek, G. Zumbusch, Numerical simulation in molecular dynamics, numerics, algorithms, parallelization, applications, Springer, (2007).
[93] W.K. Liu, E.G. Karpov, S. Zhang, H.S. Park, An introduction to computational nanomechanics and materials Computer Methods Applied Mech and Engineering, 193 (2004) 50.
[94] D.C. Rapaport, The art of molecular dynamics simulation, Cambridge University Press, (2004).
[95] M.P. Allen, Introduction to Molecular Dynamics Simulation, , NIC Series 23 (2004) 28.
[96] A.R. Khoei, H. DorMohammadi, Validity and size-dependency of Cauchy–Born hypothesis with Tersoff potential in silicon nano-structures, Computational Materials Science, 63 (2012) 10.
[97] A.R. Khoei, H. DorMohammadi, A. Aramoon, A temperature-related boundary Cauchy–Born method fo rmulti-scale modeling of silicon nano-structures, Physics Letters A, 378 (2014) 10.
[98] A.P. Sutton, J. Chen, Long-range Finnis–Sinclair potentials, Philosophical Magazine Letters 61 (1990) 8.
[99] J.E. Lennard-Jones, On the determination of molecular fields. —II. From the equation of state of a gas, Proceeding of the Royal Society (1924) 15.
[100] E. Spohr, K. Heinzinger, Molecular dynamics simulation of a water/metal interface, Chemical Physics Letters, 123 (1986) 4.
[101] S. Boyda, M. Gravelle, Nonreactive molecular dynamics force field for crystalline hexahydro-1,3,5-trinitro-1,3,5 triazine, The Journal of Chemical Physics, 124 (2006) 10.
[102] H. Heinz, R. A. Vaia, B. L. Farmer, R.R. Naik, Accurate simulation of surfaces and interfaces of face-centered cubic metals using 12-6 and 9-6 Lennard-Jones potentials, The Journal of Physical Chemistry C, 112 (2008) 10.
[103] H. Zhang, E. Iype, S. V. Nedea, C.C.M. Rindt, Molecular dynamics study on thermal dehydration process of epsomite (MgSO4·7H2O), Molecular Simulation, 40 (2013) 10.
[104] R.P. Feynman, Chapter 5 : MD, Atoms in Motion, LLC, (2018).
[105] A. C. T. van Duin, S. Dasgupta, F. Lorant, W.A. Goddard, ReaxFF: A reactive force field for hydrocarbons, The Journal of Physical Chemistry A, 105 (2001) 14.

[106] T. P. Senftle, S. Hong, M. M. Islam, S. B. Kylasa, Y. Zheng, Y. K. Shin, C. Junkermeier, R. Engel-Herbert, M. J. Janik, H. M. Aktulga, T. Verstraelen, A. Grama, A.C.T.v. Duin, The ReaxFF reactive force-field: development, applications and future directions, npj Computational Materials, 2 (2016) 14.
[107] O. Assowe, O. Politano, V. Vignal, P. Arnoux, B. Diawara, O. Verners, A.C.T.v. Duin, Reactive molecular dynamics of the initial oxidation stages of Ni(111) in pure water: effect of an applied electric field, The Journal of Physical Chemistry A, 116 (2012) 10.
[108] A. C. T. van Duin, J. M. A. Baas, B.v.d. Graaf, Delft molecular mechanics: A new approach to hydrocarbon force fields, Journal of the Chemical Society, Faraday Transactions, 90 (1994) 15.
[109] A. C. T. van Duin, A. Strachan, S. Stewman, Q. Zhang, X. Xu, W.A. Goddard, ReaxFF SiO Reactive force field for silicon and silicon oxide systems, The Journal of Physical Chemistry A, 107 (2003) 9.
[110] M. J. Buehler, A. C. T. van Duin, W.A. Goddard, Multiparadigm modeling of dynamical crack propagation in silicon using a reactive force field, Physical Review Letters, 96 (2006) 4.
[111] W. J. Mortier, S. K. Ghosh, S. Shankar, Electronegativity equalization method for the calculation of atomic charges in molecules, Journal of the American Chemical Society, 108 (1986) 6.
[112] A. K. Rappe, W.A. Goddard, Charge equilibration for molecular dynamics simulations, The Journal of Physical Chemistry, 95 (1991) 6.
[113] G. O. A. Janssens, B. G. Baekelandt, H. Toufar, W. J. Mortier, R.A. Schoonheydt, Comparison of cluster and infinite crystal calculations on zeolites with the electronegativity equalization method (EEM) The Journal of Physical Chemistry, 99 (1995) 8.
[114] A. C. T. van Duin, V. S. Bryantsev, M. S. Diallo, W. A. Goddard, O. Rahaman, D. J. Doren, D. Raymand, K. Hermansson, Development and validation of a ReaxFF Reactive Force Field for Cu cation/water interactions and copper metal/metal oxide/metal hydroxide condensed phases, The Journal of Physical Chemistry A, 114 (2010) 8.
[115] M. Aryanpour, A. C. T. van Duin, J.D. Kubicki, Development of a reactive force field for iron-oxyhydroxide systems, The Journal of Physical Chemistry A, 114 (2010) 10.
[116] D. Raymand, A. C. T. van Duin, D. Spångberg, W. A. Goddard, K. Hermansson, Water adsorption on stepped ZnO surfaces from MD simulation, Surf. Sci., (2010) 12.
[117] M. F. Russo, Jr. R. Li, M. Mench, A.C.T.v. Duin, Molecular dynamic simulation of aluminumewater reactions using the ReaxFF reactive force field, International Journal of Hydrogen Energy, 36 (2011) 8.
[118] B. Jeon, S. K. R. S. Sankaranarayanan, A.C.T.v. Duin, S. Ramanathan, Atomistic insights into aqueous corrosion of copper, The Journal of Chemical Physics, 134 (2011) 10.
[119] B. Jeon, S. K. R. S. Sankaranarayanan, A.C.T.v. Duin, S. Ramanathan, Reactive molecular dynamics study of chloride ion interaction with copper oxide surfaces in aqueous media, ACS Applied Materials & Interfaces 4(2012) 8.
[120] O. Verners, A.C.T.v. Duin, Comparative molecular dynamics study of fcc-Ni nanoplate stress corrosion in water, Surface Science, 633 (2015) 8.
[121] C. Zou, Y. K. Shin, A. C.T. van Duin, H. Fangb, Z.K. Liu, Molecular dynamics simulations of the effects of vacancies on nickel self-diffusion, oxygen diffusion and oxidation initiation in nickel, using the ReaxFF reactive force field, Acta Materialia, 83 (2015) 11.

[122] B. Jeon, Q. V. Overmeere, A.C.T.v. Duin, S. Ramanathan, Nanoscale oxidation and complex oxide growth on single crystal iron surfaces and external electric field effects, Physical Chemistry Chemical Physics, 15 (2013) 10.
[123] T. Pan, A.C.T.v. Duin, Passivation of steel surface: An atomistic modeling approach aided with X-ray analyses, Materials Letters, 65 (2011) 4.
[124] T. Pan, Quantum chemistry-based study of iron oxidation at the iron–water interface: An X-ray analysis aided study, Chemical Physics Letters, 511 (2011) 7.
[125] O. Assowe, O. Politano, V. Vignal, P. Arnoux, B. Diawara, O. Verners, A.C.T.v. Duin, Reactive molecular dynamics of the initial oxidation stages of Ni(111) in pure water: effect of an applied electric field, The Journal of Physical Chemistry A, 116 (2012) 10.
[126] R.W. Revie, H.H. Uhlig, Corrosion and corrosion control 4th ed., Wiley-Interscience, New York, 2008.
[127] H. von Helmholtz, Studien €uber electrische grenzschichten, Annalen der Physik 243 (1879) 6.
[128] G. Gouy, Constitution of the electric charge at the surace of an electrolyte Journal of Theoretical and Applied Physics, 9 (1910) 12.
[129] D.L. Chapman, A contribution to the theory of electrocapillarity, Philosophical Magazine 25 (1913) 7.
[130] O. Stern, The theory of the electrolytic double layer, Zeitschrift für Elektrochemie und Angewandte Physikalische Chemie, 30 (1924) 9.
[131] E. Gongadze, U. Van Rienen, A. Iglic, Generalized Stern models of the electric double layer considering the spatial variation of permittivity and finite size of ions in saturation regime, Cellular & Molecular Biology Letters, 16 (2011) 19.
[132] A. Bard, L. Faulkner, Electrochemical methods: fundamentals and applications, John Wiley & Sons: New York, (2001).
[133] E. Spohr, Molecular dynamics simulations of water and ion dynamics in the electrochemical double layer, Solid State Ionics, 150 (2002) 12.
[134] J.N. Glosli, M.R. Philpott, Molecular dynamics study of interfacial electric fields, Electrochemica Acta, 41 (1996) 14.
[135] S. Dewan, V. Carnevale, A. Bankura, E.-B. A., G. Fiorin, M.L. Klein, E. Borguet, Structure of water at charged interfaces: a molecular dynamics study, Langmuir, (2014) 10.
[136] D.A. Welch, B.L. Mehdi, H.J. Hatcheli, R. Faller, J.E. Evans, N.D. Browning, Using molecular dynamics to quantify the electrical double layer and examine the potential for its direct observation in the in-situ TEM, Advanced Structural and Chemical Imaging, 1 (2015) 11.
[137] P. Attard, Electrolytes and the electric double layer, Advanced Chemical Physics, 92 (1996) 159.
[138] M.R. Philpott, J.N. Glosli, Screening of charged electrodes in aqueous electrolytes, Journal of Electroanalytical Society, 142 (1995) 4.
[139] M.R. Philpott, J.N. Glosli, S.B. Zhu, Molecular dynamics simulation of adsorption in electric double layers, Surface Science, 335 (1995) 10.
[140] L. Pilon, H. Wang, A. d'Entremont, Recent advances in continuum modeling of interfacial and transport phenomena in electric double layer capacitors, J Electrochem Soc, 162 (2015) 21.
[141] H. Wang, L. Pilon, Accurate simulations of electric double layer capacitance of ultramicroelectrodes, The Journal of Physical Chemistry C, 115 (2011) 9.

[142] P. Zarzycki, S. Kerisit, K.M. Rosso, Molecular dynamics study of the electrical double layer at silver chloride-electrolyte interfaces, The Journal of Physical Chemistry C, 114 (2010) 17.
[143] J. Williamson, V. Jafari Azad, O.B. Isgor, Modeling electronic properties of the passive films on carbon steel in simulated concrete pore solutions, J Electrochem Soc, 162 (2015) 11.
[144] V. Bagotsky, Fundamentals of electrochemistry, John Wiley & Sons: New York, (2006).
[145] H.-J. Butt, M. Kappl, Surface and interfacial forces, Wiley-VCH: Weinheim, Germany, (2010).
[146] R. Hunter, Foundations of colloid science, Oxford University Press: New York, (2001).
[147] J. Lyklema, Fundamentals of interface and colloid science, Academic Press: New York, 2 (2001).
[148] H. Ohshima, Theory of colloid and interfacial electric phenomena, Academic Press: New York, (2006).

Manuscript 1

# Atomistic simulation of initial stages of iron corrosion in pure water using reactive molecular dynamics

Hossein DorMohammadi, Qin Pang, Líney Árnadóttir, O. Burkan Isgor

Published in: *Computational Materials Science*, Volume 145, January 2018, 126-133

## 2. Manuscript 1

# Atomistic simulation of initial stages of iron corrosion in pure water using reactive molecular dynamics

Hossein DorMohammadi[1], Qin Pang[2], Liney Arnadottir[2], O. Burkan Isgor[1]

**Abstract:**

Reactive Force Field Molecular Dynamics (ReaxFF-MD) was used to study the initial stages of iron corrosion in pure water. The simulations were performed on iron under various applied external electric fields and temperatures. Oxide film formation was accompanied by iron dissolution in water, indicating active corrosion and supporting the expected thermodynamic behavior of iron in pure water. Oxide film thickness and iron dissolution increased with increasing applied external electric field. Corrosion rates increased slightly with increasing temperature within the temperature range of this investigation (300 K to 350 K). Critical stages of the iron corrosion process during the simulations were identified as dissociation of water to $OH^-$ and $H^+$, adsorption of $OH^-$ on the iron surface, penetration of oxygen into iron to form iron oxides, and dissolution of iron into solution. Comparisons of the simulated charge distributions and pair distribution functions to those of reference oxides showed the formed oxide compositions were not pure phases, but rather mixture of oxides.

**Keywords:** Iron; corrosion; oxidation; reactive force field; molecular dynamics.

[1] Oregon State University, School of Civil and Construction Engineering, Corvallis, Oregon, USA

[2] Oregon State University, School of Chemical, Biological and Environmental Engineering, Corvallis, Oregon, USA

## 2.1. Introduction

Corrosion of steel reinforcement is one of the most prevalent deterioration mechanisms in reinforced concrete structures. The annual cost of corrosion in highway bridges alone is estimated to be above $8 billion, but it is widely accepted that the costs have increased over the past decade [1, 2]. Therefore, there is a critical need for the development of innovative, inexpensive, and ubiquitously effective corrosion mitigation strategies in the form of new corrosion-resistant steels and corrosion inhibitors. The development of these new materials has been hindered by the gaps in the fundamental understanding of the passivity of steels in concrete and lack of tools to intelligently design and test them. Trial-and-error procedures to produce new and affordable materials to resist steel corrosion in concrete have been, to a large degree, ineffective.

Passivity and chloride-induced depassivation of iron and carbon steel in highly alkaline environments, such as the ones provided by concrete (pH>13), have been studied extensively using electrochemical [3-14] and nano-scale surface characterization techniques [15-21]. Electrochemical studies have provided macro-scale observations of the nature of the passive films and factors affecting chloride-induced depassivation processes. Nano-scale surface characterization studies have revealed the molecular structure of passive films that form in highly alkaline environments. These studies are in agreement with theoretical passivity models that propose an inner barrier layer that forms directly on the metal substrate, and outer layer that precipitate through the hydrolysis of cations ejected from the inner layer [22, 23]. However, there is still significant debate regarding how chlorides break down these films to initiate active corrosion [24-27].

The testing of the hypotheses on the passivity and chloride-induced depassivation processes of iron or carbon steel in highly alkaline environments is inherently challenging due to the limitations of the nanoscale analytical or spectroscopic techniques in observing kinetic processes. These techniques do not allow in-situ monitoring of the surfaces where processes such as film formation and dissolution take place. On the other hand, atomistic modeling has the potential to serve as a tool in developing fundamental understanding of passivity and depassivation behaviors of steels in concrete and for designing new corrosion-resistant steels and corrosion inhibitors. In recent

years, reactive force field molecular dynamics (ReaxFF-MD) has emerged as a simulation framework to conduct such studies [28-37].

For example, Jeon et al. [38] used ReaxFF-MD to study iron oxidation as it relates to surface reactivity in catalysis and energy applications. These simulations were performed on different surface orientations of pure iron surfaces under applied external electric fields in a non-aqueous (dry) environment containing oxygen. The effect of temperature (up to 900 K) on oxidation was investigated. It was shown that ReaxFF-MD was successful in simulating oxidation kinetics of such systems and providing complementary information to existing experimental data. Although several ReaxFF-MD investigations exist for the study of oxidation and corrosion processes in non-ferrous metals in aqueous environments [31-35], the investigation of iron in such environments is limited [29, 39, 40]. Pan and van Duin [39] and Pan [40] demonstrated the possibility of using ReaxFF-MD in simulating iron oxidation at the iron-water interface and its potential to study passivation and depassivation processes. These simulations identified three distinct stages of iron oxidation based on the chemical species generated and oxidation rate. In early stages, oxides were mixed and unstable; however, in later stages stable oxides were formed, followed by a significant reduction in oxidation rates. Pan [40] described the last stage of oxide formation as passivation of the iron surface, which is not expected in pure water (pH = 7) — iron experiences active corrosion in neutral environments [41].

The present study further investigates the feasibility of using ReaxFF-MD simulations to study iron oxidation in water, with the ultimate goal of simulating passivation and depassivation processes in highly alkaline environments. ReaxFF-MD simulations were performed on pure iron surfaces for different surface orientations (i.e., (111), (110) and (100)) under various applied external electric field. Since the results of the simulations of different iron surfaces were similar, only the results of the Fe(110)-water simulations are presented in this paper. The simulations of (111) and (100) orientations are provided as supplementary material in Appendix A. The effect of temperature, in the range typical of exposure conditions of reinforced concrete structures (300 to 350 K), on oxidation was also investigated. The results of this study are compared with ReaxFF-MD simulations of nickel [34], which is known to passivate in neutral, or even more acidic, environments [42, 43]. This comparison is intended to show the difference in oxidation behavior

of these two metals, and provide support for the feasibility of using ReaxFF-MD simulations to study passivity of iron in highly alkaline environments in the future.

## 2.2. Computational methodology

The molecular dynamics simulations were based on the Reactive Force Field (ReaxFF) interatomic potentials developed by van Duin et al. [37, 44] and performed using the Large-scale Atomic/Molecular Massively Parallel Simulator (LAMMPS) framework [45] on the Extreme Science and Engineering Discovery Environment (XSEDE) [46]. Details of ReaxFF are provided by van Duin et al. [44, 47-49]; therefore, only a summary background of ReaxFF theory is presented here.

Unlike the atomic force field models that are used in non-reactive molecular dynamics (MD) simulations of non-reactive processes [50-53], ReaxFF allows modeling of chemical reactions that include breaking and forming of bonds, where bond order is determined empirically from the interatomic distances. Unlike computationally expensive quantum mechanical (QM) calculations, ReaxFF treats chemical bonding implicitly, which yields significant computational efficiency. In other words, ReaxFF bridges the gap between the non-reactive MD and the computational quantum-chemistry [34]; therefore, ReaxFF-MD approach is well suited to study complex systems such as metal-electrolyte interfaces.

The system energy, $E_{system}$, is calculated using various partial energy contributions as per:

$$E_{system} = E_{bond} + E_{over} + E_{under} + E_{val} + E_{tor} + E_{lp} + E_{H-bond} + E_{vdWaals} + E_{Coulomb} \quad (2\text{-}1)$$

where $E_{bond}$ is the energy associated with forming atomic bonds; $E_{over}$ and $E_{under}$ are, respectively, the over-coordination and under-coordination penalty energies; $E_{tor}$ is the energy associated with torsion angle terms; and $E_{lp}$ and $E_{H-bond}$ are lone-pair energies and hydrogen-bond energies, respectively. $E_{vdWaals}$ and $E_{Coulomb}$ are the terms to handle nonbonded interactions, namely, van der Waals and Coulomb interactions. The last two energy terms, $E_{vdWaals}$ and $E_{Coulomb}$, are computed for all atom pairs, while all other energy terms are calculated for the bond order between particles i and j. In ReaxFF theory, atomic charges are calculated using

a geometry-dependent charge distribution that is determined using charge equalization (QEq) methods [54-56].

In this study, oxidation is studied under applied external electric field, $E_{el}$, using the method proposed by Chen and Martinez [57], and implemented by Assowe et al. [34], which includes the modification of the electrostatic energy, by the perturbation of the potential produced by the electric field, and recalculation of the new charge distribution. Electrostatic forces associated with the external electric field are calculated for each charged particle as the product of the charge and the external electric field [57].

In this paper, force field parameters for simulating iron/water interface were obtained from Aryanpour et al. [29], which included all parameters for determining bond order, bond energy, valence angle energy, torsional angle energy, and van der Waals energy (provided as supplementary materials in Appendix A). Since Aryanpour et al. [29] used these parameters to model an iron-oxyhydroxide system, we used DFT calculations to determine the surface formation energy and water adsorption energy on the Fe(110) surface and compared these to values obtained from MD simulations using the force-field parameters from Aryanpour et al. [29]. We found good agreement between the two methods; details of this comparison are provided in supplementary material (Appendix A).

Iron-water interface were investigated for Fe(110) at 300 K and 1 atm pressure. Periodic boundary conditions were applied along x and y directions and fixed boundary conditions were imposed along the z direction. A reflecting wall was applied at the end of the simulation cell to confine the water molecules. The initial configuration for the Fe(110) system is shown in Figure 2-1. The initial inter-molecule distance between water molecules and the dimension of the vacuum slab along the z direction were determined based on the density of water which is 0.99 g/cm$^3$ at 300 K and 1 atm. The simulation cell had 480 water molecules and 2016 iron atoms. Nose-Hoover thermostat [58, 59] is employed in all simulations to maintain the prescribed system temperature for canonical (NVT) ensemble. Maxwell-Boltzman distribution was chosen to set the initial velocities for different temperatures. The equations of motion were integrated with a time step of 0.1 fs in all cases for both short-range and long-range forces. The simulations were carried out at three external electric fields: 20 MeV/cm, 25 MeV/cm and 30 MeV/cm. To study the influence of

the external electric field on the oxidation of iron, the electric field was applied 3 Å from the surface of the iron. It should be mentioned here that iron oxidation reactions with external electric field intensity of 15 MeV/cm are extremely slow or not activated at this timescale, and oxidation has not started after 150 ps. The effect of temperature is investigated (under 25 MeV/cm external electric field) to cover a practical range that represents the exposure conditions for concrete structures (300K to 350 K).

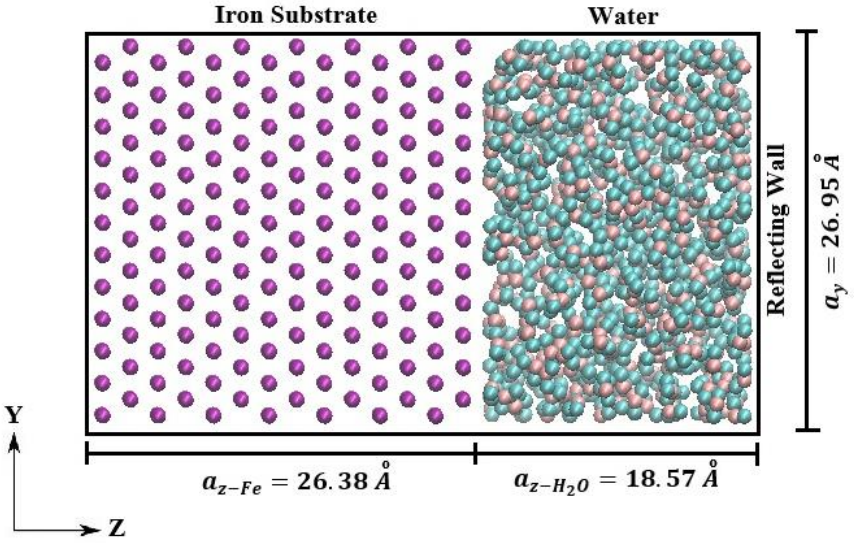


Figure 2-1: Initial configuration of the Fe(110)-water model ($a_x = 29.98\ \dot{A}$).

### 2.3. Results and discussion

#### 2.3.1. Oxidation of iron at 300 K

Figure 2-2 illustrates ReaxFF-MD simulations of the Fe(110)-water system under different external electric fields at 150 ps. In all external field intensities, oxide film formation is accompanied by iron dissolution in water, indicating active corrosion. Although there are differences in the oxide film thickness and the amount of iron dissolution for different applied external electric fields, the corrosion patterns are similar.

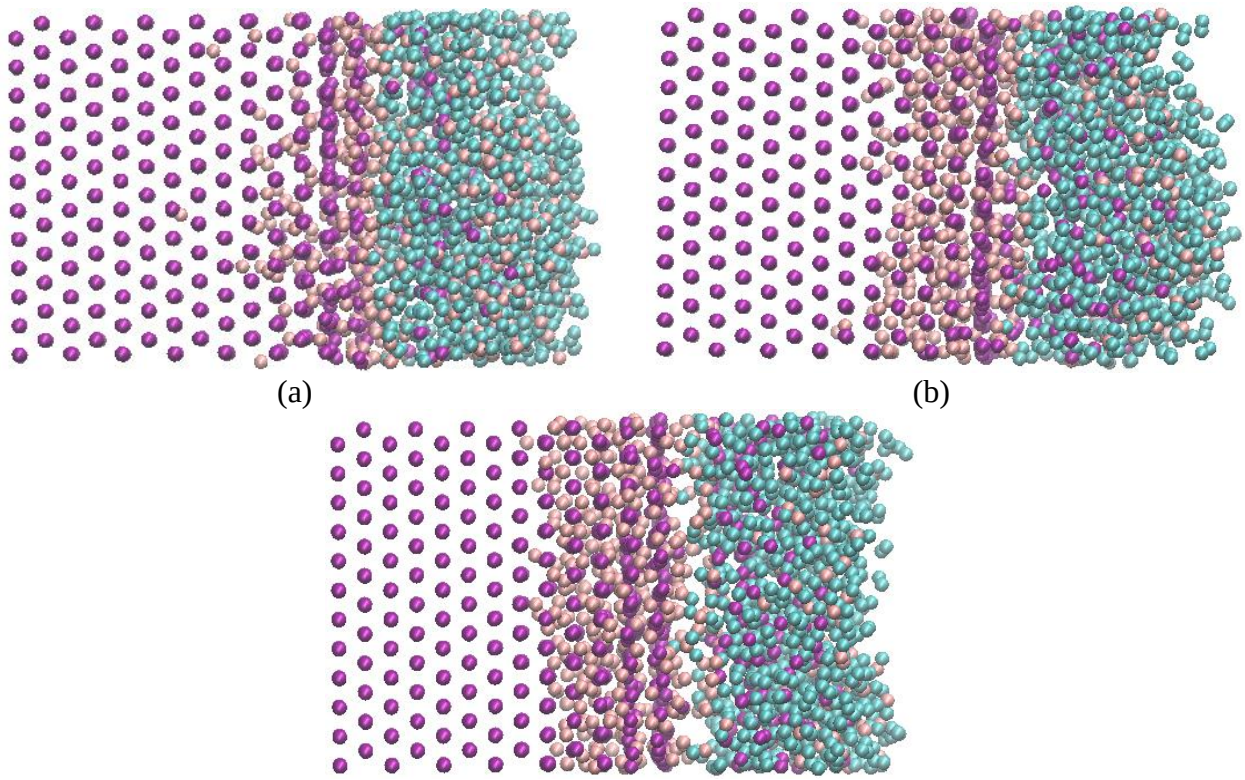

(a) (b)

(c)

Figure 2-2: Snapshots of ReaxFF-MD simulations of Fe(110)-water system under different external electric fields at 150 ps: (a) 20 MeV/cm, (b) 25 MeV/cm, and (c) 30 MeV/cm. The purple, blue and brown spheres represent iron, hydrogen and oxygen atoms, respectively.

The iron corrosion process during the simulation for external electric field intensity of 25 MeV/cm was analyzed. Several stages were observed[1]:

Step 1: The corrosion process starts with the adsorption and dissociation of water molecules on the iron surface with oxygen atoms positioned toward the iron atoms. Initially, water molecules dissociate into $H^{+}_{(aq)}$ and $OH^{-}_{(ads)}$ near the surface:

$$H_2O_{(l)} \rightarrow OH^{-}_{(ads)} + H^{+}_{(aq)} \qquad (2\text{-}2)$$

The $OH^{-}$ group adsorbs on to the iron surface, forming adsorbed iron hydroxide, $Fe(OH)_{ads}$, as shown in Figure A-1(a) of the Appendix A:

[1] These stages are illustrated in Figure A-1 of the Appendix A (supplementary materials section).

$$Fe_{(s)} + OH^-_{(ads)} \rightarrow FeOH_{(ads)} + e^- \quad (2\text{-}3)$$

and $H^+$ group bonds with a water molecule in the aqueous phase to form $H_3O^+$ (Figure A-1(b)). The average charge of the surface iron atoms is +0.32e, while those of $H_3O^+$ and $OH^-$ are +0.187 and -0.243e, respectively.

Step 2: At this step, some of adsorbed Fe(OH) start to dissolve into the solution and form aqueous iron hydroxide, $Fe(OH)_{aq}$, (Figure A-1(c)) :

$$FeOH_{(ads)} + OH^-_{(ads)} + Fe_{(s)} \rightarrow FeOH^+_{(aq)} + FeOH_{(ads)} + 2e^- \quad (2\text{-}4)$$

The average charge of the surface iron atoms is +0.39 e.

Step 3: The third step of iron oxidation starts at 2.8 ps and is characterized by the dissociation of iron atoms in the water phase. Aqueous iron hydroxide bonds with $H^+$ and produces water and iron ion (Equation 2-5 and Figure A-1(d)); the dissolved iron then forms iron oxide and hydroxide compounds in the water phase:

$$FeOH^+_{(aq)} + H^+_{(aq)} \rightarrow Fe^{2+}_{(aq)} + H_2O_{(l)} \quad (2\text{-}5)$$

The average charge of the iron ions in the solution is +0.57e. After this step, the average charge of the surface iron atoms increases relative to the last step to reach +0.48e.

Step 4: At 3.2 ps some of the adsorbed $OH^-$ also dissociate into oxygen and hydrogen, forming additional $H_3O^+$ and iron oxides. The average charges of the oxygen atoms and the surface iron atoms are -0.88e and +0.52e, respectively.

This process, iron dissolution into the water phase and oxygen penetration in the iron phase, repeats throughout the simulation resulting in active corrosion. The corrosion process starts with the adsorption of the water molecules on the iron surface with oxygen atoms positioned toward the iron atoms. Initially, water molecules break into $OH^-$, $H_3O^+$ near the surface. Some of the $OH^-$ also further dissociates into oxygen and hydrogen, and part of the hydrogen binds with water to form additional $H_3O^+$, while the oxygen forms iron oxides. Within the first 5-10 ps, the average charge of surface iron atoms increases, followed by a surge of dissolution of iron atoms into the water. After the initial surge, the iron dissolution into water stabilizes and continues at a gradually

decreasing rate, considerably slower than the initial dissolution rates. The dissolved iron forms iron oxide and hydroxide compounds in the water phase. This is accompanied by the thickening of the oxide layer, which increases with time. As an example, Figure 2-3 shows the dissociation process of water over time at 25 MeV/cm applied external electric field as a function of time. In this figure, the evolution of the number of hydrogen and oxygen atoms represent the formation of the iron oxide and iron hydroxide compounds in water, as well as the formation of the iron oxides within iron slab. The cut-off bond length between O and H atoms in $H_2O$, $OH^-$, and $H_3O^+$ are 0.97 Å, 0.96 Å, and 1.0 Å [60].

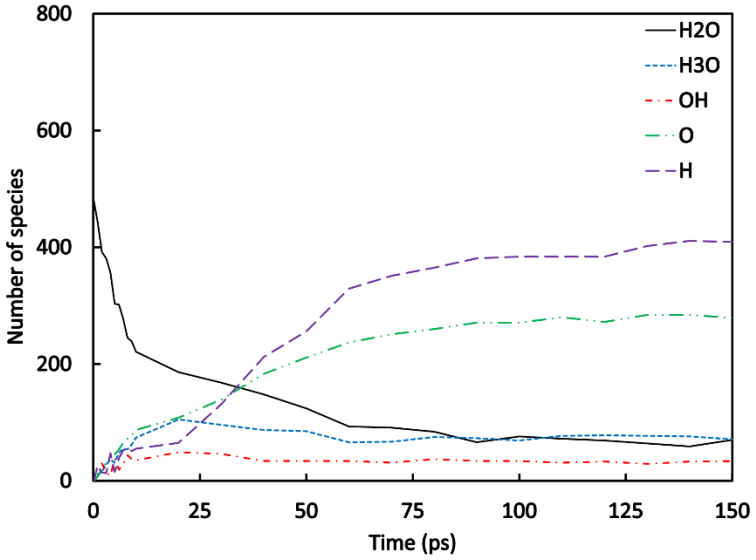


Figure 2-3: Dissociation of water as a function of time at 25 MeV/cm external electric field. H and O plots are for hydrogen and oxygen atoms that are part of iron oxide and iron hydroxide.

Figure 2-4 shows the evolution of number of oxygen atoms on the iron side (Figure 2-4a), oxygen atoms on the water side (Figure 2-4b), and iron atoms on the water side (Figure 2-4c) versus time for different external electric fields. These figures indicate active corrosion through iron dissociation and oxygen penetration into the iron phase at all external electric field intensities and increasing the intensity of the electric field increases the rate of the reactions.

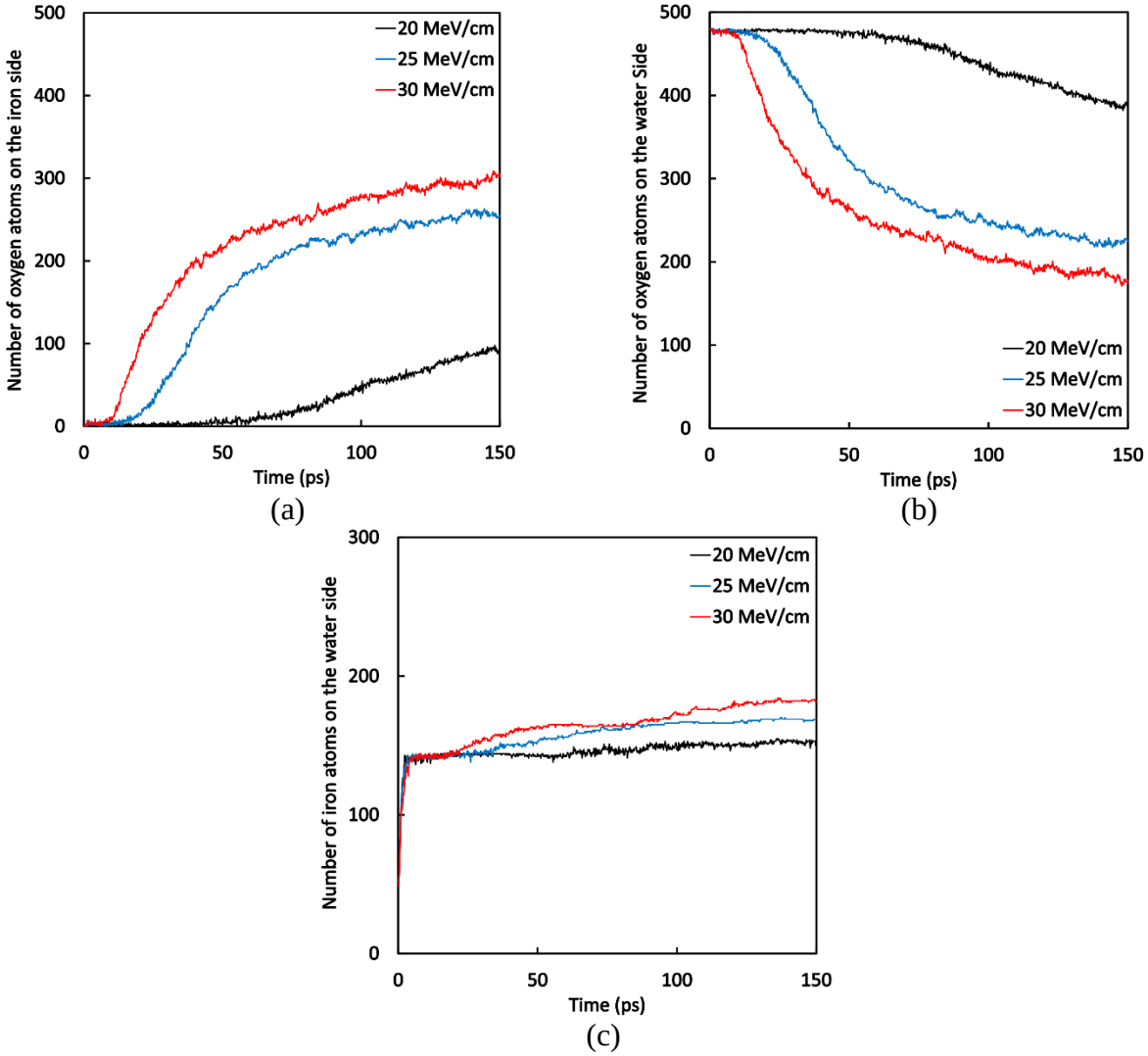


Figure 2-4: Comparison of total number of oxygen and iron atoms versus time for different external electric fields: (a) number of oxygen atoms on the iron side, (b) number of oxygen atoms on the water side, (c) number of iron atoms on the water side.

Figure 2-5 shows the evolution of oxygen atom density at the iron side (Figure 2-5a), and iron atom density on the water side (Figure 2-5b) versus z-distance from the iron-water interface at 150 ps. Figure 2-5a shows how the oxygen atom density at 150 ps changes in different intervals from the iron-water interface along the z-axis. These intervals correspond to interlayer spaces of the iron lattice, where oxygen atoms are located. We see that for all external electric fields the peak of the oxygen atom density occurs in the second interval (between second and thirds layers of iron atoms). In other words, oxygen atom density increases from the first interval to the second interval and decreases after the second interval. Note that surface oxygen is not included in the first interval.

Oxygen atom density in each interval increase by increasing applied external electric field. Figure 2-5b shows how the iron atom density in the bulk solution increases with external electric field, indicating more active corrosion.

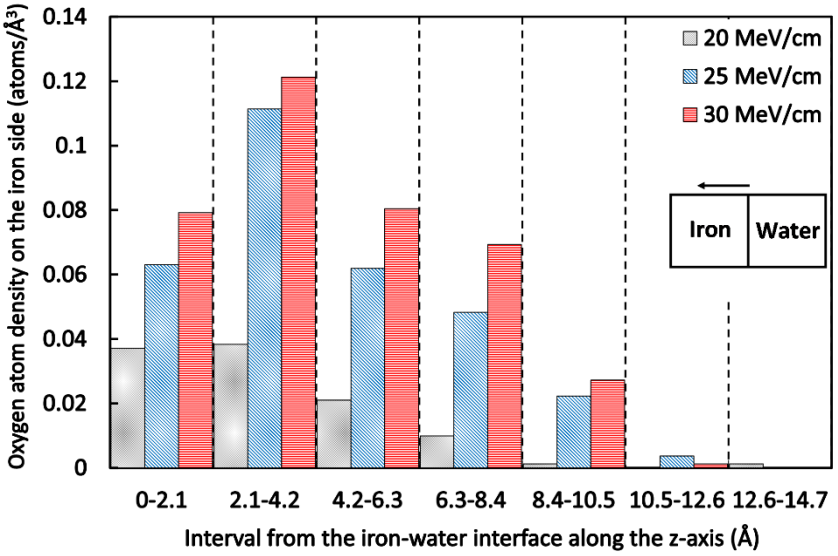


(a)

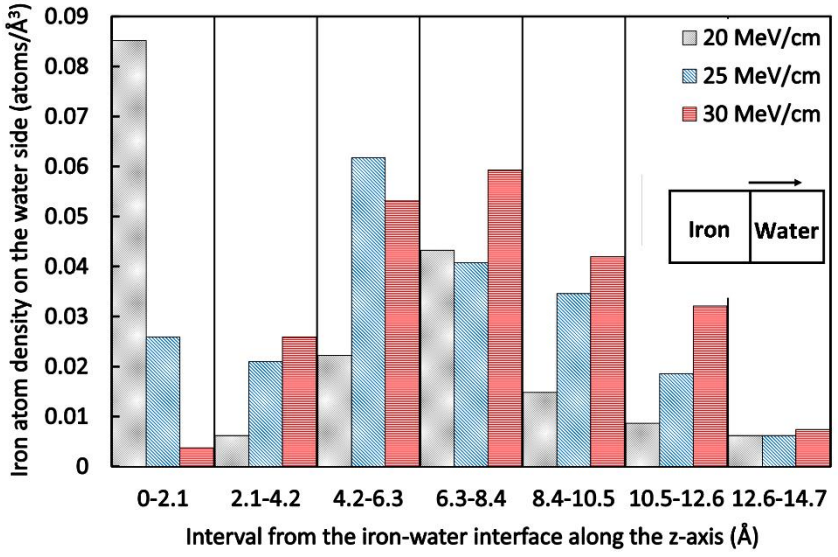


(b)

Figure 2-5: Comparison of oxygen iron atom densities in intervals from the iron-water interface along the z-axis for different external electric fields: (a) oxygen atom density on the iron side (dash lines present the locations of iron atom layers). (b) iron atom density on the water side (intervals were chosen to be consistent with plot a). The z-axis represents the position from the iron-water interface.

The charge distribution of iron, oxygen and hydrogen along the z direction of the simulation domains at 150 ps are presented in Figure 2-6.

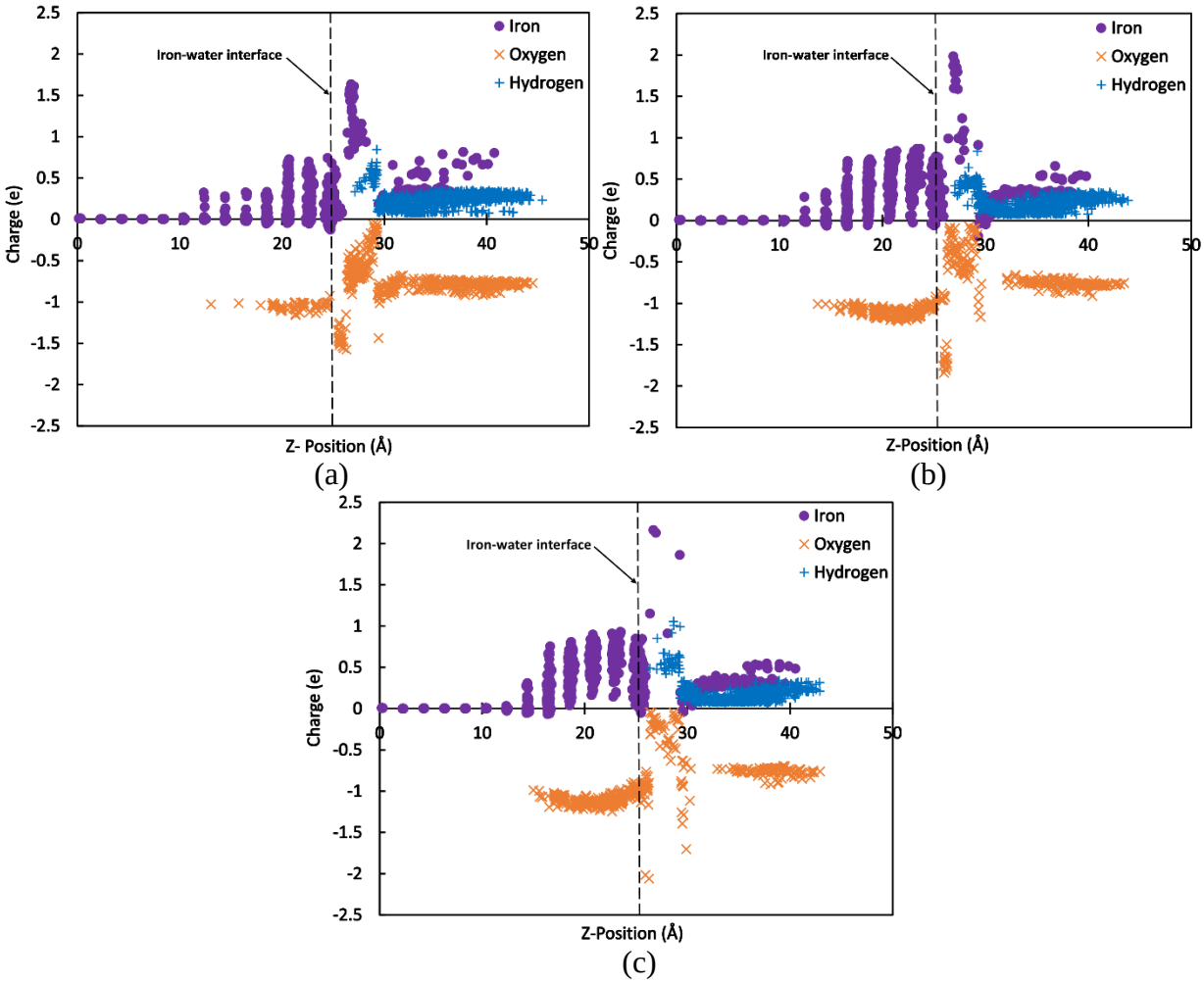


Figure 2-6: Charge distributions of iron-water system under different external electric fields at 150 ps: (a) 20 MeV/cm, (b) 25 MeV/cm, and (c) 30 MeV/cm.

The iron atoms on the iron side are positively charged and show three distinct zones. A thin layer (~1-3 Å) of iron atoms near the metal-water interface has the largest charge: +1.63e for 20 MeV/cm, +1.98e for 25 MeV/cm, and +2.16e for 30 MeV/cm. The charge of the iron atoms in the oxidized zone drops to about half of the charge of the iron atoms near the iron-water interface. The iron atoms within the zone that has not been penetrated by oxygen have a zero charge. The charges of oxygen and hydrogen away from the iron-water interface mainly represent charges of these atoms in water (i.e., the charge of oxygen is about -0.8e and the charge of hydrogen is about +0.4e).

Near the iron-water interface, the negative charge of oxygen atoms increase to around zero. The effect of the magnitude of the external electric field on the charge distribution was in general minor except for the iron and oxygen atom charges near the metal-water interface. There were no significant differences in the charge distribution patterns of different Fe surface orientations.

As shown by Jeon et al. [38], different iron oxide phases in MD simulations can be studied by comparing charge distributions or pair distribution functions (PDF) of the oxides in the simulations with those of reference iron oxides. We used both approaches to study the oxide phases in our simulations. As shown in Figure 2-6, the oxygen atoms on the iron have a charge ranging from 0 to about -1.0e, indicating oxide formation with mixed stoichiometry. It should be noted that iron in neutral (pH=7) water is not expected to produce a well-structured protective film environments [41]. The oxides that form under these conditions are the result of the active corrosion process; therefore, they are expected to be involve a mixture of various oxides that are not fully coordinated. This observation was also supported by the comparison of the PDF of the simulated oxide phases with PDF of reference oxides, as shown in Figure 2-7.

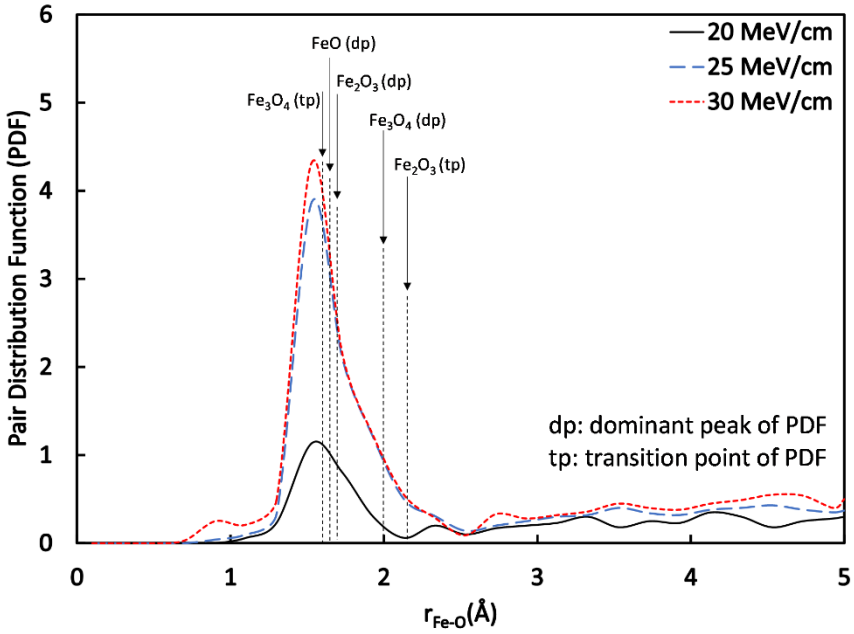


Figure 2-7: Pair distribution function of Fe-O for different external electric fields. The dominant peak and transition point of the PDF for reference oxides are included in the figure for comparison [38].

The dominant peak of the PDF of the oxides that form during simulations is observed at 1.5-1.55 Å, which is slightly smaller than the dominant peaks of wustite (FeO), hematite ($Fe_2O_3$), and magnetite ($Fe_3O_4$) that are at 1.65 Å, 1.7 Å, and 2.0 Å, respectively. The location of the dominant PDF peak is not affected by the intensity of the external electric field. The shape of the PDF for the simulated oxides indicate a transition at around 1.65 Å to 1.7 Å, which correspond to the dominant peaks of wustite and hematite. Another transition is noted at around 2.15 Å for the PDFs of the oxides formed under 25 MeV/cm and 30 MeV/cm external electric fields, which corresponds to the transition point of hematite. These results imply that the formed oxide compositions were not pure, but rather a mixture of different oxides.

In case of charge distribution of reference oxide structures at 300 K, wustite has the lowest cation and the highest anion charge distribution while the hematite has the highest cation and the lowest anion charge distribution. Magnetite charge state is between wustite and hematite [38]. For this study, the charge distribution of iron, oxygen and hydrogen along z direction of the simulation domains at 150 ps are presented in Figure 2-6. By comparing these iron oxidation results with the iron oxide equilibrium results from Jones et al. [38], oxide growth and iron surface oxidation can be discussed.

As shown in Figure 2-6, anion charges in all cases are less than -1 eV for all oxide layers beyond the first layer and anion charges are higher than cation charges. A comparison of the simulated charge distributions (as shown in Figure 2-6) and previously published oxide charge distributions [38] for pure iron oxides does not show a good match between the charge distributions of the formed oxide layers and reference oxide compositions implying that the formed oxide compositions were not pure hematite, magnetite, or wustite.

One practical conclusion of these simulations was that most of the water molecules were consumed at 150 ps (about 100 molecules remained). This observation has practical implications for future simulations of iron-water systems in alkaline systems, which are expected to show passivation behaviour that will require longer simulation times and larger number of initial water molecules.

### 2.3.2. Comparison of iron and nickel oxidation at 300 K

The corrosion process described above is considerably different from the study of the nickel-water interface described by Assowe et al. [34], which shows an expected passive film formation under neutral conditions [42, 43]. Although some steps of the interaction process show similarities to the iron corrosion (e.g. adsorption of water on the nickel surface and dissociation of water), further oxidation of $OH^-$ into oxygen and hydrogen was not prominent; hence, the pH of the zone near the nickel surface remained alkaline, which is required for a thermodynamically stable passive film to form. The Pourbaix diagram of nickel (at 25 $^oC$ and 1 atm) shows that a stable passive film, in the form of $Ni(OH)_2$ forms at pH greater than ~8 [61]. The simulations of the Ni-water interface were also different from iron-water simulations in that the amount of nickel dissolution into water was small, hence active corrosion was not observed, but instead a nickel oxide/hydroxide structure grew from the nickel-water interface. The comparison of the ReaxFF-MD simulations of iron and nickel demonstrate the differences clearly. Nickel atoms do not dissolve in water, and both O and H atoms are present inside the bulk nickel structure after 150 ps of simulations, implying the formation of a thin oxide/hydroxide structure. After about 50 ps, the oxide/hydroxide thickness remains constant at about 10 Å, which supports the expected passive behavior. The differences in oxidation behaviors of iron and nickel cases are also evident in charge distribution plots. Nickel forms a thin oxide/hydroxide layer near the metal-water interface that protects the metal from further oxidation. This thin oxide/hydroxide layer prevents oxygen atoms from penetrating further into the nickel bulk structure. The charge of nickel atoms is mostly zero except near the metal-water interface. On the other hand, iron atoms have positive charge in the oxidized zone.

### 2.3.3. Effect of temperature

In this part of the study, the influence of temperature on iron oxidation at 25MeV/cm external electric field was investigated. A comparison of the number of oxygen atoms on the iron and water side and the number of iron atoms on the water side versus time at 25 MeV/cm external electric field is shown in Figure 2-8. The pattern of corrosion, oxygen penetration into the iron, and iron dissolution into the water phase for all cases are similar. The number of oxygen atoms on the iron

side increases slightly with temperature, but the number of iron in the water side are almost the same.

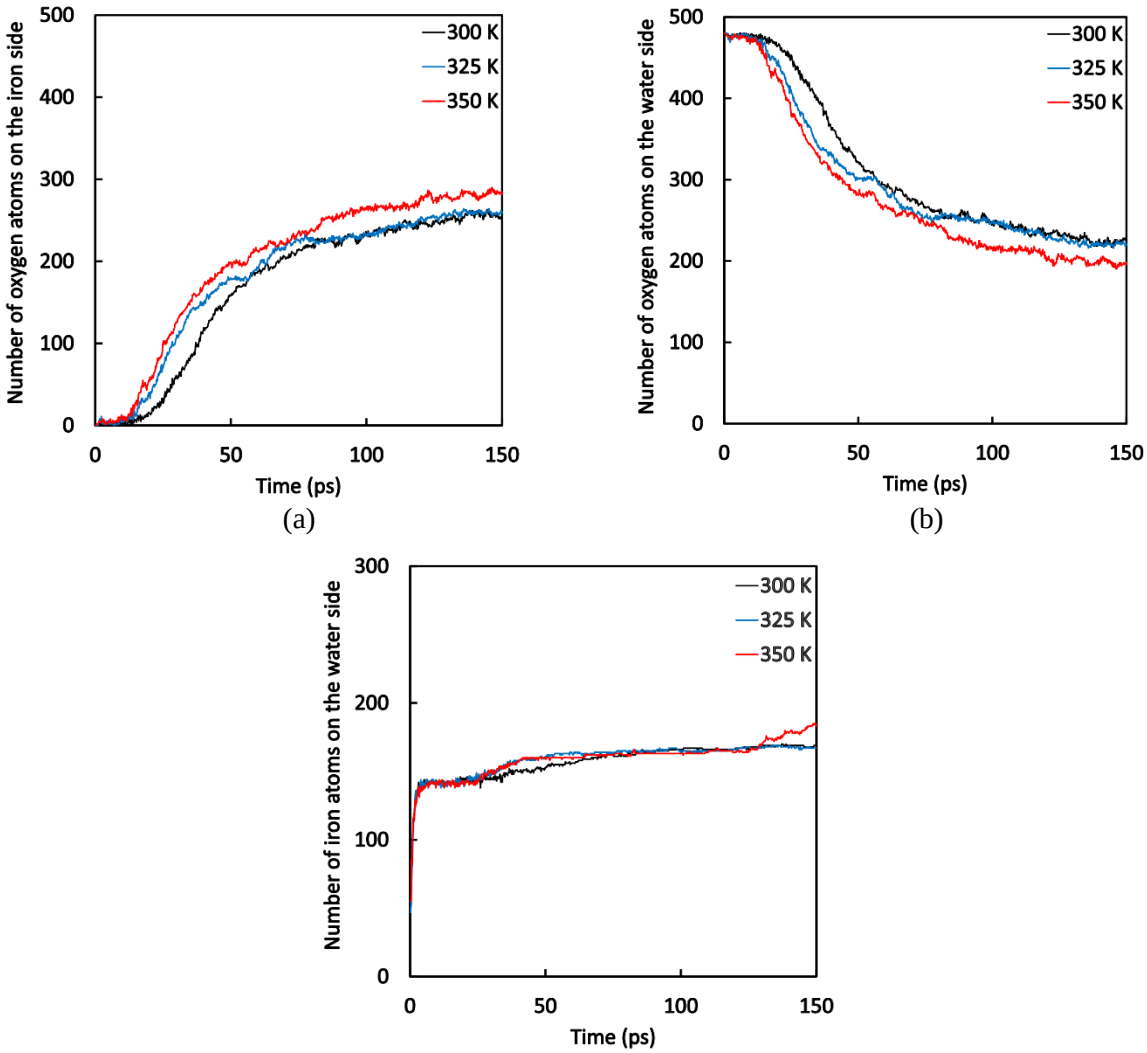


Figure 2-8: Comparison of total number of oxygen and iron atoms versus time at different temperatures: (a) number of oxygen atoms on the iron side, (b) number of oxygen atoms on the water side, (c) number of iron atoms on the water side. Applied external electric field is 25 MeV/cm.

In Figure 2-9, the oxygen atom density on the iron side and the iron atom density on the water side versus z-distance from the interface for external electric field of 25 MeV/cm at 150 ps has been plotted showing only slight increase in iron oxidation over this narrow temperature range of temperatures 300 K to 350 K.

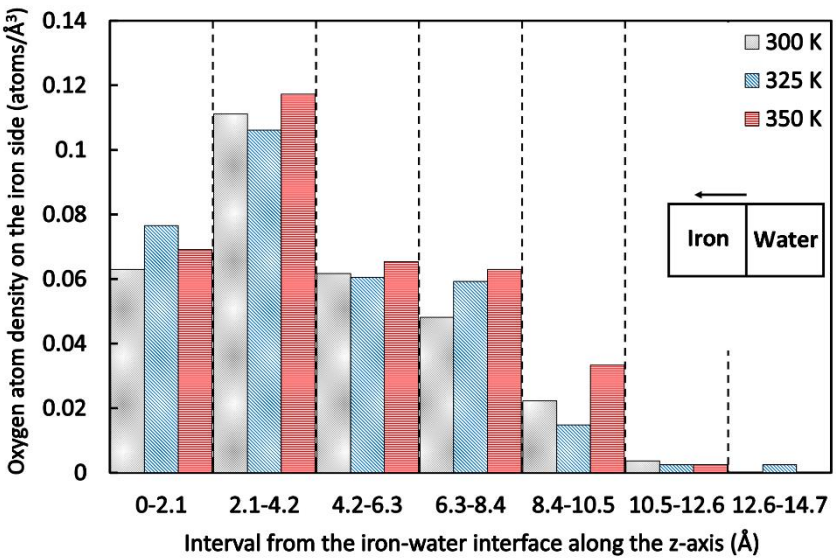


(a)

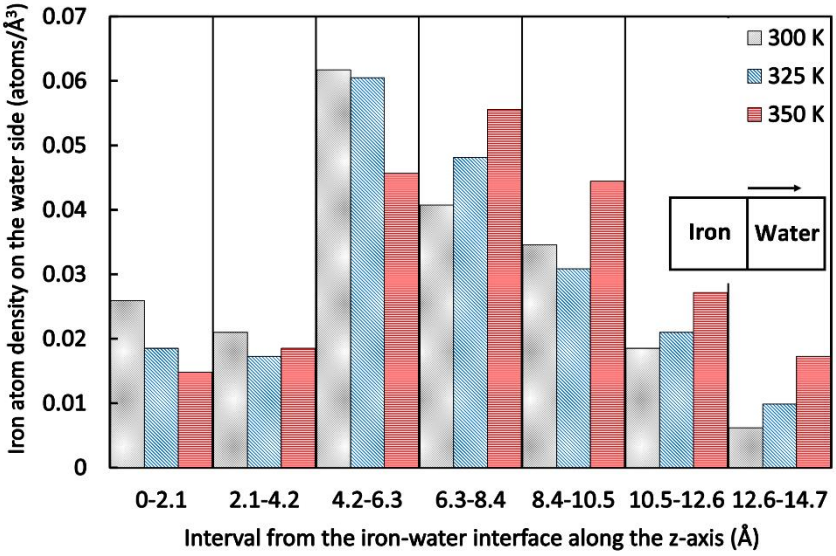


(b)

Figure 2-9: Comparison of oxygen and iron atom densities in intervals from the iron-water interface along the z-axis at different temperatures: (a) oxygen atom density on the iron side (dash lines present the locations of iron atom layers), (b) iron atom density on the water side (intervals were chosen to be consistent with plot a). Applied external electric field is 25 MeV/cm. The z-axis represents the position from the iron-water interface.

## 2.4. Conclusions

ReaxFF-MD was used to simulate iron corrosion in pure water (pH = 7). We applied an external electric field of 20 MeV/cm, 25 MeV/cm, and 30 MeV/cm between the iron and the solution.

The corrosion pattern involved different stages and started with the adsorption of water molecules on the iron surface and dissociation into $OH^-$ and $H^+$. The $OH^-$ group adsorbs on the iron surface and forms adsorbed iron hydroxide while the $H^+$ bonds with a water molecule to form $H_3O^+$. Some of adsorbed iron hydroxides dissolves into the solution and forms aqueous iron hydroxide in the next step. In the third step, aqueous iron hydroxides bonds with $H^+$ and produce water molecules and iron ions. The dissolved iron atoms form corrosion products of iron oxides/hydroxides. The last step is the penetration of oxygen into the iron slab to form iron oxide.

To study the compositions of the oxide film, charge distribution of iron and oxygen atoms and PDF of the Fe-O bond in the oxide film were used. For this purpose, both the charge result of the simulation and the PDF of the Fe-O bond were compared to the charge state and calculated PDF of Fe-O bond of reference oxide structures. It was concluded that the compositions of the oxide film were not pure phases of hematite, magnetite, or wustite.

The effect of temperature on the corrosion process was investigated in a narrow temperature range (300 K to 350 K) but typical of exposure conditions of most reinforced concrete structures. We found that the corrosion rates increased slightly with increasing temperature.

It is worth mentioning that in this study the system of water and other surface orientations of iron, Fe(100) and Fe(111), were also simulated. No significant differences in the corrosion patterns and charge distributions of the different Fe surface orientations was found so these results are presented as supplementary material (Appendix A).

The results of this study provided support for the feasibility of using ReaxFF-MD simulations to study corrosion and passivity of iron in highly alkaline environments in the future. However, one practical conclusion of the simulations in this study was that most of the water molecules were consumed at the end of the simulations. This has implications for future simulations of iron-water systems to study passivity, a process which will require longer simulation times. Larger number

of initial water molecules is necessary to avoid issues such as unrealistic acidification of the electrolyte and limitations of the total simulation time.

## 2.5. Acknowledgements

This study is fully funded by the National Science Foundation, DMMI, Grant No. 1435417. Part of this work used the Extreme Science and Engineering Discovery Environment (XSEDE) Comet at the through the San Diego Supercomputer Center (SDSC) allocation TG-ENG170002. XSEDE is supported by National Science Foundation grant number ACI-1053575.

## 2.6. References

[1] N.G. Thompson, M. Yunovich, D. Dunmire, Cost of corrosion and corrosion maintenance strategies, Corros Rev, 25 (2007) 5.
[2] C.M. Hansson, The impact of corrosion on society, Metall Mater Trans A, 42A (2011) 11.
[3] C. Andrade, C.L. Page, Pore solution chemistry and corrosion in hydrated cement systems containing chloride salts - a study of cation specific effects, Brit Corros J, 21 (1986) 5.
[4] U. Angst, B. Elsener, C.K. Larsen, O. Vennesland, Critical chloride content in reinforced concrete - A review, Cement Concrete Res, 39 (2009) 17.
[5] U.M. Angst, B. Elsener, C.K. Larsen, O. Vennesland, Chloride induced reinforcement corrosion: Electrochemical monitoring of initiation stage and chloride threshold values, Corros Sci, 53 (2011) 14.
[6] P. Ghods, O.B. Isgor, G.A. McRae, G.P. Gu, Electrochemical investigation of chloride-induced depassivation of black steel rebar under simulated service conditions, Corros Sci, 52 (2010) 11.
[7] S. Goni, C. Andrade, Synthetic concrete pore solution chemistry and rebar corrosion rate in the presence of chlorides, Cement Concrete Res, 20 (1990) 15.
[8] C.M. Hansson, A. Poursaee, A. Laurent, Macrocell and microcell corrosion of steel in ordinary Portland cement and high performance concretes, Cement Concrete Res, 36 (2006) 5.
[9] L. Li, A.A. Sagues, Chloride corrosion threshold of reinforcing steel in alkaline solutions - Open-circuit immersion tests, Corrosion, 57 (2001) 10.
[10] L. Li, A.A. Sagues, Chloride corrosion threshold of reinforcing steel in alkaline solutions - Cyclic polarization behavior, Corrosion, 58 (2002) 12.
[11] L.T. Mammoliti, L.C. Brown, C.M. Hansson, B.B. Hope, The influence of surface finish of reinforcing steel and pH of the test solution on the chloride threshold concentration for corrosion initiation in synthetic pore solutions, Cement Concrete Res, 26 (1996) 6.
[12] P. Ghods, O.B. Isgor, G. Mcrae, T. Miller, The effect of concrete pore solution composition on the quality of passive oxide films on black steel reinforcement, Cement Concrete Comp, 31 (2009) 10.

[13] R.G. Pillai, D. Trejo, Surface condition effects on critical chloride threshold of steel reinforcement, Aci Mater J, 102 (2005) 7.
[14] P. Ghods, O.B. Isgor, G.A. McRae, J. Li, G.P. Gu, Microscopic investigation of mill scale and its proposed effect on the variability of chloride-induced depassivation of carbon steel rebar, Corros Sci, 53 (2011) 9.
[15] P. Ghods, O.B. Isgor, G.J.C. Carpenter, J. Li, G.A. McRae, G.P. Gu, Nano-scale study of passive films and chloride-induced depassivation of carbon steel rebar in simulated concrete pore solutions using FIB/TEM, Cement Concrete Res, 47 (2013) 14.
[16] P. Ghods, O.B. Isgor, J. Brown, F. Bensebaa, D. Kingston, XPS depth profiling study on the passive oxide film of carbon steel in saturated calcium hydroxide solution and the effect of chloride on the film properties, Applied Surface Science, 257 (2011) 9.
[17] P. Ghods, O. Burkan Isgor, F. Bensebaa, D. Kingston, Angle-resolved XPS study of carbon steel passivity and chloride-induced depassivation in simulated concrete pore solution, Corros Sci, 58 (2012) 9.
[18] H.B. Gunay, P. Ghods, O.B. Isgor, G.J. Carpenter, X. Wu, Characterization of atomic structure of oxide films on carbon steel in simulated concrete pore solutions using EELS, Applied Surface Science, 274 (2013) 8.
[19] M. Sánchez-Moreno, H. Takenouti, J.J. García-Jareño, F. Vicente, C. Alonso, A theoretical approach of impedance spectroscopy during the passivation of steel in alkaline media, Electrochimica Acta, 54 (2009) 5.
[20] S. Joiret, M. Keddam, X.R. Novoa, M.C. Perez, C. Rangel, H. Takenouti, Use of EIS, ring-disk electrode, EQCM and Raman spectroscopy to study the film of oxides formed on iron in 1 M NaOH, Cement Concrete Comp, 24 (2002) 9.
[21] M. Sánchez, J. Gregori, C. Alonso, J.J. García-Jareño, H. Takenouti, F. Vicente, Electrochemical impedance spectroscopy for studying passive layers on steel rebars immersed in alkaline solutions simulating concrete pores, Electrochimica Acta, 52 (2007) 8.
[22] M. Sánchez, J. Gregori, M.C. Alonso, J.J. García-Jareño, F. Vicente, Anodic growth of passive layers on steel rebars in an alkaline medium simulating the concrete pores, Electrochimica Acta, 52 (2006) 7.
[23] D.D. Macdonald, S.R. Biaggio, H.K. Song, Steady-state passive films - interfacial kinetic effects and diagnostic-criteria, J Electrochem Soc, 139 (1992) 8.
[24] M.A. Heine, D.S. Keir, M.J. Pryor, Specific effects of chloride and sulfate ions on oxide covered aluminum, J Electrochem Soc, 112 (1965) 9.
[25] J. Richardson, G. Wood, A study of the pitting corrosion of Al byscanning electron microscopy, Corros Sci, 10 (1970) 11.
[26] K. Hashimoto, K. Asami, X-Ray photoelectron spectroscopic study of the passivity of ferritic 19cr stainless-steels in 1-Nhcl, Corros Sci, 19 (1979) 10.
[27] L. Lin, C. Chao, D. Macdonald, A point defect model for anodic passive films II. Chemical breakdown and pit initiation, J Electrochem Soc, 128 (1981) 5.
[28] A. C. T. van Duin, V. S. Bryantsev, M. S. Diallo, W. A. Goddard, O. Rahaman, D. J. Doren, D. Raymand, K. Hermansson, Development and validation of a ReaxFF Reactive Force Field for Cu cation/water interactions and copper metal/metal oxide/metal hydroxide condensed phases, The Journal of Physical Chemistry A, 114 (2010) 8.

[29] M. Aryanpour, A. C. T. van Duin, J.D. Kubicki, Development of a reactive force field for iron-oxyhydroxide systems, The Journal of Physical Chemistry A, 114 (2010) 10.
[30] D. Raymand, A. C. T. van Duin, D. Spångberg, W. A. Goddard, K. Hermansson, Water adsorption on stepped ZnO surfaces from MD simulation, Surface science, 604 (2010) 12.
[31] M. F. Russo, Jr. R. Li, M. Mench, A.C.T.v. Duin, Molecular dynamic simulation of aluminumewater reactions using the ReaxFF reactive force field, International Journal of Hydrogen Energy, 36 (2011) 8.
[32] B. Jeon, S. K. R. S. Sankaranarayanan, A.C.T.v. Duin, S. Ramanathan, Atomistic insights into aqueous corrosion of copper, The Journal of Chemical Physics, 134 (2011) 10.
[33] B. Jeon, S. K. R. S. Sankaranarayanan, A.C.T.v. Duin, S. Ramanathan, Reactive molecular dynamics study of chloride ion interaction with copper oxide surfaces in aqueous media, ACS Applied Materials & Interfaces 4(2012) 8.
[34] O. Assowe, O. Politano, V. Vignal, P. Arnoux, B. Diawara, O. Verners, A.C.T.v. Duin, Reactive molecular dynamics of the initial oxidation stages of Ni(111) in pure water: effect of an applied electric field, The Journal of Physical Chemistry A, 116 (2012) 10.
[35] O. Verners, A.C.T.v. Duin, Comparative molecular dynamics study of fcc-Ni nanoplate stress corrosion in water, Surface Science, 633 (2015) 8.
[36] C. Zou, Y. K. Shin, A. C.T. van Duin, H. Fangb, Z.K. Liu, Molecular dynamics simulations of the effects of vacancies on nickel self-diffusion, oxygen diffusion and oxidation initiation in nickel, using the ReaxFF reactive force field, Acta Materialia, 83 (2015) 11.
[37] T. P. Senftle, S. Hong, M. M. Islam, S. B. Kylasa, Y. Zheng, Y. K. Shin, C. Junkermeier, R. Engel-Herbert, M. J. Janik, H. M. Aktulga, T. Verstraelen, A. Grama, A.C.T.v. Duin, The ReaxFF reactive force-field: development, applications and future directions, npj Computational Materials, 2 (2016) 14.
[38] B. Jeon, Q.v. Overmeere, A.C.T.v. Duin, S. Ramanathan, Nanoscale oxidation and complex oxide growth on single crystal iron surfaces and external electric field effects, Physical Chemistry Chemical Physics, 15 (2013) 10.
[39] T. Pan, A.C.T.v. Duin, Passivation of steel surface: An atomistic modeling approach aided with X-ray analyses, Materials Letters, 65 (2011) 4.
[40] T. Pan, Quantum chemistry-based study of iron oxidation at the iron–water interface: An X-ray analysis aided study, Chemical Physics Letters, 511 (2011) 7.
[41] R.W. Revie, H.H. Uhlig, Corrosion and corrosion control 4th ed., Wiley-Interscience, New York, 2008.
[42] D.E. Davies, W. Barker, Influence of pH on corrosion and passivation of nickel, Corrosion, 20 (1964) 7.
[43] A.K.N. Reddy, B. Rao, Mechanism of formation of pre-passive films on nickel - a ahronoellipsometric study, Can J Chemistry, 47 (1969) 6.
[44] A. C. T. van Duin, S. Dasgupta, F. Lorant, W.A. Goddard, ReaxFF: A reactive force field for hydrocarbons, The Journal of Physical Chemistry A, 105 (2001) 14.
[45] S. Plimpton, Fast parallel algorithms for short–range molecular dynamics, Journal of Computational Physics, 117 (1995) 42.
[46] J. Towns, T. Cockerill, M. Dahan, I. Foster, K. Gaither, A. Grimshaw, V. Hazlewood, S. Lathrop, D. Lifka, G. D. Peterson, R. Roskies, J. R. Scott, N. Wilkins-Diehr, XSEDE: Accelerating scientific discovery, Computing in Science & Engineering, 16 (2014) 13.

[47] A. C. T. van Duin, J. M. A. Baas, B.v.d. Graaf, Delft molecular mechanics: A new approach to hydrocarbon force fields, Journal of the Chemical Society, Faraday Transactions, 90 (1994) 15.
[48] A. C. T. van Duin, A. Strachan, S. Stewman, Q. Zhang, X. Xu, W.A. Goddard, ReaxFF SiO Reactive force field for silicon and silicon oxide systems, The Journal of Physical Chemistry A, 107 (2003) 9.
[49] M. J. Buehler, A. C. T. van Duin, W.A. Goddard, Multiparadigm modeling of dynamical crack propagation in silicon using a reactive force field, Physical Review Letters, 96 (2006) 4.
[50] E. Spohr, K. Heinzinger, Molecular dynamics simulation of a water/metal interface, Chemical Physics Letters, 123 (1986) 4.
[51] S. Boyda, M. Gravelle, Nonreactive molecular dynamics force field for crystalline hexahydro-1,3,5-trinitro-1,3,5 triazine, The Journal of Chemical Physics, 124 (2006) 10.
[52] H. Heinz, R. A. Vaia, B. L. Farmer, R.R. Naik, Accurate simulation of surfaces and interfaces of face-centered cubic metals using 12-6 and 9-6 Lennard-Jones potentials, The Journal of Physical Chemistry C, 112 (2008) 10.
[53] H. Zhang, E. Iype, S. V. Nedea, C.C.M. Rindt, Molecular dynamics study on thermal dehydration process of epsomite (MgSO4·7H2O), Molecular Simulation, 40 (2013) 10.
[54] W. J. Mortier, S. K. Ghosh, S. Shankar, Electronegativity equalization method for the calculation of atomic charges in molecules, Journal of the American Chemical Society, 108 (1986) 6.
[55] A. K. Rappe, W.A. Goddard, Charge equilibration for molecular dynamics simulations, The Journal of Physical Chemistry, 95 (1991) 6.
[56] G. O. A. Janssens, B. G. Baekelandt, H. Toufar, W. J. Mortier, R.A. Schoonheydt, Comparison of cluster and infinite crystal calculations on zeolites with the electronegativity equalization method (EEM) The Journal of Physical Chemistry, 99 (1995) 8.
[57] J. Chen, T.J. Martínez, Charge conservation in electronegativity equalization and its implications for the electrostatic properties of fluctuating-charge models, The Journal of Chemical Physics, 131 (2009) 3.
[58] S. Nose, A molecular dynamics method for simulations in the canonical ensemble, Molecular Physics, 52 (1984) 14.
[59] W.G. Hoover, Canonical dynamics: Equilibrium phase-space distributions, Physical Review A, 31 (1985) 3.
[60] J.M. Hermida-Ramon, G. Karlstrom, Study of the hydronium ion in water. A combined quantum chemical and statistical mechanical treatment, J Mol Struc-Theochem, 712 (2004) 7.
[61] B. Beverskog, I. Puigdomenech, Revised Pourbaix diagrams for nickel at 25-300 degrees C, Corros Sci, 39 (1997) 12.

Manuscript 2

# Investigation of the applicability of classical electrical double layer models to study corrosion and passivity of iron in neutral and alkaline media

Hossein DorMohammadi, Qin Pang, Líney Árnadóttir, O. Burkan Isgor

To be submitted to: *Journal of The Electrochemical Society*

## 3. Manuscript 2

# Investigation of the applicability of classical electrical double layer models to study corrosion and passivity of iron in neutral and alkaline media

H. DorMohammadi[1], Q. Pang[2], L. Arnadottir[2], O. B. Isgor [1]

**Abstract:**

The applicability of the classical EDL models was investigated to study corrosion and passivity of iron in neutral and alkaline media using reactive force field molecular dynamics (ReaxFF-MD). The performance of the classical EDL models were studied in the ReaxFF-MD simulations of iron exposed to neutral (pH = 7) and highly alkaline (pH = 13.5) electrolytes under applied electric fields. Although the Helmholtz model was able to produce iron corrosion in the neutral electrolyte, it did not result in passive film formation in the highly alkaline solution system. The Gouy-Chapman model was not capable of simulating passivity for iron in the highly alkaline solution system or active corrosion in the neutral electrolyte. The Stern model was the only model that could simulate passivity and corrosion of iron for highly alkaline and neutral electrolytes, respectively. This study showed that ReaxFF-MD simulations of iron in neutral and alkaline electrolytes should use the Stern model for representing the EDL.

**Keywords:** Iron passivity, Molecular Dynamics (MD), Reactive Force Field (ReaxFF), Electrical Double Layer (EDL) models, Helmholtz model, Gouy-Chapman model, Stern model,

---

[1] Oregon State University, School of Civil and Construction Engineering, Corvallis, Oregon, USA
[2] Oregon State University, School of Chemical, Biological and Environmental Engineering, Corvallis, Oregon, USA

## 3.1. Introduction

The exposure of a metal surface to an electrolyte results in an immediate arrangement of charged species at the metal/electrolyte interface. This region is called the Electrical Double Layer (EDL) even though its structure loosely resembles two charged layers [1-6]. The EDL consists of a layer of electrons on the surface of the electrode, an inner (Helmholtz or Stern) layer of the electrolyte that is said to be "specifically adsorbed" on the metal surface, and a diffuse ionic layer in the electrolyte [6]. The properties of the EDL are important because they affect the electrochemical processes that take place at the metal/electrolyte interface. The first studies on the properties and mathematical formulation of the EDL date back as in late 1800s [1]. Since then, there have been numerous studies to model the EDL [7-11]. Among these, three models have been widely used in the past to describe the EDL in electrochemical systems: Helmholtz [1], Gouy-Chapman [2, 3] and Stern [4] models. These three models are typically referred to as the classical EDL models.

Recent years have also shown a significant increase in the use of atomistic modeling techniques to study electrochemical processes at the metal/electrolyte interfaces. In particular, Reactive Force Field Molecular Dynamics (ReaxFF-MD) [12-21] ReaxFF-MD has emerged as a simulation framework to investigate reactive processes in relatively large scales that can be correlated to physical electrochemical systems. The ReaxFF-MD has been used in several investigations to study passivity, corrosion, and oxidation processes in various metal/electrolyte systems [15-19]. The selected EDL model plays a critical role in ReaxFF-MD simulations to model realistically the interactions of the charged species in the electrolyte and the metal surface. The selection of the EDL model also depends on the processes that are simulated by ReaxFF-MD. For example, while Helmholtz model might be appropriate to study an active corrosion process that mainly involves the dissolution of the metals atoms into the electrolyte, it might not work for modeling the passivation process, which involves the participation of the ions and other species in the diffuse layer of the electrolyte in addition to the species on the metal surface. The selection of the EDL model is particularly important when the simulated electrochemical processes involve the application of external electric potentials. These challenges were captured by a number of researchers in the past [7-10, 22-28].

Helmholtz model [1] is one of the simplest EDL models, which assumes that a charged electrode immersed in an electrolyte attracts ions with opposite charges to its surface while repel the ions with the same charges (Figure 1-15a). This results in a compact (Helmholtz) layer near metal electrode surface. The main drawback of this model is that it neglects the interactions of other charged species (with each other and with the metals electrode surface) that exist beyond the Helmholtz layer [6, 29, 30]. The Gouy-Chapman model [2, 3], as is shown schematically in Figure 1-15b, does not involve a compact Helmholtz layer, but considers the fact that charged species in the diffuse layer are mobile under the combined effects of migration driven by electrical potential gradients and diffusion driven by concentration gradients [31]. These species can interact with each other and the species on the electrode surface. It has been shown that the Gouy-Chapman model has been successful for electrolytes with low ionic strength while it is known to overestimate ionic concentrations close to the charged surface [32-34]. The Stern model [35] simply combines the Helmholtz and the Gouy-Chapman models, and considers the EDL as a combination of the Helmholtz and diffuse layers (Figure 1-15c).

We investigate the applicability of the classical EDL models to study corrosion and passivity of iron in neutral and alkaline media using ReaxFF-MD. The corrosion and passivity of iron (and carbon steel) in media with different alkalinity as well as iron depassivation have been studied extensively using electrochemical methods [36-56] and nano-scale surface characterization studies [57-65]. The electrochemical techniques provide valuable information about the average electrochemical behavior of relatively large metal surfaces, typically in centimeter-square scale or larger. However, electrochemical processes on these surfaces typically occur in nanometer scale [57-59]. Although nano-scale surface characterizations provide valuable information about passive films that form on carbon steel and iron in alkaline electrolytes, and their chloride-induced depassivation, they cannot explain the dynamic processes that lead to their formation as they can only provide snapshot data. Atomistic modeling techniques such as ReaxFF-MD has the potential to fill this gap. Although several ReaxFF-MD investigations exist for the study of passivity of other metals, oxidation and corrosion processes in non-ferrous metals [15-19, 66], the investigation of iron corrosion is limited [67-74], and passivity has not been studied. The lack of knowledge on the applicability of the EDL models in simulating these processes is a hindrance for developing fundamental understanding about these processes using ReaxFF-MD.

In this paper, we compare the performance of the classical EDL models in the ReaxFF-MD simulations of iron exposed to neutral (pH = 7) and highly alkaline (pH = 13.5) electrolytes under applied electric fields.

## 3.2. Methods

### 3.2.1. Modeling EDL

The electrical potential distribution within an ionic system (e.g. electrolyte) can be obtained from the solution of the Poisson's equations with the appropriate boundary conditions. The Poisson's equation for such system can be written as [6]:

$$\nabla^2\varphi = -\frac{\rho}{\varepsilon\varepsilon_0} \tag{3-1}$$

where $\varphi$ is the electric potential distribution in the ionic domain, $\rho$ is the charge density per unit volume, $\varepsilon$ is the relative permittivity of the medium, and $\varepsilon_0$ is the permittivity of the vacuum.

The total charge density per unit volume, $\rho$, for all ionic species can be calculated as [6]:

$$\rho = \sum_i n_i z_i e \tag{3-2}$$

where $z_i$ is the charge of ion $i$, $e$ the unit charge, respectively, and $n_i$ is the distribution of the ions described by the Boltzmann distribution as [6]:

$$n_i = n_i^0 \exp\left(\frac{-z_i e\varphi}{kT}\right) \tag{3-3}$$

where $n_i^0$ is the concentration of the ion $i$ in the solution, $k$ is the Boltzman constant, and $T$ is the temperature.

Combining Equations 3-1 to 3-3, yields a specific version of the Poisson's equations, which is also called the Poisson-Boltzman equation as follows [6]:

$$\nabla^2\varphi = -\frac{e}{\varepsilon\varepsilon_0}\sum_i n_i^0 z_i \exp\left(\frac{-z_i e\varphi}{kT}\right) \tag{3-4}$$

For the Gouy-Chapman model, which involves only a diffuse layer starting from the metal surface, the distribution of the electrical potential is obtained by the solution of the Poisson-Boltzman equation with the following boundary conditions:

$\varphi = \varphi_M$ on the metal surface (3-5)

$\varphi = 0$ at the far end of the electrolyte domain (3-6)

where $\varphi_M$is the electrical potential on the metal surface.

For the Helmholtz model, the EDL layer spans from the metal surface and the Outer Helmholtz Plane (OHM) and the charges in the Helmholtz layer can be considered as point charges, hence the potential density within the Helmholtz layer would be equal to zero ($\rho = 0$). With these modifications, the Poisson-Boltzman equation can be simplified to the Laplace's equation [5]:

$\nabla^2\varphi = 0$ (3-7)

which needs to be solved with the following boundary conditions:

$\varphi = \varphi_M$ on the metal surface (3-8)

$\varphi = 0$ at the OHM (3-9)

In the Stern model, the EDL consists of a Helmholtz layer from the metal surface to the OHL (domain 1), and a diffuse layer from the OHL to the far end of the electrolyte domain (domain 2). The electrical potential distribution for such a system involves separate solutions of Equation 3-4 in domain 1 and Equation 3-5 in domain 2.

The solutions of the differential equations for electrical potential distribution for each EDL model were obtained using a commercial finite element analysis software. For all solutions, the electric field, $E_{el}$, which is a critical parameter for the ReaxFF-MD simulations, was obtained from the first derivative of the electrical potentials:

$E_{el} = \nabla\varphi$ (3-10)

### 3.2.2. ReaxFF-MD simulations

The MD simulations were carried out based on the Reactive Force Field (ReaxFF) interatomic potential developed by van Duin et al. [75] and were performed using the Large-scale Atomistic/Molecular Massively Parallel Simulator (LAMMPS) framework [76] on the Extreme Science and Engineering Discovery Environment (XSEDE) [77]. The detailed explanation of the ReaxFF is not provided here for brevity but can be found in [15, 66, 74, 78-85]. The ReaxFF parameters required for determining bond order, bond energy, valence angle energy, torsional angle energy, and van der Waals energy for iron and other interacting species in the simulations(e.g., Na, Cl, O, H) were obtained from the work of Aryanpour et al. [49], Rahaman et al. [86] and Psofogiannakis et al. [81], who developed and used parameters to model iron-oxyhydroxide systems, chloride-water and copper chloride-water systems, and hydration of zeolite, respectively. We validated these parameters by comparing ReaxFF-MD simulations of the surface formation energy and water adsorption energy on the Fe(110) surface with DFT calculations [73].

There are three well-studied surface orientations of iron: Fe(100), Fe(110) and Fe(111). The water adsorption and dissociation on Fe surfaces, Fe(100) and Fe(110), has been studied experimentally [87-89]. The comparison of the interaction of water and surface orientations has been studied using density functional theory [69, 90, 91]. In this paper, in order to simulate iron-highly alkaline solution, for the iron phase the Fe(110) surface orientation was chosen because it is a more close-packed surface than the others.

In order to investigate the applicability of EDL models to study corrosion and passivity of iron in neutral and alkaline media, Helmholtz, Gouy-Chapman and Stern models were applied to two systems: iron-neutral solution system and iron-highly alkaline solution system.

The simulations of iron in the highly alkaline electrolye involved a Fe(110) structure (24.61Å x 20.40Å x 22.87Å) containing 1080 iron atoms, as shown in Figure 3-1a, which is exposed to a 3.16 M NaOH solution (pH ~ 13.5), containing 21 Na ions, 21 OH ions, and 348 water molecules. The Na and OH ions were distributed in the electrolyte in groups of three in equally spaced seven

layers in the longitudinal z direction to maintain the pH relatively stable in all parts of the electrolyte.

In addition, Fe(110) in a neutral electrolyte was simulated. The dimensions of the iron substrate and solution domain of the system was similar to the iron-highly alkaline solution system, as shown in Figure 3-1b. The neutral solution contained 21 Na ions and 21 Cl ions to create an ionic electrolyte, which is needed for the Gouy-Chapman and the Stern models because the distributions in the diffuse layer requires the calculation of the total charge density per unit volume, ρ, using Equation 3-2.

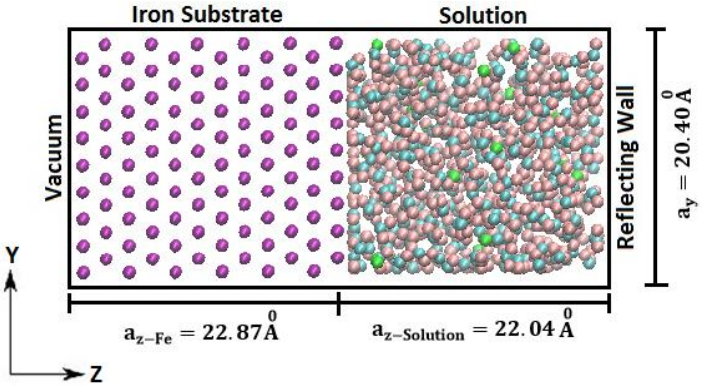


(a)

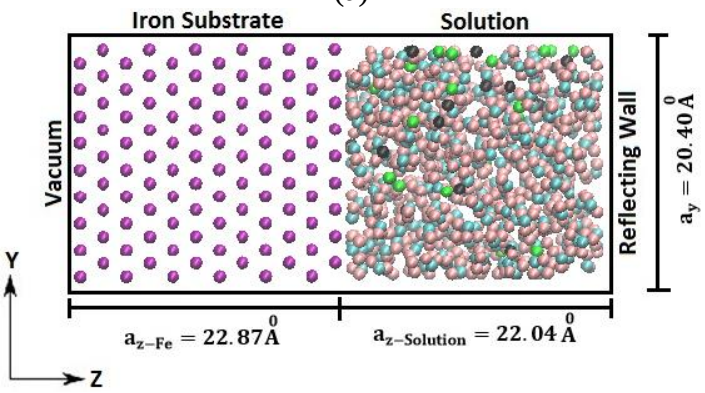


(b)

Figure 3-1: Initial configuration of ReaxFF-MD simulation: (a) iron-highly alkaline solution, and (b) iron-neutral solution. The purple, blue, brown, green and black spheres represent iron, oxygen, hydrogen, sodium and chlorine atoms, respectively.

All simulations were carried out at room temperature (300K) under one standard atmospheric pressure (1 atm). The simulations were run under different external electric fields (20 MeV/cm, 25 MeV/cm, 30 MeV/cm) for 150 ps. The velocity-Verlet time stepping scheme is used with an

integration time step of 0.1 fs in all cases. To neglect any translational movements the center of mass of the system is fixed during the simulation. Nose-Hoover thermostat [92, 93] is employed to maintain the prescribed system temperature for canonical (NVT) ensemble. Maxwell-Boltzman distribution were chosen to set the initial velocities for different temperatures and an energy-minimization was performed at the beginning of the simulation. Fixed boundary conditions were imposed along $z$ direction and periodic boundary conditions were applied along $x$ and $y$ directions. To confine the molecules in the solution phase and avoid the reaction of the solution with the surface below the sample, a reflecting wall was applied at the end of the specimen to confine the water molecules.

## 3.3. Results and discussion

### 3.3.1. Electrical potential distributions

Figure 3-2 shows the electric field distributions for the three EDL models, averaged over the x direction for the clarity of the presentation. As it can be noted from this figure, the Stern model in Figure 3-2c is a combination of the Helmholtz and the Gouy-Chapman models, Figures 3-2a and 3-2b. For all three EDL models, the electric field intensity at the iron surface is 30 MeV/cm. It should be mentioned here that the simulations of the lower electric field intensities of 20 MeV/cm and 25 MeV/cm at the iron surface were also performed. Since the results of the lower electric field intensities showed the same trend as the simulations for 30 MeV/cm, they are provided as supplementary material in Appendix B. Based on the experimental data and thermodynamic behavior of iron in solutions with different pH values, it was expected the results show the corrosion of iron in the system with neutral solution and iron passivation in the system with the highly alkaline solution.

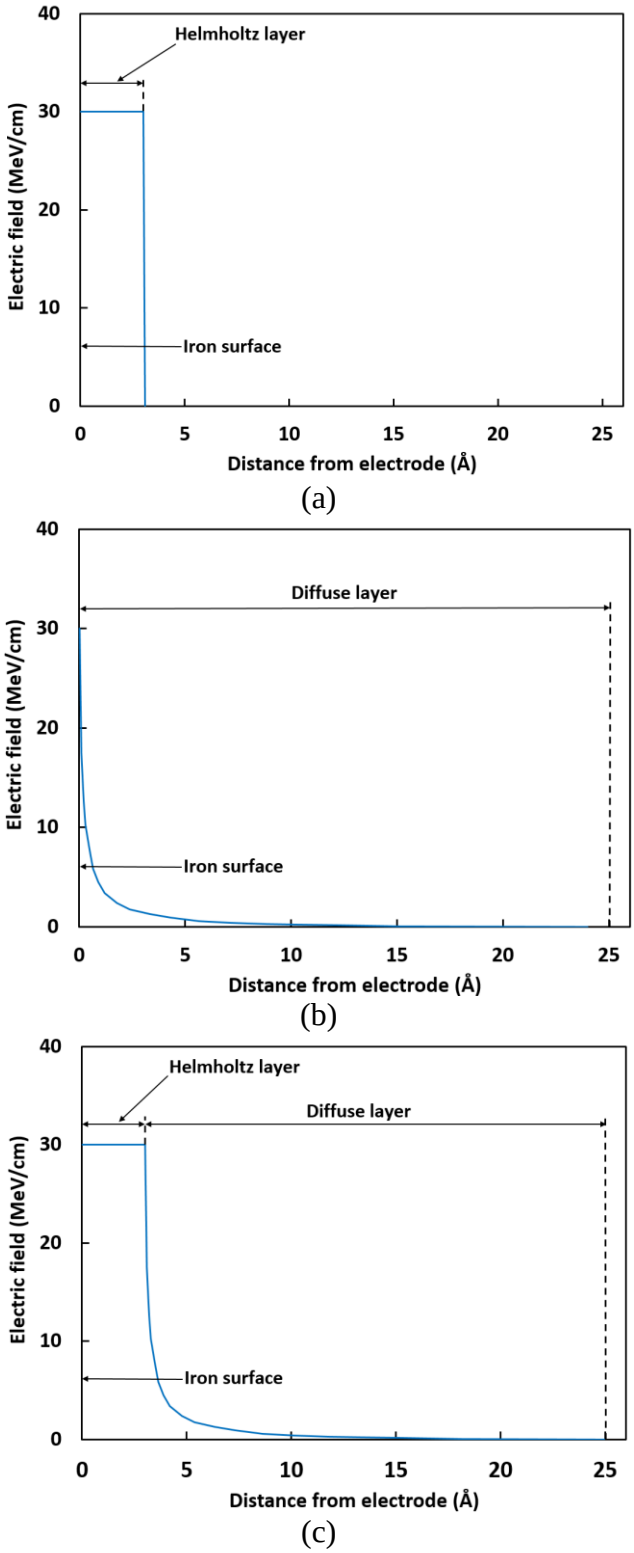


Figure 3-2: Electric field distribution for three EDL models: (a) Helmholtz model, (b) Gouy-Chapman model and (c) Stern model.

### 3.3.2. ReaxFF-MD modeling of iron corrosion in the neutral electrolyte

Figure 3-3 illustrates the ReaxFF-MD simulations of iron-neutral solution system with applied electric field distribution using three EDL models. The result of Helmholtz model (Figure 3-3a) showed that oxide film formation is accompanied by iron dissolution in the solution, indicating active corrosion. Using the Gouy-Chapman model, iron dissociation in the solution was observed, but just a few oxygen atoms diffused in the iron phase, and an iron oxide film did not form (Figure 3-3b). Like the Helmholtz model, the result of the applied electric field using Stern model in Figure 3-3c showed active corrosion.

Based on the thermodynamic behavior of iron in neutral electrolytes, active iron corrosion was expected for iron in the neutral solution [94]. The results of ReaxFF-MD simulations with applied electric filed on the iron-solution interface using three models in Figure 3-3 presented that simulations of the Helmholtz and the Stern models showed the iron corrosion for the iron-neutral solution system. On the other hand, the Gouy-Chapman model was not capable to predict the iron behavior in exposure to neutral solution.

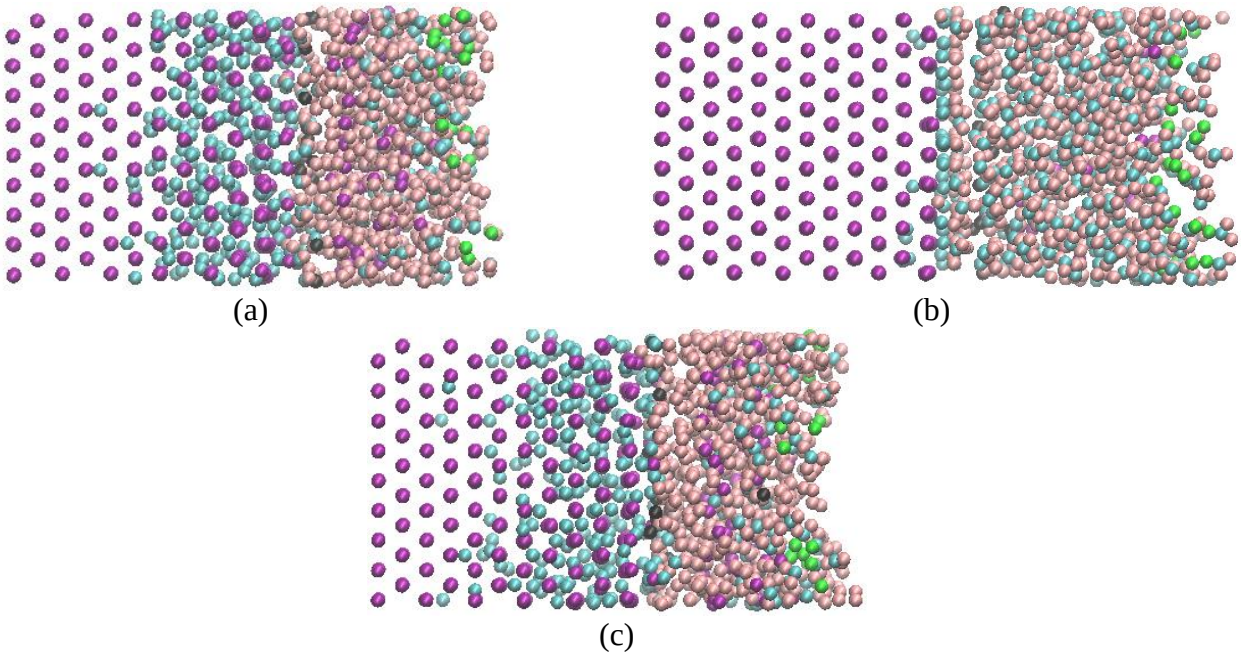


Figure 3-3: Snapshots of ReaxFF-MD simulations of iron-neutral solution system with applied electric field using EDL models at 150 ps: (a) Helmholtz model, (b) Gouy-Chapman model, (c) Stern model. The purple, blue, brown, green and black spheres represent iron, hydrogen, oxygen, sodium and chlorine atoms, respectively.

The evolution of the chemical compositions as a function of time are shown in Figure 3-4 for the iron-neutral solution system under applied electric field using the Helmholtz and the Stern models. As the oxide layer in the iron substrate did not form in the simulated system using the Gouy-Chapman model, additional results of this model are not presented here. The results of the simulated iron-neutral solution system with both the Helmholtz and the Stern models showed similar trends of species, and they were comparable to the results of the evolution of the chemical compositions of the iron-pure water system we investigated recently to study iron corrosion [73]. The results showed that the number of hydrogen atoms increased during the simulation while the number of $H_3O$ increased at first 10-50 ps and then stayed constant. The evolution of the number of hydrogen and oxygen atoms represent the formation of the iron oxides within the iron slab as well as the formation of the iron oxide and iron hydroxide compounds in the solution. The cut-off bond length between O and H atoms in $H_2O$, $OH^-$, and $H3O^+$ were 0.97 Å, 0.96 Å, and 1.0 Å, respectively [95].

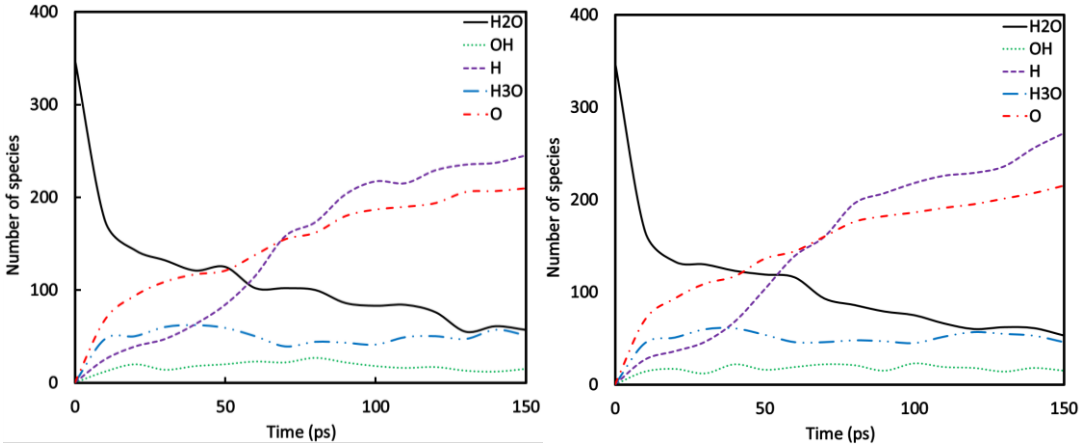


Figure 3-4: Dissociation of water as a function of time of iron-neutral solution systems with applied electric field using (a) Helmholtz model, and (b) Stern model at 150 ps. H and O plots are for hydrogen and oxygen atoms that are part of iron oxide and iron hydroxide.

The oxide films that were formed by applied electric field using the Helmholtz and the Stern models were studied using their charge distributions. In this approach, the simulated charge distributions of iron and oxygen in the iron domain were compared to those of reference pure iron

oxides from the work of Jeon et al. [74]. By simulating several iron oxide compositions like wustite, magnetite and hematite, charge states of anions and cations were shown. At 300K wustite has the lowest cation and the highest anion charge distribution while the hematite has the highest cation and the lowest anion charge distribution. Magnetite has the charge state between wustite and hematite. The charge distribution of hydrogen, oxygen and iron atoms of the simulated iron-neutral solution system using the Helmholtz and the Stern models at 150 ps are presented in Figure 3-5. The results showed that the charges of oxygen atoms of the oxide layer beyond the oxide-solution interface are less than -1 eV. A comparison between the simulated charge distributions with those ones of the reference iron oxide phases showed no match implying that the formed iron oxides were not pure hematite, magnetite, or wustite but rather a mixture of different oxides.

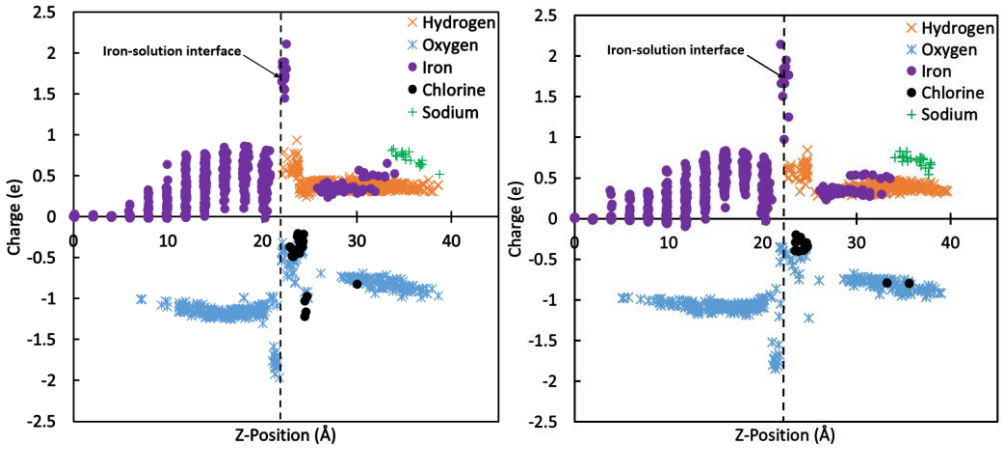


(a) (b)

Figure 3-5: Charge distributions of iron-neutral solution systems with applied electric field using EDL models at 150 ps: (a) Helmholtz model, (b) Stern model.

### 3.3.3. ReaxFF-MD modeling of iron passivation in the alkaline electrolyte

Figure 3-6 illustrates the ReaxFF-MD simulations of iron-highly alkaline solution system with applied electric field distribution using three EDL models. The results of Helmholtz model (Figure 3-6a) showed active corrosion; oxide film formation are accompanied by iron dissolution in the solution. Using the Gouy-Chapman model, an iron oxide film did not form as a few oxygen atoms diffused in the iron phase, and iron dissociation in the solution was observed (Figure 3-6b). Unlike

the Helmholtz and the Gouy-Chapman models, the result of ReaxFF-MD simulation of iron-highly alkaline solution system under applied electric fields using Stern model (Figure 3-6c) showed oxide film formation but not iron dissolution in the solution, which indicates the iron passivity. As it is expected that iron shows passivation on the exposure to the highly alkaline solution [94], the results of ReaxFF-MD results in Figure 3-6 implied that the Stern model is capable to predict the iron passivity in iron-highly alkaline solution system. The Helmholtz and the Gouy-Chapman models are not capable to predict the iron passivity.

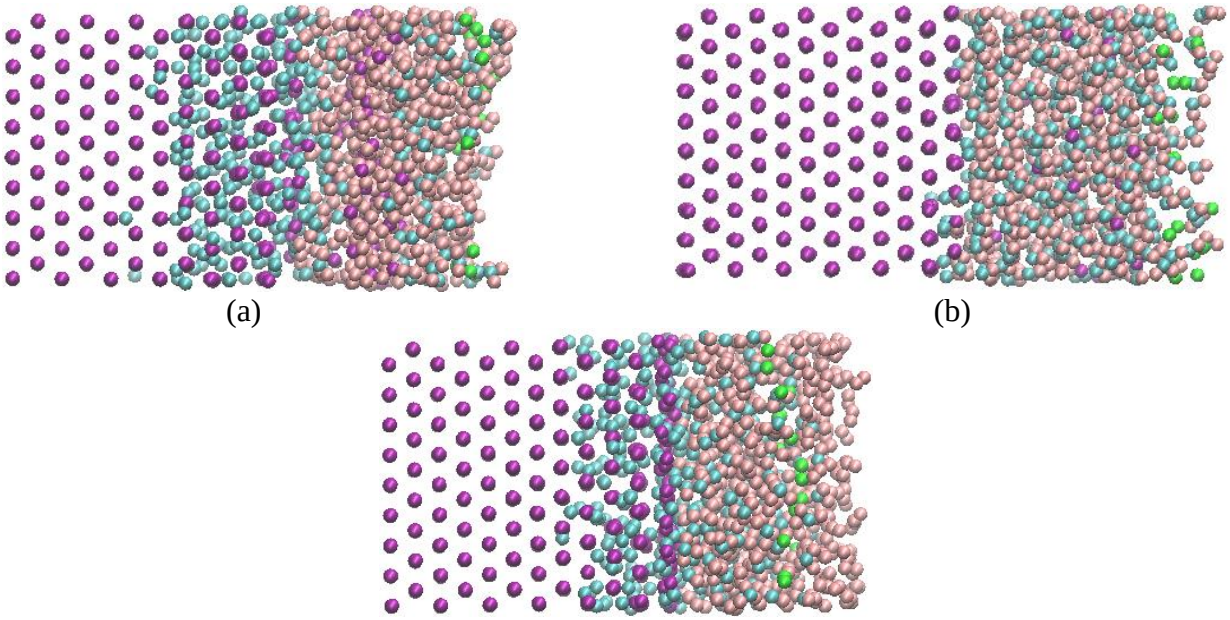


Figure 3-6: Snapshots of ReaxFF-MD simulations of iron-highly alkaline solution system with applied electric field using EDL models at 150 ps: (a) Helmholtz model, (b) Gouy-Chapman model, (c) Stern model. The purple, blue, brown, green and black spheres represent iron, hydrogen, oxygen, sodium and chlorine atoms, respectively.

The evolution of the chemical compositions as a function of time for the iron-highly alkaline system with the applied electric field using the Helmholtz and the Stern model are shown in Figure 3-7. The results of iron-highly alkaline solution using Helmholtz model (Figure 3-7a) showed similar trends of the number of species for the iron-neutral solution system. For the iron-highly alkaline solution system using Stern model (Figure 3-7b) though the number of $H_3O$ increased during the simulation while the number of hydrogen atoms increased at first 10-50 ps and then stayed constant. This implies that for the iron corrosion in the neutral electrolyte there is an

acidified zone close to the iron-solution interface; however, no acidification was observed in the case of iron passivation in the alkaline electrolyte.

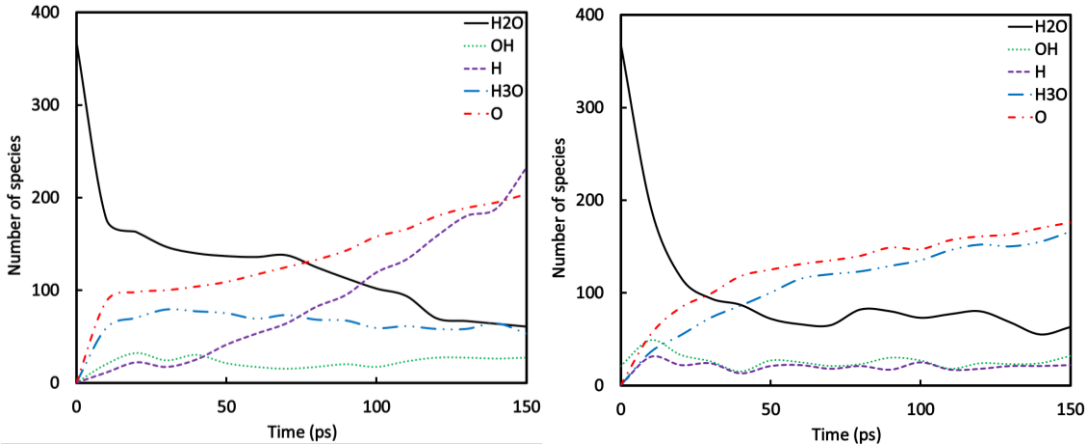


Figure 3-7: Dissociation of water as a function of time of iron-highly alkaline solution system with applied electric field using (a) Helmholtz model, and (b) Stern model at 150 ps. H and O plots are for hydrogen and oxygen atoms that are part of iron oxide and iron hydroxide.

The charge distribution of hydrogen, oxygen and iron atoms of the simulated iron-highly alkaline solution system using the Helmholtz and the Stern models at 150 ps are presented in Figure 3-8. The result of the Helmholtz model (Figure 3-8a) is similar to that one for the iron-neutral solution system, which indicates that Helmhotlz model cannot be used to simulate passive behavior.

The results of the iron-highly alkaline solution simulation using Stern model (Figure 3-8b) showed that iron atoms in the iron phase are positively charged in the oxide layer. The first layer contained the maximum charge iron atoms and it decreases layer by layer. The charge of oxygen atoms in the oxidized zone has the maximum value at the interface and it decreases to about -1e. Three main layers can be specified in the iron oxide film. The first layer close to iron-solution interface, contained the first two iron atoms layers, has the lowest anion charge and the highest cation charge states. The second layer including third and fourth layers of iron atoms and the oxygen atoms of this zone have the intermediate anion and cation charge states. The third oxide layer near the oxide-iron interface has the highest anion charge and lowest cation charge states. The presented results of anion and cation charge states in Figure 3-8 as well as the results of the Manuscript 3 implied that $Fe_2O_3$, $Fe_3O_4$ and FeO formed in the first, second and third layers, respectively, during the simulation, but further investigations are needed.

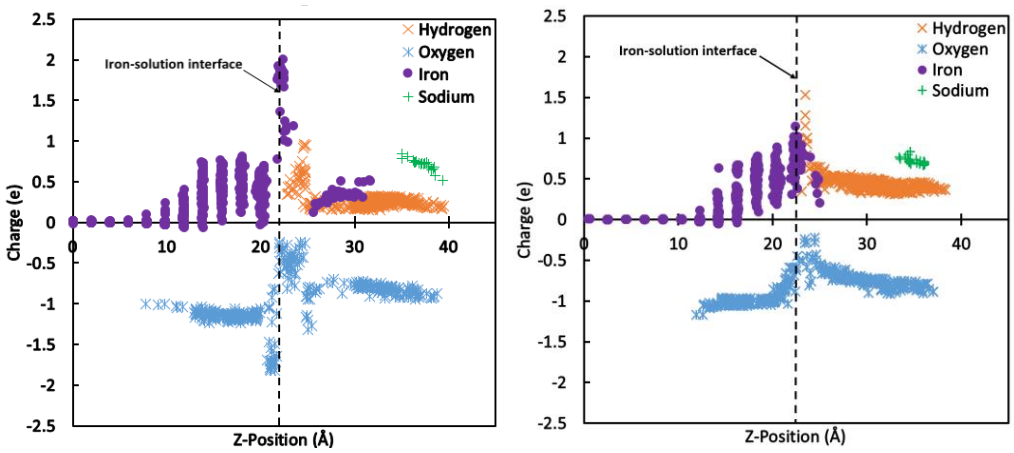


Figure 3-8: Charge distributions of iron-highly alkaline solution system with applied electric field using EDL models at 150 ps: (a) Helmholtz model, (b) Stern model.

### 3.4. Conclusions

In this paper, we investigated the applicability of the classical EDL models to study corrosion and passivity of iron in neutral and alkaline media using ReaxFF-MD. We compared the performance of the classical EDL models in the ReaxFF-MD simulations of iron exposed to neutral (pH = 7) and highly alkaline (pH = 13.5) electrolytes under applied electric fields. The following conclusions were obtained from the investigation:

- Although the Helmholtz model was able to produce iron corrosion in the neutral electrolyte, it did not result in passive film formation in the highly alkaline solution system.
- The Gouy-Chapman model was not capable of simulate passivity for iron in the highly alkaline solution system or active corrosion in the neutral electrolyte.
- The Stern model was the only model that could simulate passivity and corrosion of iron for highly alkaline and neutral electrolytes, respectively.

This study showed that ReaxFF-MD simulations of iron in neutral and alkaline electrolytes should use the Stern model for representing the EDL.

### 3.5. Acknowledgements

This study is fully funded by the National Science Foundation, DMMI, Grant No. 1435417. Part of this work used the Extreme Science and Engineering Discovery Environment (XSEDE) Comet at the through the San Diego Supercomputer Center (SDSC) allocation TG-ENG170002. XSEDE is supported by National Science Foundation grant number ACI-1053575.

### 3.6. References

[1] H. von Helmholtz, Studien €uber electrische grenzschichten, Annalen der Physik 243 (1879) 6.
[2] G. Gouy, Constitution of the electric charge at the surace of an electrolyte Journal of Theoretical and Applied Physics, 9 (1910) 12.
[3] D.L. Chapman, A contribution to the theory of electrocapillarity, Philosophical Magazine 25 (1913) 7.
[4] O. Stern, The theory of the electrolytic double layer, Z. Elektrochem. Angew. Phys. Chem., 30 (1924) 9.
[5] E. Gongadze, U. Van Rienen, A. Iglic, Generalized Stern models of the electric double layer considering the spatial variation of permittivity and finite size of ions in saturation regime, Cellular & Molecular Biology Letters, 16 (2011) 19.
[6] A. Bard, L. Faulkner, Electrochemical methods: fundamentals and applications, John Wiley & Sons: New York, (2001).
[7] E. Spohr, Molecular dynamics simulations of water and ion dynamics in the electrochemical double layer, Solid State Ionics, 150 (2002) 12.
[8] J.N. Glosli, M.R. Philpott, Molecular dynamics study of interfacial electric fields, Electrochemica Acta, 41 (1996) 14.
[9] S. Dewan, V. Carnevale, A. Bankura, E.-B. A., G. Fiorin, M.L. Klein, E. Borguet, Structure of water at charged interfaces: a molecular dynamics study, Langmuir, (2014) 10.
[10] D.A. Welch, B.L. Mehdi, H.J. Hatcheli, R. Faller, J.E. Evans, N.D. Browning, Using molecular dynamics to quantify the electrical double layer and examine the potential for its direct observation in the in-situ TEM, Advanced Structural and Chemical Imaging, 1 (2015) 11.
[11] P. Attard, Electrolytes and the electric double layer, Advanced Chemical Physics, 92 (1996) 159.
[12] A. C. T. van Duin, V. S. Bryantsev, M. S. Diallo, W. A. Goddard, O. Rahaman, D. J. Doren, D. Raymand, K. Hermansson, Development and validation of a ReaxFF Reactive Force Field for Cu cation/water interactions and copper metal/metal oxide/metal hydroxide condensed phases, J. Phys. Chem. A, 114 (2010) 8.
[13] M. Aryanpour, A. C. T. van Duin, J.D. Kubicki, Development of a reactive force field for iron-oxyhydroxide systems, J. Phys. Chem. A, 114 (2010) 10.
[14] D. Raymand, A. C. T. van Duin, D. Spångberg, W. A. Goddard, K. Hermansson, Water adsorption on stepped ZnO surfaces from MD simulation, Surf. Sci., (2010) 12.

[15] M. F. Russo, Jr. R. Li, M. Mench, A.C.T.v. Duin, Molecular dynamic simulation of aluminumewater reactions using the ReaxFF reactive force field, International Journal of Hydrogen Energy, 36 (2011) 8.
[16] B. Jeon, S. K. R. S. Sankaranarayanan, A.C.T.v. Duin, S. Ramanathan, Atomistic insights into aqueous corrosion of copper, J. Chem. Phys., 134 (2011) 10.
[17] B. Jeon, S. K. R. S. Sankaranarayanan, A.C.T.v. Duin, S. Ramanathan, Reactive molecular dynamics study of chloride ion interaction with copper oxide surfaces in aqueous media, ACS Applied Materials & Interfaces 4(2012) 8.
[18] O. Assowe, O. Politano, V. Vignal, P. Arnoux, B. Diawara, O. Verners, A.C.T.v. Duin, Reactive molecular dynamics of the initial oxidation stages of Ni(111) in pure water: effect of an applied electric field The Journal of Physical Chemistry A, 116 (2012).
[19] O. Verners, A.C.T.v. Duin, Comparative molecular dynamics study of fcc-Ni nanoplate stress corrosion in water, Surf. Sci., 633 (2015) 8.
[20] C. Zou, Y. K. Shin, A. C.T. van Duin, H. Fangb, Z.K. Liu, Molecular dynamics simulations of the effects of vacancies on nickel self-diffusion, oxygen diffusion and oxidation initiation in nickel, using the ReaxFF reactive force field, Acta Mater., 83 (2015) 11.
[21] T. P. Senftle, S. Hong, M. M. Islam, S. B. Kylasa, Y. Zheng, Y. K. Shin, C. Junkermeier, R. Engel-Herbert, M. J. Janik, H. M. Aktulga, T. Verstraelen, A. Grama, A.C.T.v. Duin, The ReaxFF reactive force-field: development, applications and future directions, npj Comput. Mater., 2 (2016) 14.
[22] H. Wang, L. Pilon, Accurate simulations of electric double layer capacitance of ultramicroelectrodes, The Journal of Physical Chemistry C, 115 (2011) 9.
[23] M.R. Philpott, J.N. Glosli, S.B. Zhu, Molecular dynamics simulation of adsorption in electric double layers, Surface Science, 335 (1995) 10.
[24] P. Zarzycki, S. Kerisit, K.M. Rosso, Molecular dynamics study of the electrical double layer at silver chloride-electrolyte interfaces, The Journal of Physical Chemistry C, 114 (2010) 17.
[25] M.R. Philpott, J.N. Glosli, Screening of charged electrodes in aqueous electrolytes, Journal of Electroanalytical Society, 142 (1995) 4.
[26] D.I. Dimitrov, N.D. Raev, Molecular dynamics simulations of the electrical double layer atthe 1 M KCl solution | Hg electrode interface Journal of Electroanalytical Chemistry 486 (2000) 8.
[27] S. Spohr, Molecular simulation of the electrochemical double layer, Electrochimica Acta 44 (1999) 9.
[28] C.D. Taylor, S.A. Wasileski, J.S. Filhol, M. Neurock, First principles reaction modeling of the electrochemical interface: Consideration and calculation of a tunable surface potential from atomic and electronic structure, Physical Review B, 73 (2006) 16.
[29] V. Bagotsky, Fundamentals of electrochemistry, John Wiley & Sons: New York, (2006).
[30] H.-J. Butt, M. Kappl, Surface and interfacial forces, Wiley-VCH: Weinheim, Germany, (2010).
[31] L. Pilon, H. Wang, A. d'Entremont, Recent advances in continuum modeling of interfacial and transport phenomena in electric double layer capacitors, J Electrochem Soc, 162 (2015) 21.
[32] R. Hunter, Foundations of colloid science, Oxford University Press: New York, (2001).
[33] J. Lyklema, Fundamentals of interface and colloid science, Academic Press: New York, 2 (2001).

[34] H. Ohshima, Theory of colloid and interfacial electric phenomena, Academic Press: New York, (2006).
[35] O. Stern, The theory of the electrolytic double layer, Zeitschrift für Elektrochemie und Angewandte Physikalische Chemie, 30 (1924) 9.
[36] C. Andrade, C.L. Page, Pore solution chemistry and corrosion in hydrated cement systems containing chloride salts - a study of cation specific effects, Brit Corros J, 21 (1986) 5.
[37] U. Angst, B. Elsener, C.K. Larsen, O. Vennesland, Critical chloride content in reinforced concrete - A review, Cement Concrete Res, 39 (2009) 17.
[38] U.M. Angst, B. Elsener, C.K. Larsen, O. Vennesland, Chloride induced reinforcement corrosion: Electrochemical monitoring of initiation stage and chloride threshold values, Corros Sci, 53 (2011) 14.
[39] P. Ghods, O.B. Isgor, G.A. McRae, G.P. Gu, Electrochemical investigation of chloride-induced depassivation of black steel rebar under simulated service conditions, Corros Sci, 52 (2010) 11.
[40] S. Goni, C. Andrade, Synthetic concrete pore solution chemistry and rebar corrosion rate in the presence of chlorides, Cement Concrete Res, 20 (1990) 15.
[41] C.M. Hansson, A. Poursaee, A. Laurent, Macrocell and microcell corrosion of steel in ordinary Portland cement and high performance concretes, Cement Concrete Res, 36 (2006) 5.
[42] L. Li, A.A. Sagues, Chloride corrosion threshold of reinforcing steel in alkaline solutions - Open-circuit immersion tests, Corrosion, 57 (2001) 10.
[43] L. Li, A.A. Sagues, Chloride corrosion threshold of reinforcing steel in alkaline solutions - Cyclic polarization behavior, Corrosion, 58 (2002) 12.
[44] L.T. Mammoliti, L.C. Brown, C.M. Hansson, B.B. Hope, The influence of surface finish of reinforcing steel and pH of the test solution on the chloride threshold concentration for corrosion initiation in synthetic pore solutions, Cement Concrete Res, 26 (1996) 6.
[45] P. Ghods, O.B. Isgor, G. Mcrae, T. Miller, The effect of concrete pore solution composition on the quality of passive oxide films on black steel reinforcement, Cement Concrete Comp, 31 (2009) 10.
[46] R.G. Pillai, D. Trejo, Surface condition effects on critical chloride threshold of steel reinforcement, Aci Mater J, 102 (2005) 7.
[47] P. Ghods, O.B. Isgor, G.A. McRae, J. Li, G.P. Gu, Microscopic investigation of mill scale and its proposed effect on the variability of chloride-induced depassivation of carbon steel rebar, Corros Sci, 53 (2011) 9.
[48] D.S. Leek, The passivity of steel in concrete, Quarterly Journal of Engineering Geology, 24 (1991) 12.
[49] M. Cohen, The formation and properties of passive films on iron, Can J Chemistry, 37 (1959) 6.
[50] O.A. Albani, L.M. Gassa, J.O. Zerbino, J.R. Vilche, A.J. Arvia, Comparative study of the passivity and the breakdown of passivity of polycrystalline iron in different alkaline solutions, Electrochemica Acta, 35 (1990) 8.
[51] Z. Ai, W. Sun, J. Jiang, D. Song, H. Ma, J. XZhang, D. Wang, Passivation characteristics of alloy corrosion-resistant steel Cr10Mo1 in simulating concrete pore solutions: combination effects of pH and chloride, Materials, 9 (2016) 17.

[52] J. Jiang, D. Wang, H. Chu, H. Ma, Y. Liu, Y. Gao, J. Shi, W. Sun, The passive film growth mechanism of new corrosion-resistant steel rebar in simulated concrete pore solution: nanometer structure and electrochemical study, Materials, 10 (2017) 14.
[53] M.A. Heine, D.S. Keir, M.J. Pryor, Specific effects of chloride and sulfate ions on oxide covered aluminum, J Electrochem Soc, 112 (1965) 9.
[54] J. Richardson, G. Wood, A study of the pitting corrosion of Al byscanning electron microscopy, Corros Sci, 10 (1970) 11.
[55] K. Hashimoto, K. Asami, X-Ray photoelectron spectroscopic study of the passivity of ferritic 19cr stainless-steels in 1-Nhcl, Corros Sci, 19 (1979) 10.
[56] L. Lin, C. Chao, D. Macdonald, A point defect model for anodic passive films II. Chemical breakdown and pit initiation, J Electrochem Soc, 128 (1981) 5.
[57] P. Ghods, O.B. Isgor, G.J.C. Carpenter, J. Li, G.A. McRae, G.P. Gu, Nano-scale study of passive films and chloride-induced depassivation of carbon steel rebar in simulated concrete pore solutions using FIB/TEM, Cement Concrete Res, 47 (2013) 14.
[58] P. Ghods, O.B. Isgor, J. Brown, F. Bensebaa, D. Kingston, XPS depth profiling study on the passive oxide film of carbon steel in saturated calcium hydroxide solution and the effect of chloride on the film properties, Applied Surface Science, 257 (2011) 9.
[59] P. Ghods, O. Burkan Isgor, F. Bensebaa, D. Kingston, Angle-resolved XPS study of carbon steel passivity and chloride-induced depassivation in simulated concrete pore solution, Corros Sci, 58 (2012) 9.
[60] H.B. Gunay, P. Ghods, O.B. Isgor, G.J. Carpenter, X. Wu, Characterization of atomic structure of oxide films on carbon steel in simulated concrete pore solutions using EELS, Applied Surface Science, 274 (2013) 8.
[61] M. Sánchez-Moreno, H. Takenouti, J.J. García-Jareño, F. Vicente, C. Alonso, A theoretical approach of impedance spectroscopy during the passivation of steel in alkaline media, Electrochimica Acta, 54 (2009) 5.
[62] S. Joiret, M. Keddam, X.R. Novoa, M.C. Perez, C. Rangel, H. Takenouti, Use of EIS, ring-disk electrode, EQCM and Raman spectroscopy to study the film of oxides formed on iron in 1 M NaOH, Cement Concrete Comp, 24 (2002) 9.
[63] M. Sánchez, J. Gregori, C. Alonso, J.J. García-Jareño, H. Takenouti, F. Vicente, Electrochemical impedance spectroscopy for studying passive layers on steel rebars immersed in alkaline solutions simulating concrete pores, Electrochimica Acta, 52 (2007) 8.
[64] M. Sánchez, J. Gregori, M.C. Alonso, J.J. García-Jareño, F. Vicente, Anodic growth of passive layers on steel rebars in an alkaline medium simulating the concrete pores, Electrochimica Acta, 52 (2006) 7.
[65] D.D. Macdonald, S.R. Biaggio, H.K. Song, Steady-state passive films - interfacial kinetic effects and diagnostic-criteria, J Electrochem Soc, 139 (1992) 8.
[66] O. Assowe, O. Politano, V. Vignal, P. Arnoux, B. Diawara, O. Verners, A.C.T.v. Duin, Reactive molecular dynamics of the initial oxidation stages of Ni(111) in pure water: effect of an applied electric field, The Journal of Physical Chemistry A, 116 (2012) 10.
[67] T. Pan, A.C.T.v. Duin, Passivation of steel surface: An atomistic modeling approach aided with X-ray analyses, Mater. Lett., 65 (2011) 4.
[68] T. Pan, Quantum chemistry-based study of iron oxidation at the iron–water interface: An X-ray analysis aided study, Chem. Phys. Lett., 511 (2011) 7.

[69] M. Eder, K. Terakura, J. Hafner, Initial stages of oxidation of (100) and (110) surfaces of iron caused by water, Phys. Rev. B. , 64 (2001) 7.
[70] H. Heinz, R. A. Vaia, B. L. Farmer, R.R. Naik, Accurate simulation of surfaces and interfaces of face-centered cubic metals using 12-6 and 9-6 Lennard-Jones potentials, The Journal of Physical Chemistry C, 112 (2008) 10.
[71] C. Soontrapa, Y. Chen, Molecular dynamics potentials in magnetite (Fe3O4) modeling, Comput. Mater. Sci. , 50 (2011) 11.
[72] Q. Pang, H. DorMohammadi, O.B. Isgor, L. Árnadóttir, Density functional theory study on the effect of OH and Cl adsorption on the surface structure of α-Fe2O3, Computational and Theoretical Chemistry, 1100 (2017) 11.
[73] H. DorMohammadi, Q. Pang, O.B. Isgor, L. Árnadóttir, Atomistic simulation of initial stages of iron corrosion in pure water using reactive molecular dynamics, Computational Materials Science, 145 (2018) 8.
[74] B. Jeon, Q. V. Overmeere, A.C.T.v. Duin, S. Ramanathan, Nanoscale oxidation and complex oxide growth on single crystal iron surfaces and external electric field effects, Physical Chemistry Chemical Physics, 15 (2013) 10.
[75] A. C. T. van Duin, S. Dasgupta, F. Lorant, W.A. Goddard, ReaxFF: A reactive force field for hydrocarbons, The Journal of Physical Chemistry A, 105 (2001) 14.
[76] S. Plimpton, Fast parallel algorithms for short–range molecular dynamics, Journal of Computational Physics, 117 (1995) 42.
[77] J. Towns, T. Cockerill, M. Dahan, I. Foster, K. Gaither, A. Grimshaw, V. Hazlewood, S. Lathrop, D. Lifka, G. D. Peterson, R. Roskies, J. R. Scott, N. Wilkins-Diehr, XSEDE: Accelerating scientific discovery, Computing in Science & Engineering, 16 (2014) 13.
[78] A. C. T. van Duin, A. Strachan, S. Stewman, Q. Zhang, X. Xu, W.A. Goddard, $ReaxFF_{SiO}$ reactive force field for silicon and silicon oxide systems, The Journal of Physical Chemistry A, 107 (2003) 9.
[79] A. C. T. van Duin, V. S. Bryantsev, M. S. Diallo, W. A. Goddard, O. Rahaman, D. J. Doren, D. Raymand, K. Hermansson, Development and validation of a ReaxFF Reactive Force Field for Cu cation/water interactions and copper metal/metal oxide/metal hydroxide condensed phases, The Journal of Physical Chemistry A, 114 (2010) 8.
[80] T. P. Senftle, S. Hong, M. M. Islam, S. B. Kylasa, Y. Zheng, Y. K. Shin, C. Junkermeier, R. Engel-Herbert, M. J. Janik, H. M. Aktulga, T. Verstraelen, A. Grama, A.C.T.v. Duin, The ReaxFF reactive force-field: development, applications and future directions, npj Computational Materials, 2 (2016) 14.
[81] G.M. Psofogiannakis, J.F. McCleerey, E. Jaramillo, A.C.T.v. Duin, ReaxFF reactive molecular dynamics simulation of the hydration of Cu-SSZ-13 zeolite and the formation of Cu dimers, The Journal of Physical Chemistry C, 119 (2015) 9.
[82] O. Verners, A.C.T.v. Duin, Comparative molecular dynamics study of fcc-Ni nanoplate stress corrosion in water, Surface Science, 633 (2015) 8.
[83] C. Zou, Y. K. Shin, A. C.T. van Duin, H. Fangb, Z.K. Liu, Molecular dynamics simulations of the effects of vacancies on nickel self-diffusion, oxygen diffusion and oxidation initiation in nickel, using the ReaxFF reactive force field, Acta Materialia, 83 (2015) 11.

[84] B. Jeon, Q.v. Overmeere, A.C.T.v. Duin, S. Ramanathan, Nanoscale oxidation and complex oxide growth on single crystal iron surfaces and external electric field effects, Physical Chemistry Chemical Physics, 15 (2013) 10.
[85] M. Aryanpour, A. C. T. van Duin, J.D. Kubicki, Development of a reactive force field for iron-oxyhydroxide systems, The Journal of Physical Chemistry A, 114 (2010) 10.
[86] O. Rahaman, A.C.T. van Duin, V.S. Bryantsev, J.E. Mueller, S.D. Solares, W.A. Goddard III, D.J. Doren, Development of a ReaxFF Reactive Force Field for aqueous chloride and copper chloride, Journal of Physical Chemistry A, 114 (2010) 13.
[87] D.J. Dwyer, S.R. Kelemen, A. Kaldor, The water dissociation reaction on clean and oxidized iron (110), The Journal of Chemical Physics, 76 (1982) 6.
[88] D.J. Dwyer, G.W. Simmons, A study of the initial reaction of water vapor with Fe(001) surface, Surface Science, 64 (1977) 16.
[89] S. Hung, W.H. Schwartz, J. Bernasek, Sequential oxidation of Fe (100) by water adsorption: formation of an ordered hydroxylated surface, Surface Science, 248 (1991) 11.
[90] X. Liu, X. Tian, T. Wang, X. Wen, Y. Li, J. Wang, H. Jiao, Coverage dependent water dissociative adsorption on Fe(110) from DFT computation, Physical Chemistry Chemical Physics, 17 (2015) 11.
[91] S. Liu, X. Tian, T. Wang, X. Wen, Y. Li, J. Wang, H. Jiao, Coverage dependent water dissociative adsorption on the clean and O-precovered Fe(111) surfaces, The Journal of Physical Chemistry C, 119 (2015) 11.
[92] S. Nose, A molecular dynamics method for simulations in the canonical ensemble, Molecular Physics, 52 (1984) 14.
[93] W.G. Hoover, Canonical dynamics: Equilibrium phase-space distributions, Physical Review A, 31 (1985) 3.
[94] R.W. Revie, H.H. Uhlig, Corrosion and corrosion control 4th ed., Wiley-Interscience, New York, 2008.
[95] J.M. Hermida-Ramon, G. Karlstrom, Study of the hydronium ion in water. A combined quantum chemical and statistical mechanical treatment, J Mol Struc-Theochem, 712 (2004) 7.

Manuscript 3

# Molecular dynamics modeling of Fe(110) passivity in 0.316 M NaOH solution

Hossein DorMohammadi, Qin Pang, Pratik Murkute, Líney Árnadóttir, O. Burkan Isgor

To be submitted to: *Corrosion Science*

## 4. Manuscript 3

# Molecular dynamics modeling of Fe(110) passivity in 0.316 M NaOH solution

Hossein DorMohammadi[1], Qin Pang[2], Pratik Murkute[3], Liney Arnadottir[2], O. Burkan Isgor[1]

**Abstract:**

The passivity of Fe(110) in a 0.316 M NaOH solution (pH = 13.5) was investigated using Reactive Force Field Molecular Dynamics (ReaxFF-MD). The simulations were carried out under an applied electric field of 30 MeV/cm. The electrical double layer was modeled using the Stern model. Under these conditions, following the expected thermodynamic behavior, a protective passive film formed during 500 ps simulation time. The initial stages of passivation differed from simulations that had been carried out in neutral electrolytes such that the highly alkaline environment allowed the stabilization of the metal through the formation of an $Fe(OH)_2$ layer on the metal surface. This created conditions for oxygen diffusion into metal without dissolution of iron atoms into the electrolyte. The passive film had a multiple oxide structure such that outer layers were in the form of $Fe_2O_3$, middle layers were in the form of $Fe_3O_4$, and the inner layer was in the form of FeO. This multi-layer structure is in agreement with theoretical passivity models that are based on an inner barrier layer that forms directly on the metal substrate (FeO), and outer layers ($Fe_3O_4$ and $Fe_2O_3$) that precipitates through the further oxidation of the iron ejected from the inner layer. A parallel XPS investigation confirmed the findings of ReaxFF-MD simulations.

**Keywords:** Iron passivity, alkaline electrolyte, Molecular Dynamics (MD), Reactive Force Field (ReaxFF), Stern model, X-ray photoelectron spectroscopy (XPS).

---

[1] Oregon State University, School of Civil and Construction Engineering, Corvallis, Oregon, USA
[2] Oregon State University, School of Chemical, Biological and Environmental Engineering, Corvallis, Oregon, USA

[3] Oregon State University, Materials Science Program, Mechanical, Industrial and Manufacturing Engineering, Corvallis, Oregon, USA

## 4.1. Introduction

Within the highly alkaline environment provided by concrete (pH > 13), carbon steel is covered with a protective layer, the so-called passive film, such that the rate of metal loss is not significant. However, in the presence of deteriorative processes such as chloride ingress or carbonation of concrete cover, steel can lose its passive film. The breakdown of passivity, also called depassivation, can lead to higher rates of metal loss (active corrosion) and concerns for the structural integrity of reinforced concrete elements [1-4].

Passivity and chloride-induced depassivation of carbon steels and iron in high pH concrete environments have been extensively studied using electrochemical methods [5-15]. These techniques provide valuable information about the average electrochemical behavior of relatively large metal surfaces, typically in centimeter-square scale or larger. However, passive films that form on carbon steel and iron in alkaline environments are typically 5-15-nm thick [16-18]; therefore, a deeper understanding of passivity can only be obtained through techniques that can characterize them in nanometer scale.

Several researchers used nanoscale surface characterization techniques to develop a fundamental understanding of the mechanisms of the passivity of iron and steel in alkaline environments. For example, Sanchez et al. [19, 20] proposed a model that was based on a two-layered film. The inner layer was composed of mixed iron oxides with a stoichiometry similar to that of magnetite (i.e., $Fe_3O_4$ or $FeO+Fe_2O_3$), where oxidation and reduction processes take place between the iron substrate and $Fe^{II}$ oxides. It was hypothesized that passivity was mainly related to the formation of the $Fe^{II}$ oxide layer. The outer layer mainly composed of $Fe^{III}$ oxides. This two-layer model is in agreement with theoretical passivity models that are based on an inner barrier layer that forms directly on the metal substrate, and an outer layer that precipitates through the hydrolysis of cations ejected from the inner layer [21, 22].

A number of other studies provided evidence for this two-layer passivity model. Joiret et al. [23] made similar observations to those of Sanchez et al. [19, 20] using in-situ Raman spectroscopy on the passive film structure of carbon steel exposed to NaOH solutions. Ghods et al. [16-18, 24] investigated the nano-scale properties of passive films that form on carbon steel in simulated

concrete pore solutions using multiple techniques including transmission electron microscopy (TEM) [16], x-ray photoelectron spectroscopy (XPS) [17, 18], and electron energy-loss spectroscopy (EELS) [24]. These studies showed that oxide films that form on carbon steel in simulated concrete pore solutions were composed of multiple oxide/hydroxide layers with a total thickness of 5 to 15 nm. XPS studies [17, 18] showed that the inner film was mainly composed of $Fe^{II}$ oxides while the outer region consisted mostly of $Fe^{III}$ oxides. EELS studies [24] provided additional evidence that the films that had formed on carbon steel in the simulated concrete pore solutions contained indistinctly layered regions. Regardless of the simulated pore solution used for passivation, the inner regions were mainly composed of FeO, which is known to be protective in alkaline media [25]. Above this layer, some traces of $Fe_3O_4$ was found in the intermediate region, while FeO was less evident. The outer regions of the oxide film contained $Fe_3O_4$, and $\alpha$-$Fe_2O_3$, but the composition of this layer was affected by the composition of the pore solution used in the experiments.

Even though these nano-scale surface characterizations studies provide valuable information about passive films that form on carbon steel (and iron) in alkaline electrolytes, they cannot explain the dynamic processes that lead to their formation as they can only provide snapshot data. The understanding of the dynamic processes that lead to passivation is critical in explaining the potential effects of chlorides on them and developing new corrosion mitigation strategies such as customized corrosion inhibitors and inexpensive corrosion-resistant steels. Unfortunately, experimental techniques that can give detailed dynamic information about these electrochemical processes are not satisfactory in nanometer scale. On the other hand, atomistic modeling techniques, such as Reactive Force Field Molecular Dynamics (ReaxFF-MD) [26-35] and Density Functional Theory (DFT) [36-41], have shown great potential to develop such fundamental understanding. In particular, ReaxFF-MD has emerged as a simulation framework to investigate reactive processes in relatively large scales that can be correlated to physical systems.

Although several ReaxFF-MD investigations exist for the study of the passivity of other metals, oxidation and corrosion processes in non-ferrous metals [29-33], the investigation of iron oxidation in such environments is limited [42-44]. Assowe et al. [32] investigated the interaction of a nickel substrate with water molecules using the ReaxFF-MD method. Their results supported the

expected thermodynamic behavior of nickel in pure water. Different steps of nickel oxidation including adsorption, dissociation of water, deprotonation, dissolution, and growth of hydroxide/oxide were simulated successfully. Similarly, Russo et al. [29] used ReaxFF-MD to examine the reaction dynamics associated with the dissociation of water on an aluminum cluster. The interaction of copper substrates and chlorine under aqueous conditions was investigated using ReaxFF-MD by Jeon et al. [30]. Pan and van Duin [42] and Pan [43] demonstrated the possibility of using ReaxFF-MD in simulating iron oxidation at the iron-water (pH = 7) interface. These simulations identified different stages of iron oxidation based on the generated chemical species generated and oxidation rate. In a recent study, DorMohammadi et al. [44] simulated the initial stages of iron corrosion in a neutral electrolyte (pH = 7). Critical stages of the iron corrosion process were identified as dissociation of water to $OH^-$ and $H^+$, adsorption of $OH^-$ on the iron surface, penetration of oxygen into iron to form iron oxides, and dissolution of iron into solution. It was shown that the formed oxide film was not pure phases (e.g., FeO, $Fe_2O_3$ and $Fe_3O_4$) but rather a mixture of oxides which is in agreement with expectations [45]. So far, ReaxFF-MD has not been used to simulate iron passivation in alkaline electrolytes.

The main goal of this research is to simulate the passivation process of pure iron in 0.316M NaOH solution, which is a surrogate concrete pore solution, using ReaxFF-MD and provide compositional information on oxide films that form during the passivation process. A parallel XPS investigation was performed on pure iron specimens after 15 days exposure to 13.5 pH NaOH solution to validate the ReaxFF-MD simulation results. The authors acknowledge that concrete provides a different environment for reinforcing steel from that of the surrogate simulated pore solution used in this study. Concrete pore solution is rather complex and contains several ions including $Ca^{+2}$, $K^+$, $(SO_4)^{-2}$ [18]. Although these ions affect the passivation process, they also confound the interpretation of the simulation results and present computational challenges. As a result, for a first study that investigates the passivation of iron in high alkaline environments using ReaxFF-MD, a simplified electrolyte in the form of NaOH was chosen. The concentration of the NaOH solution was chosen to be representative of typical concrete pore solutions, i.e., pH = 13.5. Similar concerns were behind the reason for choosing pure iron, rather than carbon steel, as the subject of investigation. Although carbon steel might show differences in passivation behavior, particularly because of its defect structure, the main species that passivate in both meals is iron.

Therefore, as a first study of its kind, pure iron, with no defects were studied in the ReaxFF-MD simulations. The corresponding XPS investigation, which was intended to provide complimentary data to the simulations, was also conducted on pure iron passivated in 0.316M NaOH solution.

## 4.2. Materials and Methods

### 4.2.1. ReaxFF-MD simulations

The simulated system involved a Fe(110) structure (24.61Å x 20.40Å x 22.87Å) containing 1080 Fe iron atoms, as shown in Figure 4-1, which is exposed to a 3.16 M NaOH solution (pH ~ 13.5), containing 21 Na ions, 21 OH ions, and 348 water molecules. The Na and OH ions were distributed in the electrolyte in groups of three in equally spaced seven layers in the longitudinal z direction to maintain the pH relatively stable in all parts of the electrolyte. Fe(110) surface orientation was chosen because it has a more closely packed surface than Fe(100) and Fe(111) structures. However, previous studies have shown that different surface orientations do not affect the oxidation behavior of iron significantly [44, 46-51]. Periodic boundary conditions were applied along $x$ and $y$ directions, while fixed boundary condition was imposed along $z$ direction. A reflecting wall was applied at the end of the specimen in order to confine the molecules in the solution phase and avoid the reaction of the solution with the surface below the sample.

Simulations were performed using the Large-scale Atomistic/Molecular Massively Parallel Simulator (LAMMPS) framework [52] and the Extreme Science and Engineering Discovery Environment (XSEDE) [53]. The ReaxFF framework was based on the interatomic potential theory developed by van Duin et al. [54]. The detailed explanation of the framework is not provided here for brevity but can be found in [29, 55-64]. The specific ReaxFF parameters for iron and other interacting species (e.g., Na, O, H) (i.e., parameters required for determining bond order, bond energy, valence angle energy, torsional angle energy, and van der Waals energy) were obtained from the work of Aryanpour et al. [49], who used these parameters to model an iron-oxyhydroxide systems. We validated these parameters by comparing ReaxFF-MD simulations of the surface formation energy and water adsorption energy on the Fe(110) surface with DFT calculations [44].

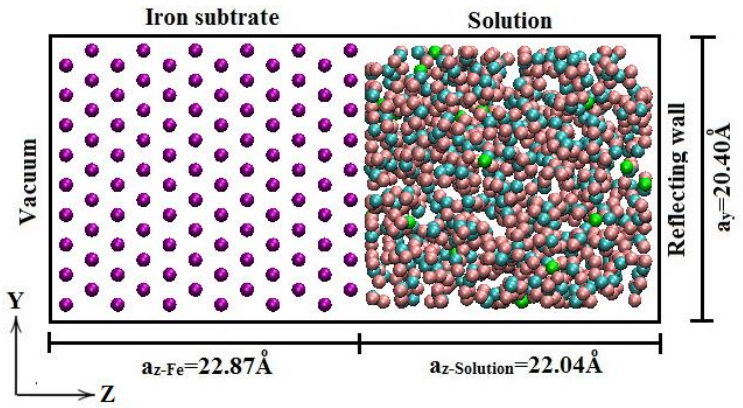


Figure 4-1: Initial configuration of the iron-highly alkaline solution. The purple, blue, brown, green and black spheres represent iron, oxygen, hydrogen and sodium atoms, respectively ($a_x$=25.0Å).

All simulations were performed at room temperature (300K) under one standard atmospheric pressure (1 atm). The initial inter-molecule distance between water and sodium hydroxide molecules, and the dimension of the vacuum slab along the z-direction were determined based on the density of the solution which is 1.05 g/cm$^3$ at 300 K and 1 atm. Nose-Hoover thermostat [65, 66] was employed to maintain the prescribed system temperature for canonical (NVT) ensemble. The Velocity-Verlet time stepping scheme [67] was used with an integration time step of 0.1 fs. The Maxwell-Boltzmann distribution [68, 69] was chosen to set the initial velocities and an energy-minimization was performed at the beginning of the simulation. Center of the mass of the system was fixed during the simulation to neglect any translational movements.

The simulations were run under an external electric field for 500 ps. The external electric field was necessary to overcome the challenges associated with long passivation times of iron in alkaline media under open circuit conditions [9, 16, 70]. Even with the externally applied electric field, the simulations presented in this paper represent early stages of passivation. The electrical double layer (EDL) between the metal surface and the electrolyte was modeled using the Stern model [71] based on a previous investigation comparing different EDL models for simulating the interface between iron and alkaline electrolytes [72]. The stern model describes the EDL as two layers: the Helmholtz layer, representing the compact layer of immobile ions that adsorb on the electrode surface and are located at a finite distance from the electrode, and a diffuse layer where the ions are mobile and spread out in the electrolyte. Figure 4-2 shows the electrical potential distribution across the electrolyte based on the Stern model.

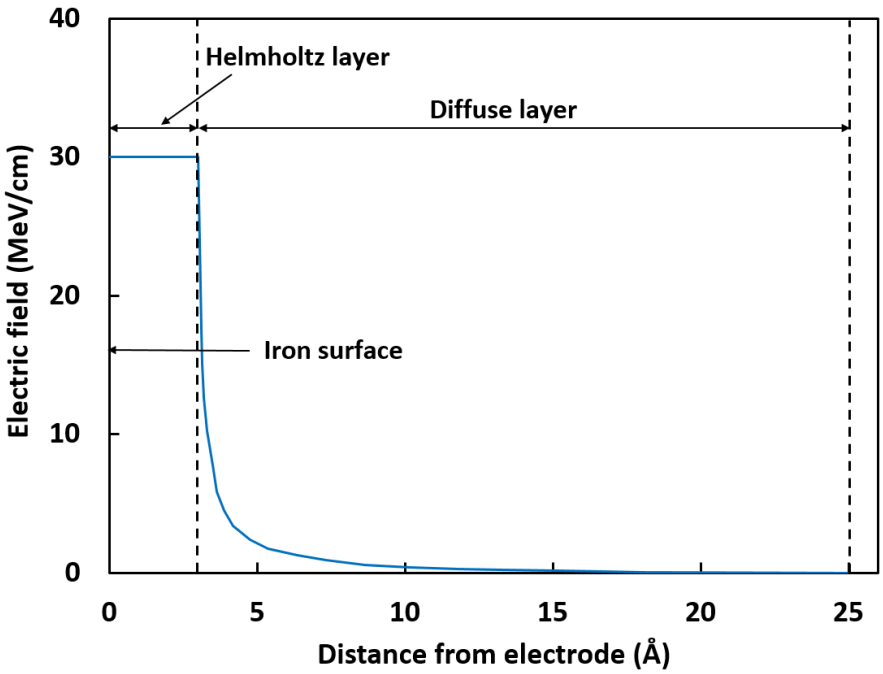


Figure 4-2: Applied electric field distribution using the Stern model. Helmholtz and diffuse layers are shown.

### 4.2.2. XPS investigation

XPS scans were performed on circular discs (Ø = 15 mm, thickness = 2 mm) of 99.95% pure iron. Both sides of the discs were polished to 2000 grade silicon carbide paper followed by cloth polishing with 0.3μm and 0.05 μm alumina suspension in anhydrous isopropyl alcohol (water content: <0.05% weight). Anhydrous Isopropyl alcohol suspension was used in place of water suspension to minimize surface oxidation during the polishing process. After surface preparation, iron specimens were ultrasonically cleaned, dried and stored in an anaerobic nitrogen chamber to minimize surface oxidation.

A NaOH solution with pH of 13.5 was used as the passivating medium. The solution was prepared by dissolving 0.316M NaOH (analytical grade 99.99%) in 1 L of deionized water. Iron specimens were exposed to passivating NaOH solution in an anaerobic nitrogen chamber to minimize the carbonation of high pH solution. The pH of the solution was continually monitored and was maintained at around 13.5 for the entire duration of the experiment. Two specimens were taken out of the solution at 2 weeks exposure period. The long passivation time was chosen to guarantee

full passivation under open circuit conditions. Open circuit potential and electrochemical impedance spectroscopy (EIS) measurements on specimens prepared in the same way and exposed to the solution with the same composition as the XPS tests confirmed full passivation after two weeks.

Upon removal from the passivating solution, all the specimens were rinsed with anhydrous isopropyl alcohol, dried in nitrogen chamber, and kept in nitrogen filled desiccator. Although the specimens were prepared and handled with minimum exposure to air and moisture until XPS investigation, they were briefly exposed to air during transfer to the nitrogen chamber. As a result, a thin film of air-formed iron oxide was likely to be present on the specimens before they were immersed in the test solution.

All the specimens were analyzed in angle resolved XPS, within a few hours of taking out of the solution. Specimens were mounted on the specimen holder and subsequently transferred directly to the fore-chamber of the XPS spectrometer and purged with dry nitrogen gas. This chamber was evacuated to $\sim 10^{-6}$ Pa before the specimens were transferred to the analytical chamber for examination. The analytical chamber was an ultra-high vacuum (UHV) chamber with a vacuum of $10^{-9}$ Pa. The specimens were analyzed using the Physical Electronics PHI 5600 ESCA system equipped with a monochromatic Al X-ray source (X-ray photon characteristic energy, $h\nu$ = 1486.6 eV). The X-ray gun was operated at 300 W (15 kV, 20 mA). The work function of the spectrometer was adjusted using ultra-pure gold metal (Au $4f_{7/2}$ = 84.0 eV), and the instrument linearity was set to yield a difference of 857.5 eV between the Cu $2p_{3/2}$ and Cu 3p photoelectron lines. The data were collected using a spherical capacitor analyzer (SCA) equipped with a seven-element "Omni-Focus V" lens. The angle between the analyzer and the X-ray source was 90°. The neutralizing electron gun was not used for analysis since no evidence of surface charging, or charge build-up was observed.

The XPS scans consisted of a survey scan to identify all the species present, followed by high resolutions scans of the species of interest. Survey scans were performed using an energy range of 1440 eV, analyzer pass energy of 187.85 eV, the step size of 1.6 eV. High-resolution scans were performed using analyzer pass energy of 23.5 eV with a step size of 0.1 eV. High-resolution analyses were calibrated to C 1s (hydrocarbon) signal of 285.0 eV. The high-energy resolution

spectra were collected for elements assigned in the survey spectra: oxygen (O 1s), carbon (C 1s), iron (Fe 2p), chlorine (Cl 2p) and sodium (Na 1s). The survey scans and high-resolution scans were performed at an emission angle (θ) of 5°, 25°, 45°, 65° and 85° which correspond to oxide film depth of 8.4 nm, 7.7 nm, 6 nm, 3.6 nm and 0.7 nm respectively. The higher the emission angle, the shallower the oxide film depth being analyzed, and hence all the XPS results would be presented in terms of passive oxide film depth.

The XPS data curve fitting and analysis was done using CasaXPS (V 2.3.18PR1.0) data processing software. The XPS data was semi-quantitatively analyzed using the areas under curve fitted (de-convoluted) spectra, and sensitivity factors provided by CasaXPS's Scofield element library. High-resolution XPS spectra were curve fitted and deconvoluted to quantify the contribution of each chemical species (element associations) that comprise the spectra. Curve fitting requires various constraints to be met simultaneously [17, 18, 73, 74]. Shirley background correction procedures and Gaussian (70%)-Lorentzian (30%) function were used for curve fitting procedures of high-resolution spectra. All high-resolution XPS spectra envelopes were smoothed by SG Quadratic method with smoothing width parameter of 21[74]. All spectra were curve fitted to the minimum number of peaks required for an optimum fit and needed for corresponding chemical assignments using Casa-XPS data library (ver. 2.3.18) [74]. The details procedure for the curve fitting process is provided in [74, 75].

Accurate determination of the atomic structure of the oxide film could not be based on the variations of the sodium, carbon and oxygen spectra since these elements are also present in the precipitates from the NaOH solutions on the specimen surface. Despite the best cleaning practices, complete removal of precipitates is not ensured, as the harsh cleaning procedures might damage the oxide film. Since iron is not incorporated into the precipitates, only Fe 2p XPS spectra were used in the analysis of the characteristics of oxide films. Assuming a uniform oxide film formation on the iron substrate, the film thickness was calculated from the oxide to metal intensity ratios at an emission angle of 5° following the procedure described in Ghods et al. [9].

## 4.3. Results and discussion

### 4.3.1 ReaxFF-MD simulations

Figure 4-3 presents the ReaxFF-MD simulation result of iron-highly alkaline solution system at 14 ps (Figure 4-3a), 40 ps (Figure 4-3b), 150 ps (Figure 4-3c), and 500 ps (Figure 4-3d). It was observed that during oxide film formation, iron atoms did not dissociate into the electrolyte, indicating iron passivity. It is shown that the thickness of the oxide layer and the number of diffused oxygen atoms in the oxide layer increased over the time. The iron oxidation reactions after 500 ps were slow and the number of diffused oxygen atoms in the oxide layer did not change considerably in later stages. The reason behind this was that oxygen penetration rate slowed down over time, controlling the thickness of the passive film.

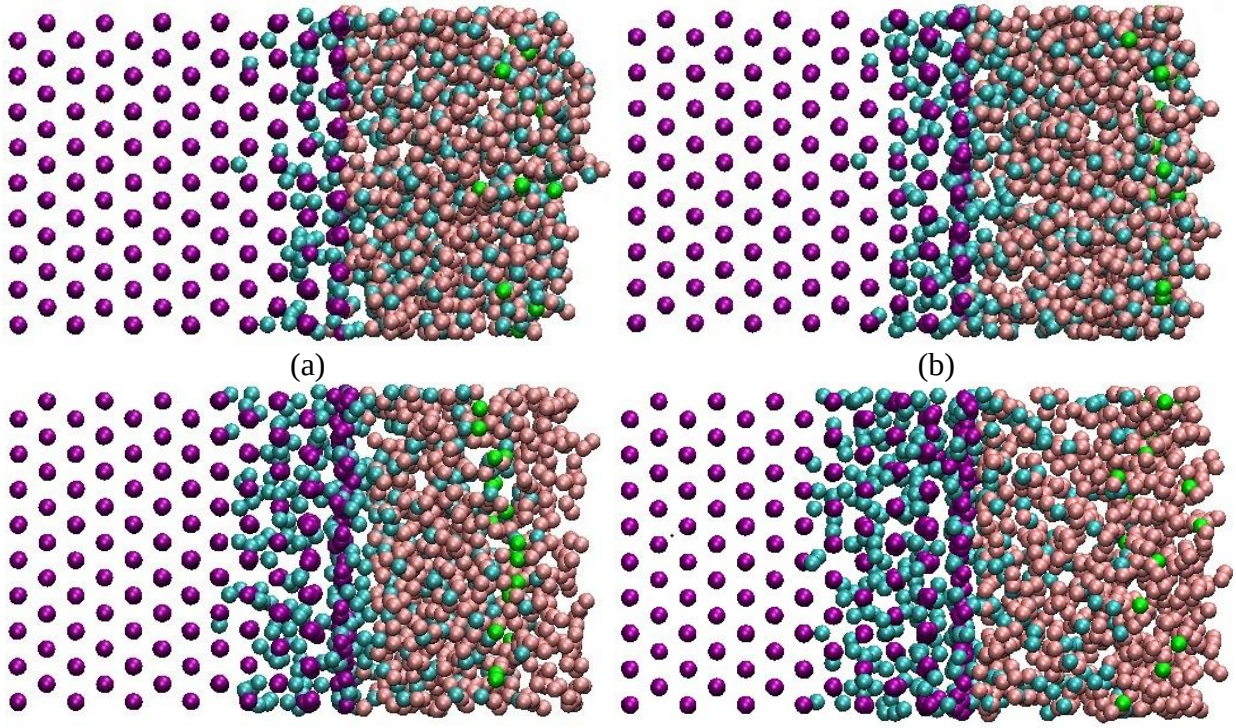


Figure 4-3: Snapshot of ReaxFF-MD simulation result of passive film formation at different times: (a) 14 ps, (b) 40 ps, (c) 150 ps, and (d) 500 ps. The purple, blue, brown and green spheres represent iron, oxygen, hydrogen and sodium atoms, respectively.

Initial stages of iron passivation process during the simulation was assessed, and several steps were observed as follows:

**Step 1:** The iron passivation process started with the adsorption and dissociation of water molecules and sodium hydroxides on the iron surface. Water molecules dissociated to $H^+_{(aq)}$ and $OH^-_{(ads)}$, and sodium hydroxides dissociated to $Na^+_{(aq)}$ and $OH^-_{(ads)}$ with oxygen atoms positioned toward the iron surface (Figure 4-4a):

$$H_2O_{(l)} \rightarrow OH^-_{(ads)} + H^+_{(aq)} \quad (4\text{-}1)$$

$$NaOH \rightarrow OH^-_{(ads)} + Na^+_{(aq)} \quad (4\text{-}2)$$

Some of $H^+_{(aq)}$ bonded with water molecules and formed $H_3O^+$ (Figure 4-4a):

$$H_2O_{(l)} + H^+_{(aq)} \rightarrow H_3O^+ \quad (4\text{-}3)$$

**Step 2:** The $OH^-$ groups from Equation 4-1 and 4-2 adsorbed on to the iron surface and formed adsorbed iron hydroxides (Figure 4-4b):

$$Fe_{(s)} + OH^-_{(ads)} \rightarrow FeOH + e^- \quad (4\text{-}4)$$

**Step 3:** Another $OH^-$ group adsorbed to the iron surface, bonded with $FeOH$ and formed $Fe(OH)_2$, as it is shown in Figure 4-4c:

$$FeOH + OH^-_{(ads)} \rightarrow Fe(OH)_2 + e^- \quad (4\text{-}5)$$

**Step 4:** For some $Fe(OH_2$, one hydroxide from a $Fe(OH)_2$ bonded with hydrogen from another $Fe(OH)_2$ to form a water molecule and left an adsorbed oxygen atom on the iron surface (Figure 4-4d).

**Step 5:** Released oxygen atoms from some $Fe(OH)_2$ started penetrating the iron substrate (Figure 4-4e) and oxidized iron in deeper layers.

This five-step oxidation process repeated itself throughout the simulation resulting in a passive iron film. During the iron passivation process, no iron atom dissociation in the solution was observed. This five-step process that led to oxygen diffusion into the iron layers is different from the process that had been observed in simulations done in neutral (pH = 7) electrolytes [44]. As shown by Dormohammadi et al. [44], when the electrolyte does not have reserve alkalinity, we observe that $Fe(OH)_2$ layer does not form, which results in the dissolution of the iron atoms into the solution while oxygen penetrated into the metal substrate to form complex oxides. The $Fe(OH)_2$

layer that forms and remains on the iron surface creates conditions for oxygen diffusion into metal without excessive dissolution of iron atoms into the electrolyte, hence, without iron vacancy formation. The oxygen penetration without iron dissolution or iron vacancy formation, followed by iron oxidation in the metal substrate, is the driving force for the formation of the passive film in alkaline environments.

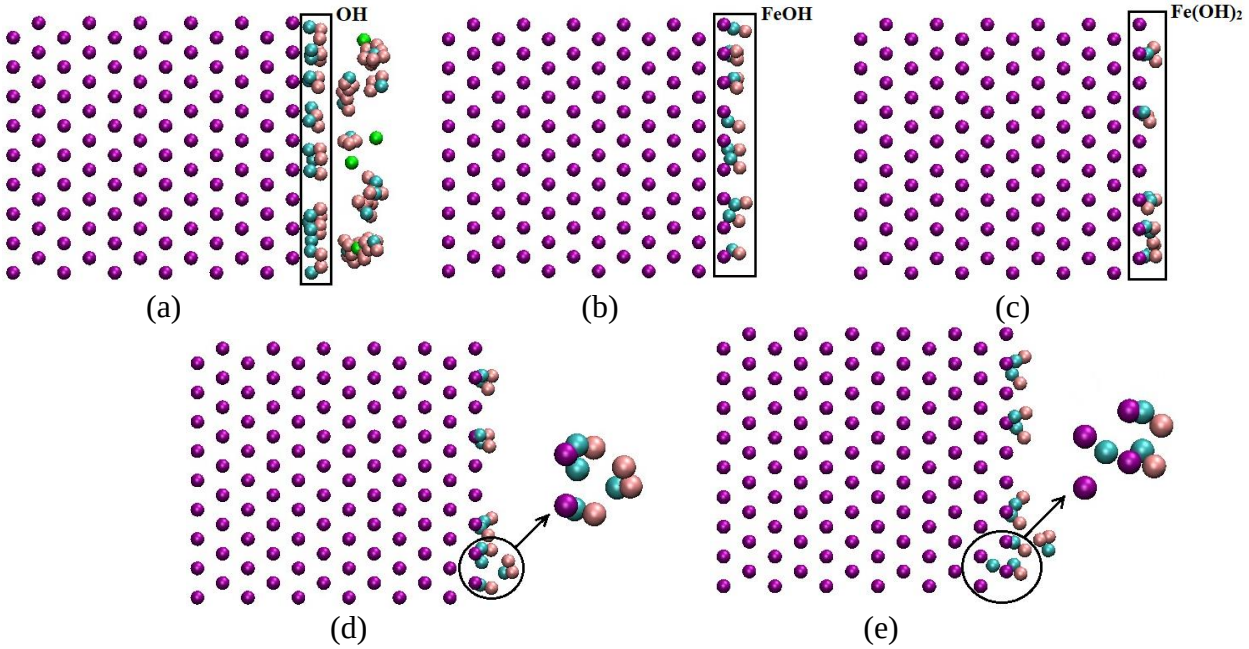


Figure 4-4: Snapshots from the ReaxFF-MD simulation showing the early stages of iron passive film formation: (a) water molecules and sodium hydroxides adsorbed on the iron surface and dissociated to $H^{+}_{(aq)}$ and $OH^{-}_{(ads)}$, and $Na^{+}_{(aq)}$ and $OH^{-}_{(ads)}$, respectively. Some of $H^{+}_{(aq)}$ bonded with water molecules and formed $H_3O^{+}_{(aq)}$. (b) $OH^{-}$ groups adsorbed on to the iron surface and formed FeOH. (c) Another $OH^{-}$ group adsorbed to the iron surface, bonded with FeOH and formed $Fe(OH)_2$. (d) One hydroxide from a $Fe(OH)_2$ bonded with hydrogen from another $Fe(OH)_2$. (e) Oxygen atom penetrated in the iron substrate.

In order to study the composition of the iron passive film that formed during ReaxFF-MD simulations, we compared the Fe-O Pair Distribution Functions (PDF) within the iron oxides with those of reference iron oxides [58], namely, hematite ($Fe_2O_3$), magnetite ($Fe_3O_4$) and wustite (FeO). Jeon et al. [58] investigated reference oxide structures mentioned above and provided the Fe-O PDF signature patterns for different reference oxides. It was shown that the PDF of $Fe_3O_4$ has a main peak at about 2.0 Å with a slight transition at about 1.6 Å, while the location of the

main peak of the PDF for $Fe_2O_3$ occurs at 1.7 Å with a transition at 2.15 Å. The PDF of FeO shows a dominant peak at about 1.65 Å with no transition point.

We tracked the iron oxidation process over time as oxygen atoms penetrated into the iron substrate without causing iron dissolution into the electrolyte. We specifically monitored the oxidation states of the second (Figure 4-5a), third (Figure 4-5b), and fourth layers (Figure 4-5c) by comparing their Fe-O PDF patterns with those of reference oxides. Figure 4-5a shows that the composition of the second iron oxide layer was similar to FeO at 14 ps. Over the time, it changed to $Fe_3O_4$ (at 40 ps), and then to $Fe_2O_3$ (at 500 ps). These transformations, as shown in the following equations, require additional oxygen atoms to penetrate through the iron substrate:

$$6FeO + 2O \rightarrow 2Fe_3O_4 \quad (4\text{-}6)$$

$$4Fe_3O_4 + 2O \rightarrow 6Fe_2O_3 \quad (4\text{-}7)$$

For the third and fourth layers, as shown in Figures 4-5b and 4-5c respectively, it was observed that the composition transformed from FeO to $Fe_3O_4$ (Equation 4-6). It is expected that in later stages of the simulation, additional oxygen atoms would penetrate into the passive film, and as a result, these layers would also observe the transformation of $Fe_3O_4$ to $Fe_2O_3$.

Figure 4-6 shows the Fe-O PDF of the six iron oxide layers, with the outer layer on the film/solution interface as the "first layer" and the inner layer on the film/metal interface as the "sixth layer." The first two outer oxide layers (first and second layers) show distinct transition points at 2.13Å and 2.17Å, while their dominant main peaks are located at 1.71Å and 1.73Å, respectively. For the middle two layers (third and fourth layers), main peaks are found at 2.01Å and 1.98Å, but also slight transitions are observed at 1.67Å and 1.63Å. The inner two layers (fifth and sixth layers) show dominant peaks at 1.66Å and 1.63Å, with no transition points. The PDF results of the six oxide layers imply that the formed oxide compositions in the two outer oxide layers are similar to $Fe_2O_3$. While the two middle layers and the two inner layers, respectively, are similar to $Fe_3O_4$ and FeO. These results are in agreement with the experimental results of the iron passive film [17, 24].

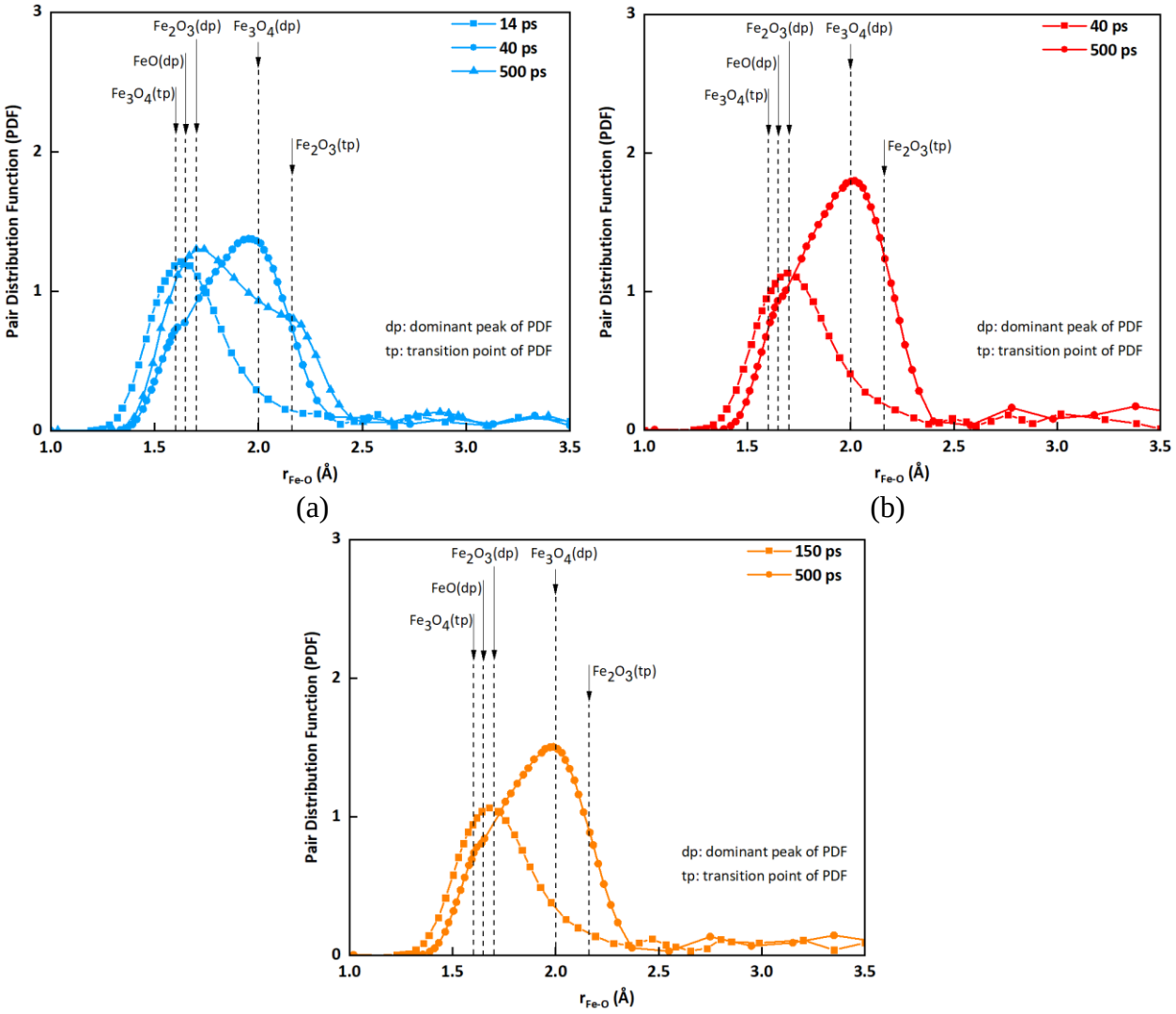


Figure 4-5: Pair distribution function of Fe-O over time for the (a) second iron oxide layer, (b) third iron oxide layer, and (c) fourth iron oxide layer. The dominant peak and transition point of the PDF for reference oxides are included in the figure for comparison [58].

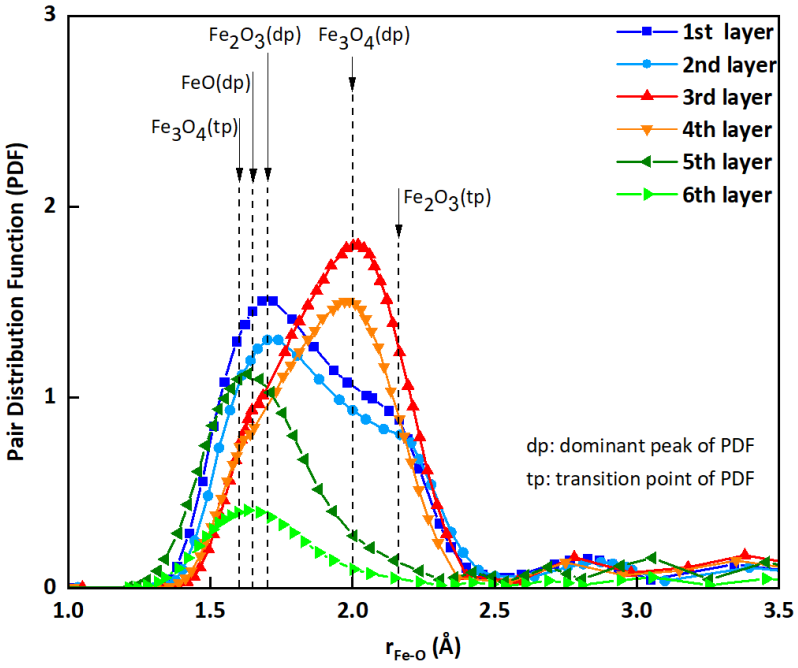


Figure 4-6: Pair distribution function of Fe-O for six different iron oxide layers of the passive film. The dominant peak and transition point of the PDF for reference oxides are included in the figure for comparison [58].

Figure 4-7 shows the evolution of oxygen atom density at the iron side versus z-distance from the iron/water interface at 500 ps. The intervals correspond to interlayer spaces of the iron lattice, where oxygen atoms are located. The figure shows how the oxygen atom density increases progressively with depth. This is different from oxygen distribution that is typically observed in an actively corroding system such as the one observed for iron in near neutral water (pH = 7) [42]. In an actively corroding (not passivating) system, it was observed that the oxygen atom density increases from the first interval to the second interval (the peak of the atom density occurs in the second interval) and decreases after the second interval. Dormohammadi et al. [44] showed that when iron oxidation is accompanied by iron dissolution and iron vacancy formation, unlike the oxide layers of the passive film, formed oxide compositions were not identifiable because they contained a mixture of several different oxides in each layer.

The transformation of the compositions of different iron oxide layers in the passive film can be also explained using Figure 4-7, regarding to the oxygen to iron ratio of different iron oxide phases,

i.e., FeO, $Fe_3O_4$ and $Fe_2O_3$. As the number of iron atoms of different layers were about the same, the oxygen-to-iron atom ratio was highest in the first iron oxide layer and the lowest in the sixth iron oxide layer. The iron oxide phase FeO has the lowest oxygen to iron ratio, and $Fe_2O_3$ has the highest one. Therefore, more oxygen atoms penetration over the time transformed the third and fourth iron oxide layers from the FeO to $Fe_3O_4$, and the second iron oxide layer from FeO to $Fe_3O_4$ and then to $Fe_2O_3$ during the simulation.

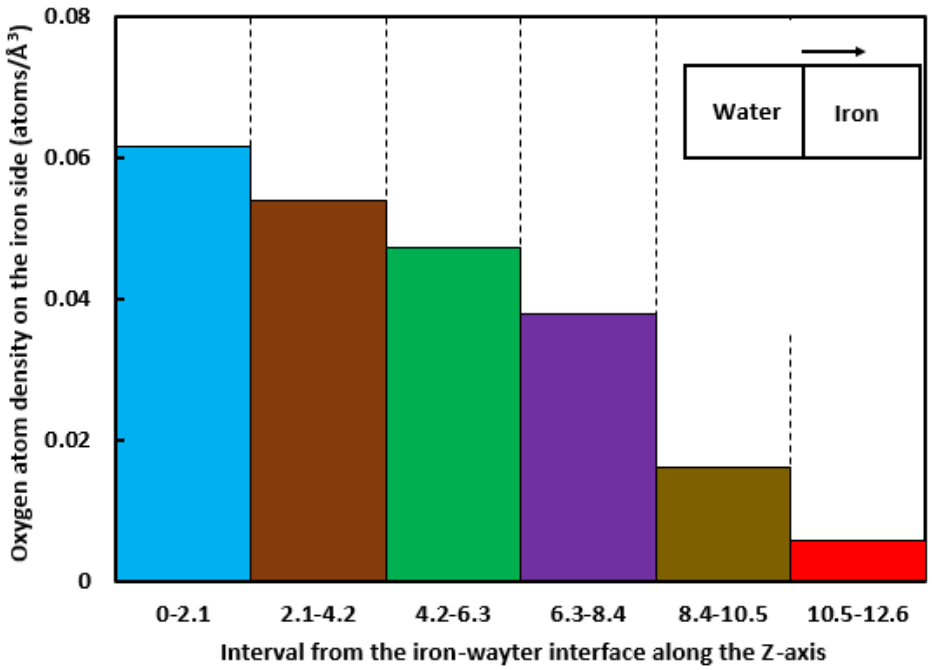


Figure 4-7: Oxygen atom density on the iron side in intervals from the iron-water interface along the Z-axis

The charge distribution of iron, oxygen, hydrogen and sodium atoms along the z-direction of iron-highly alkaline solution system at 500 ps are presented in Figure 4-8. The six layers of iron atoms in the iron passive film are positively charged. The first layer (outer layer) and the sixth layer (inner layer) consist of the highest and lowest charged cations in them, respectively. The highest charged iron atoms decrease from the outer layer to the inner layer in the passive film. The charge of iron atoms within the zone that has not been penetrated by oxygen is zero. The charges of oxygen atoms in the oxidized zone are between 0 and -1 e and show three zones. Oxygen atoms of the first and second iron atom layers are the highest anions in the passive film. In the middle of

the oxide layer, consist of third and fourth iron atom layers, oxygen atoms have intermediate charges while on the oxide-metal interface including the two inner iron atom layers oxygen atoms have the highest negative charges.

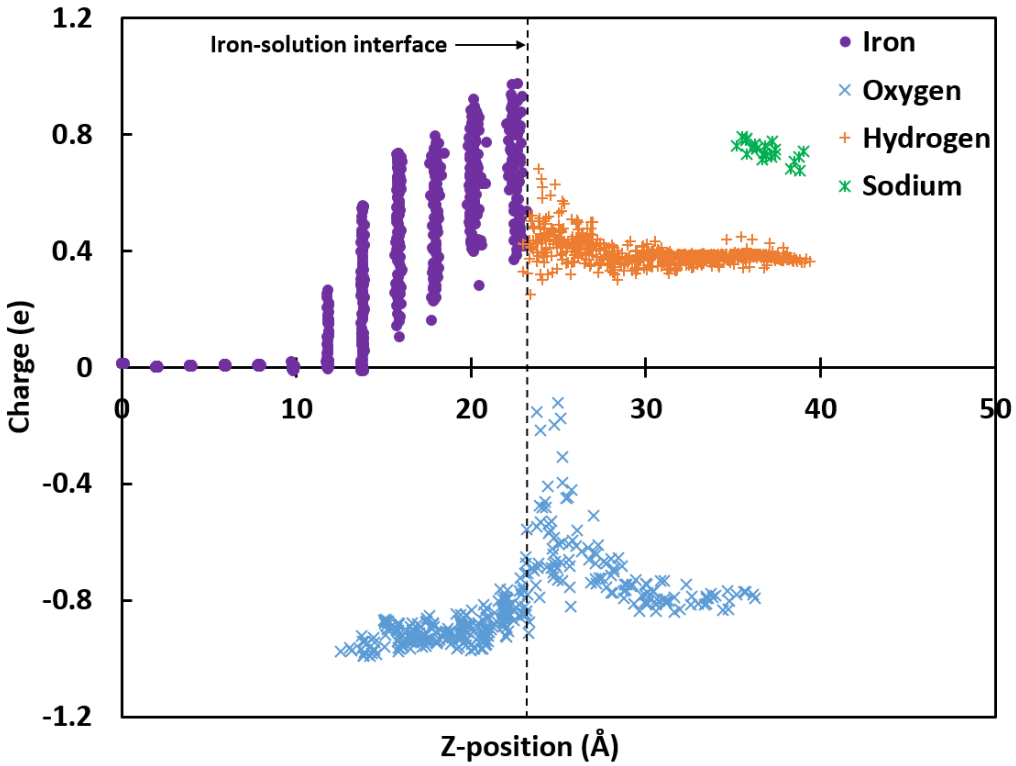


Figure 4-8: Charge distributions of iron-highly alkaline solution at 500 ps

It was shown by Jeon et al. [50] that at 300K, FeO has the lowest cation and the highest anion charge distribution while the $Fe_2O_3$ has the highest cation and the lowest anion charge distribution. $Fe_3O_4$ charge state is an intermediate between wustite and hematite. A comparison of simulated charge states of iron and oxygen atoms of the iron passive film in Figure 4-6 with those of reference oxide structures, i.e. FeO, $Fe_2O_3$ and $Fe_3O_4$, shows that the outer zone consists of two outer iron atom layers is $Fe_2O_3$-rich zone, while the middle and inner zones consist of two middle and inner iron atom layers, respectively, are $Fe_3O_4$-rich and FeO-rich zones.

It is worth mentioning that the charge states of the iron and oxygen atoms in the oxidized zone of the iron-highly alkaline solution were presented here are different from the ones of the iron- neutral electrolyte we studied recently [42]. In the case of actively corroding iron the iron oxide film is a mixture of the iron oxide phases and the highest cation charges do not exist in the outermost layer

at the oxide-solution interface. Instead, it occurs within the oxide film. While, in the case of iron passivation, the outmost layer contained $Fe_2O_3$, which has the higher cation charge than FeO and $Fe_3O_4$. Therefore the highest cation charges exist in the outer oxide layer of the iron passive film.

### 4.3.2 XPS results

The XPS results for the fully passivated iron specimen exposed to 13.5 pH NaOH solution are presented in Figure 4-9. The XPS analyses investigated the chemical build-up of the oxide film with increasing passivation time and oxide film depth. The composition of the oxide film is presented in terms of the ratio of $Fe^{III}$ and $Fe^{II}$ ionic concentrations. The $Fe^{II}$ ionic state includes $Fe_3O_4$/FeO and $Fe^{II}$ ionic includes $\alpha$-$Fe_2O_3$/$\gamma$-$Fe_2O_3$/FeOOH. The ratio $Fe^{III}/Fe^{II}$ takes into consideration all the oxidation products formed on the iron surface. Figure 4-9(a) shows the variation of $Fe^{III}/Fe^{II}$ ratio at various film depths at different passivation times leading up to full passivation at 2 weeks. The minimum depth of 0.7 nm corresponds to the top surface of the oxide film at an corresponding emission angle of 85° and maximum depth corresponds to emission angle of 5°.

Using the data interpreted from XPS curve fitting results, it was observed that for all the passivation durations, it was observed that the $Fe^{III}/Fe^{II}$ ratio decreased with increasing oxide film depth. Although the presence of $Fe^{III}$ ions diminished with increasing passive oxide film depth, the concentration of $Fe^{II}$ ions increased. These trends indicated the presence of $Fe^{III}$ oxides ($Fe_2O_3$) in the shallower depths or the outer layers of passive film and $Fe^{II}$ oxides (FeO and $Fe_3O_4$) in the inner layers of passive film i.e. close to metal-oxide interface. In addition, it could be inferred that the concentration of $Fe^{III}$ oxides decrease and that protective $Fe^{II}$ oxides increase, with increasing oxide film depth.

The $Fe^{III}/Fe^{II}$ ratio increases from 0.93 (at 10 minutes) to 3.38 (at 2 weeks). This indicates that within the outer regions of the film (top surface and subsurface layers), the concentration of $Fe^{III}$ oxides increases with increasing passivation time and is higher than the $Fe^{II}$ oxides. In addition, the ratio of 0.93 (< 1) at 10 minutes reflects the presence of more $Fe^{II}$ phases than $Fe^{III}$ phases. This provides an essential insight into passivation mechanism of iron in high pH solution. Iron

oxide products formed at early passivation stages mainly consist of protective $Fe^{II}$ oxides ($Fe_3O_4$/FeO/$Fe(OH)_2$), and as the passivation progresses, $Fe^{II}$ oxides are converted to $Fe^{III}$ oxides ($\alpha$-$Fe_2O_3$, $\gamma$-$Fe_2O_3$, FeOOH). This is supported by the observation that at shallower depths, for early passivation, the $Fe^{II}$ oxides are majorly present, whereas at full passivation, the presence of $Fe^{III}$ oxides is dominant.

In addition, the oxide fractions plotted with increasing. oxide film depths are shown in Figure 4-9b. Where, the oxide fraction is the ratio of oxide phases to the total sum all oxide (FeO+$Fe_2O_3$+$Fe_3O_4$). As presented in the figure, the $Fe_2O_3$ oxide fraction decreases with increasing film depth, whereas, FeO+$Fe_3O_4$ oxide fraction increases with increasing film depth. These two trends reconfirm the abundant presence of $Fe^{III}$ oxides in the outer layers of passive film and the increasing presence of $Fe^{II}$ oxides near the metal-oxide interface. Thus, in conclusion, the increasing $Fe^{III}$ oxide concentration with increasing passivation time, in outer region of oxide film layers, indicate the oxidation of $Fe^{II}$ oxides to $Fe^{III}$ oxide phases. However, the $Fe^{II}$ oxides are dominantly present only near the metal-oxide interface and their concentration increases with increasing oxide film depth. Although, the XPS results validate the findings of the ReaxFF-MD simulations, it is to be noted that the timescales of the ReaxFF-MD and the XPS studies were different. The ReaxFF-MD simulation was performed under applied electric field for 500 ps and the passive film thickness was about 1.2 nm, whereas for the XPS study, the full passivation took two weeks under open circuit potential conditions and the passive film thickness was about 5 nm.

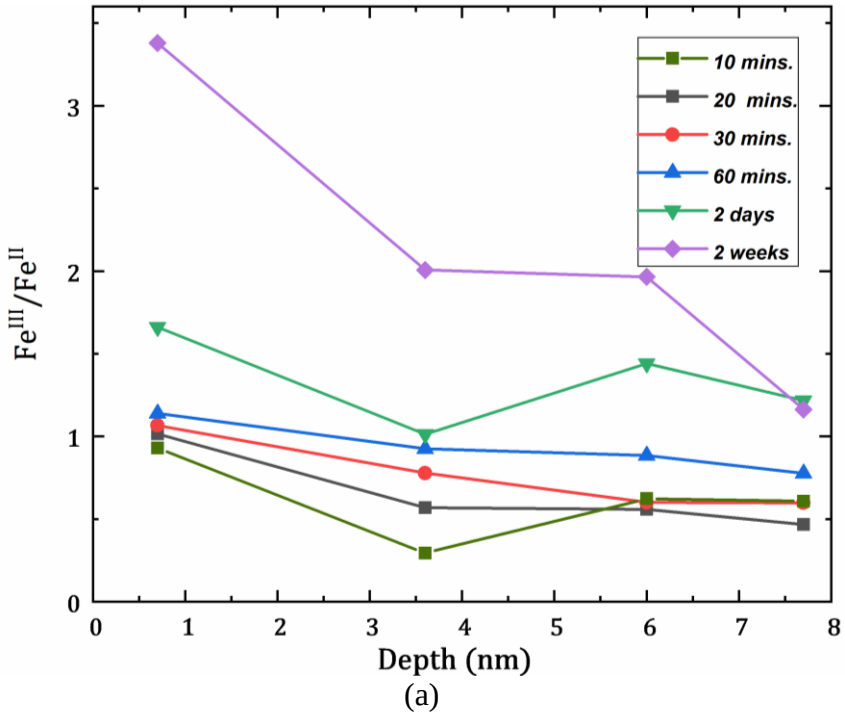


(a)

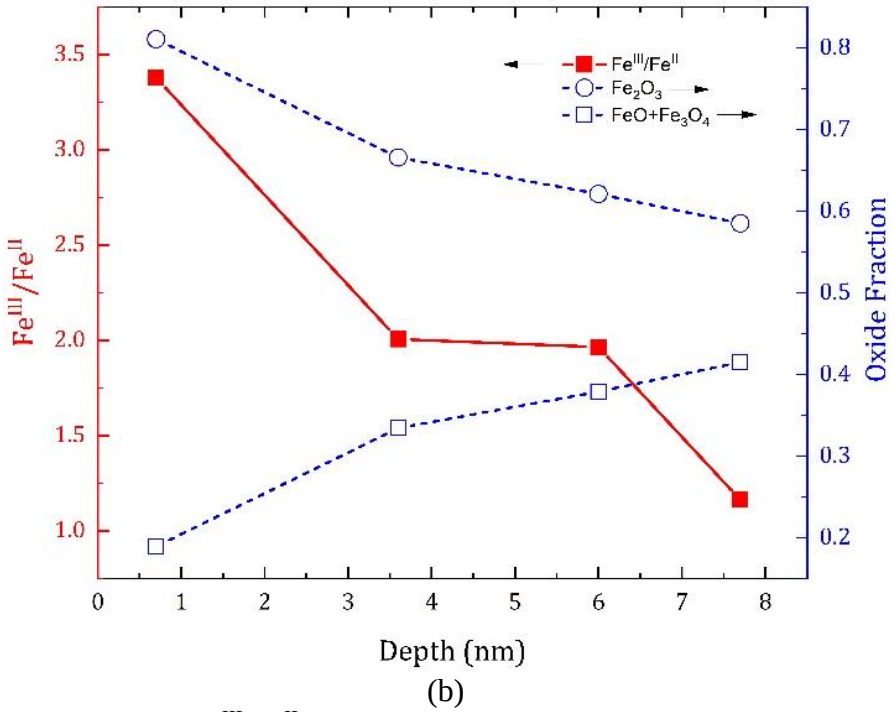


(b)

Figure 4-9: (a) Variation of $Fe^{III}/Fe^{II}$ ratio with increasing passivation time and oxide film depth. (b) Change in $Fe^{III}/Fe^{II}$ ratio and oxide phase fractions at full passivation at varying oxide film depth.

## 4.4. Conclusions

The iron oxidation in exposure to the highly alkaline solution was investigated using ReaxFF-MD to study the compositions of the iron passive film and the initial stages of the passivation process. Iron surface orientation Fe(110), as the more close-packed surface than the other orientations, was chosen and the solution contained sodium hydroxides to model a highly alkaline electrolyte. An external electric field was applied using the Stern model with the intensity of 30 MeV/cm at the iron surface. The simulation was performed for 500 ps, and iron oxidation with no iron dissociation in the electrolyte was observed during the simulations, indicating iron passivation and supports the thermodynamic behavior of iron-highly alkaline solution system. The XPS scans were performed to study the oxide film chemical buildup and time-dependent passivation of iron surface exposed to 13.5 pH NaOH aqueous solution. The XPS findings validated the ReaxFF-MD results regarding oxide film buildup and passivation mechanism.

The critical stages of the iron passivation process were studied. It was shown that passivation initiated with the formation of an $Fe(OH)_2$ layer on the metals surface followed by oxygen penetration into the metal substrate. This initiation is different from the process that had been observed in simulations done in neutral (pH = 7) electrolytes [44]. When the electrolyte does not have reserve alkalinity, $Fe(OH)_2$ layer does not form, which results in the dissolution of the iron atoms in to the solution while oxygen penetrate into the metal substrate to form complex oxides. The $Fe(OH)_2$ layer that forms and remains on the iron surface creates conditions for oxygen diffusion into metal without excessive dissolution of iron atoms into the electrolyte, hence without iron vacancy formation. The oxygen penetration without iron dissolution or iron vacancy formation, followed by iron oxidation in the metal substrate, was the driving force for the formation of the passive film in alkaline environments.

In order to analyze the compositions of the oxidized zone, the iron oxide layers were studied for different times during the simulation. The PDFs of Fe-O for the iron oxide layers were compared to those of the reference oxide structures, i.e., $Fe_2O_3$, $Fe_3O_4$ and FeO. By comparing the locations of the dominant and transition points of each iron oxide layer to those of iron oxide phase, it was shown that during the iron oxidation the compositions of different layers changed over time from

FeO to $Fe_2O_3$, and finally to $Fe_2O_3$, if adequate amount of oxygen was able to penetrate the layer. Oxygen penetration rate slowed down over time, controlling the thickness of the passive film and resulting in a multilayer oxide structure. The surface of the film contained $Fe(OH)_2$, which was identified as responsible for the prevention of iron dissolution while allowing oxygen penetration into the substrate. The analysis of Fe-O PDF patterns of different layers in the passive film showed that the outer layers of the passive film were mainly in the form of $Fe_2O_3$; the middle layers were in the form of $Fe_3O_4$; and the inner layers were mainly in the form of FeO.

Studying the oxygen atom densities of different intervals in the oxidized zone showed that outer iron oxide layers contained more oxygen atoms than the inner iron oxide layers. By comparing the oxygen-to-iron ratio of different layers, it was also concluded that the outer layers are similar to $Fe_2O_3$, while the middle and inner layers are similar to $Fe_3O_4$ and FeO.

The XPS results showed the dominant presence of $Fe^{III}$ ions ($Fe_2O_3$ oxide) in outer regions of oxide film, however the ion concentration decreased with increasing film depth. On the contrary, the $Fe^{II}$ ion concentration increased with increasing film depth suggesting a $Fe^{II}$ rich inner layers consisting of FeO and $Fe_3O_4$ oxides near the metal-oxide interface. Furthermore, the time dependent passivation study indicated the transformation of $Fe^{II}$ to $Fe^{III}$ oxides, which was confirmed by increasing $Fe^{III}$ concentration at the top surface of the oxide layer.

### 4.5. Acknowledgments

This study is fully funded by the National Science Foundation, DMMI, Grant No. 1435417. Part of this work used the Extreme Science and Engineering Discovery Environment (XSEDE) Comet at the through the San Diego Supercomputer Center (SDSC) allocation TG-ENG170002. XSEDE is supported by National Science Foundation grant number ACI-1053575.

### 4.6. References

[1] L. Bertolini, B. Elsener, P. Pedeferri, R. and Polder, Corrosion of Steel in Concrete: Prevention, Diagnosis, Repair, Weinheim: Wiley-VCH, (2000).
[2] H. Bohni, Corrosion in concrete structures, New York: CRC Press, (2005).
[3] J.P. Broomfield, Corrosion of steel in concrete New York: Taylor & Francis, (2007).

[4] P.K. Mehta, P.J.M. Monteiro, Concrete: microstructure, properties, and materials, New York: McGraw-Hill Professional., (2005).
[5] P. Ghods, O.B. Isgor, G. Mcrae, T. Miller, The effect of concrete pore solution composition on the quality of passive oxide films on black steel reinforcement, Cement Concrete Comp, 31 (2009) 10.
[6] L. Li, A.A. Sagues, Chloride corrosion threshold of reinforcing steel in alkaline solutions - Cyclic polarization behavior, Corrosion, 58 (2002) 12.
[7] C.M. Hansson, A. Poursaee, A. Laurent, Macrocell and microcell corrosion of steel in ordinary Portland cement and high performance concretes, Cement Concrete Res, 36 (2006) 5.
[8] U.M. Angst, B. Elsener, C.K. Larsen, O. Vennesland, Chloride induced reinforcement corrosion: Electrochemical monitoring of initiation stage and chloride threshold values, Corros Sci, 53 (2011) 14.
[9] P. Ghods, O.B. Isgor, G.A. McRae, G.P. Gu, Electrochemical investigation of chloride-induced depassivation of black steel rebar under simulated service conditions, Corros Sci, 52 (2010) 11.
[10] G.K. Glass, N.R. Buenfeld, The presentation of the chloride threshold level for corrosion of steel in concrete, Corros Sci, 39 (1997) 13.
[11] L.T. Mammoliti, L.C. Brown, C.M. Hansson, B.B. Hope, The influence of surface finish of reinforcing steel and pH of the test solution on the chloride threshold concentration for corrosion initiation in synthetic pore solutions, Cement Concrete Res, 26 (1996) 6.
[12] L. Li, A.A. Sagues, Chloride corrosion threshold of reinforcing steel in alkaline solutions - Open-circuit immersion tests, Corrosion, 57 (2001) 10.
[13] S. Goni, C. Andrade, Synthetic concrete pore solution chemistry and rebar corrosion rate in the presence of chlorides, Cement Concrete Res, 20 (1990) 15.
[14] C. Andrade, C.L. Page, Pore solution chemistry and corrosion in hydrated cement systems containing chloride salts - a study of cation specific effects, Brit Corros J, 21 (1986) 5.
[15] U. Angst, B. Elsener, C.K. Larsen, O. Vennesland, Critical chloride content in reinforced concrete - A review, Cement Concrete Res, 39 (2009) 17.
[16] P. Ghods, O.B. Isgor, G.J.C. Carpenter, J. Li, G.A. McRae, G.P. Gu, Nano-scale study of passive films and chloride-induced depassivation of carbon steel rebar in simulated concrete pore solutions using FIB/TEM, Cement Concrete Res, 47 (2013) 14.
[17] P. Ghods, O.B. Isgor, J. Brown, F. Bensebaa, D. Kingston, XPS depth profiling study on the passive oxide film of carbon steel in saturated calcium hydroxide solution and the effect of chloride on the film properties, Applied Surface Science, 257 (2011) 9.
[18] P. Ghods, O. Burkan Isgor, F. Bensebaa, D. Kingston, Angle-resolved XPS study of carbon steel passivity and chloride-induced depassivation in simulated concrete pore solution, Corros Sci, 58 (2012) 9.
[19] M. Sánchez-Moreno, H. Takenouti, J.J. García-Jareno, F. Vicente, C. Alonso, A theoretical approach of impedance spectroscopy during the passivation ofsteel in alkaline media, Electrochimica Acta, 54 (2009) 5.
[20] M. Sánchez, J. Gregori, C. Alonso, J.J. García-Jareño, H. Takenouti, F. Vicente, Electrochemical impedance spectroscopy for studying passive layers on steel rebars immersed in alkaline solutions simulating concrete pores, Electrochimica Acta, 52 (2007) 8.

[21] M. Sánchez, J. Gregori, M.C. Alonso, J.J. García-Jareño, F. Vicente, Anodic growth of passive layers on steel rebars in an alkaline medium simulating the concrete pores, Electrochimica Acta, 52 (2006) 7.
[22] D.D. Macdonald, S.R. Biaggio, H.K. Song, Steady-state passive films - interfacial kinetic effects and diagnostic-criteria, J Electrochem Soc, 139 (1992) 8.
[23] S. Joiret, M. Keddam, X.R. Novoa, M.C. Perez, C. Rangel, H. Takenouti, Use of EIS, ring-disk electrode, EQCM and Raman spectroscopy to study the film of oxides formed on iron in 1 M NaOH, Cement Concrete Comp, 24 (2002) 9.
[24] H.B. Gunay, P. Ghods, O.B. Isgor, G.J. Carpenter, X. Wu, Characterization of atomic structure of oxide films on carbon steel in simulated concrete pore solutions using EELS, Applied Surface Science, 274 (2013) 8.
[25] C. Colliex, T. Manoubi, C. Ortiz, Electron-Energy-Loss-Spectroscopy near-edge fine-structures in the iron-oxygen system. , Physical Review B, 44 (1991) 10.
[26] A. C. T. van Duin, V. S. Bryantsev, M. S. Diallo, W. A. Goddard, O. Rahaman, D. J. Doren, D. Raymand, K. Hermansson, Development and validation of a ReaxFF Reactive Force Field for Cu cation/water interactions and copper metal/metal oxide/metal hydroxide condensed phases, J. Phys. Chem. A, 114 (2010) 8.
[27] M. Aryanpour, A. C. T. van Duin, J.D. Kubicki, Development of a reactive force field for iron-oxyhydroxide systems, J. Phys. Chem. A, 114 (2010) 10.
[28] D. Raymand, A. C. T. van Duin, D. Spångberg, W. A. Goddard, K. Hermansson, Water adsorption on stepped ZnO surfaces from MD simulation, Surf. Sci., (2010) 12.
[29] M. F. Russo, Jr. R. Li, M. Mench, A.C.T.v. Duin, Molecular dynamic simulation of aluminumewater reactions using the ReaxFF reactive force field, International Journal of Hydrogen Energy, 36 (2011) 8.
[30] B. Jeon, S. K. R. S. Sankaranarayanan, A.C.T.v. Duin, S. Ramanathan, Atomistic insights into aqueous corrosion of copper, J. Chem. Phys., 134 (2011) 10.
[31] B. Jeon, S. K. R. S. Sankaranarayanan, A.C.T.v. Duin, S. Ramanathan, Reactive molecular dynamics study of chloride ion interaction with copper oxide surfaces in aqueous media, ACS Applied Materials & Interfaces 4(2012) 8.
[32] O. Assowe, O. Politano, V. Vignal, P. Arnoux, B. Diawara, O. Verners, A.C.T.v. Duin, Reactive molecular dynamics of the initial oxidation stages of Ni(111) in pure water: effect of an applied electric field The Journal of Physical Chemistry A, 116 (2012).
[33] O. Verners, A.C.T.v. Duin, Comparative molecular dynamics study of fcc-Ni nanoplate stress corrosion in water, Surf. Sci., 633 (2015) 8.
[34] C. Zou, Y. K. Shin, A. C.T. van Duin, H. Fangb, Z.K. Liu, Molecular dynamics simulations of the effects of vacancies on nickel self-diffusion, oxygen diffusion and oxidation initiation in nickel, using the ReaxFF reactive force field, Acta Mater., 83 (2015) 11.
[35] T. P. Senftle, S. Hong, M. M. Islam, S. B. Kylasa, Y. Zheng, Y. K. Shin, C. Junkermeier, R. Engel-Herbert, M. J. Janik, H. M. Aktulga, T. Verstraelen, A. Grama, A.C.T.v. Duin, The ReaxFF reactive force-field: development, applications and future directions, npj Comput. Mater., 2 (2016) 14.
[36] K. Otte, W.W. Schmahl, R. Pentcheva, Density functional theory study of water adsorption on FeOOH surfaces, Surface science, 606 (2012) 10.

[37] M.T. Nguyen, N. Seriani, R. Gebauer, Water adsorption and dissociation on alpha-Fe2O3(0001): PBE+U calculations. , 2013. 138(19): p. 8., Journal of Chemical Physics, 138 (2013) 8.
[38] Q. Pang, H. DorMohammadi, O.B. Isgor, L. Árnadóttir, Density functional theory study on the effect of OH and Cl adsorption on the surface structure of α-Fe2O3, Computational and Theoretical Chemistry, 1100 (2017) 11.
[39] S. Yin, X. Ma, D.E. Ellis, Initial stages of $H_2O$ adsorption and hydroxylation of Fe-terminateda-$Fe_2O_3$(0 0 0 1) surface, Surface science, 601 (2007) 12.
[40] A. Soon, M. RTodorova, B. Delley, C. Stampfl, Oxygen adsorption and stability ofsurface oxides on Cu(111): a first-principles investigation, Physical Review B - Condensed Matter and Materials Physics, 73 (2006) 12.
[41] C.H. Zhang, M. Liu, Y. Jin, D.B. Sun, The corrosive influence of chloride ionspreference adsorption ona-$Al_2O_3$(0001) surface, Applied Surface Science, 347 (2015) 6.
[42] T. Pan, A.C.T.v. Duin, Passivation of steel surface: An atomistic modeling approach aided with X-ray analyses, Mater. Lett., 65 (2011) 4.
[43] T. Pan, Quantum chemistry-based study of iron oxidation at the iron–water interface: An X-ray analysis aided study, Chem. Phys. Lett., 511 (2011) 7.
[44] H. DorMohammadi, Q. Pang, O.B. Isgor, L. Árnadóttir, Atomistic simulation of initial stages of iron corrosion in pure water using reactive molecular dynamics, Computational Materials Science, 145 (2018) 8.
[45] R.W. Revie, H.H. Uhlig, Corrosion and corrosion control 4th ed., Wiley-Interscience, New York, 2008.
[46] D.J. Dwyer, S.R. Kelemen, A. Kaldor, The water dissociation reaction on clean and oxidized iron (110), The Journal of Chemical Physics, 76 (1982) 6.
[47] D.J. Dwyer, G.W. Simmons, A study of the initial reaction of water vapor with Fe(001) surface, Surface Science, 64 (1977) 16.
[48] S. Hung, W.H. Schwartz, J. Bernasek, Sequential oxidation of Fe (100) by water adsorption: formation of an ordered hydroxylated surface, Surface Science, 248 (1991) 11.
[49] M. Eder, K. Terakura, J. Hafner, Initial stages of oxidation of (100) and (110) surfaces of iron caused by water, Phys. Rev. B. , 64 (2001) 7.
[50] X. Liu, X. Tian, T. Wang, X. Wen, Y. Li, J. Wang, H. Jiao, Coverage dependent water dissociative adsorption on Fe(110) from DFT computation, Physical Chemistry Chemical Physics, 17 (2015) 11.
[51] S. Liu, X. Tian, T. Wang, X. Wen, Y. Li, J. Wang, H. Jiao, Coverage dependent water dissociative adsorption on the clean and O-precovered Fe(111) surfaces, The Journal of Physical Chemistry C, 119 (2015) 11.
[52] S. Plimpton, Fast parallel algorithms for short–range molecular dynamics, Journal of Computational Physics, 117 (1995) 42.
[53] J. Towns, T. Cockerill, M. Dahan, I. Foster, K. Gaither, A. Grimshaw, V. Hazlewood, S. Lathrop, D. Lifka, G. D. Peterson, R. Roskies, J. R. Scott, N. Wilkins-Diehr, XSEDE: Accelerating scientific discovery, Computing in Science & Engineering, 16 (2014) 13.
[54] A. C. T. van Duin, S. Dasgupta, F. Lorant, W.A. Goddard, ReaxFF: A reactive force field for hydrocarbons, The Journal of Physical Chemistry A, 105 (2001) 14.

[55] A. C. T. van Duin, A. Strachan, S. Stewman, Q. Zhang, X. Xu, W.A. Goddard, ReaxFF$_{SiO}$ reactive force field for silicon and silicon oxide systems, The Journal of Physical Chemistry A, 107 (2003) 9.
[56] A. C. T. van Duin, V. S. Bryantsev, M. S. Diallo, W. A. Goddard, O. Rahaman, D. J. Doren, D. Raymand, K. Hermansson, Development and validation of a ReaxFF Reactive Force Field for Cu cation/water interactions and copper metal/metal oxide/metal hydroxide condensed phases, The Journal of Physical Chemistry A, 114 (2010) 8.
[57] O. Assowe, O. Politano, V. Vignal, P. Arnoux, B. Diawara, O. Verners, A.C.T.v. Duin, Reactive molecular dynamics of the initial oxidation stages of Ni(111) in pure water: effect of an applied electric field, The Journal of Physical Chemistry A, 116 (2012) 10.
[58] B. Jeon, Q. V. Overmeere, A.C.T.v. Duin, S. Ramanathan, Nanoscale oxidation and complex oxide growth on single crystal iron surfaces and external electric field effects, Physical Chemistry Chemical Physics, 15 (2013) 10.
[59] T. P. Senftle, S. Hong, M. M. Islam, S. B. Kylasa, Y. Zheng, Y. K. Shin, C. Junkermeier, R. Engel-Herbert, M. J. Janik, H. M. Aktulga, T. Verstraelen, A. Grama, A.C.T.v. Duin, The ReaxFF reactive force-field: development, applications and future directions, npj Computational Materials, 2 (2016) 14.
[60] G.M. Psofogiannakis, J.F. McCleerey, E. Jaramillo, A.C.T.v. Duin, ReaxFF reactive molecular dynamics simulation of the hydration of Cu-SSZ-13 zeolite and the formation of Cu dimers, The Journal of Physical Chemistry C, 119 (2015) 9.
[61] O. Verners, A.C.T.v. Duin, Comparative molecular dynamics study of fcc-Ni nanoplate stress corrosion in water, Surface Science, 633 (2015) 8.
[62] C. Zou, Y. K. Shin, A. C.T. van Duin, H. Fangb, Z.K. Liu, Molecular dynamics simulations of the effects of vacancies on nickel self-diffusion, oxygen diffusion and oxidation initiation in nickel, using the ReaxFF reactive force field, Acta Materialia, 83 (2015) 11.
[63] B. Jeon, Q.v. Overmeere, A.C.T.v. Duin, S. Ramanathan, Nanoscale oxidation and complex oxide growth on single crystal iron surfaces and external electric field effects, Physical Chemistry Chemical Physics, 15 (2013) 10.
[64] M. Aryanpour, A. C. T. van Duin, J.D. Kubicki, Development of a reactive force field for iron-oxyhydroxide systems, The Journal of Physical Chemistry A, 114 (2010) 10.
[65] S. Nose, A molecular dynamics method for simulations in the canonical ensemble, Molecular Physics, 52 (1984) 14.
[66] W.G. Hoover, Canonical dynamics: Equilibrium phase-space distributions, Physical Review A, 31 (1985) 3.
[67] M.P. Allen, D.J. Tildesley, Computer simulation of liquids, Clarendon Press, Oxford, (1987).
[68] R.C. Dunbar, Deriving the Maxwell distribution, Journal of Chemical Education, 59 (1982) 2.
[69] G.D. Peckham, I.J. McNaught, Applications of Maxwell-Boltzmann distribution diagrams, Journal of Chemical Education, 69 (1992) 5.
[70] A. Poursaee, C.M. Hansson, Reinforcing steel passivation in mortar and ore solution Cement Concrete Res, 37 (2007) 7.
[71] O. Stern, The theory of the electrolytic double layer, Zeitschrift für Elektrochemie und Angewandte Physikalische Chemie, 30 (1924) 9.

[72] H. DorMohammadi, Q. Pang, L. Árnadóttir, O.B. Isgor, Investigation of the applicability of classical electrical double layer models to study corrosion and passivity of iron in neutral and alkaline media, J Electrochem Soc, To be submitted (2018).
[73] P. Ghods, Multi-Scale investigation of the formation and breakdown of passive films on carbon steel rebar in concrete, (20010).
[74] N. Fairely, CasaXPS Manual 2.3. 15, Casa Softw. Ltd., http://scholar.google.com/scholar?hl=en&btnG=Search&q=intitle:CasaXPS+Manual+2.3.15#2, (2009) 177.
[75] P. van der Heide, X-Ray photoelectron spectroscopy: an introduction to principles and practices, John Wiley & Sons, Inc, (2011).

# Manuscript 4

## Chloride-induced depassivation of iron in alkaline media

Hossein DorMohammadi, Qin Pang, Pratik Murkute, Líney Árnadóttir, O. Burkan Isgor

To be submitted to: *Nature Materials*

## 5. Manuscript 4

# Chloride-induced depassivation of iron in alkaline media

Hossein DorMohammadi[1], Qin Pang[2], Pratik Murkute[3], Liney Arnadottir[2], O. Burkan Isgor[1]

**Abstract:**

Chloride-induced depasivation of iron in pH 13.5 NaOH solution was studied using reactive force field molecular dynamics (ReaxFF-MD), electrochemical tests and x-ray photoelectron spectroscopy (XPS). The breakdown of the passive film by chlorides initiates with iron dissolution from the first layer of the passive film into the electrolyte. Iron dissolution and corresponding iron vacancy formation in the first layer of the passive film take place in four stages that involves local acidification of the electrolyte adjacent to the metal surface, followed by iron dissolution into the electrolyte in the form of $Fe(OH)Cl_2$ and $FeCl_3$. Chloride in the electrolyte mainly acts as a catalyst and do not penetrate into the passive film. The four-step process for the initiation of the passive film breakdown was used to explain the concept of a critical chloride threshold and the well-documented electrochemical observation that critical chloride thresholds are higher in solution with solution with higher pH. The ReaxFF-MD simulations support the depassivation hypothesis that is described by the point defect model. Both ReaxFF-MD simulations and XPS analysis showed that chlorides increase the $Fe^{+3}/Fe^{+2}$ of the passive film, and this increase is more evident in the inner and middle layers of the film.

**Keywords:** Chloride-induced depassivation, Iron passivity, alkaline electrolyte, Molecular Dynamics (MD), Reactive Force Field (ReaxFF), X-ray photoelectron spectroscopy (XPS)

---

[1] Oregon State University, School of Civil and Construction Engineering, Corvallis, Oregon, USA
[2] Oregon State University, School of Chemical, Biological and Environmental Engineering, Corvallis, Oregon, USA
[3] Oregon State University, Materials Science Program, Mechanical, Industrial and Manufacturing Engineering, Corvallis, Oregon, USA

## 5.1. Introduction

Steel corrosion is the most common and costly deterioration mechanism of reinforced concrete structures [1-6]. Within the highly alkaline environment provided by concrete (pH > 13), steel is covered with a protective oxide film, so-called the passive film, such that the rate of metal loss is not significant. However, in the presence of deteriorative species such as chlorides, which can get into concrete as part of deicing chemicals or marine salts, steel can lose its passive film. The breakdown of passivity, also called depassivation, can lead to higher rates of metal loss (active corrosion) and concerns for the structural integrity of reinforced concrete elements [7-10].

The passivity and chloride-induced depassivation of iron and carbon steel in the highly alkaline environment provided by concrete pore solutions have been studied extensively using electrochemical techniques [11-14]. These techniques provide valuable information about the average electrochemical behavior of relatively large metal surfaces, typically in centimeter-square scale or larger. However, passive films that form on carbon steel and iron in alkaline environments are typically 5-15-nm thick [15-17]; therefore, a deeper understanding of passivity can only be obtained through techniques that can characterize them in nanometer scale.

In recent years, researchers have used nano-scale surface characterization techniques to provide data on the structure of the passive films of iron that form in highly alkaline media and their chloride-induced breakdown [15-21]. These studies typically show that the passive films of iron in highly alkaline electrolytes consist of $Fe^{+2}$-rich inner oxide layers and $Fe^{3+}$-rich outer oxide layers. This multi-layer film structure is in agreement with theoretical passivity models that suggest that an inner barrier layer forms directly on the metal substrate, and the outer layer precipitates via the hydrolysis of cations ejected from the inner layer [15-17]. Some of these studies also show that chlorides alter the passive film stoichiometry such that near the metal/film interface the ratio of $Fe^{3+}$ to $Fe^{2+}$ increases.

Even though these nano-scale surface characterizations studies provide valuable information about passive films that form on carbon steel and iron in alkaline electrolytes, and their chloride-induced depassivation, they cannot explain the dynamic processes that lead to their formation as they can only provide snapshot data. Specifically, we still do not fully understand how chlorides initiate the depassivation process, and how they are involved in passive film breakdown. Some of the

depassivation models claim that chlorides penetrate into the passive film through ion exchange processes or simple diffusion [22-24]. However, other models hypothesize that chlorides only act as a catalyst in the formation of iron vacancies that eventually lead to the breakdown of the passive film [25]. Similarly, we know from electrochemical studies that sufficient concentrations of chloride ions should be present at the metal/electrolyte interface to initiate the depassivation process; however, we do not know exactly why this "critical chloride threshold" exists. We also do not have a strong explanation on the concept of "induction time," which is the delay in the breakdown of the passive film even after chloride concentration near the metal surface exceed critical thresholds. The absence of well-supported answers to these fundamental questions hinders the development of new corrosion mitigation strategies such as customized corrosion inhibitors and inexpensive corrosion-resistant steels.

Atomistic modeling techniques, such as Reactive Force Field Molecular Dynamics (ReaxFF-MD) [26-35] and Density Functional Theory (DFT) [36-41], have shown great potential to provide answers to such questions. In particular, ReaxFF-MD has emerged as a simulation framework to investigate reactive processes in relatively large spatial scales that can be correlated to physical systems. In this paper, we use ReaxFF-MD to answer fundamental questions on chloride-induced depassivation of iron in alkaline media. The simulations were supported with electrochemical tests and x-ray photoelectron spectroscopy (XPS) studies.

## 5.2. Methods

### 5.2.1. ReaxFF-MD simulations

ReaxFF-MD simulations were performed using the Large-scale Atomistic/Molecular Massively Parallel Simulator (LAMMPS) framework [42] and the Extreme Science and Engineering Discovery Environment (XSEDE) [43]. The ReaxFF framework was based on the interatomic potential theory developed by van Duin et al. [44]. The detailed explanation of the framework is provided by van Duin et al. [29, 45-54]. The specific ReaxFF parameters for iron and other interacting species (e.g., Na, O, H, Cl) were obtained from the works of Aryanpour et al. [49], Rahaman et al. [55] and Psofogiannakis et al. [50], who developed and used parameters to model

iron-oxyhydroxide systems, chloride-water and copper chloride-water systems, and hydration of zeolite, respectively. We validated these parameters (that are required for determining the bond order, bond energy, valence angle energy, torsional angle energy, and van der Waals energy) by comparing ReaxFF-MD simulations of the surface formation energy and water adsorption energy on the Fe(110) surface with DFT calculations [56].

All ReaxFF-MD simulations were performed at room temperature (300K) under standard atmospheric pressure (1 atm). The initial distance between molecules and ions in the electrolyte and the dimensions of the vacuum slab were determined based on the density of the solution 300 K and 1 atm. Nose-Hoover thermostat [57, 58] was employed to maintain the prescribed system temperature for canonical (NVT) ensemble. The Velocity-Verlet time stepping scheme [59] was used with an integration time step of 0.1 fs. The Maxwell-Boltzmann distribution [60, 61] was chosen to set the initial velocities and an energy-minimization was performed at the beginning of the simulation. The center of the mass of the system was fixed during the simulation to neglect any translational movements.

### 5.2.2. Specimen preparation for XPS scans and electrochemical tests

The electrochemical tests and XPS scans were performed on circular discs (Ø = 15 mm, thickness = 2 mm) of 99.95% pure iron. Both sides of the discs were polished to 2000 grade silicon carbide paper followed by cloth polishing with 0.3μm and 0.05 μm alumina suspension in anhydrous isopropyl alcohol (water content: <0.05% weight). Anhydrous Isopropyl alcohol suspension was used in place of water suspension to minimize surface oxidation during the polishing process. After surface preparation, iron specimens were ultrasonically cleaned, dried and stored in an anaerobic nitrogen chamber to minimize surface oxidation.

Three specimens were placed in three-electrode electrochemical cells containing the passivating solution for electrochemical testing. For XPS testing additional 6 specimens were placed in a container with the passivating solution. A NaOH solution with a pH of 13.5 was used as the passivating solution for both XPS and electrochemical test specimens. The solution was prepared by dissolving 0.316M NaOH (analytical grade 99.99%) in 1 L of deionized water. The XPS

specimens were exposed to passivating NaOH solution in an anaerobic nitrogen chamber to minimize the carbonation of high pH solution. The pH of the solution was continually monitored and was maintained at around 13.5 for the entire duration of the passivation period.

Three specimens that were separately tested in the electrochemical cells were exposed to the passivating solution for 2 weeks. Two XPS specimens were taken out of the solution at 2 weeks exposure period. The 2-week-long passivation time was chosen to guarantee full passivation under open circuit conditions as confirmed by the electrochemical tests. After full passivation, chloride concentration of the electrolyte in the electrochemical cells and in the container with the XPS specimens was increased incrementally using 99.99% analytical grade NaCl addition. In electrochemical tests, the chloride increments ranged from 0.01M to 2.5M NaCl. However, based on electrochemical test results, the chloride increments for XPS - specimens were 1M and 2.5M NaCl, so that they cover ranges both below, and beyond critical chloride threshold. Two specimens were removed from the solution after 24 hours of each chloride increment, for XPS tests.

All XPS specimens that were removed from exposure solutions were rinsed with anhydrous isopropyl alcohol, dried in nitrogen chamber, and kept in nitrogen filled desiccator. Although the specimens were prepared and handled with minimum exposure to air and moisture until XPS investigation, they were briefly exposed to air during transfer to the nitrogen chamber. As a result, a thin film of air-formed iron oxide was likely to be present on the specimens before they were immersed in the test solution.

### 5.2.3. Electrochemical tests

Repeated cycles of open circuit potential (OCP) and electrochemical impedance spectroscopy (EIS) measurements were performed on the specimens placed in the three-electrode cells during passivation period and the following period during which chlorides are incrementally added. All the electrochemical tests were performed using a Gamry 3000 Reference potentiostat and frequency response analyzer. Graphite counter electrode and saturated calomel reference electrode (SCE) were used. For 2 weeks exposure, in each cycle, OCP was monitored for two hours, followed by an EIS scan. The frequency scan range for EIS measurements was 50000-0.001 Hz

during the passivation period and 50000-0.01 Hz during chloride additions, 10 points per decade. The amplitude of the AC voltage was 5 mV rms.

### 5.2.4. XPS scans

All the specimens were analyzed in angle-resolved XPS within a few hours of taking out of the solution. Specimens were mounted on the specimen holder and subsequently transferred directly to the fore-chamber of the XPS spectrometer and purged with dry nitrogen gas. This chamber was evacuated to $\sim 10^{-6}$ Pa before the specimens were transferred to the analytical chamber for examination. The analytical chamber was an ultra-high vacuum (UHV) chamber with a vacuum of $10^{-9}$ Pa. The specimens were analyzed using the Physical Electronics PHI 5600 ESCA system equipped with a monochromatic Al X-ray source (X-ray photon characteristic energy, $h\nu$ = 1486.6 eV). The X-ray gun was operated at 300 W (15 kV, 20 mA). The work function of the spectrometer was adjusted using ultra-pure gold metal (Au $4f_{7/2}$ = 84.0 eV), and the instrument linearity was set to yield a difference of 857.5 eV between the Cu $2p_{3/2}$ and Cu 3p photoelectron lines. The data were collected using a spherical capacitor analyzer (SCA) equipped with a seven-element "Omni-Focus V" lens. The angle between the analyzer and the X-ray source was 90°. The neutralizing electron gun was not used for analysis since no evidence of surface charging, or charge build-up was observed.

The XPS scans consisted of a survey scan to identify all the species present, followed by high resolutions scans of the species of interest. Survey scans were performed using an energy range of 1440 eV, analyzer pass energy of 187.85 eV, the step size of 1.6 eV. High-resolution scans were performed using an analyzer pass energy of 23.5 eV with a step size of 0.1 eV. High-resolution analyses were calibrated to C 1s (hydrocarbon) signal of 285.0 eV. The high-energy resolution spectra were collected for elements assigned in the survey spectra: oxygen (O 1s), carbon (C 1s), iron (Fe 2p), chlorine (Cl 2p) and sodium (Na 1s). The survey scans and high-resolution scans were performed at an emission angle ($\theta$) of 5°, 25°, 45°, 65° and 85° which correspond to oxide film depth of 8.4 nm, 7.7 nm, 6 nm, 3.6 nm, and 0.7 nm respectively. The higher the emission angle, the shallower the oxide film depth being analyzed, and hence all the XPS results would be presented in terms of passive oxide film depth.

### 5.2.5. XPS data analysis

The XPS data curve fitting and analysis was done using CasaXPS (V 2.3.18PR1.0) data processing software. The XPS data was semi-quantitatively analyzed using the areas under curve fitted (de-convoluted) spectra, and sensitivity factors provided by CasaXPS's Scofield element library. High-resolution XPS spectra were curve fitted and deconvoluted to quantify the contribution of each chemical species (element associations) that comprise the spectra. Curve fitting required various constraints to be met simultaneously [16, 17, 62, 63]. Shirley background correction procedures and Gaussian (70%)-Lorentzian (30%) function were used for curve fitting procedures of high-resolution spectra. All high-resolution XPS spectra envelopes were smoothed by SG Quadratic method with smoothing width parameter of 21 [63]. All spectra were curve fitted to the minimum number of peaks required for an optimum fit and needed for corresponding chemical assignments using Casa-XPS data library (ver. 2.3.18) [63]. The details procedure for the curve fitting process is provided in other references [63, 64].

Accurate determination of the atomic structure of the oxide film could not be based on the variations of the sodium, chloride, carbon and oxygen spectra since these elements are also present in the precipitates from the NaOH and NaCl solutions on the specimen surface. Despite the best cleaning practices, complete removal of precipitates is not ensured, as the harsh cleaning procedures might damage the oxide film. Since iron is not incorporated into the precipitates, only Fe 2p XPS spectra were used in the analysis of the characteristics of oxide films.

The Fe 2p XPS spectrum is composed of a doublet structure (2 peaks). The doublet structure is due to multiplets splitting (i.e., Fe $2p_{3/2}$ and Fe $2p_{1/2)}$. Based on the average of the binding energies reported for each compound in the literature[8,12,13], iron compounds of the passive film in this study can be classified into three groups as Fe-metal, $Fe^{2+}$, $Fe^{3+}$. Furthermore, an additional component $Fe^{3+}$ satellite was used in curve fitting analysis of Fe 2p, as suggested in other studies [8,14–16]. Although it is possible to obtain much better curve fitting when additional peaks are used, but their presence is improbable in the case of pure iron passivating in [35]. The accurate identification of these peaks is quite challenging due to the proximity of peak positions; therefore,

only the reported peaks were used in the analysis and the iron 2p spectra were fitted to four iron components. The peak parameters of each component are presented in another reference [17].

Assuming a uniform oxide film formation on the iron substrate, the film thickness was calculated from the oxide to metal intensity ratios at an emission angle of 5°. Using the procedure described in Ghods et al. [9] the oxide film thickness was calculated. Accordingly, the thickness of iron oxide film can be calculated using [7]:

$$d_{ox} = \lambda_{ox}^{Fe} \cos\theta \ln\left(1 + \frac{I_{ox}^{Fe}}{I_{m}^{Fe}} * \frac{N_{m}^{Fe}}{N_{ox}^{Fe}} * \frac{\lambda_{m}^{Fe}}{\lambda_{ox}^{Fe}}\right) \quad (5\text{-}1)$$

where $d_{ox}$ (nm) is the thickness of iron oxide; $I_{ox}^{Fe}$ and $I_{m}^{Fe}$ are, respectively, the intensities of the total iron oxides and the metallic iron obtained from Fe 2p spectra; $N_{m}^{Fe}$ and $N_{ox}^{Fe}$ are average atomic densities of iron oxides and metallic iron, respectively; and $\lambda_{ox}^{Fe}$and $\lambda_{m}^{Fe}$ (nm) are attenuation lengths of iron oxide and metallic iron [7].

### 5.3. Analysis, results, and discussion

First, we needed to create a passive film as the starting domain for the chloride-induced depassivation simulations. We used ReaxFF-MD to create such a film. The simulated system involved a Fe(110) structure (24.61Å x 20.40Å x 22.87Å) containing 1080 Fe iron atoms, which is exposed to a 3.16 M NaOH solution (pH ~ 13.5), containing 21 Na and OH ions and 348 water molecules. The Na and OH ions were distributed in the electrolyte in groups of three in equally spaced seven layers in the longitudinal z direction to maintain the pH relatively stable in all parts of the electrolyte. Fe(110) surface orientation was chosen because it has a more closely packed surface than Fe(100) and Fe(111) structures, and previous studies have shown that different surface orientations do not affect the oxidation behavior of iron significantly [56, 65-70]. Periodic boundary conditions were applied along cross-sectional plane of the iron domain, while fixed boundary condition was imposed along the longitudinal direction. A reflecting wall was applied at the end of the solution domain in order to confine the molecules in the solution phase and avoid the reaction of the solution with the surface below the sample. The simulations were run under an external electric potential for 500 ps. The external potential was necessary to overcome the

challenge s associated with long passivation times of iron in alkaline media under open circuit conditions [15, 71, 72]. The electrical double layer (EDL) between the metal surface and the electrolyte was modeled using the Stern model [73] which involved a 3 Å-thick Helmholtz layer, and a diffuse layer where the ions are mobile and spread out in the electrolyte. The electric potential of at the iron surface was set as 30 MeV/cm.

Figure 5-1(a) shows the created passive film at the beginning of the ReaxFF-MD simulations in the electrolyte containing chloride ions. As shown in Figure 5-1(b), passive film after 500 ps of simulations was about 12 Å and involved six layers of iron atoms. The charge of iron atoms in each layer showed a high degree of variability, indicating that each layer contained various iron oxide structures. However, we also observe that overall charge of iron atoms in each layer decrease from the metal/electrolyte interface to the metal/film interface. We divided the passive film into three zones (inner, middle and outer layers), each containing two iron layers, in order to analyze their oxide structures. Fe-O pair distribution functions (PDF) of each layer are plotted in Figure 5-1(c), which also shows the dominant peak and transition points of PDFs of reference oxides (i.e., FeO, $Fe_3O_4$, and $Fe_2O_3$) for comparison purposes [48]. The PDF of the outer layer shows its dominant peak at 1.69 Å and has a distinct transition at 2.17 Å, which match the reference signature for $Fe_2O_3$. The PDF of the middle layer has a dominant peak at 1.98 Å and a slight transition point at 1.6Å, which are very close to the corresponding locations for $Fe_3O_4$. Finally, the PDF of the inner layer has a dominant peak location at 1.63 Å, which coincides with the dominant peak of FeO. In summary, the Fe-O PDF for the three oxide layers illustrate that the outer, middle and inner layers have oxides structures similar to those for $Fe_2O_3$, $Fe_3O_4$, and FeO, respectively.

These observations are in agreement with existing experimental data, which indicate that passive films of iron in highly alkaline electrolytes consist of $Fe^{+2}$-rich inner oxide layers and $Fe^{3+}$-rich outer oxide layers. Similar supporting evidence was obtained in our XPS investigation which was performed on the passive film that was grown on 99.95% pure iron exposed to pH 13.5 NaOH solution for two weeks under open circuit conditions. As shown in Figure 5-1(d), the ratio of $Fe^{3+}$ to $Fe^{2+}$ decreases from the film/electrolyte interface toward the metal/film interface. Furthermore, $Fe_2O_3$ fraction decreases, and FeO + $Fe_3O_4$ fractions increase toward the inner layers of the passive film. Since the XPS data are shown in Figure 5-1(d) were obtained from passive films that were

grown in the passivating solution for two weeks, they are thicker and more mixed than the film obtained from ReaxFF-MD. However, the overall comparison indicates that the passive film that is produced in the ReaxFF-MD simulations is a realistic starting structure to investigate the processes associated with chloride-induced depassivation.

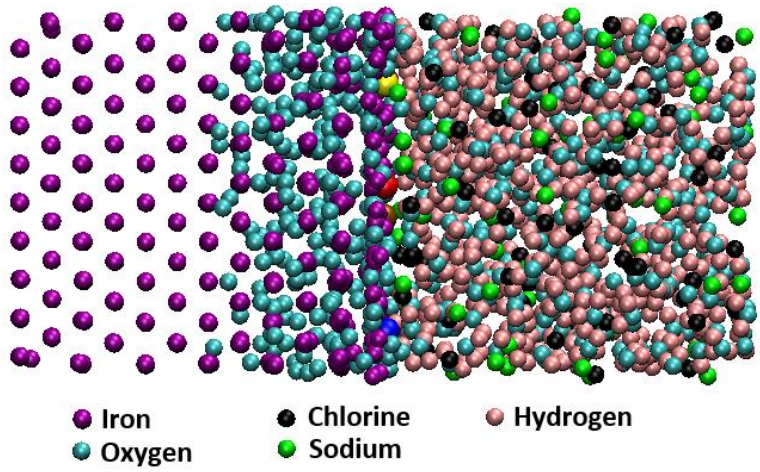


(a)

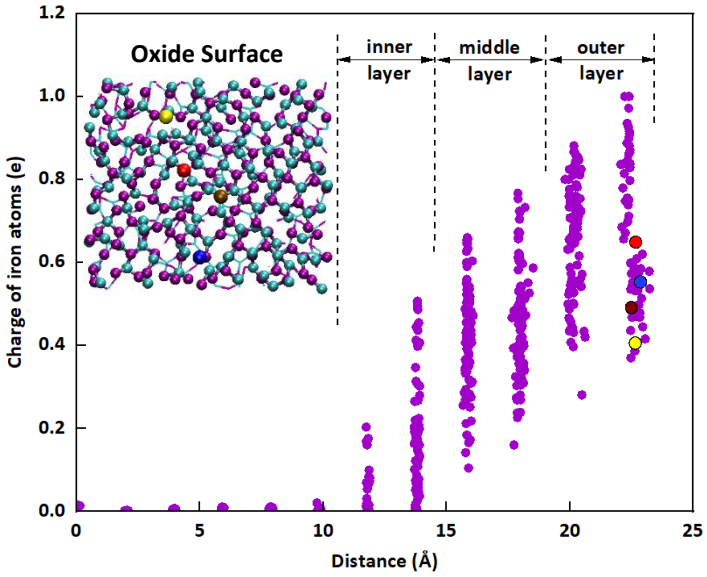


(b)

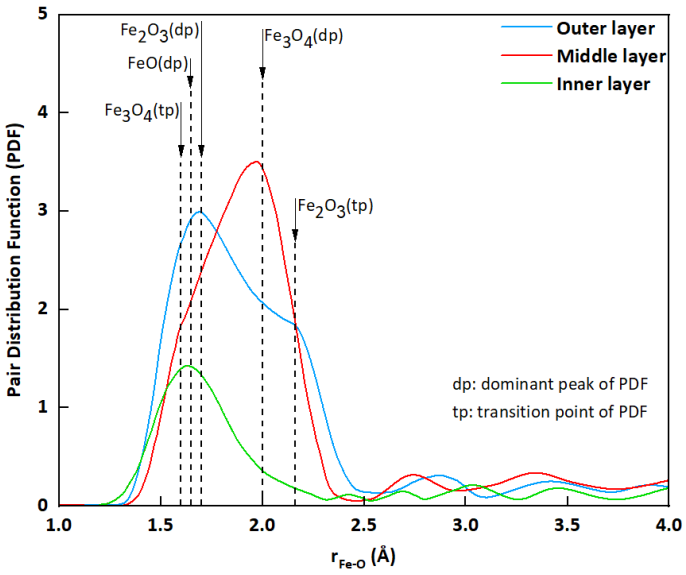


(c)

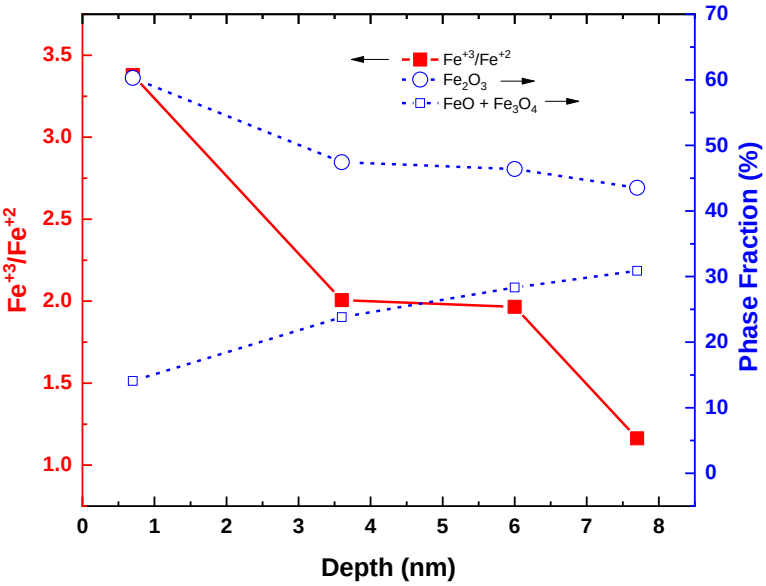


(d)

**Figure 5- 1:** (a) Starting configuration of simulations indicating the passive film and the electrolyte. (b) Charge distribution of iron atoms in the metal; the charges that are shown in this figure represent the charges of individual atoms as part of the crystal structure, not for a single oxide molecule. (c) Pair distribution function (PDF) of the inner and outer layers of the passive film. (d) XPS data on the oxides in the passive film; iron metal and other minor oxides and satellite phases are not shown for clarity. Yellow, red, brown, and blue atoms in figures (a) and (b) are iron atoms that are discussed in detail in Fig. 2.

The passive film that is generated after 500 ps of ReaxFF-MD simulations in pH 13.5 NaOH solution was used as the starting domain for the depassivation simulations. The electrolyte domain size was 24.46Å x 21.46Å x 21.59Å and three different NaCl concentrations were studied: 2 M (293 $H_2O$, 14 NaCl), 5 M (232 $H_2O$, 34 NaCl), and 10 M (147 $H_2O$, 68 NaCl). The simulations were performed for 2000 ps. An electric field using the Stern model was applied on the oxide-solution during the simulation with the intensity of 15 MeV/cm at the oxide layer.

The breakdown of the passive film by chlorides initiates with iron dissolution from the first (outermost) layer of the passive film into the electrolyte. Iron dissolution and corresponding iron vacancy formation in the first layer of the passive film take place in four. In the first and second stages, chlorides facilitate the consumption of hydroxide ions in the electrolyte by the iron surface to form of $Fe(OH)_3$ and $Fe(OH)_2Cl$, respectively, which do not dissociate into the electrolyte but remain on the metal surface. These two processes cause local acidification, and eventual depletion of OH, in the electrolyte adjacent to the metal surface. The following third and fourth stages lead to the dissolution of iron into the electrolyte in the form of $Fe(OH)Cl_2$ and $FeCl_3$, respectively. Chloride in these compounds return to water; therefore, it can be stated that chloride in the electrolyte mainly acts as a catalyst in the depassivation process. We explain these four stages in Figure 2 with reference to four different iron atoms on the metal surface; each atom is used to demonstrate one stage. These atoms are shown in yellow (Stage 1), brown (Stage 2), blue (Stage 3) and red (Stage 4) in Figure 5-1(a) and 5-1(b) as part of the first layer of the passive film.

**Stage 1 – Formation of $Fe(OH)_3$:** Chloride ions in the electrolyte come in contact with the iron atoms with low electrical charges in the first layer of the passive film. Such an iron atom (shown in yellow), with a charge of 0.4e, and its interactions with three chloride ions are shown in Figure 5-2(a). As the solution is highly alkaline, hydroxide ions are present around the chlorides. The chloride ions approach the iron atom in a trigonal pyramidal configuration (4.6 ps). The chlorides pull the iron atom out by 0.55Å from position A to position B (6.5 ps). At its disturbed position, the iron atom prefers to bond with hydroxides to form $Fe(OH)_3$ (8.7 ps). $Fe(OH)_3$ stays on the surface and does not dissociate in the solution, while chloride ions return to the electrolyte (14.0 ps). This process results in the removal of three hydroxide ions from the electrolyte for each iron atom. Multiple processes like this, as shown in Figure 5-3(a), lead to the reduction of hydroxide ion concentration near the metal-electrolyte interface.

**Stage 2 – Formation of $Fe(OH)_2Cl$:** Chloride ions in the electrolyte come in contact with the iron atoms with low electrical charges in the first layer of the passive film. Such an iron atom (shown in brown), with a charge of 0.49e, and its interactions with three chloride ions are shown in Figure 5-2(b). Because of the formation of $Fe(OH)_3$ as a result of processes described in Stage 1, there are only two hydroxide ions around the chlorides. The chloride ions approach the iron atom in a trigonal pyramidal configuration (20.2 ps). The chlorides pull the iron atom out by 0.54Å from position A to position B (22.3 ps). At its disturbed position, one chloride and two hydroxides bond with the iron atom to $Fe(OH)_2Cl$ (24.3 ps). $Fe(OH)_2Cl$ stays on the surface and does not dissociate in the solution, while other two chloride ions return to the electrolyte (29.0 ps). This process results in the additional removal of two hydroxide ions from the electrolyte for each iron atom. Multiple processes like this, as shown in Figure 5-3(a), lead to further reduction of hydroxide in the ion concentration near the metal-electrolyte interface, and the depletion of hydroxide ions around some of the iron atoms on the metal surface.

**Stage 3 – Formation of $Fe(OH)Cl_2$:** Figure 5-2(c) shows an iron atom (shown in blue) which is exposed to a locally acidified electrolyte due to repeated processes described in Stages 1 and 2. Three chloride ions approach the iron atom in a trigonal pyramidal configuration (23.0 ps). The chlorides pull the iron atom out by 0.53 Å from position A to position B (25.2 ps). At its disturbed position, two chloride and one hydroxide ions bond with the iron atom to $Fe(OH)Cl_2$ (27.1 ps). $Fe(OH)Cl_2$ dissociates from the surface, and the one chloride ion returns to the electrolyte (29.0 ps). This is the first form of iron dissolution from the passive film. $Fe(OH)Cl_2$ is an intermediate phase that typically reverts to $Fe(OH)_3$ in water with the release of chloride and hydrogen ions, causing further acidification of the electrolyte [74].

**Stage 4 – Formation of $FeCl_3$:** Figure 5-2(d) shows an iron atom (shown in red) which is exposed to a locally acidified electrolyte due to repeated processes described in Stages 1-3. Three chloride ions approach the iron atom in a trigonal pyramidal configuration (28.6 ps). There are no hydroxide ions in this local zone. The chlorides pull the iron atom out by 0.52 Å from position A to position B (31.0 ps). At its disturbed position, three chloride ions bond with the iron atom to $FeCl_3$ (32.7 ps). $FeCl_3$ dissociates into the electrolyte (38.0 ps). The solubility of $FeCl_3$ is high (912 g/L at 25$^o$C); therefore, chloride ions return to the electrolyte after iron dissolution from the passive film.

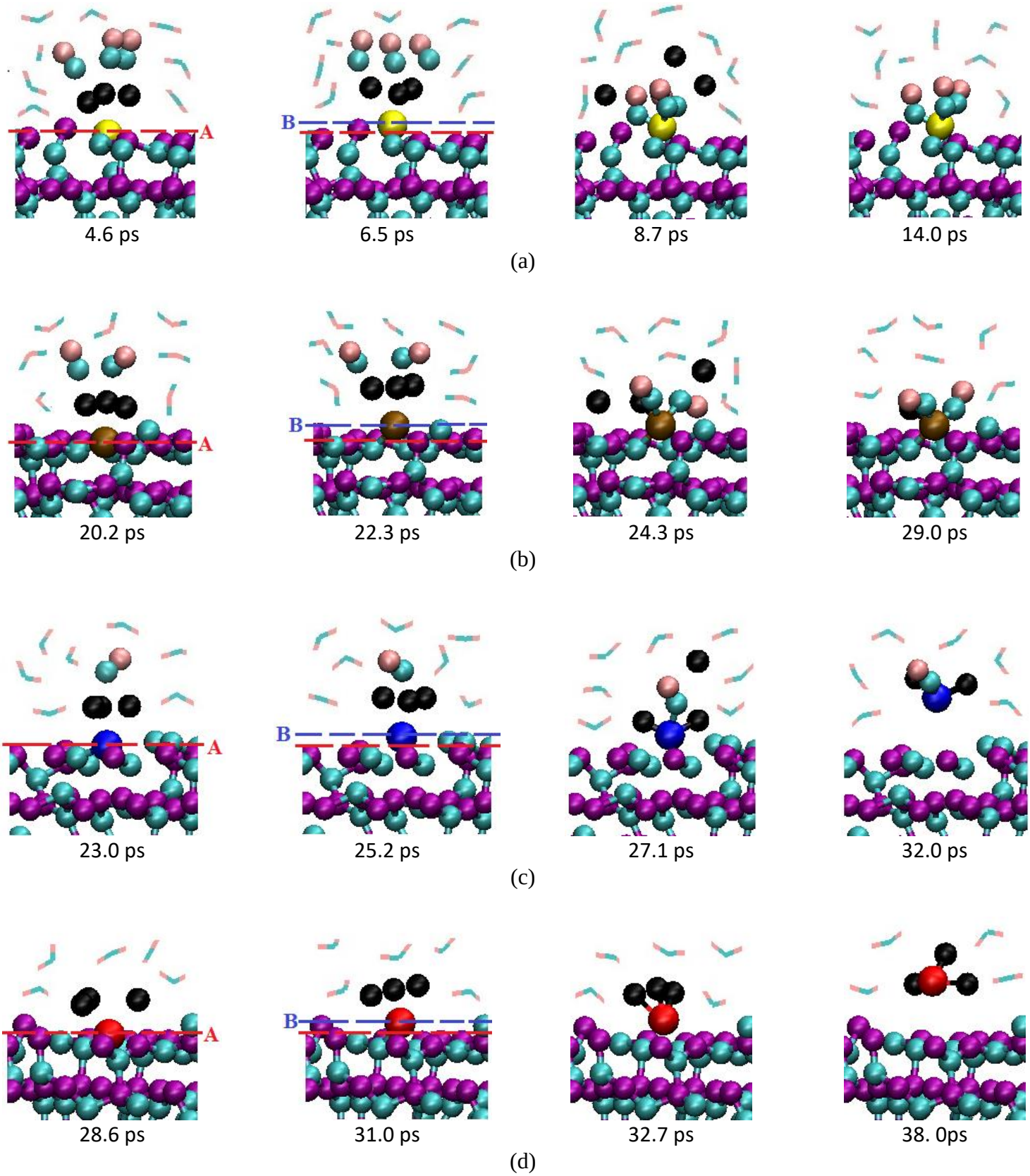


**Figure 5-2:** Different stages of interactions of chlorine atoms with the iron oxide surface: (a) Formation of $Fe(OH)_3$. (b) Formation of $Fe(OH)_2Cl$. (c) Formation of $Fe(OH)Cl_2$. (d) Formation of $FeCl_3$. The locations of the yellow, brown, blue and red iron atoms in the analysis domain are shown in Fig. 1(a) and (b).

Figure 5-3(a) illustrates the evolution of species in the analysis domain over the analysis period of 2000 ps. The four stages can be tracked for all species in this figure. One of the critical observations in this figure is that the breakdown of the passive film does not start until hydroxide ions near the metal surface are consumed sufficiently. The consumption of hydroxide is driven by the formation of four $Fe(OH)_3$ and three $Fe(OH)_2Cl$ within the first 71 ps of simulations. Note that the numbers of these species do not change throughout the simulations; they remain attached to the passive film. This ensures that electrolyte near the metal surface remains locally acidified, as shown by the stable hydroxide concentration throughout the simulations. The iron atoms that are exposed to locally acidified electrolyte dissociate from the passive film in the form of $Fe(OH)Cl_2$ and $FeCl_3$. The first $Fe(OH)Cl_2$ dissociates from the passive film after the formation of two $Fe(OH)_3$ and one $Fe(OH)_2Cl$, in other words, after removal of eight hydroxide ions from the electrolyte. First $FeCl_3$ dissociates into the electrolyte soon after that. Once iron starts to leave the passive film, chlorides play the role of a catalyst: After they are released back to the electrolyte from $Fe(OH)Cl_2$ and $FeCl_3$ come back to the iron oxide surface, and they detach another iron atom from the passive film. This process repeats to the end of the simulation. Iron ions remain in the electrolyte, and their cumulative numbers increase over time, while the number of chlorides oscillates around a constant number of about 50. The final configuration of atoms at 2000 ps, which is shown in Figure 5-3(b), clearly illustrates the dissociated iron atoms in the electrolyte and the initiation of the breakdown of the passive film.

The four-step process for the initiation of the passive film breakdown also helps explain the concept of a critical chloride threshold. It has been widely shown through electrochemical studies that chloride ion concentration in the electrolyte must exceed a certain critical threshold to initiate the breakdown of the passive film. As shown in our simulations, chlorides play the role of a catalyst and have two main functions in the depassivation process: First, they cause the local acidification of the electrolyte through the processes described in Stages 1 and 2. Second, they dissociate iron atoms that are exposed to the OH-depleted zones of the electrolyte, as depicted in Stages 3 and 4. Both roles require that there is a sufficient number of chloride ions in the electrolyte. Simulations with 2 M NaCl in the electrolyte have shown that either local acidification could not take place, a step that is required to initiate the iron dissolution into the electrolyte, or the removal of the iron atoms from the passive film surface was too slow to initiate the depassivation process of the film.

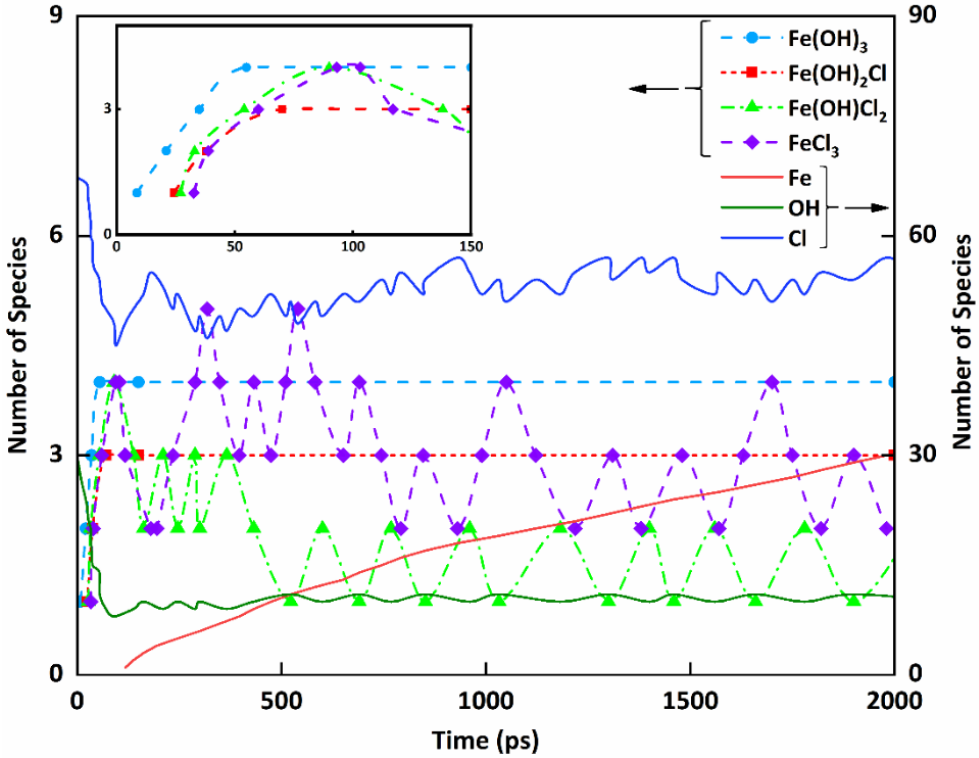


(a)

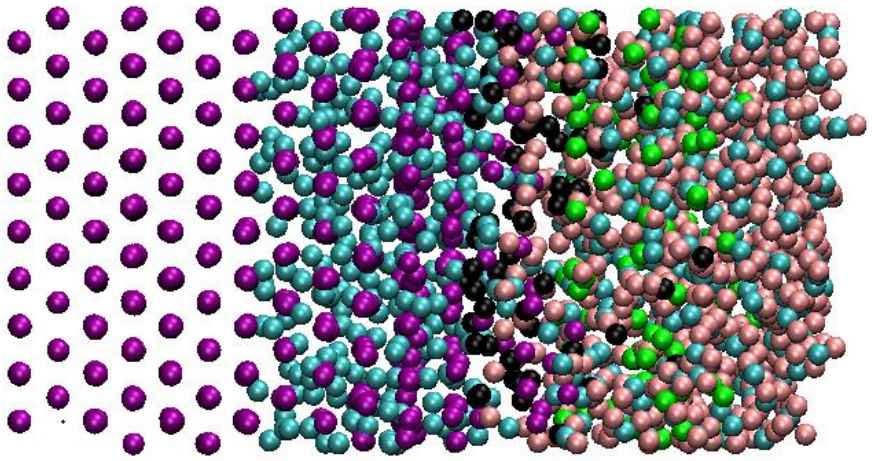

(b)

**Figure 5-3:** (a) Evolution of the species in the analysis domain over the analysis time. (b) Configuration of the atoms at 2000 ns indicating the dissolution of the iron atoms from the metal surface into the electrolyte.

On the other hand, the simulations in 5 M NaCl solution have shown similar behavior to those in 10 M NaCl solution, which eventually leads to iron dissolution into the electrolyte and iron vacancy formation. Our electrochemical tests on pure iron that is passivated in pH 13.5 NaOH solution loses its passivity when the chloride concentration in the solution reaches 2 to 2.5 M. This critical chloride threshold is in agreement with similar electrochemical tests results from the literature [75]. Therefore, our simulations are in agreement with electrochemical studies. Our results also explain a well-documented electrochemical observation that critical chloride thresholds are higher in solution with solution with higher pH [75]. This effect of pH on chloride threshold can be explained with respect to the need for local acidification of the electrolyte near the film surface. Higher pH implies there are larger number of hydroxides close to the surface, and hence, increased number of chloride ions are needed to acidify the electrolyte.

Electrochemical tests also showed that the critical chloride threshold goes up from 1.25 M to 2.5 M when passivation time increases from 1 day to 5 days. However, the critical chloride threshold remain the same (i.e., 2.5M) for 5 days and 2 weeks of passivation periods. This shows that critical chloride threshold initially increases with increasing passivation time, but eventually plateaus after a stable passive film structure is established. This behavior relates to the increasing film thickness and densification of the oxide film with passivation time and the relative resistance for ion and vacancy transfer. The XPS results showed an increase in oxide film thickness from 3.02 nm at 10 minutes passivation to 5.27 nm at full passivation.

Another point of debate in the literature has been the actual mechanism of breakdown of the passive film. Some of the proposed mechanisms for passive film breakdown hypothesize the adsorption and ingress of chlorides though the outer layers of oxides into the passive film. In these models, the penetrated chlorides cause the dissolution of the passive film from within and/or increase the iron oxidation rate of the metal substrate such that the passive film breaks down due to excessive generation of oxides. Among these models, the ion exchange model [22] suggests the penetration of chloride ions though oxide film through an ion exchange process (e.g., $Cl^-$ for lattice $O^{2-}$). The pore models [23, 24] are based on the fact that all oxide layers contain flaws and are porous in nature; therefore, chlorides can pass through the pores and reach metal/film interface to disturb passivity. Our simulations do not support the depassivation models that are based on the ingress of chlorides into the passive film. In fact, in all simulations, chlorides remained either adsorbed on the surface of the passive film or in the electrolyte and caused the generation of iron

vacancies within the first iron oxide layer. Therefore, another explanation for the eventual breakdown of the passive film is needed.

Figure 5-4, which illustrates several time steps in a single plot, tracks the movement of these iron vacancies as well as the iron and oxygen atoms within the passive film. The passive film is depicted at the end of the simulations with six distinct iron oxide layers. The process starts with the dissolution of the iron atoms with low electrical charge (typically less than 0.5e) on the first (outermost) layer of the passive film into the electrolyte. The dissolved iron atoms, shown in blue, typically have a charge of 1.0e. The vacancies that are left from the dissolved iron atoms are filled with lower charged iron atoms, shown in brown, from the second layer of the passive film. In later stages, these iron atoms dissociate into the electrolyte as well as indicated by the brown atoms with a charge of 1.0 e in the electrolyte. The vacancies left in the second layer are filled with the lower charged iron atoms from the third layer (shown in green). These chain processes lead to the movement of iron atoms from deeper layers of the passive film into the electrolyte, while the iron vacancies move in the opposite direction. Eventually, the iron vacancies reach iron/iron oxide interface. The movements of iron atoms and their vacancies are accompanied by the movement of oxygen atoms toward the metal/film interface, where additional iron atoms are oxidized as more oxygen becomes available. Meanwhile, oxygen vacancies move toward the oxide/electrolyte interface.

These processes support the depassivation hypothesis that is described by the point defect model [25], which states that when a sufficient number of iron vacancies reach the iron/iron oxide interface, they will cause the localized detachment of the oxide film. At these detached sites, iron oxidation (i.e., oxide film growth or oxygen vacancy formation) stops. As this occurs, the film begins to thin due to the continued dissolution if iron from the film/electrolyte interface. This process will continue until passive film breaks down, either due to complete dissolution or until mechanical rupture because of residual or induced stresses.

Although our simulations do not extent to full breakdown of the passive film due to long time scales which are beyond our current computational resources, they provide evidence for another electrochemical observation that is widely reported in the literature: the induction period [75]. The induction period refers to the period between the accumulation of adequate concentration of chloride ions in the electrolyte and the actual breakdown of the passive film. Several researchers

reported the induction period using electrochemical methods [76, 77]. In our simulations, we also show that the passive film remains intact during iron dissolution from the surface of the film, and iron vacancy formation and diffusion.

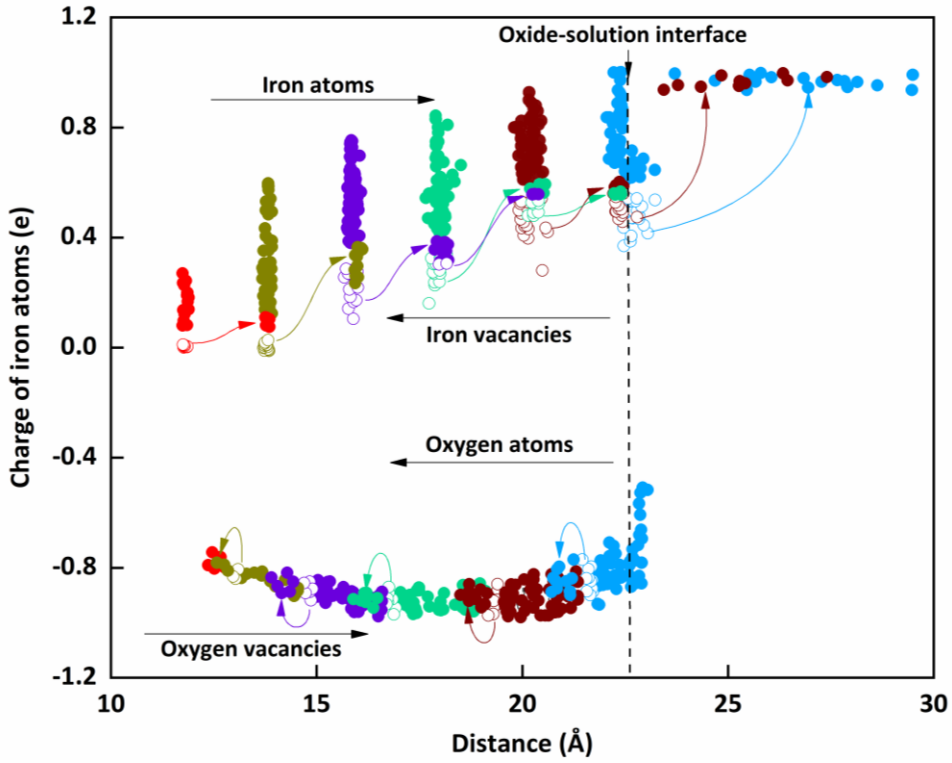


**Figure 5-4:** Changes in charge distribution of the iron and oxygen atoms as a result of iron dissolution, indicating iron vacancy formation. The figure covers diferent time steps during simulations.

Figure 5-5(a) illustrates the changes in the Fe-O PDF of the outer, middle and inner layers of the passive film after 10 M chloride exposure at 2000 ps. The solid lines represent the passive state, and the dashed lines indicate the state after chloride exposure. The reduction of the intensity of the PDFs indicates the thinning of the passive film, as predicted by the point defect method. We also observe clear shifts in the dominant peak locations of the inner and middle layers, which were originally identified as FeO and $Fe_3O_4$ in the passive state. The PDF of the middle layer after chloride exposure showed that the main peak decreased from 1.98 Å to 1.75 Å and a distinct transition point became visible around 2.17 Å. This change indicates that $Fe_3O_4$ of the middle layer was transformed to the $Fe_2O_3$ structure. For the inner layer the dominant peak increased from 1.63 Å to 1.68 Å, and a slight transition point was observed at about 2.14 Å. This is an indication that

FeO structure transforms into oxides with higher charges. The PDF pattern of the outer layer after chloride exposure was very similar to the passive state, indicating that oxide structure remained in the form of $Fe_2O_3$. Overall, it can be stated that chlorides increase the $Fe^{+3}/Fe^{+2}$ of the passive film, and this increase is more evident in the inner and middle layers of the film. As shown in Figure 5-5(b), our XPS results also confirm this conclusion such that $Fe^{+3}/Fe^{+2}$ increases significantly after 2.5 M chloride addition to the electrolyte, which has been shown to be higher than the critical chloride threshold by our electrochemical tests. $Fe^{+3}/Fe^{+2}$ does not show a significant difference between a passive state (no chloride) and 1 M chloride addition (which is below the critical chloride threshold). The XPS results also indicate that chlorides do not penetrate into the passive film, but can exist in the first layer of the passive film as demonstrated in the first two stages of the iron dissolution process. The increase in the chloride signature near the film/electrolyte interface after exposure to 2.5 M chlorides is likely due to the presence of $Fe(OH)_2Cl$ on the first layer of the passive film, as indicated by our simulations. The presence of chloride signatures in the deep layers is likely an artifact of the low XPS resolution, which picks up the chloride signal from $Fe(OH)_2Cl$ species in the first layer of the passive film. The absence of chloride signature throughout the passive film when it is exposed to 1 M chlorides indicate that, at the levels below critical chloride threshold, neither $Fe(OH)_2Cl$ forms nor chlorides penetrate into the passive film.

Furthermore, the XPS and EIS results show a decrease in the thickness of the passive film and its charge transfer resistance. It was observed that the film thickness decreased from 5.27 nm at full passivation to 4.17 nm at 2.5 M NaCl concentrations. Similarly, the charge transfer resistance decreased from $3.174 \times 10^6$ ohm.cm$^2$ at full passivation to $3.220 \times 10^4$ ohm.cm$^2$ at 2.5 M NaCl concentration. Furthermore the low frequency impedance (e.g. at 0.01 Hz) was observed to decrease by 2 orders of magnitude going from full passivation ($5.89 \times 10^5$ ohm.cm$^2$) to depassivation at 2.5 M Cl concentration (2896 ohm.cm$^2$).

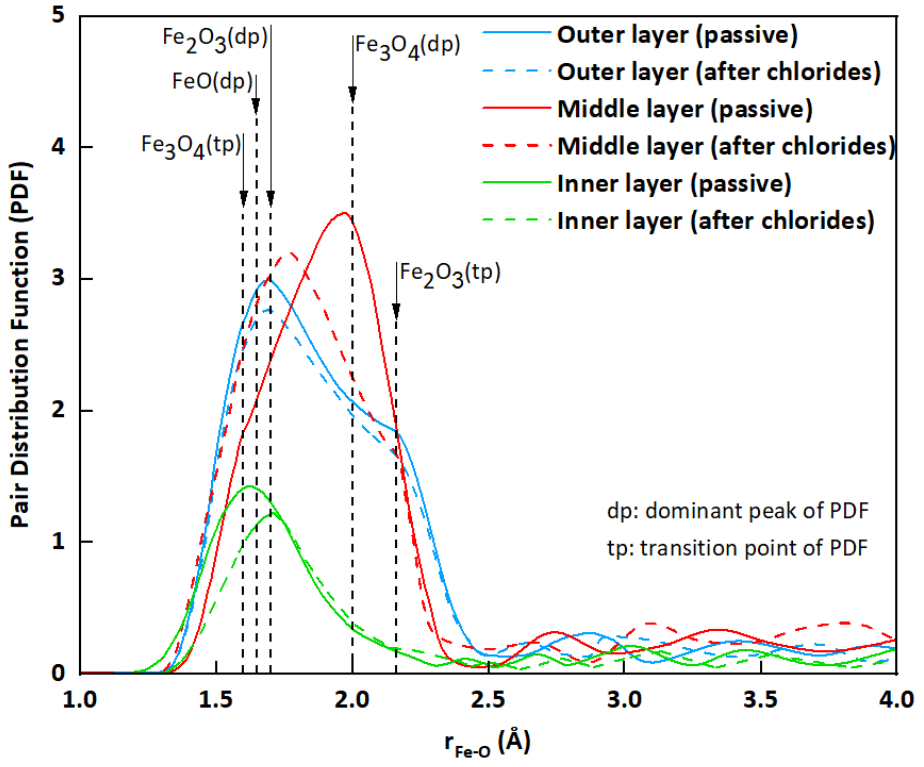


(a)

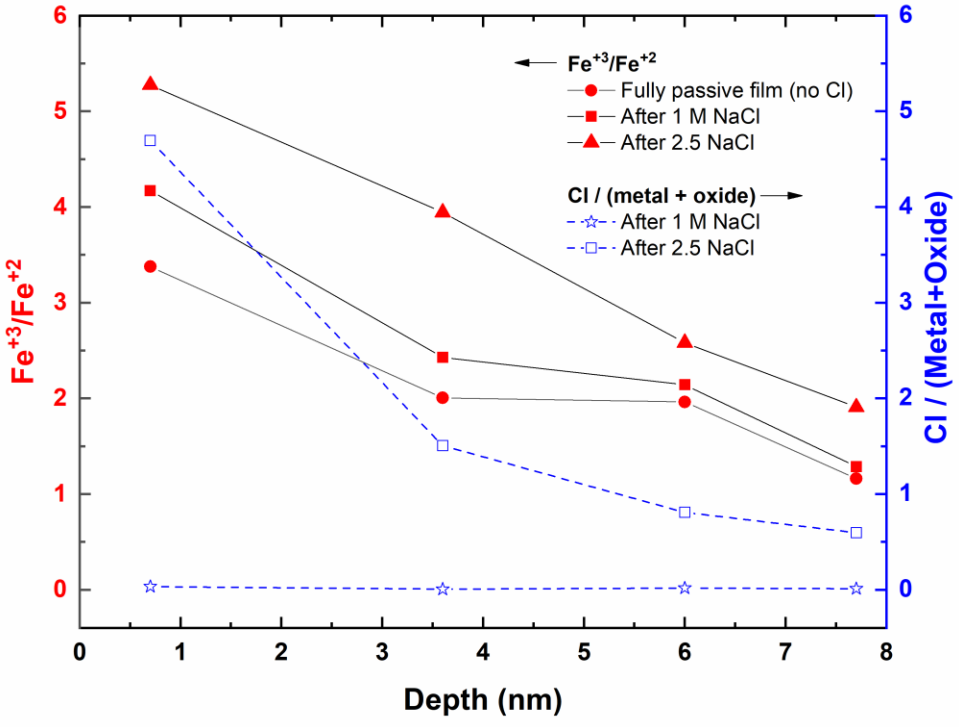


(b)

**Figure 5-5:** (a) Pair distribution function (PDF) of the inner and outer layers of the passive film after chloride exposure. (b) ) XPS data on the oxides in the passive film after chloride exposure.

## 5.4. Conclusions

In this paper, we use ReaxFF-MD to answer fundamental questions on chloride-induced depassivation of iron in alkaline media. The simulations were supported with electrochemical tests and x-ray photoelectron spectroscopy (XPS) studies. The studied passive film was created using ReaxFF-MD simulations in pH 13.5 NaOH solution and contained multiple oxide layers. The outer, middle and inner layers of the passive film had oxides structures similar to those for $Fe_2O_3$, $Fe_3O_4$, and FeO, respectively.

The breakdown of the passive film by chlorides initiates with iron dissolution from the first layer of the passive film into the electrolyte. Iron dissolution and corresponding iron vacancy formation in the first layer of the passive film take place in four stages. In the first and second stages, chlorides facilitate the consumption of hydroxide ions in the electrolyte by the iron surface to form of $Fe(OH)_3$ and $Fe(OH)_2Cl$, respectively, which do not dissociate into the electrolyte but remain on the metal surface. These two processes cause local acidification, and eventual depletion of OH, in the electrolyte adjacent to the metal surface. The following third and fourth stages lead to the dissolution of iron into the electrolyte in the form of $Fe(OH)Cl_2$ and $FeCl_3$, respectively. Chloride in these compounds return to water; therefore, it can be stated that chloride in the electrolyte mainly acts as a catalyst in the depassivation process.

The four-step process for the initiation of the passive film breakdown helps explain the concept of a critical chloride threshold. Sufficient amount of chloride ions are necessary to cause the local acidification of the electrolyte and subsequent iron dissociation that are exposed to the OH-depleted zones of the electrolyte. When chloride concentration in the electrolyte is below a threshold, these processes do not proceed, and passive film remains stable. The same reasoning also explains the well-documented electrochemical observation that critical chloride thresholds are higher in solution with higher pH. Higher pH implies there are larger number of hydroxides close to the surface, and hence, increased number of chloride ions are needed to acidify the electrolyte.

Our simulations do not support the depassivation models that are based on the ingress of chlorides into the passive film. In fact, in all simulations, chlorides remained either adsorbed on the surface of the passive film or in the electrolyte and caused the generation of iron vacancies within the first iron oxide layer. The ReaxFF-MD simulations support the depassivation hypothesis that is

described by the point defect model, which states that when a sufficient number of iron vacancies reach the iron/iron oxide interface, they will cause the localized detachment of the oxide film. At these detached sites, iron oxidation stops, and the film begins to thin due to the continued dissolution of iron from the film/electrolyte interface. XPS results also indicate that chlorides do not penetrate into the passive film, but can exist in the first layer of the passive film as demonstrated in the first two stages of the iron dissolution process.

## 5.5. Acknowledgements

This study is fully funded by the National Science Foundation, DMMI, Grant No. 1435417. Part of this work used the Extreme Science and Engineering Discovery Environment (XSEDE) Comet at the through the San Diego Supercomputer Center (SDSC) allocation TG-ENG170002. XSEDE is supported by National Science Foundation grant number ACI-1053575.

## 5.6. References

[1] L. Bertolini, B. Elsener, P. Pedeferri, R. Polder, Corrosion of Steel in Concrete: Prevention, Diagnosis, Repair, Wiley-VCH, Weinheim, 2000.
[2] H. Bohni, Corrosion in Concrete Structures CRC Press, New York, 2005.
[3] J.P. Broomfield, Corrosion of Steel in Concrete Taylor & Francis, New York, 2007.
[4] K.E. Kurtis, P.K. Mehta, A Critical Review of Deterioration of Concrete Due to Corrosion of Reinforcing Steel, ACI Special Publication, 170 (1997) 535-554.
[5] P.K. Mehta, P.J.M. Monteiro, Concrete: Microstructure, Properties, and Materials, McGraw-Hill Professional, New York, 2005.
[6] G.H. Koch, M. Brongers, P.H., N.G. Thompson, Y.P. Virmani, J.H. Payer, Corrosion Cost and Preventative Strategies in the United States, in, NACE International, 2003.
[7] L. Bertolini, B. Elsener, P. Pedeferri, R. and Polder, Corrosion of Steel in Concrete: Prevention, Diagnosis, Repair, Weinheim: Wiley-VCH, (2000).
[8] H. Bohni, Corrosion in concrete structures, New York: CRC Press, (2005).
[9] J.P. Broomfield, Corrosion of steel in concrete New York: Taylor & Francis, (2007).
[10] P.K. Mehta, P.J.M. Monteiro, Concrete: microstructure, properties, and materials, New York: McGraw-Hill Professional., (2005).
[11] P. Ghods, O.B. Isgor, G. McRae, T. Miller, The effect of concrete pore solution composition on the quality of passive oxide films on black steel reinforcement, Cement and Concrete Composites, 31 (2009) 2-11.
[12] L. Li, A.A. Sagues, Chloride corrosion threshold of reinforcing steel in alkaline solutions - Cyclic polarization behavior, Corrosion, 58 (2002) 305-316.

[13] C.M. Hansson, A. Poursaee, A. Laurent, Macrocell and microcell corrosion of steel in ordinary Portland cement and high performance concretes, Cement Concrete Res, 36 (2006) 2098-2102.
[14] U.M. Angst, B. Elsener, C.K. Larsen, O. Vennesland, Chloride induced reinforcement corrosion: Electrochemical monitoring of initiation stage and chloride threshold values, Corros Sci, 53 (2011) 1451-1464.
[15] P. Ghods, O.B. Isgor, G.J.C. Carpenter, J. Li, G.A. McRae, G.P. Gu, Nano-scale study of passive films and chloride-induced depassivation of carbon steel rebar in simulated concrete pore solutions using FIB/TEM, Cement Concrete Res, 47 (2013) 14.
[16] P. Ghods, O.B. Isgor, J. Brown, F. Bensebaa, D. Kingston, XPS depth profiling study on the passive oxide film of carbon steel in saturated calcium hydroxide solution and the effect of chloride on the film properties, Applied Surface Science, 257 (2011) 9.
[17] P. Ghods, O. Burkan Isgor, F. Bensebaa, D. Kingston, Angle-resolved XPS study of carbon steel passivity and chloride-induced depassivation in simulated concrete pore solution, Corros Sci, 58 (2012) 9.
[18] M. Sánchez-Moreno, H. Takenouti, J.J. García-Jareno, F. Vicente, C. Alonso, A theoretical approach of impedance spectroscopy during the passivation ofsteel in alkaline media, Electrochimica Acta, 54 (2009) 5.
[19] M. Sánchez, J. Gregori, C. Alonso, J.J. García-Jareño, H. Takenouti, F. Vicente, Electrochemical impedance spectroscopy for studying passive layers on steel rebars immersed in alkaline solutions simulating concrete pores, Electrochimica Acta, 52 (2007) 8.
[20] S. Joiret, M. Keddam, X.R. Novoa, M.C. Perez, C. Rangel, H. Takenouti, Use of EIS, ring-disk electrode, EQCM and Raman spectroscopy to study the film of oxides formed on iron in 1 M NaOH, Cement Concrete Comp, 24 (2002) 9.
[21] H.B. Gunay, P. Ghods, O.B. Isgor, G.J. Carpenter, X. Wu, Characterization of atomic structure of oxide films on carbon steel in simulated concrete pore solutions using EELS, Applied Surface Science, 274 (2013) 8.
[22] M.A. Heine, D.S. Keir, M.J. Pryor, Specific Effects of Chloride and Sulfate Ions on Oxide Covered Aluminum, J. Electrochem. Soc., 112 (1965) 24-&.
[23] J. Richardson, G. Wood, A study of the pitting corrosion of Al byscanning electron microscopy, Corros. Sci., 10 (1970) 313-323.
[24] K. Hashimoto, K. Asami, X-Ray Photoelectron Spectroscopic Study of the Passivity of Ferritic 19cr Stainless-Steels in 1-Nhcl, Corros. Sci., 19 (1979) 251-260.
[25] L. Lin, C. Chao, D. Macdonald, A point defect model for anodic passive films II. Chemical breakdown and pit initiation, J. Electrochem. Soc., 128 (1981) 1194-1198.
[26] A. C. T. van Duin, V. S. Bryantsev, M. S. Diallo, W. A. Goddard, O. Rahaman, D. J. Doren, D. Raymand, K. Hermansson, Development and validation of a ReaxFF Reactive Force Field for Cu cation/water interactions and copper metal/metal oxide/metal hydroxide condensed phases, J. Phys. Chem. A, 114 (2010) 8.
[27] M. Aryanpour, A. C. T. van Duin, J.D. Kubicki, Development of a reactive force field for iron-oxyhydroxide systems, J. Phys. Chem. A, 114 (2010) 10.
[28] D. Raymand, A. C. T. van Duin, D. Spångberg, W. A. Goddard, K. Hermansson, Water adsorption on stepped ZnO surfaces from MD simulation, Surf. Sci., (2010) 12.
[29] M. F. Russo, Jr. R. Li, M. Mench, A.C.T.v. Duin, Molecular dynamic simulation of aluminumewater reactions using the ReaxFF reactive force field, International Journal of Hydrogen Energy, 36 (2011) 8.

[30] B. Jeon, S. K. R. S. Sankaranarayanan, A.C.T.v. Duin, S. Ramanathan, Atomistic insights into aqueous corrosion of copper, J. Chem. Phys., 134 (2011) 10.
[31] B. Jeon, S. K. R. S. Sankaranarayanan, A.C.T.v. Duin, S. Ramanathan, Reactive molecular dynamics study of chloride ion interaction with copper oxide surfaces in aqueous media, ACS Applied Materials & Interfaces 4(2012) 8.
[32] O. Assowe, O. Politano, V. Vignal, P. Arnoux, B. Diawara, O. Verners, A.C.T.v. Duin, Reactive molecular dynamics of the initial oxidation stages of Ni(111) in pure water: effect of an applied electric field The Journal of Physical Chemistry A, 116 (2012).
[33] O. Verners, A.C.T.v. Duin, Comparative molecular dynamics study of fcc-Ni nanoplate stress corrosion in water, Surf. Sci., 633 (2015) 8.
[34] C. Zou, Y. K. Shin, A. C.T. van Duin, H. Fangb, Z.K. Liu, Molecular dynamics simulations of the effects of vacancies on nickel self-diffusion, oxygen diffusion and oxidation initiation in nickel, using the ReaxFF reactive force field, Acta Mater., 83 (2015) 11.
[35] T. P. Senftle, S. Hong, M. M. Islam, S. B. Kylasa, Y. Zheng, Y. K. Shin, C. Junkermeier, R. Engel-Herbert, M. J. Janik, H. M. Aktulga, T. Verstraelen, A. Grama, A.C.T.v. Duin, The ReaxFF reactive force-field: development, applications and future directions, npj Comput. Mater., 2 (2016) 14.
[36] K. Otte, W.W. Schmahl, R. Pentcheva, Density functional theory study of water adsorption on FeOOH surfaces, Surface science, 606 (2012) 10.
[37] M.T. Nguyen, N. Seriani, R. Gebauer, Water adsorption and dissociation on alpha-Fe2O3(0001): PBE+U calculations. , 2013. 138(19): p. 8., Journal of Chemical Physics, 138 (2013) 8.
[38] Q. Pang, H. DorMohammadi, O.B. Isgor, L. Árnadóttir, Density functional theory study on the effect of OH and Cl adsorption on the surface structure of α-Fe2O3, Computational and Theoretical Chemistry, 1100 (2017) 11.
[39] S. Yin, X. Ma, D.E. Ellis, Initial stages of $H_2O$ adsorption and hydroxylation of Fe-terminateda-$Fe_2O_3$(0 0 0 1) surface, Surface science, 601 (2007) 12.
[40] A. Soon, M. RTodorova, B. Delley, C. Stampfl, Oxygen adsorption and stability ofsurface oxides on Cu(111): a first-principles investigation, Physical Review B - Condensed Matter and Materials Physics, 73 (2006) 12.
[41] C.H. Zhang, M. Liu, Y. Jin, D.B. Sun, The corrosive influence of chloride ionspreference adsorption ona-$Al_2O_3$(0001) surface, Applied Surface Science, 347 (2015) 6.
[42] S. Plimpton, Fast parallel algorithms for short–range molecular dynamics, Journal of Computational Physics, 117 (1995) 42.
[43] J. Towns, T. Cockerill, M. Dahan, I. Foster, K. Gaither, A. Grimshaw, V. Hazlewood, S. Lathrop, D. Lifka, G. D. Peterson, R. Roskies, J. R. Scott, N. Wilkins-Diehr, XSEDE: Accelerating scientific discovery, Computing in Science & Engineering, 16 (2014) 13.
[44] A. C. T. van Duin, S. Dasgupta, F. Lorant, W.A. Goddard, ReaxFF: A reactive force field for hydrocarbons, The Journal of Physical Chemistry A, 105 (2001) 14.
[45] A. C. T. van Duin, A. Strachan, S. Stewman, Q. Zhang, X. Xu, W.A. Goddard, $ReaxFF_{SiO}$ reactive force field for silicon and silicon oxide systems, The Journal of Physical Chemistry A, 107 (2003) 9.
[46] A. C. T. van Duin, V. S. Bryantsev, M. S. Diallo, W. A. Goddard, O. Rahaman, D. J. Doren, D. Raymand, K. Hermansson, Development and validation of a ReaxFF Reactive Force Field for Cu cation/water interactions and copper metal/metal oxide/metal hydroxide condensed phases, The Journal of Physical Chemistry A, 114 (2010) 8.

[47] O. Assowe, O. Politano, V. Vignal, P. Arnoux, B. Diawara, O. Verners, A.C.T.v. Duin, Reactive molecular dynamics of the initial oxidation stages of Ni(111) in pure water: effect of an applied electric field, The Journal of Physical Chemistry A, 116 (2012) 10.
[48] B. Jeon, Q. V. Overmeere, A.C.T.v. Duin, S. Ramanathan, Nanoscale oxidation and complex oxide growth on single crystal iron surfaces and external electric field effects, Physical Chemistry Chemical Physics, 15 (2013) 10.
[49] T. P. Senftle, S. Hong, M. M. Islam, S. B. Kylasa, Y. Zheng, Y. K. Shin, C. Junkermeier, R. Engel-Herbert, M. J. Janik, H. M. Aktulga, T. Verstraelen, A. Grama, A.C.T.v. Duin, The ReaxFF reactive force-field: development, applications and future directions, npj Computational Materials, 2 (2016) 14.
[50] G.M. Psofogiannakis, J.F. McCleerey, E. Jaramillo, A.C.T.v. Duin, ReaxFF reactive molecular dynamics simulation of the hydration of Cu-SSZ-13 zeolite and the formation of Cu dimers, The Journal of Physical Chemistry C, 119 (2015) 9.
[51] O. Verners, A.C.T.v. Duin, Comparative molecular dynamics study of fcc-Ni nanoplate stress corrosion in water, Surface Science, 633 (2015) 8.
[52] C. Zou, Y. K. Shin, A. C.T. van Duin, H. Fangb, Z.K. Liu, Molecular dynamics simulations of the effects of vacancies on nickel self-diffusion, oxygen diffusion and oxidation initiation in nickel, using the ReaxFF reactive force field, Acta Materialia, 83 (2015) 11.
[53] B. Jeon, Q.v. Overmeere, A.C.T.v. Duin, S. Ramanathan, Nanoscale oxidation and complex oxide growth on single crystal iron surfaces and external electric field effects, Physical Chemistry Chemical Physics, 15 (2013) 10.
[54] M. Aryanpour, A. C. T. van Duin, J.D. Kubicki, Development of a reactive force field for iron-oxyhydroxide systems, The Journal of Physical Chemistry A, 114 (2010) 10.
[55] O. Rahaman, A.C.T. van Duin, V.S. Bryantsev, J.E. Mueller, S.D. Solares, W.A. Goddard III, D.J. Doren, Development of a ReaxFF Reactive Force Field for aqueous chloride and copper chloride, Journal of Physical Chemistry A, 114 (2010) 13.
[56] H. DorMohammadi, Q. Pang, O.B. Isgor, L. Árnadóttir, Atomistic simulation of initial stages of iron corrosion in pure water using reactive molecular dynamics, Computational Materials Science, 145 (2018) 8.
[57] S. Nose, A molecular dynamics method for simulations in the canonical ensemble, Molecular Physics, 52 (1984) 14.
[58] W.G. Hoover, Canonical dynamics: Equilibrium phase-space distributions, Physical Review A, 31 (1985) 3.
[59] M.P. Allen, D.J. Tildesley, Computer simulation of liquids, Clarendon Press, Oxford, (1987).
[60] R.C. Dunbar, Deriving the Maxwell distribution, Journal of Chemical Education, 59 (1982) 2.
[61] G.D. Peckham, I.J. McNaught, Applications of Maxwell-Boltzmann distribution diagrams, Journal of Chemical Education, 69 (1992) 5.
[62] P. Ghods, Multi-Scale investigation of the formation and breakdown of passive films on carbon steel rebar in concrete, (20010).
[63] N. Fairely, CasaXPS Manual 2.3. 15, Casa Softw. Ltd., http://scholar.google.com/scholar?hl=en&btnG=Search&q=intitle:CasaXPS+Manual+2.3.15#2, (2009) 177.
[64] P. van der Heide, X-Ray photoelectron spectroscopy: an introduction to principles and practices, John Wiley & Sons, Inc, (2011).

[65] D.J. Dwyer, S.R. Kelemen, A. Kaldor, The water dissociation reaction on clean and oxidized iron (110), The Journal of Chemical Physics, 76 (1982) 6.
[66] D.J. Dwyer, G.W. Simmons, A study of the initial reaction of water vapor with Fe(001) surface, Surface Science, 64 (1977) 16.
[67] S. Hung, W.H. Schwartz, J. Bernasek, Sequential oxidation of Fe (100) by water adsorption: formation of an ordered hydroxylated surface, Surface Science, 248 (1991) 11.
[68] M. Eder, K. Terakura, J. Hafner, Initial stages of oxidation of (100) and (110) surfaces of iron caused by water, Phys. Rev. B. , 64 (2001) 7.
[69] X. Liu, X. Tian, T. Wang, X. Wen, Y. Li, J. Wang, H. Jiao, Coverage dependent water dissociative adsorption on Fe(110) from DFT computation, Physical Chemistry Chemical Physics, 17 (2015) 11.
[70] S. Liu, X. Tian, T. Wang, X. Wen, Y. Li, J. Wang, H. Jiao, Coverage dependent water dissociative adsorption on the clean and O-precovered Fe(111) surfaces, The Journal of Physical Chemistry C, 119 (2015) 11.
[71] P. Ghods, O.B. Isgor, G.A. McRae, G.P. Gu, Electrochemical investigation of chloride-induced depassivation of black steel rebar under simulated service conditions, Corros Sci, 52 (2010) 11.
[72] A. Poursaee, C.M. Hansson, Reinforcing steel passivation in mortar and ore solution Cement Concrete Res, 37 (2007) 7.
[73] O. Stern, The theory of the electrolytic double layer, Zeitschrift für Elektrochemie und Angewandte Physikalische Chemie, 30 (1924) 9.
[74] A. Goel, Colloidal chemistry Discovery Publishing House, New Delhi, (2006).
[75] H. Burak Gunay, O.B. Isgor, P. Ghods, Kinetics of passivation and chloride-induced depassivation of iron in simulated concrete pore solutions using electrochemical quartz crystal nanobalance, Corrosion, 71 (2015) 13.
[76] K. Ogura, M. Kaneko, The pit initiation mechanism on passive iron under both open-circuit and controlled potential conditions, Corros Sci, 23 (1983) 10.
[77] T. Zakroczymsk, C.J. Fan, Z. Szklarska-Smialowska, Passive film formation on iron and film breakdown in a sodium hydroxide solution containing chloride ions J Electrochem Soc, 132 (1985) 4.

# 6. Conclusions

The research presented in this dissertation is an investigation of iron passivity and chloride-induced depassivation in alkaline electrolytes using Reactive Force Field Molecular Dynamics (ReaxFF-MD). The research was conducted in four thrusts, which are presented in four separate papers. The conclusions and key findings of each paper are summarized here.

## 6.1. Atomistic simulation of initial stages of iron corrosion in pure water using reactive molecular dynamics

ReaxFF-MD was used to simulate iron corrosion in pure water (pH = 7). We applied an external electric field of 20 MeV/cm, 25 MeV/cm, and 30 MeV/cm between the iron and the solution.

The corrosion pattern involved different stages and started with the adsorption of water molecules on the iron surface and dissociation into $OH^-$ and $H^+$. The $OH^-$ group adsorbs on the iron surface and forms adsorbed iron hydroxide while the $H^+$ bonds with a water molecule to form $H_3O^+$. Some of adsorbed iron hydroxides dissolves into the solution and forms aqueous iron hydroxide in the next step. In the third step, aqueous iron hydroxides bonds with $H^+$ and produce water molecules and iron ions. The dissolved iron atoms form corrosion products of iron oxides/hydroxides. The last step is the penetration of oxygen into the iron slab to form iron oxide.

To study the compositions of the oxide film, charge distribution of iron and oxygen atoms and PDF of the Fe-O bond in the oxide film were used. For this purpose, both the charge result of the simulation and the PDF of the Fe-O bond were compared to the charge state and calculated PDF of Fe-O bond of reference oxide structures. It was concluded that the compositions of the oxide film were not pure phases of hematite, magnetite, or wustite.

The effect of temperature on the corrosion process was investigated in a narrow temperature range (300 K to 350 K) but typical of exposure conditions of most reinforced concrete structures. We found that the corrosion rates increased slightly with increasing temperature.

It is worth mentioning that in this study the system of water and other surface orientations of iron, Fe(100) and Fe(111), were also simulated. No significant differences in the corrosion patterns and

charge distributions of the different Fe surface orientations was found so these results are presented as supplementary material (Appendix A).

The results of this study provided support for the feasibility of using ReaxFF-MD simulations to study corrosion and passivity of iron in highly alkaline environments in the future. However, one practical conclusion of the simulations in this study was that most of the water molecules were consumed at the end of the simulations. This has implications for future simulations of iron-water systems to study passivity, a process which will require longer simulation times. Larger number of initial water molecules is necessary to avoid issues such as unrealistic acidification of the electrolyte and limitations of the total simulation time.

### 6.2. Investigation of the applicability of classical electrical double layer models to study corrosion and passivity of iron in neutral and alkaline media

The applicability of the classical EDL models to study corrosion and passivity of iron in neutral and alkaline media using ReaxFF-MD was investigated. We compared the performance of the classical EDL models in the ReaxFF-MD simulations of iron exposed to neutral (pH = 7) and highly alkaline (pH = 13.5) electrolytes under applied electric fields. The following conclusions were obtained from the investigation:

- Although the Helmholtz model was able to produce iron corrosion in the neutral electrolyte, it did not result in passive film formation in the highly alkaline solution system.
- The Gouy-Chapman model was not capable of simulate passivity for iron in the highly alkaline solution system or active corrosion in the neutral electrolyte.
- The Stern model was the only model that could simulate passivity and corrosion of iron for highly alkaline and neutral electrolytes, respectively.

This study showed that ReaxFF-MD simulations of iron in neutral and alkaline electrolytes should use the Stern model for representing the EDL.

### 6.3. Molecular dynamics modeling of Fe(110) passivity in 0.316 M NaOH solution

The iron oxidation in exposure to the highly alkaline solution was investigated using ReaxFF-MD to study the compositions of the iron passive film and the initial stages of the passivation process. Iron surface orientation Fe(110), as the more close-packed surface than the other orientations, was chosen and the solution contained sodium hydroxides to model a highly alkaline electrolyte. An external electric field was applied using the Stern model with the intensity of 30 MeV/cm at the iron surface. The simulation was performed for 500 ps, and iron oxidation with no iron dissociation in the electrolyte was observed during the simulations, indicating iron passivation and supports the thermodynamic behavior of iron-highly alkaline solution system. The XPS scans were performed to study the oxide film chemical buildup and time-dependent passivation of iron surface exposed to 13.5 pH NaOH aqueous solution. The XPS findings validated the ReaxFF-MD results regarding oxide film buildup and passivation mechanism.

The critical stages of the iron passivation process were studied. It was shown that passivation initiated with the formation of an $Fe(OH)_2$ layer on the metals surface followed by oxygen penetration into the metal substrate. This initiation is different from the process that had been observed in simulations done in neutral (pH = 7) electrolytes [44]. When the electrolyte does not have reserve alkalinity, $Fe(OH)_2$ layer does not form, which results in the dissolution of the iron atoms in to the solution while oxygen penetrate into the metal substrate to form complex oxides. The $Fe(OH)_2$ layer that forms and remains on the iron surface creates conditions for oxygen diffusion into metal without excessive dissolution of iron atoms into the electrolyte, hence without iron vacancy formation. The oxygen penetration without iron dissolution or iron vacancy formation, followed by iron oxidation in the metal substrate, was the driving force for the formation of the passive film in alkaline environments.

In order to analyze the compositions of the oxidized zone, the iron oxide layers were studied for different times during the simulation. The PDFs of Fe-O for the iron oxide layers were compared to those of the reference oxide structures, i.e., $Fe_2O_3$, $Fe_3O_4$ and FeO. By comparing the locations of the dominant and transition points of each iron oxide layer to those of iron oxide phase, it was shown that during the iron oxidation the compositions of different layers changed over time from

FeO to $Fe_2O_3$, and finally to $Fe_2O_3$, if adequate amount of oxygen was able to penetrate the layer. Oxygen penetration rate slowed down over time, controlling the thickness of the passive film and resulting in a multilayer oxide structure. The surface of the film contained $Fe(OH)_2$, which was identified as responsible for the prevention of iron dissolution while allowing oxygen penetration into the substrate. The analysis of Fe-O PDF patterns of different layers in the passive film showed that the outer layers of the passive film were mainly in the form of $Fe_2O_3$; the middle layers were in the form of $Fe_3O_4$; and the inner layers were mainly in the form of FeO.

Studying the oxygen atom densities of different intervals in the oxidized zone showed that outer iron oxide layers contained more oxygen atoms than the inner iron oxide layers. By comparing the oxygen-to-iron ratio of different layers, it was also concluded that the outer layers are similar to $Fe_2O_3$, while the middle and inner layers are similar to $Fe_3O_4$ and FeO.

The XPS results showed the dominant presence of $Fe^{III}$ ions ($Fe_2O_3$ oxide) in outer regions of oxide film, however the ion concentration decreased with increasing film depth. On the contrary, the $Fe^{II}$ ion concentration increased with increasing film depth suggesting a $Fe^{II}$ rich inner layers consisting of FeO and $Fe_3O_4$ oxides near the metal-oxide interface. Furthermore, the time dependent passivation study indicated the transformation of $Fe^{II}$ to $Fe^{III}$ oxides, which was confirmed by increasing $Fe^{III}$ concentration at the top surface of the oxide layer.

### 6.4. Chloride-induced depassivation of iron in alkaline media

We used ReaxFF-MD to answer fundamental questions on chloride-induced depassivation of iron in alkaline media. The simulations were supported with electrochemical tests and x-ray photoelectron spectroscopy (XPS) studies. The studied passive film created using ReaxFF-MD simulations in pH 13.5 NaOH solution and contained multiple oxide layers. The outer, middle and inner layers of the passive film had oxides structures similar to those for $Fe_2O_3$, $Fe_3O_4$, and FeO, respectively.

The breakdown of the passive film by chlorides initiates with iron dissolution from the first layer of the passive film into the electrolyte. Iron dissolution and corresponding iron vacancy formation in the first layer of the passive film take place in four stages. In the first and second stages, chlorides

facilitate the consumption of hydroxide ions in the electrolyte by the iron surface to form of $Fe(OH)_3$ and $Fe(OH)_2Cl$, respectively, which do not dissociate into the electrolyte but remain on the metal surface. These two processes cause local acidification, and eventual depletion of OH, in the electrolyte adjacent to the metal surface. The following third and fourth stages lead to the dissolution of iron into the electrolyte in the form of $Fe(OH)Cl_2$ and $FeCl_3$, respectively. Chloride in these compounds return to water; therefore, it can be stated that chloride in the electrolyte mainly acts as a catalyst in the depassivation process.

The four-step process for the initiation of the passive film breakdown helps explain the concept of a critical chloride threshold. Sufficient amount of chloride ions are necessary to cause the local acidification of the electrolyte and subsequent iron dissociation that are exposed to the OH-depleted zones of the electrolyte. When chloride concentration in the electrolyte is below a threshold, these processes do not proceed, and passive film remains stable. The same reasoning also explains the well-documented electrochemical observation that critical chloride thresholds are higher in solution with solution with higher pH. Higher pH implies there are larger number of hydroxides close to the surface, and hence, increased number of chloride ions are needed to acidify the electrolyte.

Our simulations do not support the depassivation models that are based on the ingress of chlorides into the passive film. In fact, in all simulations, chlorides remained either adsorbed on the surface of the passive film or in the electrolyte and caused the generation of iron vacancies within the first iron oxide layer. The ReaxFF-MD simulations support the depassivation hypothesis that is described by the point defect model, which states that when a sufficient number of iron vacancies reach the iron/iron oxide interface, they will cause the localized detachment of the oxide film. At these detached sites, iron oxidation stops, and the film begins to thin due to the continued dissolution if iron from the film/electrolyte interface. XPS results also indicate that chlorides do not penetrate into the passive film, but can exist in the first layer of the passive film as demonstrated in the first two stages of the iron dissolution process.

## 7. Bibliography

S. Ahn, H. Kwon, D.D. Macdonald, Role of chloride ion in passivity breakdown on iron and nickel, J Electrochem Soc, 152 (2005) 9.

Z. Ai, W. Sun, J. Jiang, D. Song, H. Ma, J. XZhang, D. Wang, Passivation characteristics of alloy corrosion-resistant steel Cr10Mo1 in simulating concrete pore solutions: combination effects of pH and chloride, Materials, 9 (2016) 17.

O. A. Albani, L.M. Gassa, J.O. Zerbino, J.R. Vilche, A.J. Arvia, Comparative study of the passivity and the breakdown of passivity of polycrystalline iron in different alkaline solutions, Electrochemica Acta, 35 (1990) 8.

M. P. Allen, D.J. Tildesley, Computer simulation of liquids, Clarendon Press, Oxford, (1987).

M. P. Allen, Introduction to Molecular Dynamics Simulation, , NIC Series 23 (2004) 28.

G. C. Allen, P.M. Tucker, R.K. Wild, Characterization of iron/oxygen surface reactions by X-ray photoelectron spectroscopy, Philosophy Magazine B, 46 (1982) 11.

C. Alonso, C. Andrade, M. Castellote, P. Castro, Chloride threshold values to depassivate reinforcing bars embedded in a standardized OPC mortar, Cement & Concrete Research, 30 (2000) 9.

C. Andrade, C.L. Page, Pore solution chemistry and corrosion in hydrated cement systems containing chloride salts - a study of cation specific effects, Brit Corros J, 21 (1986) 5.

U. Angst, B. Elsener, C.K. Larsen, O. Vennesland, Chloride induced reinforcement corrosion: Electrochemical monitoring of initiation stage and chloride threshold values, Corros Sci, 53 (2011) 14.

U. Angst, B. Elsener, C.K. Larsen, O. Vennesland, Critical chloride content in reinforced concrete - A review, Cement Concrete Res, 39 (2009) 17.

M. Aryanpour, A. C. T. van Duin, J.D. Kubicki, Development of a reactive force field for iron-oxyhydroxide systems, The Journal of Physical Chemistry A, 114 (2010) 10.

M. Aryanpour, A. C. T. van Duin, J.D. Kubicki, Development of a reactive force field for iron-oxyhydroxide systems, J. Phys. Chem. A, 114 (2010) 10.

O. Assowe, O. Politano, V. Vignal, P. Arnoux, B. Diawara, O. Verners, A.C.T.v. Duin, Reactive molecular dynamics of the initial oxidation stages of Ni(111) in pure water: effect of an applied electric field, The Journal of Physical Chemistry A, 116 (2012) 10.

P. Attard, Electrolytes and the electric double layer, Advanced Chemical Physics, 92 (1996) 159.

V. Bagotsky, Fundamentals of electrochemistry, John Wiley & Sons: New York, (2006).

A. Bard, L. Faulkner, Electrochemical methods: fundamentals and applications, John Wiley & Sons: New York, (2001).

S. Behrens, Preparation of functional magnetic nanocomposites and hybrid materials: recent progress and future directions. , Nanoscale, 3 (2011) 6.

L. Bertolini, B. Elsener, P. Pedeferri, R. and Polder, Corrosion of Steel in Concrete: Prevention, Diagnosis, Repair, Weinheim: Wiley-VCH, (2000).

B. Beverskog, I. Puigdomenech, Revised Pourbaix diagrams for nickel at 25-300 degrees C, Corros Sci, 39 (1997) 12.

H. E. H. Bird, B.R. OPearson, P.A. Brook, The breakdown of passive films on iron, Corros Sci, 28 (1988) 6.

P. E. Blöchl, Projector augmented-+rave method, Physical Review B, 50 (1994) 27.

H. Bohni, Corrosion in Concrete Structures CRC Press, New York, 2005.
H. Bohni, Corrosion in concrete structures, New York: CRC Press, (2005).
S. Boyda, M. Gravelle, Nonreactive molecular dynamics force field for crystalline hexahydro-1,3,5-trinitro-1,3,5 triazine, The Journal of Chemical Physics, 124 (2006) 10.
J. P. Broomfield, Corrosion of steel in concrete New York: Taylor & Francis, (2007).
J. P. Broomfield, Corrosion of Steel in Concrete Taylor & Francis, New York, 2007.
M. J. Buehler, A. C. T. van Duin, W.A. Goddard, Multiparadigm modeling of dynamical crack propagation in silicon using a reactive force field, Physical Review Letters, 96 (2006) 4.
H. –J. Butt, M. Kappl, Surface and interfacial forces, Wiley-VCH: Weinheim, Germany, (2010).
N. Cabrera, N.F. Mott, Theory of the oxidation of metals, Reports on Progress in Physics, 163 (1949) 22.
C. Y. Chao, A point defect model for anodic passive films. I. film growth kinetics, J Electrochem Soc, 128 (1981) 8.
D. L. Chapman, A contribution to the theory of electrocapillarity, Philosophical Magazine 25 (1913) 7.
J. Chen, T.J. Martínez, Charge conservation in electronegativity equalization and its implications for the electrostatic properties of fluctuating-charge models, The Journal of Chemical Physics, 131 (2009) 3.
M. Cohen, The formation and properties of passive films on iron, Can J Chemistry, 37 (1959) 6.
C. Colliex, T. Manoubi, C. Ortiz, Electron-Energy-Loss-Spectroscopy near-edge fine-structures in the iron-oxygen system. , Physical Review B, 44 (1991) 10.
Corrosion Cost and Preventive Strategies in the United States, FHWA-RD-01-156
A. J. Davenport, M. Sansone, High resolution in situ XANES investigation of the nature of the passive film on iron in a pH 8.4 borate buffer, J Electrochem Soc, 142 (1999) 6.
D. E. Davies, W. Barker, Influence of pH on corrosion and passivation of nickel, Corrosion, 20 (1964) 7.
S. Dewan, V. Carnevale, A. Bankura, E.-B. A., G. Fiorin, M.L. Klein, E. Borguet, Structure of water at charged interfaces: a molecular dynamics study, Langmuir, (2014) 10.
I. Diez-Perez, C. Vericat, P. Gorostiza, F. Sanz, The iron passive film breakdown in chloride media may be mediated by transient chloride-induced surface states located within the band gap, Electrochemistry Communications, 8 (2006) 6.
D. I. Dimitrov, N.D. Raev, Molecular dynamics simulations of the electrical double layer atthe 1 M KCl solution | Hg electrode interface Journal of Electroanalytical Chemistry 486 (2000) 8.
H. DorMohammadi, Q. Pang, L. Árnadóttir, O.B. Isgor, Investigation of the applicability of classical electrical double layer models to study corrosion and passivity of iron in neutral and alkaline media, J Electrochem Soc, To be submitted (2018).
H. DorMohammadi, Q. Pang, O.B. Isgor, L. Árnadóttir, Atomistic simulation of initial stages of iron corrosion in pure water using reactive molecular dynamics, Computational Materials Science, 145 (2018) 8.
R. C. Dunbar, Deriving the Maxwell distribution, Journal of Chemical Education, 59 (1982) 2.
D. J. Dwyer, G.W. Simmons, A study of the initial reaction of water vapor with Fe(001) surface, Surface Science, 64 (1977) 16.

D. J. Dwyer, S.R. Kelemen, A. Kaldor, The water dissociation reaction on clean and oxidized iron (110), The Journal of Chemical Physics, 76 (1982) 6.
M. Eder, K. Terakura, J. Hafner, Initial stages of oxidation of (100) and (110) surfaces of iron caused by water, Phys. Rev. B. , 64 (2001) 7.
N. Fairely, CasaXPS Manual 2.3. 15, Casa Softw. Ltd., http://scholar.google.com/scholar?hl=en&btnG=Search&q=intitle:CasaXPS+Manual+2.3.15#2, (2009) 177.
R. P. Feynman, Chapter 5 : MD, Atoms in Motion, LLC, (2018).
A. T. Fromhold Jr, J. Kruger, Space-Charge and Concentration-Gradient effects on anodic oxide film formation. , J Electrochem Soc, 120 (1973) 8.
T. Fujii, F.M.F. De Groot, G.A. Sawatzky, F.C. Voogt, T. Hibma, K. Okada, In situ XPS analysis of various iron oxide films grown by NO2-assisted molecular-beam epitaxy, Physical Review B, 59 (1999) 8.
P. Ghods, Multi-Scale investigation of the formation and breakdown of passive films on carbon steel rebar in concrete, (20010).
P. Ghods, O. Burkan Isgor, F. Bensebaa, D. Kingston, Angle-resolved XPS study of carbon steel passivity and chloride-induced depassivation in simulated concrete pore solution, Corros Sci, 58 (2012) 9.
P. Ghods, O.B. Isgor, G. Mcrae, T. Miller, The effect of concrete pore solution composition on the quality of passive oxide films on black steel reinforcement, Cement Concrete Comp, 31 (2009) 10.
P. Ghods, O.B. Isgor, G. McRae, T. Miller, The effect of concrete pore solution composition on the quality of passive oxide films on black steel reinforcement, Cement and Concrete Composites, 31 (2009) 2-11.
P. Ghods, O.B. Isgor, G.A. McRae, G.P. Gu, Electrochemical investigation of chloride-induced depassivation of black steel rebar under simulated service conditions, Corros Sci, 52 (2010) 11.
P. Ghods, O.B. Isgor, G.A. McRae, J. Li, G.P. Gu, Microscopic investigation of mill scale and its proposed effect on the variability of chloride-induced depassivation of carbon steel rebar, Corros Sci, 53 (2011) 9.
P. Ghods, O.B. Isgor, G.J.C. Carpenter, J. Li, G.A. McRae, G.P. Gu, Nano-scale study of passive films and chloride-induced depassivation of carbon steel rebar in simulated concrete pore solutions using FIB/TEM, Cement Concrete Res, 47 (2013) 14.
P. Ghods, O.B. Isgor, J. Brown, F. Bensebaa, D. Kingston, XPS depth profiling study on the passive oxide film of carbon steel in saturated calcium hydroxide solution and the effect of chloride on the film properties, Applied Surface Science, 257 (2011) 9.
G.K. Glass, The influence of chloride binding on the chloride induced corrosion risk in reinforced concrete, Corros Sci, 42 (2000) 16.
G. K. Glass, N.R. Buenfeld, The inhibitive effects of electrochemical treatment applied to steel in concrete, Corros Sci, 42 (2000) 5.
G. K. Glass, N.R. Buenfeld, The presentation of the chloride threshold level for corrosion of steel in concrete, Corros Sci, 39 (1997) 13.
J. N. Glosli, M.R. Philpott, Molecular dynamics study of interfacial electric fields, Electrochemica Acta, 41 (1996) 14.

A. Goel, Colloidal chemistry Discovery Publishing House, New Delhi, (2006).
Gongadze, U. Van Rienen, A. Iglic, Generalized Stern models of the electric double layer considering the spatial variation of permittivity and finite size of ions in saturation regime, Cellular & Molecular Biology Letters, 16 (2011) 19.
Goni, C. Andrade, Synthetic concrete pore solution chemistry and rebar corrosion rate in the presence of chlorides, Cement Concrete Res, 20 (1990) 15.
E. Gonzalez, E. Otero, S. Feliu, W. Lopez, Initial steps of corrosion in the steel/Ca(OH)ZCl system: The role of heterogeneities on the steel surface and oxygen supply, Cement Concrete Res, 23 (1993) 8.
V. K. Gouda, Corrosion and corrosion inhibition of reinforcing steel: 1-Immersion in alkaline solution, Brit Corros J, 5 (1970) 6.
G. Gouy, Constitution of the electric charge at the surace of an electrolyte Journal of Theoretical and Applied Physics, 9 (1910) 12.
N. N. Greenwood, A. Earnshaw, Chemistry of elements, Elsevier, (1997).
M. Griebel, S. Knapek, G. Zumbusch, Numerical simulation in molecular dynamics, numerics, algorithms, parallelization, applications, Springer, (2007).
A. P. Grosvenor, B.A. Kobe, M.C. Biesinger, N.S. McIntyre, Investigation of multiplet splitting of Fe 2p XPS spectra and bonding in iron compounds, Surface and Interface Analysis, 36 (2004b) 11.
J. Gui, T.M. Devine, Analytical characterization of the passive film formed on steel in solutions simulating the concrete interstitial electrolyte, Corros Sci, 36 (1994) 21.
J. Gui, T.M. Devine, In situ vibrational spectra of the passive film on iron in buffered borate solution, Corros Sci, 32 (1991) 20.
B. Gunay, O.B. Isgor, P. Ghods, Kinetics of passivation and chloride-induced depassivation of iron in simulated concrete pore solutions using electrochemical quartz crystal nanobalance, Corrosion, 71 (2015) 13.
B. Gunay, P. Ghods, O.B. Isgor, G.J. Carpenter, X. Wu, Characterization of atomic structure of oxide films on carbon steel in simulated concrete pore solutions using EELS, Applied Surface Science, 274 (2013) 8.
C. M. Hansson, A. Poursaee, A. Laurent, Macrocell and microcell corrosion of steel in ordinary Portland cement and high performance concretes, Cement Concrete Res, 36 (2006) 5.
C. M. Hansson, B. Sorensen, The threshold concentration of chloride in concrete for the initiation of reinforcement corrosion, in: N.S. Berke, V. Chaker, D. Whitting (Eds.), Corrosion Rates of Steel in Concrete, ASTM (STP1065), (1988) 14.
C. M. Hansson, The impact of corrosion on society, Metall Mater Trans A, 42A (2011) 11.
S. P. Harrington, F. Wang, T.M. Devine, The structure and electronic properties of passive and prepassive films of iron in borate buffer, Electrochimica Acta, 55 (2010) 11.
K. Hashimoto, K. Asami, X-Ray photoelectron spectroscopic study of the passivity of ferritic 19cr stainless-steels in 1-Nhcl, Corros Sci, 19 (1979) 10.
K. Hashimoto, K. Asami, X-Ray Photoelectron Spectroscopic Study of the Passivity of Ferritic 19cr Stainless-Steels in 1-Nhcl, Corros. Sci., 19 (1979) 251-260.
S. Haupt, C. Calinski, U. Collisi, H.W. Hoppe, H.D. Speckmann, H.H. Strehblow, XPS and ISS examinations of electrode surfaces and passive layers with a specimen transfer in a closed system, Surface and Interface Analysis, 9 (1986) 9.

M. A. Heine, D.S. Keir, M.J. Pryor, Specific effects of chloride and sulfate ions on oxide covered aluminum, J Electrochem Soc, 112 (1965) 9.
H. Heinz, R. A. Vaia, B. L. Farmer, R.R. Naik, Accurate simulation of surfaces and interfaces of face-centered cubic metals using 12-6 and 9-6 Lennard-Jones potentials, The Journal of Physical Chemistry C, 112 (2008) 10.
J. M. Hermida-Ramon, G. Karlstrom, Study of the hydronium ion in water. A combined quantum chemical and statistical mechanical treatment, J Mol Struc-Theochem, 712 (2004) 7.
Highwas and bridges: Corrosion resources for highways and bridges, NACE International, (2013).
T. P. Hoar, D.C. Mears, G.P. Rothwell, The relationships between anodic passivity, brightening and pitting, Corros Sci, 5 (1965) 11.
W. G. Hoover, Canonical dynamics: Equilibrium phase-space distributions, Physical Review A, 31 (1985) 3.
S. Hung, W.H. Schwartz, J. Bernasek, Sequential oxidation of Fe (100) by water adsorption: formation of an ordered hydroxylated surface, Surface Science, 248 (1991) 11.
R. Hunter, Foundations of colloid science, Oxford University Press: New York, (2001).
S. E. Hussain, A.S. Al-Gahtani, Chloride threshold for corrosion of reinforcement in concrete, Aci Mater J, 93 (1996) 5.
S. E. Hussain, Rasheeduzzafar, A. Al-Musallam, A.S. Al-Gahtani, Factors affecting threshold chloride for reinforcement corrosion in concrete, Cement Concrete Res, 25 (1995) 13.
G. O. A. Janssens, B. G. Baekelandt, H. Toufar, W. J. Mortier, R.A. Schoonheydt, Comparison of cluster and infinite crystal calculations on zeolites with the electronegativity equalization method (EEM) The Journal of Physical Chemistry, 99 (1995) 8.
B. Jeon, Q. V. Overmeere, A.C.T.v. Duin, S. Ramanathan, Nanoscale oxidation and complex oxide growth on single crystal iron surfaces and external electric field effects, Physical Chemistry Chemical Physics, 15 (2013) 10.
B. Jeon, Q.v. Overmeere, A.C.T.v. Duin, S. Ramanathan, Nanoscale oxidation and complex oxide growth on single crystal iron surfaces and external electric field effects, Physical Chemistry Chemical Physics, 15 (2013) 10.
B. Jeon, S. K. R. S. Sankaranarayanan, A.C.T.v. Duin, S. Ramanathan, Atomistic insights into aqueous corrosion of copper, The Journal of Chemical Physics, 134 (2011) 10.
B. Jeon, S. K. R. S. Sankaranarayanan, A.C.T.v. Duin, S. Ramanathan, Reactive molecular dynamics study of chloride ion interaction with copper oxide surfaces in aqueous media, ACS Applied Materials & Interfaces 4(2012) 8.
B. Jeon, S. K. R. S. Sankaranarayanan, A.C.T.v. Duin, S. Ramanathan, Atomistic insights into aqueous corrosion of copper, J. Chem. Phys., 134 (2011) 10.
J. Jiang, D. Wang, H. Chu, H. Ma, Y. Liu, Y. Gao, J. Shi, W. Sun, The passive film growth mechanism of new corrosion-resistant steel rebar in simulated concrete pore solution: nanometer structure and electrochemical study, Materials, 10 (2017) 14.
S. Joiret, M. Keddam, X.R. Novoa, M.C. Perez, C. Rangel, H. Takenouti, Use of EIS, ring-disk electrode, EQCM and Raman spectroscopy to study the film of oxides formed on iron in 1 M NaOH, Cement Concrete Comp, 24 (2002) 9.
M. Kamrunnahar, J.E. Bao, D.D. Macdonald, Challenges in the theory of electron transfer at passive interfaces, Corros Sci, 47 (2005) 29.

O. A. Kayyali, M.N. Haque, The Cl-/OH-ratio in chloride-contaminated concrete-A most important criterion, Magazine of Concrete Research, 47 (1995) 8.
A. R. Khoei, H. DorMohammadi, A. Aramoon, A temperature-related boundary Cauchy–Born method fo rmulti-scale modeling of silicon nano-structures, Physics Letters A, 378 (2014) 10.
A. R. Khoei, H. DorMohammadi, Validity and size-dependency of Cauchy–Born hypothesis with Tersoff potential in silicon nano-structures, Computational Materials Science, 63 (2012) 10.
G. H. Koch, M. P. H. Brongers, N.G. Thompson, Y.P. Virmani, J.H. Payer, Corrosion Cost and Preventative Strategies in the United States, in, NACE International, 2003.
J. M. Kolotyrkin, Effects of anions on the dissolution kinetics of metals, J Electrochem Soc, 108 (1961) 8.
G. Kresse, J. Furthmüller, Efficiency of ab-initio total energy calculations for metals and semiconductors using a plane-wave basis set, Computational Materials Science, 6 (1996) 36.
G. Kresse, J. Furthmüller, Efficient iterative schemes for ab initio total-energy calculations using a plane-wave basis set, Physical Review B, 54 (1996) 18.
G. Kresse, J. Hafner, Ab initio molecular dynamics for liquid metals, Physical Review B, 47 (1993) 4.
G. Kresse, J. Hafner, Ab initio molecular-dynamics simulation of the liquid-metal —amorphous-semiconductor transition in germanium, Physical Review B, 49 (1994) 21.
J. Kruger, Passivity and its breakdown on iron and iron base alloys, USA-Japan Seminar, NACE, Houston TX, (1976).
J. Kruger, Passivity of metals-A materials perspective, International Materials Reviews, 33 (1988) 18.
K. E. Kurtis, P.K. Mehta, A Critical Review of Deterioration of Concrete Due to Corrosion of Reinforcing Steel, ACI Special Publication, 170 (1997) 535-554.
K. Lau, A.A. Sagues, R.G. Powers, Corrosion of epoxy-coated rebar in marine bridges-Part 2: Corrosion in cracked concrete, Corrosion, 66 (2010) 16.
H. P. Leckie, H.H. Uhlig, Environmental factors affecting the critical potential for pitting in 18–8 stainless steel, J Electrochem Soc, 113 (1966) 6.
D. S. Leek, The passivity of steel in concrete, Quarterly Journal of Engineering Geology, 24 (1991) 12.
J. E. Lennard-Jones, On the determination of molecular fields. —II. From the equation of state of a gas, Proceeding of the Royal Society (1924) 15.
L. Li, A.A. Sagues, Chloride corrosion threshold of reinforcing steel in alkaline solutions - Open-circuit immersion tests, Corrosion, 57 (2001) 10.
L. Li, A.A. Sagues, Chloride corrosion threshold of reinforcing steel in alkaline solutions - Cyclic polarization behavior, Corrosion, 58 (2002) 12.
L. Li, A.A. Sagues, Chloride corrosion threshold of reinforcing steel in alkaline solutions - Cyclic polarization behavior, Corrosion, 58 (2002) 305-316.
L. F. Lin, C. Chao, D. Macdonald, A point defect model for anodic passive films II. Chemical breakdown and pit initiation, J Electrochem Soc, 128 (1981) 5.
W. K. Liu, E.G. Karpov, S. Zhang, H.S. Park, An introduction to computational nanomechanics and materials Computer Methods Applied Mech and Engineering, 193 (2004) 50.

S. Liu, X. Tian, T. Wang, X. Wen, Y. Li, J. Wang, H. Jiao, Coverage dependent water dissociative adsorption on the clean and O-precovered Fe(111) surfaces, The Journal of Physical Chemistry C, 119 (2015) 11.

S. Liu, X. Tian, T. Wang, X. Wen, Y. Li, J. Wang, H. Jiao, Coverage dependent water dissociative adsorption on Fe(110) from DFT computation, Physical Chemistry Chemical Physics, 17 (2015) 11.

J. Lyklema, Fundamentals of interface and colloid science, Academic Press: New York, 2 (2001).

D. D. Macdonald, S.R. Biaggio, H.K. Song, Steady-state passive films - interfacial kinetic effects and diagnostic-criteria, J Electrochem Soc, 139 (1992) 8.

D. D. Macdonald, The point defect model for the passive state, Journal of Electroanalytical Society, 139 (1992) 16.

L. Mammoliti, C.M. Hansson, B.B. Hope, Corrosion inhibitors in concrete - Part II: Effect on chloride threshold values for corrosion of steel in synthetic pore solutions, Cement Concrete Res, 29 (1999) 7.

L. T. Mammoliti, L.C. Brown, C.M. Hansson, B.B. Hope, The influence of surface finish of reinforcing steel and pH of the test solution on the chloride threshold concentration for corrosion initiation in synthetic pore solutions, Cement Concrete Res, 26 (1996) 6.

P. S. Mangat, B.T. Molloy, Factors influencing chloride-induced corrosion of reinforcement in concrete, Materials and Structures, 25 (1992) 8.

N. S. McIntyre, D.G. Zetaruk, X-ray photoelectron spectroscopic studies of iron oxides, Analytical Chemistry, 49 (1977) 9.

P. K. Mehta, P.J.M. Monteiro, Concrete: microstructure, properties, and materials, New York: McGraw-Hill Professional., (2005).

G. R. Meira, C. Andrade, E.O. Vilar, K.D. Nery, Analysis of chloride threshold from laboratory and field experiments in marine atmosphere zone, Construction and Building Materials, 55 (2014) 10.

M. F. Montemor, A.M.P. Simoes, M.G.S. Ferreira, Analytical characterization of the passive film formed on steel in solutions simulating the concrete interstitial electrolyte, Corros Rev, 54 (1998) 7.

W. J. Mortier, S. K. Ghosh, S. Shankar, Electronegativity equalization method for the calculation of atomic charges in molecules, Journal of the American Chemical Society, 108 (1986) 6.

M. Nagayama, M. Cohen, The anodic oxidation of iron in a neutral solution, J Electrochem Soc, 109 (1962) 10.

M. T. Nguyen, N. Seriani, R. Gebauer, Water adsorption and dissociation on alpha-Fe2O3(0001): PBE+U calculations. , 2013. 138(19): p. 8., Journal of Chemical Physics, 138 (2013) 8.

S. Nose, A molecular dynamics method for simulations in the canonical ensemble, Molecular Physics, 52 (1984) 14.

L. J. Oblonsky, T.M. Devine, A surface enhanced Raman spectroscopic study of the passive films formed in borate buffer on iron, nickel, chromium and stainless steel, Corros Sci, 37 (1995) 25.

K. Ogura, M. Kaneko, The pit initiation mechanism on passive iron under both open-circuit and controlled potential conditions, Corros Sci, 23 (1983) 10.

B. H. Oh, S.Y. KJang, Y.S. Shin, Experimental investigation of the threshold chloride concentration for corrosion initiation in reinforced concrete structures, Magazine of Concrete Research, 55 (2003) 8.
H. Ohshima, Theory of colloid and interfacial electric phenomena, Academic Press: New York, (2006).
K. Otte, W.W. Schmahl, R. Pentcheva, Density functional theory study of water adsorption on FeOOH surfaces, Surface science, 606 (2012) 10.
C. L. Page, Initiation of chloride-induced corrosion of steel in concrete: role of the interfacial zone, Materials and Corrosion, 60 (2009) 7.
T. Pan, A.C.T.v. Duin, Passivation of steel surface: An atomistic modeling approach aided with X-ray analyses, Materials Letters, 65 (2011) 4.
T. Pan, Quantum chemistry-based study of iron oxidation at the iron–water interface: An X-ray analysis aided study, Chemical Physics Letters, 511 (2011) 7.
Q. Pang, H. DorMohammadi, O.B. Isgor, L. Árnadóttir, Density functional theory study on the effect of OH and Cl adsorption on the surface structure of α-Fe2O3, Computational and Theoretical Chemistry, 1100 (2017) 11.
Q. Pang, H. DorMohammadi, O.B. OIsgor, L. Árnadóttir, Effects of surface defects on the interactions of Cl and α-$Fe_2O$-$_3$ (0001) surface: A density functional theory study, AVS Symposium, Oregon State University, (2017).
G. D. Peckham, I.J. McNaught, Applications of Maxwell-Boltzmann distribution diagrams, Journal of Chemical Education, 69 (1992) 5.
J. P. Perdew, K. Burke, M. Ernzerhof, ERRATA: Generalized Gradient Approximation Made Simple [Phys. Rev. Lett. 77, 3865 (1996)], Physical Review Letters, 78 (1997) 1
J. P. Perdew, K. Burke, M. Ernzerhof, Generalized Gradient Approximation Made Simple, Physical Review Letters, 77 (1996) 4.
K. Pettersson, Chloride threshold value and the corrosion rate in reinforced concrete, Cement Concrete Res, 24 (1994) 10.
K. H. Pettersson, Factors influencing chloride induced corrosion of reinforcement in concrete, Durability Build, Material Components, 1 (1996) 8.
M. R. Philpott, J.N. Glosli, S.B. Zhu, Molecular dynamics simulation of adsorption in electric double layers, Surface Science, 335 (1995) 10.
M. R. Philpott, J.N. Glosli, Screening of charged electrodes in aqueous electrolytes, Journal of Electroanalytical Society, 142 (1995) 4.
R. G. Pillai, D. Trejo, Surface condition effects on critical chloride threshold of steel reinforcement, Aci Mater J, 102 (2005) 7.
L. Pilon, H. Wang, A. d'Entremont, Recent advances in continuum modeling of interfacial and transport phenomena in electric double layer capacitors, J Electrochem Soc, 162 (2015) 21.
S. Plimpton, Fast parallel algorithms for short–range molecular dynamics, Journal of Computational Physics, 117 (1995) 42.
B. Poter, I. Parezanovic, M. Spiegel, In-situ scanning electron microscopy and electron backscatter diffraction investigation on the oxidation of pure iron, Materials at High Temperatures, 22 (2005) 9.
T. E. Pou, O.J. Murphy, V. Young, J.O.M. Bockris, L.L. Tongson, Passive films on iron: The mechanism of breakdown in chloride containing solutions, J Electrochem Soc, 131 (1984) 9.

A. Poursaee, C.M. Hansson, Reinforcing steel passivation in mortar and ore solution Cement Concrete Res, 37 (2007) 7.

G. M. Psofogiannakis, J.F. McCleerey, E. Jaramillo, A.C.T.v. Duin, ReaxFF reactive molecular dynamics simulation of the hydration of Cu-SSZ-13 zeolite and the formation of Cu dimers, The Journal of Physical Chemistry C, 119 (2015) 9.

O. Rahaman, A.C.T. van Duin, V.S. Bryantsev, J.E. Mueller, S.D. Solares, W.A. Goddard III, D.J. Doren, Development of a ReaxFF Reactive Force Field for aqueous chloride and copper chloride, Journal of Physical Chemistry A, 114 (2010) 13.

D. C. Rapaport, The art of molecular dynamics simulation, Cambridge University Press, (2004).

A. K. Rappe, W.A. Goddard, Charge equilibration for molecular dynamics simulations, The Journal of Physical Chemistry, 95 (1991) 6.

S. Rasheeduzzafar, E. Hussain, S.S. Al-Saadoun, Effect of tricalcium aluminate content of cement on chloride binding and corrosion of reinforcing steel in concrete, Aci Mater J, 89 (1993) 10.

D. Raymand, A. C. T. van Duin, D. Spångberg, W. A. Goddard, K. Hermansson, Water adsorption on stepped ZnO surfaces from MD simulation, Surf. Sci., (2010) 12.

D. Raymand, A. C. T. van Duin, D. Spångberg, W. A. Goddard, K. Hermansson, Water adsorption on stepped ZnO surfaces from MD simulation, Surface science, 604 (2010) 12.

A. K. N. Reddy, B. Rao, Mechanism of formation of pre-passive films on nickel - a ahronoellipsometric study, Can J Chemistry, 47 (1969) 6.

R. W. Revie, H.H. Uhlig, Corrosion and corrosion control 4th ed., Wiley-Interscience, New York, 2008.

J. A. Richardson, G. Wood, A study of the pitting corrosion of Al byscanning electron microscopy, Corros Sci, 10 (1970) 11.

M. F. Russo, Jr. R. Li, M. Mench, A.C.T.v. Duin, Molecular dynamic simulation of aluminumewater reactions using the ReaxFF reactive force field, International Journal of Hydrogen Energy, 36 (2011) 8.

M. P. Ryan, R.C. Newman, G.E. Thompson, An STM study of the passive film formed on iron in borate buffer solution, J Electrochem Soc, 142 (1995) 3.

A. A. Sagues, K. Lau, R.G. Powers, R.J. Kessler, Corrosion of epoxy-coated rebar in marine bridges-Part 1: A 30-year perspective, Corrosion, 66 (2010) 13.

M. Sakashita, N. Sato, Bipolar fixed charge-induced passivity, Passivity of metals, J Electrochem Soc, (1978) 5.

M. Sánchez, J. Gregori, C. Alonso, J.J. García-Jareño, H. Takenouti, F. Vicente, Electrochemical impedance spectroscopy for studying passive layers on steel rebars immersed in alkaline solutions simulating concrete pores, Electrochimica Acta, 52 (2007) 8.

M. Sánchez, J. Gregori, M.C. Alonso, J.J. García-Jareño, F. Vicente, Anodic growth of passive layers on steel rebars in an alkaline medium simulating the concrete pores, Electrochimica Acta, 52 (2006) 7.

Sánchez-Moreno, H. Takenouti, J.J. García-Jareno, F. Vicente, C. Alonso, A theoretical approach of impedance spectroscopy during the passivation ofsteel in alkaline media, Electrochimica Acta, 54 (2009) 5.

M. Sánchez-Moreno, H. Takenouti, J.J. García-Jareño, F. Vicente, C. Alonso, A theoretical approach of impedance spectroscopy during the passivation of steel in alkaline media, Electrochimica Acta, 54 (2009) 5.

N. Sato, M. Cohen, The kinetics of anodic oxidation of iron in neutral solution, J Electrochem Soc, 111 (1964) 8.

V. Schroeder, T.M. Devine, Surface enhanced Raman spectroscopy study of the galvanostatic reduction of the passive film on iron, J Electrochem Soc, 146 (1999) 10.

T. P. Senftle, S. Hong, M. M. Islam, S. B. Kylasa, Y. Zheng, Y. K. Shin, C. Junkermeier, R. Engel-Herbert, M. J. Janik, H. M. Aktulga, T. Verstraelen, A. Grama, A.C.T.v. Duin, The ReaxFF reactive force-field: development, applications and future directions, npj Computational Materials, 2 (2016) 14.

A. Soon, M. RTodorova, B. Delley, C. Stampfl, Oxygen adsorption and stability ofsurface oxides on Cu(111): a first-principles investigation, Physical Review B - Condensed Matter and Materials Physics, 73 (2006) 12.

C. Soontrapa, Y. Chen, Molecular dynamics potentials in magnetite (Fe3O4) modeling, Comput. Mater. Sci. , 50 (2011) 11.

E. Spohr, K. Heinzinger, Molecular dynamics simulation of a water/metal interface, Chemical Physics Letters, 123 (1986) 4.

E. Spohr, Molecular dynamics simulations of water and ion dynamics in the electrochemical double layer, Solid State Ionics, 150 (2002) 12.

S. Spohr, Molecular simulation of the electrochemical double layer, Electrochimica Acta 44 (1999) 9.

O. Stern, The theory of the electrolytic double layer, Z. Elektrochem. Angew. Phys. Chem., 30 (1924) 9.

A. P. Sutton, J. Chen, Long-range Finnis–Sinclair potentials, Philosophical Magazine Letters 61 (1990) 8.

C. D. Taylor, S.A. Wasileski, J.S. Filhol, M. Neurock, First principles reaction modeling of the electrochemical interface: Consideration and calculation of a tunable surface potential from atomic and electronic structure, Physical Review B, 73 (2006) 16.

M. Thomas, Chloride thresholds in marine concrete, Cement Concrete Res, (1996) 7.

N. G. Thompson, M. Yunovich, D. Dunmire, Cost of corrosion and corrosion maintenance strategies, Corros Rev, 25 (2007) 5.

J. Towns, T. Cockerill, M. Dahan, I. Foster, K. Gaither, A. Grimshaw, V. Hazlewood, S. Lathrop, Lifka, G. D. Peterson, R. Roskies, J. R. Scott, N. Wilkins-Diehr, XSEDE: Accelerating scientific discovery, Computing in Science & Engineering, 16 (2014) 13.

S. M. Trepanier, B.B. Hope, C.M. Hansson, Corrosion inhibitors in concrete - Part III. Effect on time to chloride-induced corrosion initiation and subsequent corrosion rates of steel in mortar, Cement Concrete Res, 31 (2001) 6.

P. van der Heide, X-Ray photoelectron spectroscopy: an introduction to principles and practices, John Wiley & Sons, Inc, (2011).

A. C. T. van Duin, A. Strachan, S. Stewman, Q. Zhang, X. Xu, W.A. Goddard, $ReaxFF_{SiO}$ reactive force field for silicon and silicon oxide systems, The Journal of Physical Chemistry A, 107 (2003) 9.

A. C. T. van Duin, J. M. A. Baas, B.v.d. Graaf, Delft molecular mechanics: A new approach to hydrocarbon force fields, Journal of the Chemical Society, Faraday Transactions, 90 (1994) 15.

A. C. T. van Duin, S. Dasgupta, F. Lorant, W.A. Goddard, ReaxFF: A reactive force field for hydrocarbons, The Journal of Physical Chemistry A, 105 (2001) 14.

A. C. T. van Duin, V. S. Bryantsev, M. S. Diallo, W. A. Goddard, O. Rahaman, D. J. Doren, D. Raymand, K. Hermansson, Development and validation of a ReaxFF Reactive Force Field for Cu cation/water interactions and copper metal/metal oxide/metal hydroxide condensed phases, The Journal of Physical Chemistry A, 114 (2010) 8.

A. Veluchamy, D. Sherwood, B. Emmanuel, I.S. Cole, Critical review on the passive film formation and breakdown on iron electrode and the models for the mechanisms underlying passivity, Journal of Electroanalytical Chemistry, 785 (2017) 20.

O. Verners, A.C.T.v. Duin, Comparative molecular dynamics study of fcc-Ni nanoplate stress corrosion in water, Surface Science, 633 (2015) 8.

H. von Helmholtz, Studien €uber electrische grenzschichten, Annalen der Physik 243 (1879) 6.

H. Wang, L. Pilon, Accurate simulations of electric double layer capacitance of ultramicroelectrodes, The Journal of Physical Chemistry C, 115 (2011) 9.

D. A. Welch, B.L. Mehdi, H.J. Hatcheli, R. Faller, J.E. Evans, N.D. Browning, Using molecular dynamics to quantify the electrical double layer and examine the potential for its direct observation in the in-situ TEM, Advanced Structural and Chemical Imaging, 1 (2015) 11.

R. E. Weyers, W. Pyc, M.M. Sprinkel, Estimating the service life of epoxy-coated reinforcing steel., Aci Mater J, 95 (1998) 12.

J. Williamson, O.B. Isgor, The effect of simulated concrete pore solution composition and chlorides on the electronic properties of passive films on carbon steel rebar, Corros Sci, 106 (2016) 14.

J. Williamson, V. Jafari Azad, O.B. Isgor, Modeling electronic properties of the passive films on carbon steel in simulated concrete pore solutions, J Electrochem Soc, 162 (2015) 11.

K. Yazdanfar, X. Zhang, P.G. Keech, D.W. Shoesmith, J.C. Wren, Film conversion and breakdown processes on carbon steel in the presence of halides, Corros Sci, 52 (2010) 8.

S. Yin, X. Ma, D.E. Ellis, Initial stages of $H_2O$ adsorption and hydroxylation of Fe-terminateda-$Fe_2O_3$(0 0 0 1) surface, Surface science, 601 (2007) 12.

T. Zakroczymsk, C.J. Fan, Z. Szklarska-Smialowska, Passive film formation on iron and film breakdown in a sodium hydroxide solution containing chloride ions J Electrochem Soc, 132 (1985) 4.

P. Zarzycki, S. Kerisit, K.M. Rosso, Molecular dynamics study of the electrical double layer at silver chloride-electrolyte interfaces, The Journal of Physical Chemistry C, 114 (2010) 17.

H. Zhang, E. Iype, S. V. Nedea, C.C.M. Rindt, Molecular dynamics study on thermal dehydration process of epsomite (MgSO4·7H2O), Molecular Simulation, 40 (2013) 10.

C. H. Zhang, M. Liu, Y. Jin, D.B. Sun, The corrosive influence of chloride ionspreference adsorption ona-$Al_2O_3$(0001) surface, Applied Surface Science, 347 (2015) 6.

C. Zou, Y. K. Shin, A. C.T. van Duin, H. Fangb, Z.K. Liu, Molecular dynamics simulations of the effects of vacancies on nickel self-diffusion, oxygen diffusion and oxidation initiation in nickel, using the ReaxFF reactive force field, Acta Materialia, 83 (2015) 11.

# Appendix A

# A. Appendix A: Supplementary Material of Manuscript 1

## A.1. ReaxFF parameter study

In the Manuscript 1 (Chapter2), force field parameters for simulating iron/water interface were obtained from Aryanpour et al. [1] which included all parameters for determining bond order, bond energy, valence angle energy, torsional angle energy, and van der Waals energy, as shown in Tables A1-A5. Since Aryanpour et al. [1] used these parameters to model as iron-oxyhydroxide system, we used DFT calculations to determine the surface formation energy and water adsorption energy on a Fe(110) surface and compared these values to the same energies obtained from MD simulations using the force-field parameters from Aryanpour et al. [1]. We found good agreement between the two methods.

DFT results of water adsorption energy and surface energy of Fe(110) were compared with the results of ReaxFF simulations to investigate the accuracy of ReaxFF parameters from Aryanpour et al. [1]. All DFT calculations were done using Vienna Ab Initio Simulation Package (VASP) [2-4]. The pseudopotential was described by projector augmented wave potential (PAW) [5]. The exchange-correlation potential was described by the generalized gradient approximation (GGA) of the Perdew-Burke-Ernzerhof (PBE) functional [6-8]. All calculations were considered converged when the force reached below 0.01 eV/Å.

For the calculation of the adsorption energy, a 3x3x3 surface slab was used. All Fe atoms were kept fixed while the adsorbate was relaxed. A k-point grid with a 5x5x1 Monkhorst-Pack mesh was used. The adsorption energy was defined as:

$$E_{ads} = E_{total} - E_{surface} - E_{adsorbate} \quad \text{(A-1)}$$

where $E_{ads}$ is the adsorbate energy, $E_{total}$, the energy of the adsorbate on the surface, $E_{surface}$, the energy of the surface without the adsorbate and $E_{adsorbate}$, the energy of the adsorbate in gasphase. A smaller adsorption energy, more negative, corresponds to a more favored adsorption. The calculated water adsorption energies by DFT and ReaxFF were -0.35 eV and -0.31 eV, respectively, for the most stable adsorption configuration (on a top sites), and -0.23 eV and -0.26 eV, respectively, on the second most stable site (a bridge sites).

For the calculation of surface formation energy, a 2x2x6 system and the k-point grid of 2x2x1 were used. The top two layers were relaxed while the bottom four layers were kept fixed. The surface formation energy was defined as

$$E_{formation} = E_{surface} - E_{bulk} \quad \text{(A-2)}$$

where $E_{formation}$ is the formation energy of the surface, $E_{surface}$ is the energy of the surface and $E_{bulk}$ is the energy of the bulk. A smaller formation energy corresponds to a more favored configuration or lower surface energy. The calculated surface formation energy of the Fe(110) by DFT and ReaxFF were 6.47 eV and 6.27 eV, respectively. The good agreement between the DFT calculations and ReaxFF for water adsorption energy and surface formation energy, confirms that these ReaxFF potential parameters for iron-water modeling yield meaningful match between the two methods.

Table A-1: Atomic parameters

| | **Bond radii** | | |
|---|---|---|---|
| | $r_0$ $(\dot{A})$ | $r_{0,\pi}$ $(\dot{A})$ | $r_{0,\pi\pi}$ $(\dot{A})$ |
| Fe | 1.9506 | - | - |
| O | 1.245 | 1.0548 | 0.9049 |
| H | 0.8930 | - | - |

Table A-2: Parameters for determining bond order and bond energy

| **Bond** | $P_{bo,1}$ | $P_{bo,2}$ | $P_{bo,3}$ | $P_{bo,4}$ | $P_{bo,5}$ | $P_{bo,6}$ | $P_{be,1}$ | $P_{be,2}$ | $D_e(kcal/mol)$ |
|---|---|---|---|---|---|---|---|---|---|
| Fe-H | -0.1216 | 4.5062 | 1.0000 | 0.0000 | 0.0000 | 6.0000 | -0.0717 | 0.1000 | 105.0054 |
| Fe-O | -0.0555 | 7.9897 | -0.3500 | 15.0000 | -0.3000 | 36.0000 | 0.1366 | 0.9495 | 65.7713 |
| Fe-Fe | -0.0771 | 6.4477 | -0.2000 | 15.0000 | -0.2000 | 16.0000 | 0.3595 | 1.0000 | 38.7471 |
| H-O | -0.0920 | 4.2790 | 1.0000 | 0.0000 | 0.0000 | 6.0000 | -0.5725 | 1.1150 | 160.0000 |
| H-H | -0.0790 | 6.0552 | 1.0000 | 0.0000 | 0.0000 | 6.0000 | -0.4600 | 6.2500 | 153.3934 |
| O-O | -0.1225 | 5.5000 | -0.1055 | 9.0000 | -0.1000 | 29.7503 | 0.2506 | 0.3451 | 142.2858 |

Table A-3: Parameters for determining valence angel energy

| **Angle** | $\boldsymbol{\theta_0(deg)}$ | $\boldsymbol{P_{val,1}(kcal/mol)}$ | $\boldsymbol{P_{val,2}(1/radian^2)}$ | $\boldsymbol{P_{val,3}}$ | $\boldsymbol{P_{val,4}}$ |
|---|---|---|---|---|---|
| O-Fe-H | 34.0653 | 20.1868 | 4.7461 | 1.6752 | 0.1000 |
| O-H-Fe | 0.0000 | 4.6026 | 2.5343 | 1.1051 | 0.7284 |
| O-Fe-Fe | 65.7545 | 5.6268 | 4.0645 | 2.6730 | 1.7794 |
| O-O-Fe | 73.6721 | 32.633 | 1.7223 | 1.4351 | 1.0221 |
| H-O-Fe | 59.4556 | 10.2025 | 0.7481 | 1.0000 | 1.4521 |
| Fe-O-Fe | 57.6787 | 4.8566 | 2.5768 | 1.0000 | 0.7552 |
| O-Fe-O | 79.7335 | 0.0100 | 0.1392 | 2.1948 | 0.4968 |
| H-Fe-Fe[1] | 180.0000 | -6.9970 | 24.3956 | 1.3672 | 0.7878 |
| H-Fe-Fe[2] | 21.2590 | 6.5954 | 0.9951 | 1.0000 | 2.8006 |
| Fe-H-Fe | 0.0000 | 8.2994 | 5.7832 | 1.7716 | 2.9873 |
| H-H-Fe | 0.1000 | 30.0000 | 3.4094 | 1.5166 | 2.4379 |
| H-Fe-H | 34.1965 | 6.6782 | 6.5943 | 1.5365 | 1.3895 |

Table A-4: Parameters for determining torsional angle energy

| **Torsion angle** | $\boldsymbol{V_1(kcal/mol)}$ | $\boldsymbol{V_2(kcal/mol)}$ | $\boldsymbol{V_3(kcal/mol)}$ | $\boldsymbol{P_{tor}}$ |
|---|---|---|---|---|
| O-O-O-O | -2.5000 | -25.0000 | 1.0000 | -2.5000 |
| H-O-O-O | -2.5000 | -2.5103 | -1.0000 | -2.5000 |
| H-O-O-H | 2.5000 | -22.9397 | 0.6991 | -3.3961 |

Table A-5: Parameters for determining van der Waals energy

| **Pair** | $\boldsymbol{D_{ij}(kcal/mol)}$ | $\boldsymbol{r_{vdW}(A)}$ | $\boldsymbol{\gamma_w}$ | $\boldsymbol{P_{vdW}}$ |
|---|---|---|---|---|
| Fe-H | 0.0640 | 1.6974 | 11.5167 | -1.0000 |
| Fe-O | 0.0846 | 1.4284 | 10.0808 | -1.0000 |
| H-O | 0.0283 | 1.2885 | 10.9190 | -1.0000 |

## A.2. Stages of iron corrosion in water

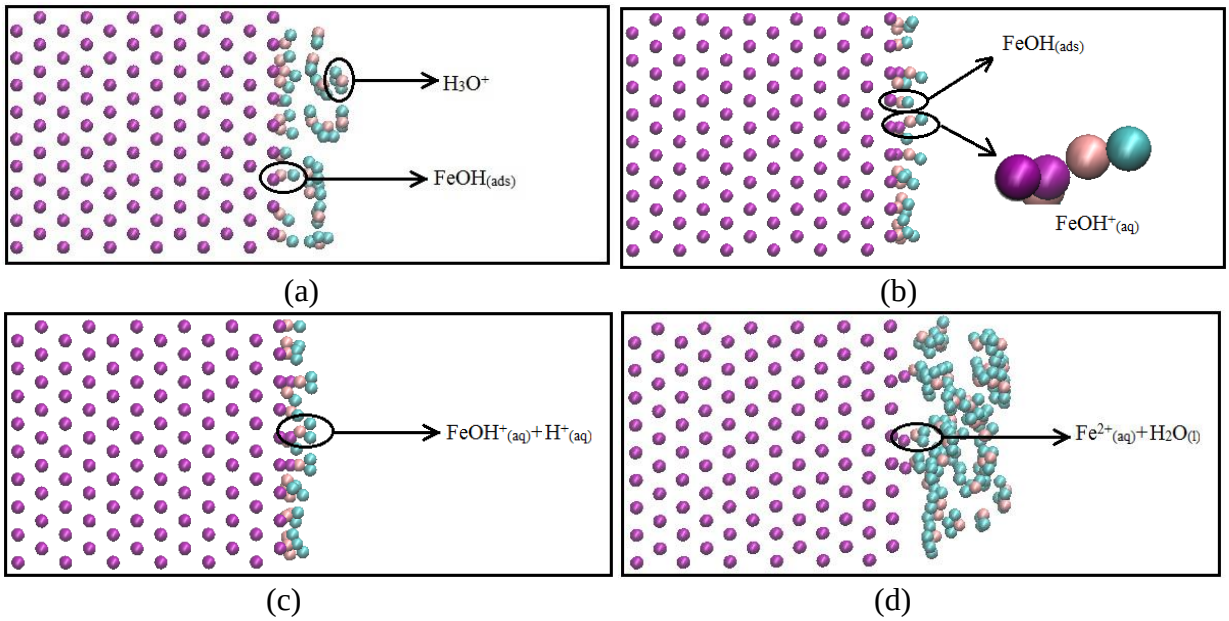


Figure A-1: Critical stages of the iron corrosion process: (a) adsorption of a $OH^-$ group on the iron surface and formation of $Fe(OH)_{ads}$ and $H_3O^+$, (b) formation of aqueous iron hydroxide, (c) bonding of aqueous iron hydroxide with $H^+$, (d) dissociation of iron atoms from the iron surface. Note that in figure (d) the species near the iron surface have been taken out to show the dissociation of iron atoms. The purple, blue and brown spheres represent iron, hydrogen and oxygen atoms, respectively.

### A.3. Simulation results for Fe(100)-water and Fe(111)-water systems

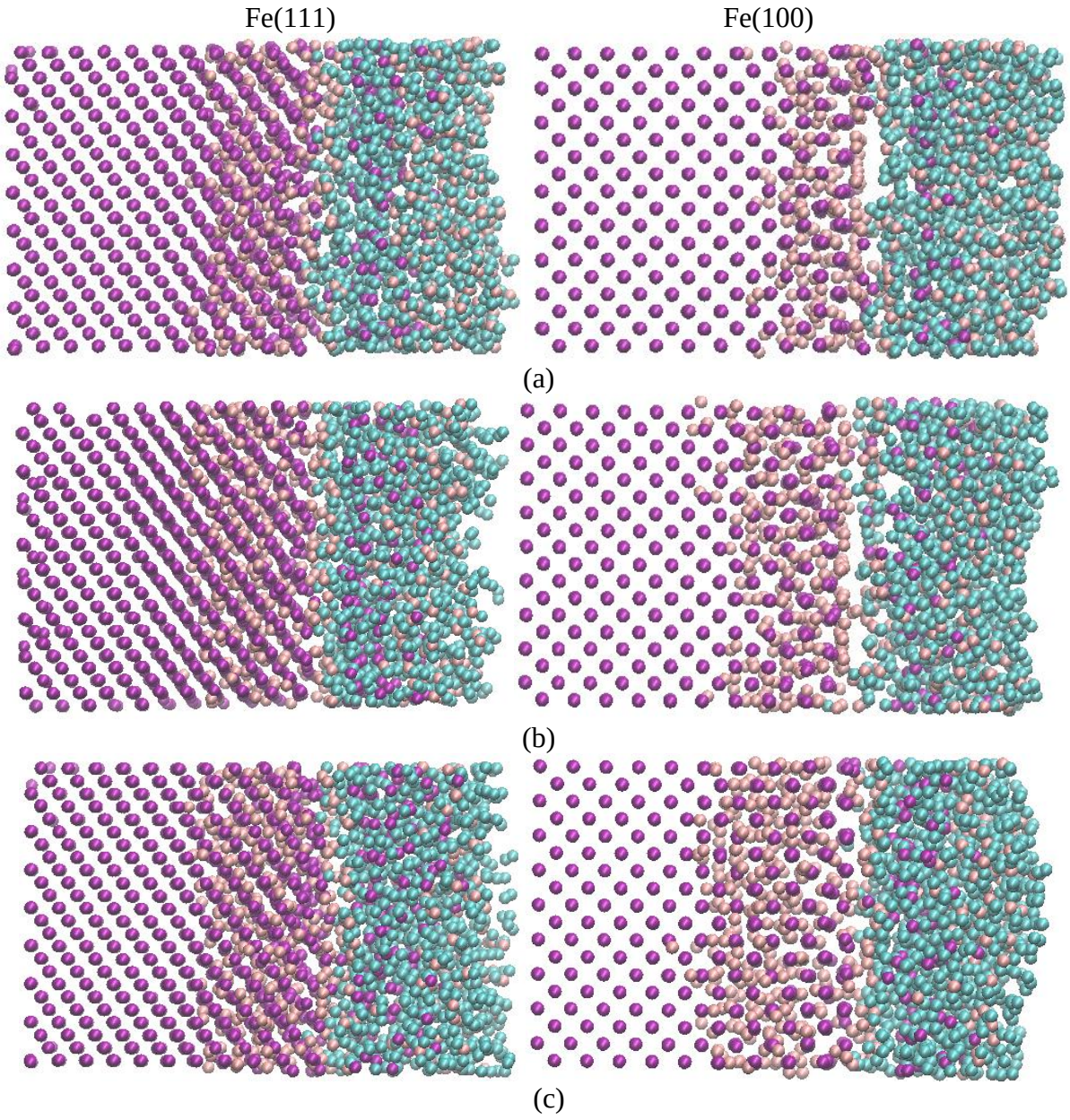


Figure A-2: Snapshots of ReaxFF-MD simulations of Fe(111)-water and Fe(100)-water systems under different external electric fields at 150 ps: (a) 20 MeV/cm, (b) 25 MeV/cm, and (c) 30 MeV/cm. The purple, blue and brown spheres represent iron, hydrogen and oxygen atoms, respectively.

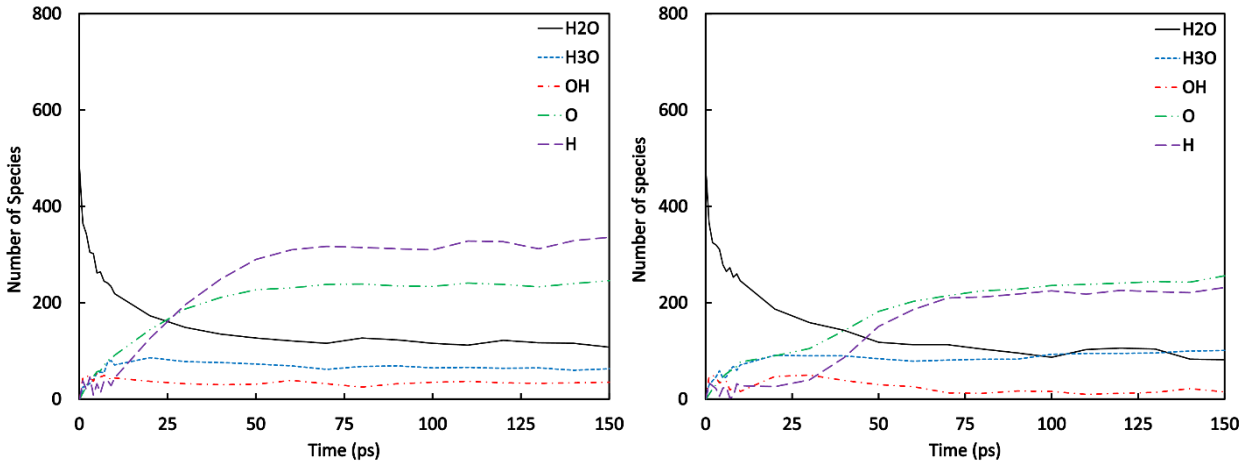


Figure A-3: Dissociation of water as a function of time under an external electric field intensity of 25 MeV/cm: (a) Fe(111)-water, and (b) Fe(100)-water. H and O plots are for oxygen and hydrogen atoms that are part of iron oxide and iron hydroxide.

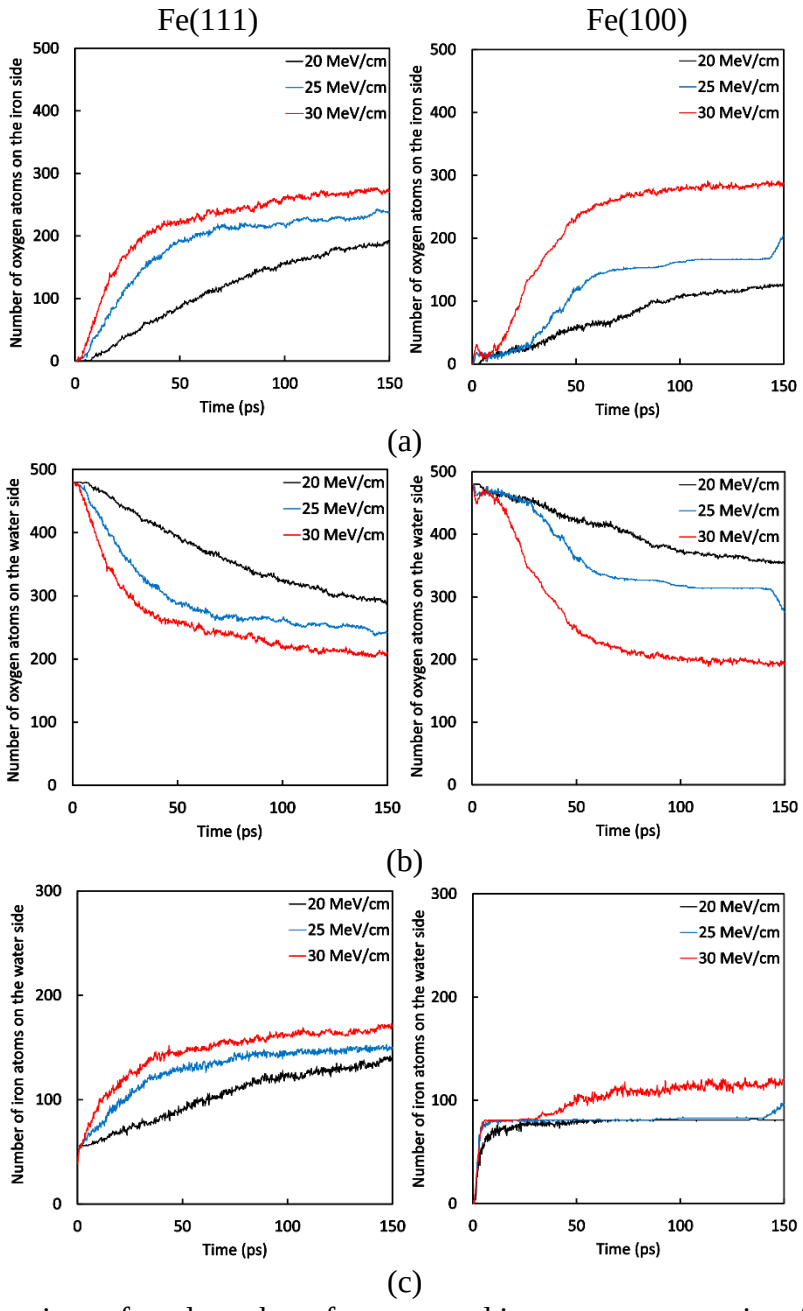


Figure A-4: Comparison of total number of oxygen and iron atoms versus time for Fe(111)-water and Fe(100)-water systems under different external electric fields: (a) number of oxygen atoms on the iron side, (b) number of oxygen atoms on the water side, (c) number of iron atoms on the water side.

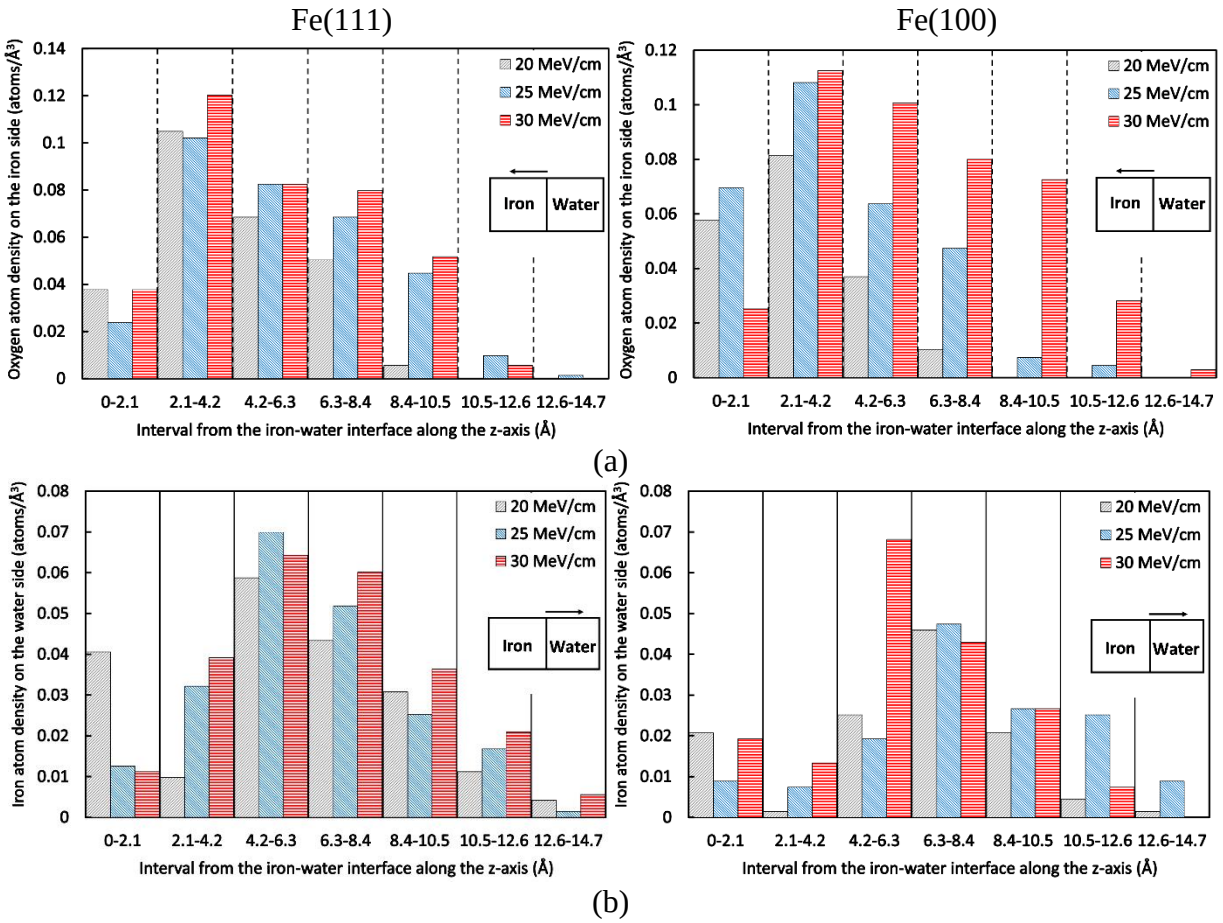


Figure A-5: Comparison of oxygen atom density and iron atom density versus z-distance from the iron-water interface for Fe(111)-water and Fe(100)-water systems under different external electric fields: (a) oxygen atom density on the iron side (Left: Fe(111); Right: Fe(100)), (b) iron atom density on the water side (Left: Fe(111); Right: Fe(100). Y-axis represents the position of the iron-water interface.

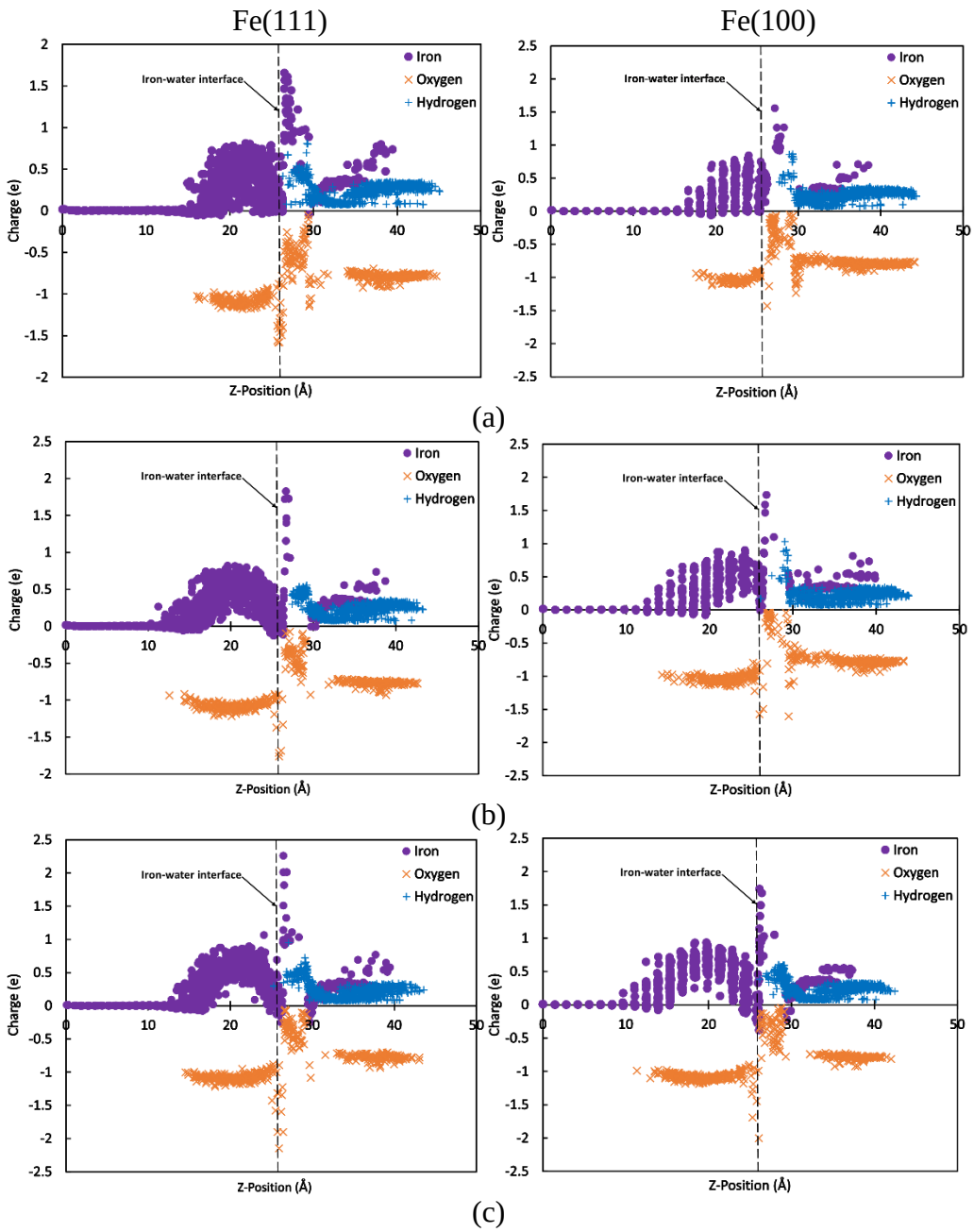


Figure A-6: Charge distributions of Fe(111)-water and Fe(100)-water systems under different external electric fields at 150 ps: (a) 20 MeV/cm, (b) 25 MeV/cm, and (c) 30 MeV/cm.

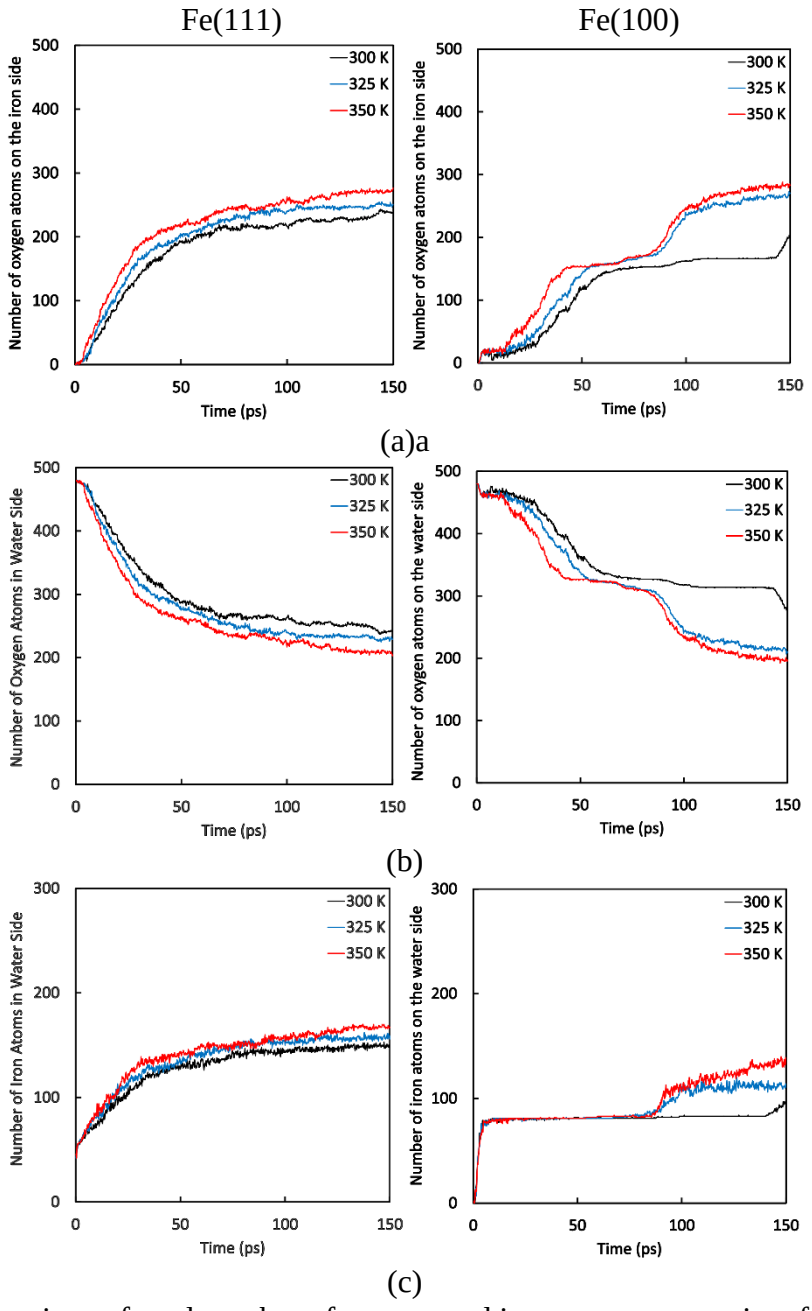


Figure A-7: Comparison of total number of oxygen and iron atoms versus time for Fe(111)-water and Fe(100)-water systems at different temperatures: (a) number of oxygen atoms on the iron side, (b) number of oxygen atoms in water side, (c) number of iron atoms on the water side. Applied external electric field in all simulations in this figure is 25 MeV/cm.

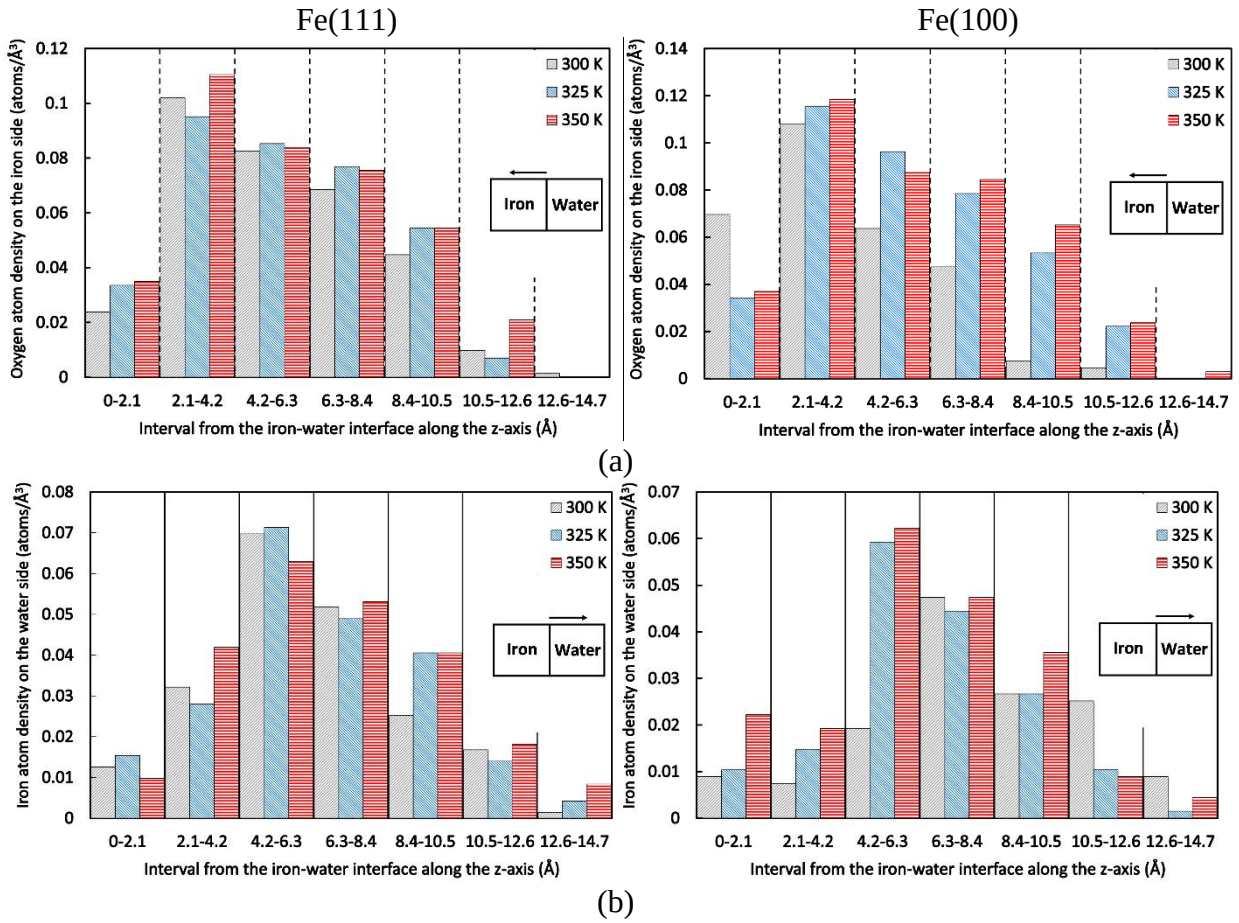


Figure A-8: Comparison of oxygen atom density and iron atom density versus z-distance from the iron-water interface for Fe(111)-water and Fe(100)-water systems at different temperatures: (a) oxygen atom density on the iron side (Left: Fe(111); Right: Fe(100)), (b) iron atom density on the water side (Left: Fe(111); Right: Fe(100)). Applied external electric field in all simulations in this figure is 25 MeV/cm. Y-axis represents the position of the iron-water interface.

**A.4. References:**

[1] M. Aryanpour, A. C. T. van Duin, J.D. Kubicki, Development of a reactive force field for iron-oxyhydroxide systems, The Journal of Physical Chemistry A, 114 (2010) 10.
[2] G. Kresse, J. Furthmüller, Efficient iterative schemes for ab initio total-energy calculations using a plane-wave basis set, Physical Review B, 54 (1996) 18.
[3] G. Kresse, J. Furthmüller, Efficiency of ab-initio total energy calculations for metals and semiconductors using a plane-wave basis set, Computational Materials Science, 6 (1996) 36.
[4] G. Kresse, J. Hafner, Ab initio molecular dynamics for liquid metals, Physical Review B, 47 (1993) 4.
[5] G. Kresse, J. Hafner, Ab initio molecular-dynamics simulation of the liquid-metal — amorphous-semiconductor transition in germanium, Physical Review B, 49 (1994) 21.
[6] P.E. Blöchl, Projector augmented-+rave method, Physical Review B, 50 (1994) 27.
[7] J.P. Perdew, K. Burke, M. Ernzerhof, Generalized Gradient Approximation Made Simple, Physical Review Letters, 77 (1996) 4.
[8] J.P. Perdew, K. Burke, M. Ernzerhof, ERRATA: Generalized Gradient Approximation Made Simple [Phys. Rev. Lett. 77, 3865 (1996)], Physical Review Letters, 78 (1997) 1.

# Appendix B

# B. Appendix B: Supplementary material of Manuscript 2

## B.1. ReaxFF-MD modeling of iron corrosion in the neutral electrolyte

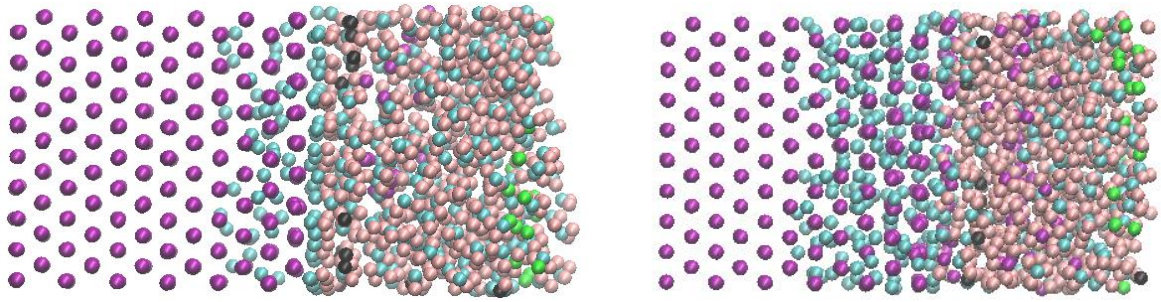

(a) (b)

Figure B-1: Snapshots of ReaxFF-MD simulations of iron-neutral solution system with various applied electric field distributions using Helmholtz model at 150 ps. The electric field intensity at the iron surface is (a) 20 Mev/cm, (b) 25 Mev/cm. The purple, blue, brown, green and black spheres represent iron, hydrogen, oxygen, sodium and chlorine atoms, respectively.

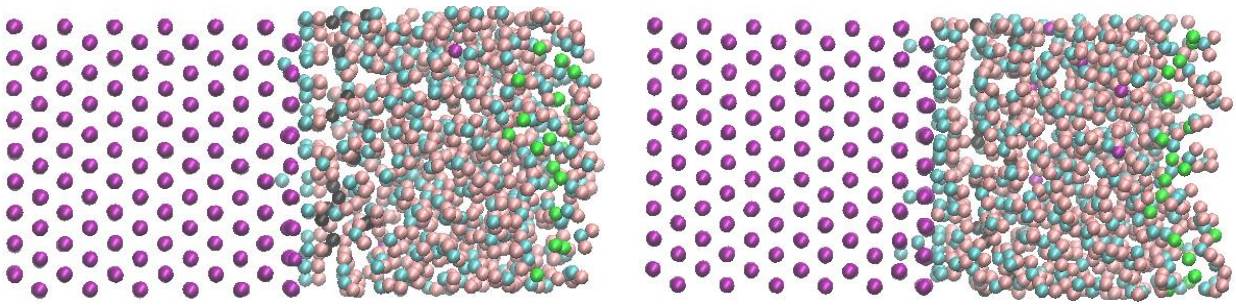

(a) (b)

Figure B-2: Snapshots of ReaxFF-MD simulations of iron-neutral solution system with various applied electric field distributions using Gouy-Chapman model at 150 ps. The electric field intensity at the iron surface is (a) 20 Mev/cm, (b) 25 Mev/cm. The purple, blue, brown, green and black spheres represent iron, hydrogen, oxygen, sodium and chlorine atoms, respectively.

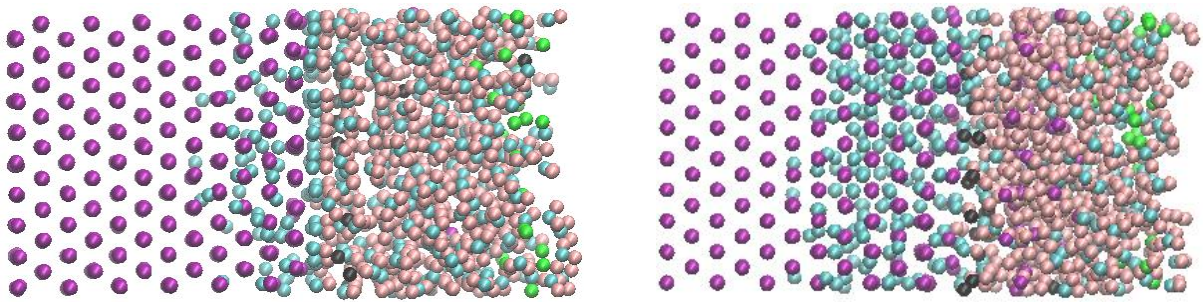

(a) (b)

Figure B-3: Snapshots of ReaxFF-MD simulations of iron-neutral solution system with various applied electric field distributions using Stern model at 150 ps. The electric field intensity at the iron surface is (a) 20 Mev/cm, (b) 25 Mev/cm. The purple, blue, brown, green and black spheres represent iron, hydrogen, oxygen, sodium and chlorine atoms, respectively.

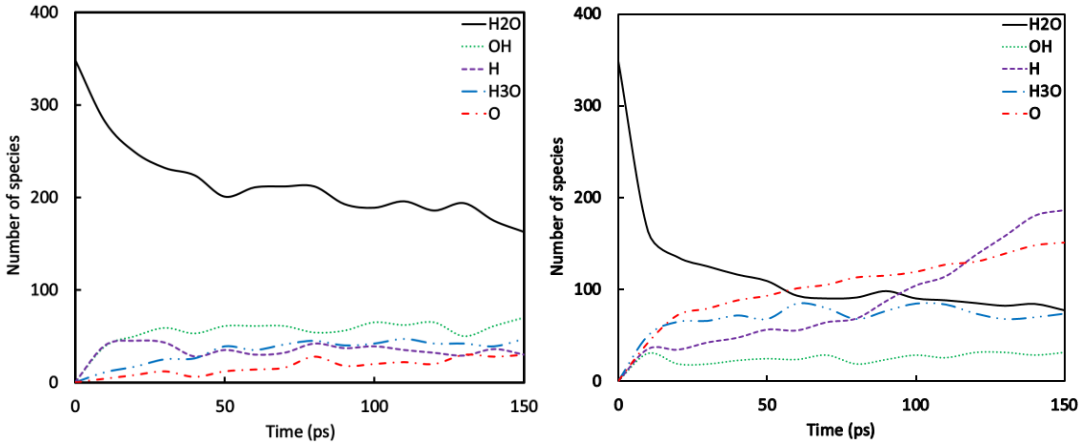


(a) (b)

Figure B-4: Dissociation of water as a function of time of iron-neutral solution system with various applied electric field distributions using Helmholtz model at 150 ps. The electric field intensity at the iron surface is (a) 20 Mev/cm, (b) 25 Mev/cm. H and O plots are for hydrogen and oxygen atoms that are part of iron oxide and iron hydroxide.

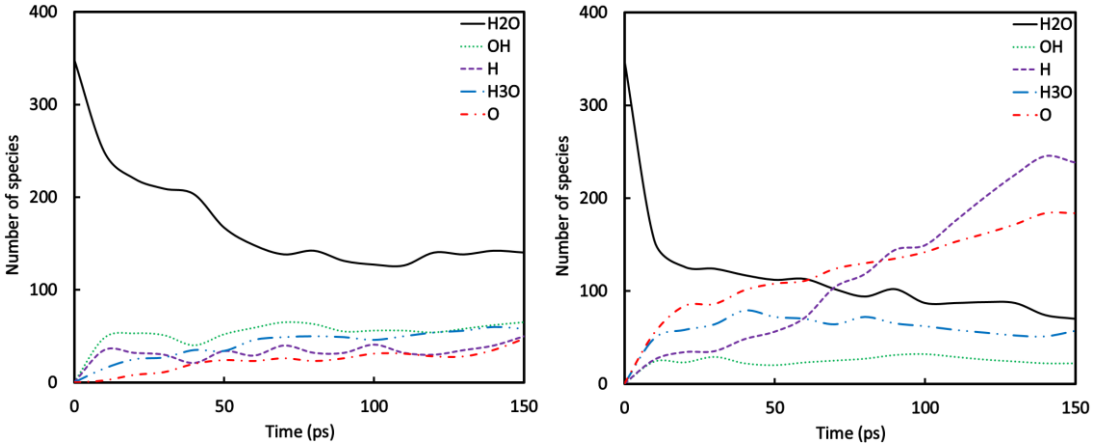


(a) (b)

Figure B-5: Dissociation of water as a function of time of iron-neutral solution system with various applied electric field distributions using Stern model at 150 ps. The electric field intensity at the iron surface is (a) 20 Mev/cm, (b) 25 Mev/cm. H and O plots are for hydrogen and oxygen atoms that are part of iron oxide and iron hydroxide.

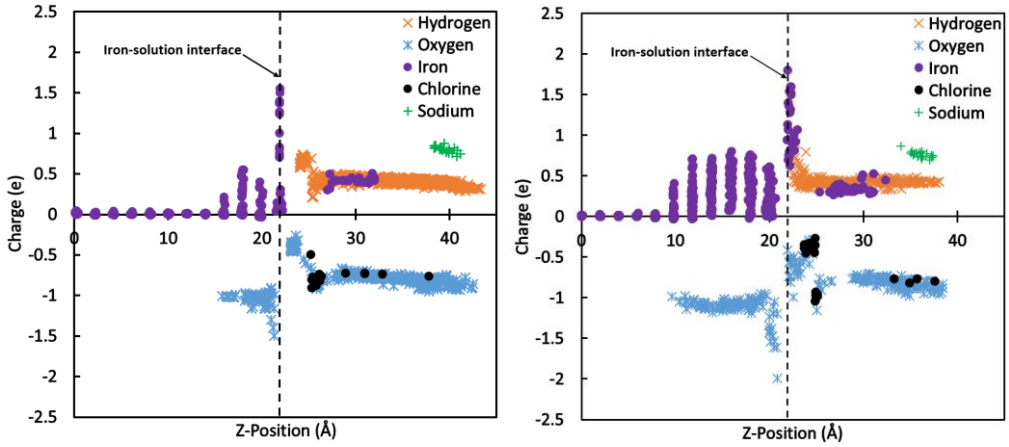


(a) (b)

Figure B-6: Charge distributions of iron-neutral solution system with various applied electric field using Helmholtz model at 150 ps. The electric field intensity at the iron surface is (a) 20 Mev/cm, (b) 25 Mev/cm.

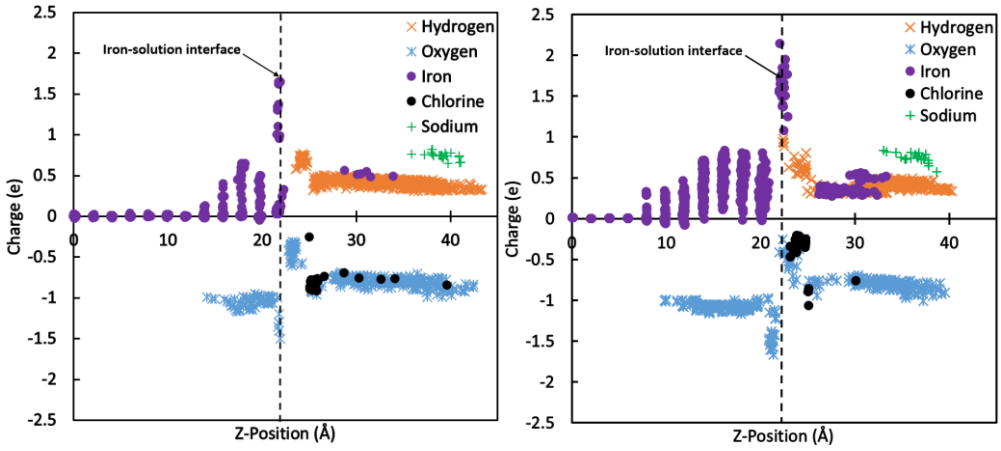


(a) (b)

Figure B-7: Charge distributions of iron-neutral solution system with various applied electric field using Stern model at 150 ps. The electric field intensity at the iron surface is (a) 20 Mev/cm, (b) 25 Mev/cm.

**B.2. ReaxFF-MD modeling of iron passivation in the alkaline electrolyte**

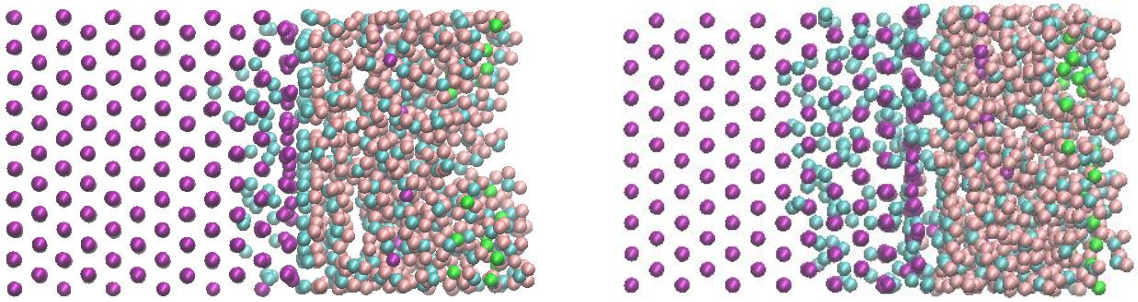

(a) (b)

Figure B-8: Snapshots of ReaxFF-MD simulations of iron-highly alkaline solution system with various applied electric field distributions using Helmholtz model at 150 ps. The electric field intensity at the iron surface is (a) 20 Mev/cm, (b) 25 Mev/cm. The purple, blue, brown, green and black spheres represent iron, hydrogen, oxygen, sodium and chlorine atoms, respectively.

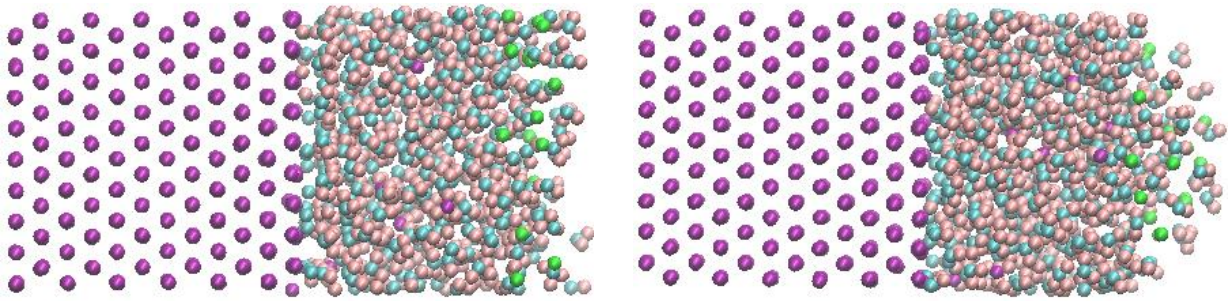

(a) (b)

Figure B-9: Snapshots of ReaxFF-MD simulations of iron-highly alkaline solution system with various applied electric field distributions using Gouy-Chapman model at 150 ps. The electric field intensity at the iron surface is (a) 20 Mev/cm, (b) 25 Mev/cm. The purple, blue, brown, green and black spheres represent iron, hydrogen, oxygen, sodium and chlorine atoms, respectively.

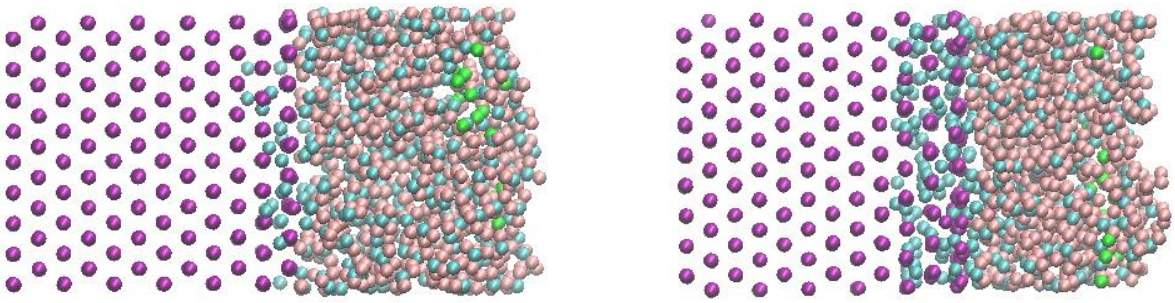

(a) (b)

Figure B-10: Snapshots of ReaxFF-MD simulations of iron-highly alkaline solution system with various applied electric field distributions using Stern model at 150 ps. The electric field intensity at the iron surface is (a) 20 Mev/cm, (b) 25 Mev/cm. The purple, blue, brown, green and black spheres represent iron, hydrogen, oxygen, sodium and chlorine atoms, respectively.

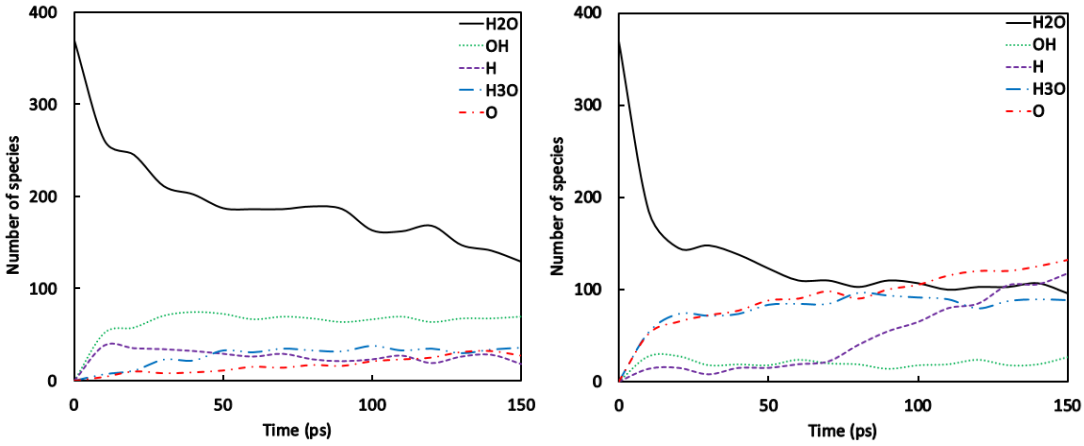


(a) (b)

Figure B-11: Dissociation of water as a function of time of different iron-solution systems with various applied electric field distributions using Helmholtz model at 150 ps. The electric field intensity at the iron surface is (a) 20 Mev/cm, (b) 25 Mev/cm. H and O plots are for hydrogen and oxygen atoms that are part of iron oxide and iron hydroxide.

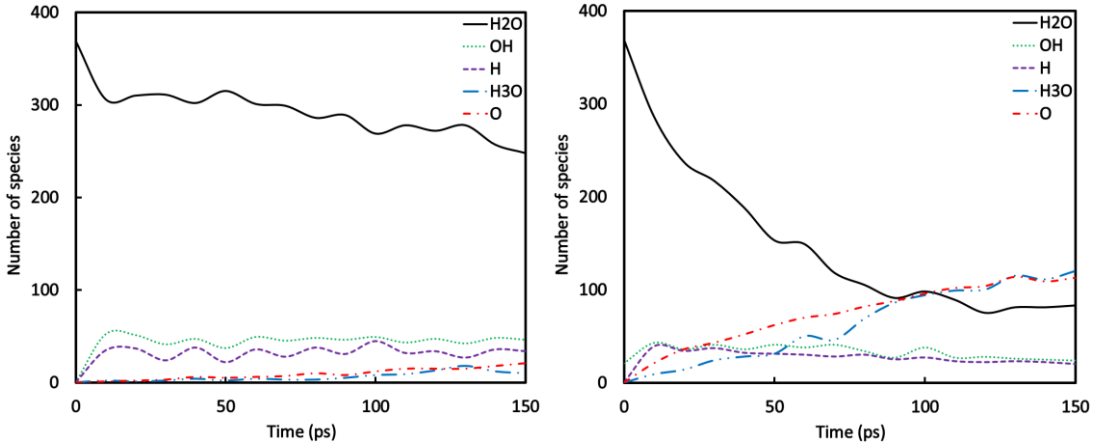


(a) (b)

Figure B-12: Dissociation of water as a function of time of iron-highly alkaline solution system with various applied electric field distributions using Stern model at 150 ps. The electric field intensity at the iron surface is (a) 20 Mev/cm, (b) 25 Mev/cm. H and O plots are for hydrogen and oxygen atoms that are part of iron oxide and iron hydroxide.

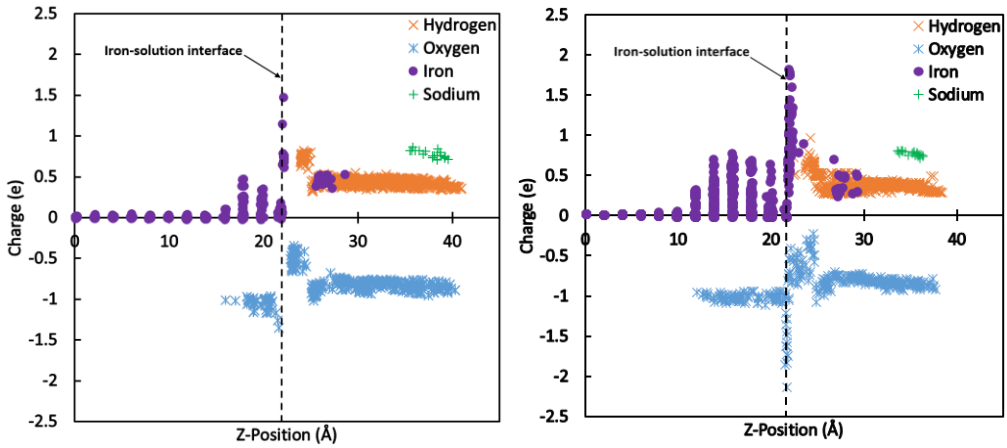


(a) (b)

Figure B-13: Charge distributions of iron-highly alkaline solution system with various applied electric field using Helmholtz model at 150 ps. The electric field intensity at the iron surface is (a) 20 Mev/cm, (b) 25 Mev/cm.

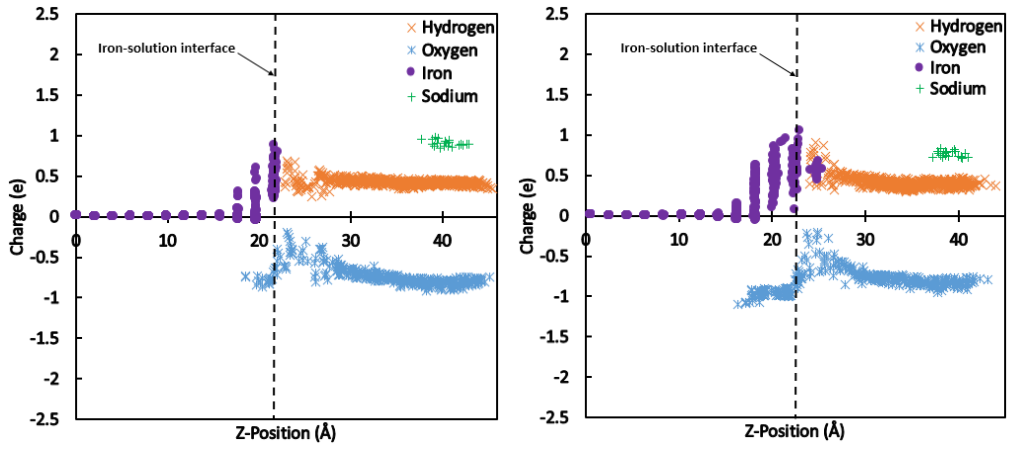


(a) (b)

Figure B-14: Charge distributions of iron-highly alkaline solution system with various applied electric field using Stern model at 150 ps. The electric field intensity at the iron surface is (a) 20 Mev/cm, (b) 25 Mev/cm.